EXTRAPLANETARY EXPLORATION USING ELECTRIC SOLAR WIND SAIL

CHONGGANG DU

A DISSERTATION SUBMITTED TO
THE FACULTY OF GRADUATE STUDIES
IN PARTIAL FULFILLMENT OF THE REQUIREMENTS
FOR THE DEGREE OF

DOCTOR OF PHILOSOPHY

GRADUATE PROGRAM IN
EARTH AND SPACE SCIENCE AND ENGINEERING
YORK UNIVERSITY
TORONTO, ONTARIO
APRIL 2022

Abstract

This doctoral research investigates the problem of the dynamics and control of extraplanetary exploration using an electric solar wind sail (E-sail). The E-sail is a novel propellantless propulsion technology that harvests energy by repelling the charged particles in solar wind. It consists of a spinning central spacecraft connected by kilometer-long and thin positively charged tethers with remote units at their tips. The mathematical formulation of the E-sail is modeled by the nodal position finite element method to capture the coupling effects of orbital and self-spinning motions of the E-sail, and the elastic deformation of tethers. Further extension of this model is developed to investigate the rigid-flexible coupling effect on the attitude dynamics and spin control of E-sail by considering the attitude dynamics of the central spacecraft using natural coordinate formulation. To thoroughly investigate the stability control of the flexible E-sail in attitude maneuver by the high-fidelity tether dynamic model, a simplified reduced-order analytical model is derived. Based on the above models, the main contributions of this dissertation are introduced as follow. First, the unknown mechanism behind the periodic coning motion is revealed and the analytic solution of its frequency is derived and verified. In particular, the equilibrium shape of the main tether of the E-sail is estimated.

The upper and lower spin rate bounds are revisited to reveal the physics that dictates these bounds and analytic expressions are provided to ensure the proper operation of E-sail. It also indicates that the auxiliary tethers are essential for a stable configuration of E-sail at non-zero sail angle. Second, it is found that the deformation motion of flexible tethers will cause the offset of center of mass and thrust of E-sail, which generates disturbance torques on the central spacecraft. The analysis indicates that E-sail is more stable if the spin plane passes the center of mass of the central spacecraft, and the control performance of E-sail spin rate is demonstrated even in the tether deployment process. Finally, the attitude of the E-sail can be controlled by a simple PD controller, or stably controlled by a control law developed from the reduced-order analytical model. It also shows that the high-fidelity E-sail model provides virtual testbed to evaluate the control performance of the control strategy for E-sail attitude control. Based on the reduced-order analytical model, the trajectory tracking problems in extraplanetary exploration missions are studied.

Dedication

I dedicate my dissertation work to my family.

Acknowledgements

The work for this dissertation was done at the Space Engineering Design Laboratory, Department of Mechanical Engineering, York University.

First of all, I would like to express my heartfelt gratitude to my supervisor Prof. George Z. H. Zhu, for the continuous support and constructive suggestions of my PhD study and related research. I benefit greatly from his rigorous academic attitude, motivation, unremitting efforts, and immense knowledge. I could not have imaging having a better supervisor for my Ph.D. study.

Besides, I would like to thank my supervisory committee: Prof. Dan Zhang, and Prof. Franz Newland, for their valuable comments, instruction, and encouragements during this doctoral research.

My sincere appreciation also goes to my fellow group members, Dr. Gangqi Dong, Dr. Gangqiang Li, Dr. Peng Li, Dr. Junjie Kang, Dr. Udai Bindra, Dr. Latheepan Murugathasan, Mr. Jude Furtal, for their accompanied and help me during my Ph.D. study.

To my family, this dissertation is dedicated to you. I can hardly imagine myself going all the way down without your unconditional understanding, supporting, and encouragement throughout the years. In particular, my

deepest gratitude goes to my girlfriend Huang Huang, for her firmest support and great companion from thousands of miles away. Without your support, it would not be possible to complete this Ph.D. program.

Finally, I would thank you everyone for your support during my PhD study, I wish you all the best.

Table of Contents

Abstract ii

Dedication iv

Acknowledgements v

Table of Contents vii

List of Tables xiv

List of Figures xv

List of Symbols xxv

List of Abbreviations xxix

Chapter 1 Introduction and Justification 1

- 1.1 Backgrounds 1
  - 1.1.1 E-sail Configurations 2
  - 1.1.2 Pros and Cons of the E-sail 6
- 1.2 Justification of Research 7
  - 1.2.1 Dynamic modeling of the E-sail 8
    - 1.2.1.1 Challenges 8
    - 1.2.1.2 Limitations of Existing Treatments 10
  - 1.2.2 Attitude Control and Orbital Maneuver of the E-sail 12
    - 1.2.2.1 Challenges 12

1.2.2.2 Limitations of Existing Treatments 13

1.3 Objectives of Proposed Research 14

1.4 Methodology of Approach 15

1.5 Assumption of Dissertation 18

1.6 Layout of Dissertation 19

1.7 List of Publications 20

Chapter 2 Literature Review 22

2.1 Propulsive Force 22

2.2 Propulsive Acceleration and Sail Angle Models 24

2.3 Dynamic Modeling of the E-sail 27

2.4 Attitude Control of the E-sail 30

2.4.1 Orientation Control of the E-sail 30

2.4.2 Spin Rate Control of E-sail 32

2.5 E-sail Missions 33

2.5.1 Non-Keplerian Orbit Missions 33

2.5.2 Outer Solar System Missions 35

2.5.3 Terrestrial Planets and Asteroids Missions 36

2.5.4 Artificial Lagrangian Point Maintenance Missions 37

2.5.5 Mitigate Earth-threatening Asteroid Missions 37

Chapter 3 Mathematical Formulation of E-sail 39

3.1 System Description 39

3.1.1 Coordinate Systems 39

3.1.2 Relative Orientation of the Coordinate Systems.................. 43

3.2 Propulsive Force Formulation.. 52

3.3 Modeling of E-sail by Nodal Position Finite Element Method .. 55

3.3.1 Kinetic Energy 57

3.3.2 Strain Energy.. 59

3.3.3 Potential Energy and the External Forces 59

3.3.4 Equations of motion of the E-sail.. 61

3.4 Mathematic Formulation of the Generalized E-sail Model 62

3.4.1 Kinetic Energy of Central Spacecraft 64

3.4.2 Potential Energy of the Central Spacecraft.......................... 67

3.4.3 Angular Velocity and Acceleration of Central Spacecraft..... 69

3.4.4 Constraint Equations of the Central spacecraft................... 70

3.4.5 Equations of motion of the E-sail.. 71

3.4.6 Disturbance Torques 73

3.5 Reduced Order Model of Attitude Equations of E-sail.............. 75

3.5.1 Moment of Inertia of Reduced Order Model of E-sail 77

3.5.2 Derivation of Kinematic Differential Equations of E-sail..... 80

3.5.3 Attitude Dynamical Equations of E-sail............................... 81

Chapter 4 Research on Model Validation and Dynamic Characteristics of the E-sail.. 83

4.1 Convergence of Tether Element Mesh 83

4.2 Dynamic Performance of the E-sail without Propulsive Force.. 86

  4.2.1 NPFEM E-sail Model.. 88

  4.2.2 Generalized E-sail Model 92

4.3 Coning Motion of the E-sail.. 97

  4.3.1 Mechanism of Periodic Coning Motion 97

  4.3.2 Influence of the E-sail Parameters on Coning Motion........ 102

4.4 Spin Rate of the E-sail... 109

  4.4.1 Upper Bound of Spin Rate.. 110

  4.4.2 Lower Bound of Spin Rate.. 112

  4.4.3 Influence of the E-sail Parameters on Spin Rate 119

Chapter 5 Parametric Analyses of the NPFEM E-sail Model.................. 124

5.1 Stability of the E-sail Configuration Subject to Solar Wind Speed Fluctuations 124

  5.1.1 Stability of the E-sail Configuration with and without Auxiliary Tethers.. 125

  5.1.2 Dynamic Responses of the E-sail with Auxiliary Tethers .. 130

5.2 Influence of Propulsive Force Magnitude on E-sail Response. 135

5.3 Influence of the Sail Angle on E-sail Response 141

Chapter 6 Parametric Analyses of the Generalized E-sail Model 150

6.1 Dynamic Response of E-sail with Different Attitudes 150

6.2 Dynamic Response of E-sail with Different Configurations 158
6.3 Dynamic Response of E-sail with Solar Wind Fluctuations 163
  6.3.1 Influence of Solar Wind Fluctuations on E-sail Dynamic Performance 163
  6.3.2 Influence of Geometrical Configuration on E-sail Dynamic Performance 168
6.4 Spin Rate Control of E-sail 173
  6.4.1 Spin Rate Control Strategy 173
  6.4.2 Spin Rate Control of the Fully Deployment E-sail 176
  6.4.3 Spin Rate Control of E-sail in Tether Deployment Process 179
Chapter 7 Attitude Control and Trajectory Tracking of E-sail 182
7.1 E-sail Sail Angle Control with a Simple PD Control Strategy 182
7.2 Attitude Control and Stability Analysis of E-sail 187
  7.2.1 Attitude Control Law 188
    7.2.1.1 Derivation of Control Strategy 188
    7.2.1.2 Mapping of Control Torque to Control Force 193
    7.2.1.3 Mapping of Control Torque to Control Voltage 194
  7.2.2 Parameter Analysis 195
    7.2.2.1 Attitude Control of Reduced Order E-sail Model 196
    7.2.2.2 Attitude Control of NPFEM E-sail Model 203
    7.2.2.3 Influence of Control Gains on Attitude Control of

NPFEM E-sail Model 210

7.2.2.4 Attitude Control of NPFEM Model by Modulating the Voltage of Main Tethers 214

7.3 Trajectory Design and Tracking for Mars Exploration Using E-sail 216

7.3.1 Minimum-time Earth-Mars Trajectory of E-sail 217

7.3.1.1 Mathematical Model of E-sail Propulsive Force...... 217

7.3.1.2 Orbital Dynamic Equations and Trajectory Optimization of E-sail 220

7.3.1.3 Numerical Results 221

7.3.2 Earth-Mars Trajectory Tracking of E-sail with Voltage Modulation 225

7.3.2.1 Mathematical Model of E-sail Propulsive Force Torque 225

7.3.2.2 Attitude Tracking Control of the E-sail using Charged Main Tethers... 227

7.3.2.3 Numerical Results 229

Chapter 8 Conclusion and Future Work 232

8.1 General Conclusion.. 232

8.2 Thesis Contributions 233

8.2.1 Mathematic Formulations of the E-sail.............................. 233

8.2.2 Dynamic Characteristics of the E-sail 234

8.2.3 Control Strategy of the E-sail 235

8.3 Further Work 235

Bibliography 237

List of Tables

Table 2-1 Coefficients of the sail and thrust angles relationship. 25

Table 2-2 Coefficients of dimensionless acceleration vs sail angle. 25

Table 4-1 Parameters of the E-sail system. 88

Table 4-2 Properties of the generalized E-sail model. 93

Table 4-3 Parameters of the parametric investigation. 103

Table 4-4 Periods of the coning motion. 103

Table 4-5 Parameters of the spin rate bounds investigation. 120

Table 5-1 Parameters of the E-sail configuration. 127

Table 5-2 Parameters of the parametric investigation of E-sail. 131

Table 5-3 Coefficients of the sail and thrust angles relationship. 146

Table 5-4 Coefficients of dimensionless acceleration vs sail angle. 147

Table 6-1 Parameters of the parametric investigation. 163

Table 7-1 Parameters in attitude control. 196

Table 7-2 Parameters in feedback linearization controller. 202

Table 7-3 Parameters of the control gains. 210

Table 7-4 Parameters of the Earth-Mars trajectory optimization. 222

List of Figures

Figure 1-1 The Sketch of E-sail configuration. 2

Figure 1-2 Sketch of the solar wind. 4

Figure 1-3 Two basic types of E-sail. 4

Figure 1-4 Material of the (a) main tether and (b) auxiliary tether [4] 5

Figure 1-5 Deployment strategies of the E-sail (a) radial deployment and (b) tangential deployment [7]. 6

Figure 1-6 Time histories of solar wind velocity obtained from Voyager 2. 10

Figure 1-7 Methodology of approach. 16

Figure 2-1 Sketch of E-sail sail and thrust angles. 24

Figure 2-2 Sketch of non-Keplerian orbit 35

Figure 3-1 Schematic of E-sail coordinate systems. 41

Figure 3-2 E-sail orientation and the related angles 44

Figure 3-3 Three configurations of the E-sail. 51

Figure 3-4 Schematic of the disturbance torque. 74

Figure 4-1 Convergence of the E-sail with different numbers of the tether elements 85

Figure 4-2 E-Sail initial configuration on $O_bX_bY_b$ plane. 87

Figure 4-3 Time histories of (a) the Sun/E-sail distance and (b) the sail angle with zero propulsive force. 90

Figure 4-4 Time histories of the adjacent angles with zero propulsive force. 91

Figure 4-5 Time histories of distances of remote unit to the reference plane with zero propulsive force. 91

Figure 4-6 Time histories of (a) the length of 1st main and auxiliary tethers (b) tensions in the main and auxiliary tethers and (c) spin rate of the E-sail with zero propulsive force. 92

Figure 4-7 Time histories of (a) the Sun-E-sail distance (b) in-plane libration angle with zero propulsive force. 95

Figure 4-8 Time histories of (a) the spin rate and (b) accelerations of the central spacecraft in the $O_{cb}X_{cb}Y_{cb}Z_{cb}$ coordinate system. 96

Figure 4-9 Time histories of (a) the tensions in the main and auxiliary tethers (b) the spin rate (c) the coning angle (d) the nutation angle (e) CM and (f) CT of the E-sail, respectively. 96

Figure 4-10 Free-body diagram of E-sail.. 102

Figure 4-11 Time histories of the coning motion of different masses m_{re} without (a) and with (b) the auxiliary tethers. 107

Figure 4-12 Time histories of the coning motion of different initial spin rates ω_0 without (a) and with (b) the auxiliary tethers. 107

Figure 4-13 Tensions acting on the (a) main and (b) auxiliary tethers with Case D. 108

Figure 4-14 Comparisons of (a) the torques and (b) the coning angles with different cases. 108

Figure 4-15 Free-body diagram of the tether. 111

Figure 4-16 Ratio of centrifugal force over propulsive force vs the strain in main tether. 119

Figure 4-17 Upper bound of the spin rate as the functions of (a) the coning angle and (b) the mass of remote unit. 121

Figure 4-18 Lower bound of the spin rate as the functions of (a) the coning angle (b) the mass of remote unit and (c) the sail angle. 122

Figure 5-1 Time histories of the adjacent angles with the solar wind fluctuations. 129

Figure 5-2 Time histories of the distances of remote units to the reference plane with the solar wind fluctuations. 130

Figure 5-3 Time histories of E-sail responses with different masses m_{re} subject to solar wind velocity fluctuations. 133

Figure 5-4 Time histories of E-sail responses with different spin rate ω subject to solar wind velocity fluctuations. 134

Figure 5-5 Time histories of (a) the increment of orbit radius of the central spacecraft and (b) the E-sail thrust with different coefficients K_i. 138

Figure 5-6 Time histories of (a) the sail angle and (b) the thrust angle with different coefficients K_i. 138

Figure 5-7 Variation trends of the E-sail configuration with different coefficients K_i (a) $K_1=3.09$ [13] (b) $K_2=11.74$ [44] and (c) $K_3=56.36$ [47]. 139

Figure 5-8 Time histories of (a) coning angle and (b) spin rate ratio with different coefficients K_i. 141

Figure 5-9 E-sail orientation in the orbital plane $O_oY_oZ_o$. 143

Figure 5-10 Time histories of (a) the increment of orbital radius of the central spacecraft and (b) the E-sail thrust with the different initial sail angles. 143

Figure 5-11 Time histories of (a) the sail angle and (b) the thrust angle with the different initial E-sail sail angles. 144

Figure 5-12 Time histories of (a) the increment of orbital radius of the central spacecraft and (b) the E-sail thrust with the different initial sail angles. 145

Figure 5-13 Time history of (a) the sail angle and (b) the thrust angle with the different initial sail angles. 146

Figure 5-14 (a) Thrust angle vs sail angle, (b) dimensionless acceleration vs the sail angle. 148

Figure 6-1 E-sail attitude with different sail angles. 151

Figure 6-2 Time histories of (a) the Sun/E-sail distance increment (b) in-plane libration angle with different sail angles. 152

Figure 6-3 Time histories of angular velocities of the central spacecraft in the $O_{cb}X_{cb}Y_{cb}Z_{cb}$ coordinate system with different sail angles. 153

Figure 6-4 Time histories of (a) and (b) the E-sail resultant propulsive force components in the $O_{cb}X_{cb}Y_{cb}Z_{cb}$ coordinate system with different sail angles. 155

Figure 6-5 Time histories of the CM (a) and (b) and the CT (c) and (d) of the E-sail in the $O_{cb}X_{cb}Y_{cb}Z_{cb}$ coordinate system with different sail angles. 155

Figure 6-6 Time histories of (a) tension in the main and auxiliary tethers (b) E-sail spin rate (c) nutation angle and (d) coning angle with different sail angles. 157

Figure 6-7 Variation trends of the E-sail configuration. 158

Figure 6-8 Time histories of (a) the Sun/E-sail distance increment (b) in-plane libration angle with different configurations. 160

Figure 6-9 Time histories of angular velocities of the central spacecraft in the

$O_{cb}X_{cb}Y_{cb}Z_{cb}$ coordinate system with different configurations. ... 161

Figure 6-10 Time histories of the E-sail resultant propulsive force components in the $O_{cb}X_{cb}Y_{cb}Z_{cb}$ frame with different configurations. 161

Figure 6-11 Time histories of (a) CM and (b) CT of the E-sail in the $O_{cb}X_{cb}Y_{cb}Z_{cb}$ coordinate system with different configurations. 162

Figure 6-12 Time histories of (a) tension in main and auxiliary tethers (b) spin rate (c) nutation angle and (d) coning angle of the E-sail with different configurations... 162

Figure 6-13 Time histories of (a) the Sun/E-sail distance increment (b) in-plane libration angle with the solar wind fluctuations. 165

Figure 6-14 Time histories of the E-sail resultant propulsive force components in the $O_{cb}X_{cb}Y_{cb}Z_{cb}$ frame with the solar wind fluctuations....... 165

Figure 6-15 Time histories of angular velocity of the central spacecraft in the $O_{cb}X_{cb}Y_{cb}Z_{cb}$ frame with the solar wind fluctuations. 166

Figure 6-16 Time histories of (a) CM and (b) CT of the E-sail in the $O_{cb}X_{cb}Y_{cb}Z_{cb}$ frame with the solar wind fluctuations. 167

Figure 6-17 Time histories of (a) tension in main and auxiliary tethers (b) spin rate (c) nutation angle and (d) coning angle of the E-sail with the solar wind fluctuations... 168

Figure 6-18 Time histories of (a) the Sun/E-sail distance increment (b) in-plane libration angle with different configurations. 169

Figure 6-19 Time histories of the E-sail resultant propulsive force components in the $O_{cb}X_{cb}Y_{cb}Z_{cb}$ frame with different configurations. 169

Figure 6-20 Time histories of angular velocity of the central spacecraft in the $O_{cb}X_{cb}Y_{cb}Z_{cb}$ frame with different configurations. 171

Figure 6-21 Time histories of CM (a) and (b) and CT (c) and (d) of the E-sail in the $O_{cb}X_{cb}Y_{cb}Z_{cb}$ frame with different configurations. 171

Figure 6-22 Time histories of (a) tension in main and auxiliary tethers (b) spin rate (c) nutation angle and (d) coning angle of the E-sail with different configurations. 172

Figure 6-23 Block diagram of the E-sail control system. 175

Figure 6-24 Control forces acting on the E-sail. 176

Figure 6-25 Time histories of E-sail's spin rate by controlling the spin rate of the central spacecraft with different lengths of main tethers. 178

Figure 6-26 Time histories of (a) the E-sail's spin rate (b) tensions in the main and auxiliary tethers (c) the control torque at the central spacecraft (d) the control force at the remote units with 10km long main tethers. 179

Figure 6-27 Time histories of (a) spin rates of the E-sail and central spacecraft (b) lengths of main and auxiliary tethers (c) control torque and (d) control forces at the central spacecraft and remote units in the tether deployment process. 180

Figure 7-1 Control forces applied to the remote units. 183

Figure 7-2 Time histories of the sail angle control with the desired 30° sail angle. 185

Figure 7-3 Time histories of the sail angle control with the desired 10° sail angle. 186

Figure 7-4 Block diagram of the E-sail attitude control strategy. 188

Figure 7-5 Time histories of (a) Euler angles (b) Euler angular rates and (c) sail and clock angles with the desired 55° sail angle. 197

Figure 7-6 Time histories of (a) control torques in the $O_{sp}X_{sp}Y_{sp}Z_{sp}$ frame and (b) sliding surfaces with the desired 55° sail angle. 198

Figure 7-7 Time histories of (a) the Euler angles (b) the Euler angular rates and (c) the sail and clock angles with the desired 45° sail angle. 199

Figure 7-8 Time histories of (a) control torques in the $O_{sp}X_{sp}Y_{sp}Z_{sp}$ frame and (b) sliding surfaces with the desired 45° sail angle. 200

Figure 7-9 Time histories of (a) the Euler angles and (b) the sail and clock angles with and without model uncertainty. 201

Figure 7-10 Time histories of (a) the Euler angles and (b) the sail and clock angles with both controllers. 203

Figure 7-11 Time histories of (a) the Euler angles (b) the Euler angular rates and (c) the sail and clock angles with the desired 55° sail angle. 206

Figure 7-12 Time histories of (a) the control torques in the $O_{sp}X_{sp}Y_{sp}Z_{sp}$ frame and (b) sliding surfaces with the desired 55° sail angle. 207

Figure 7-13 Time histories of control forces acting on the 1st remote unit in the $O_sX_sY_sZ_s$ frame with the desired 55° sail angle.......................... 207

Figure 7-14 Time histories of (a) the Euler angles (b) the Euler angular rates and (c) the sail and clock angles with the desired 45° sail angle. 208

Figure 7-15 Time histories of (a) the control torques in the $O_{sp}X_{sp}Y_{sp}Z_{sp}$ frame and (b) sliding surfaces with the desired 45° sail angle. 209

Figure 7-16 Time histories of control forces acting on the 1st remote unit in the $O_sX_sY_sZ_s$ frame with the desired 45° sail angle.......................... 209

Figure 7-17 Comparison of time histories of attitude results of two models with different control gains. 212

Figure 7-18 Comparison of time histories of control outputs of two models with different control gains. 213

Figure 7-19 Time histories of (a) Euler angles (b) Euler angular rates and (c) sail and clock angles with the voltage control. 215

Figure 7-20 Time histories of the 1st main tether's voltage.......................... 216

Figure 7-21 Transfer trajectory of E-sail from Earth to Mars. 223

Figure 7-22 Time histories of attitude angles... 224

Figure 7-23 Time histories of propulsive force coefficient............................. 225

Figure 7-24 Time histories of mesh refinement iteration. 225

Figure 7-25 Time histories of the desired, real and error distances from the Sun to E-sail... 229

Figure 7-26 Time histories of the desired, real and error attitude angles. .. 230

Figure 7-27 Time histories of the 1st main tether's voltage.......................... 231

List of Symbols

$\boldsymbol{a}$ = Propulsive acceleration vector

$\mathrm{a}_{\square}$ = E-sail characteristic acceleration, mm/s^2

A_k = Cross-section area of the k_{th} element, m^2

A_m = Cross-sectional area of the main tether, m^2

e = Elementary charge, C

E_{au} = Young's modulus of the auxiliary tether, Gpa

E_k = Young's modulus of the k_{th} element, Gpa

$\boldsymbol{f}_{dl}$ = Propulsive force per unit tether length, N/m

$\boldsymbol{F}_t$ = Total propulsive force, N

$\boldsymbol{g}_{\square}$ = Gravitational acceleration of k_{th} element, m/s^2

H = Height of the central spacecraft, m

K_i = Propulsive force coefficients

$L_{0,k}$ = Undeformed length of k_{th} element, m

$L_{e,k}$ = Instantaneous length of the k_{th} element, m

m_{au} = Mass of i^{th} auxiliary tether, kg

m_E = Total mass of the E-sail, kg

m_p = Mass of the solar wind proton, kg

m_{re} = Mass of i^{th} remote unit, kg

m_s = Mass of the central spacecraft, kg

m_t = Mass of i^{th} main tether, kg

n = Solar wind electron density, m^{-3}

$\boldsymbol{n}$ = Unit spin vector of the E-sail

$\boldsymbol{n}_s$ = Unit spin vector of the E-sail in the $O_sX_sY_sZ_s$ frame

$\boldsymbol{n}_o$ = Unit spin vector of the E-sail in the $O_oX_oY_oZ_o$ frame

r = Sun-spacecraft distance, au

r_0 = Two times of the electron Debye length, m

r_w = Tether effective radius, m

$\boldsymbol{r}$ = Sun-spacecraft position vector

R_s = Radius of the central spacecraft, m

$\boldsymbol{S}_k$ = Element shape function

T_e = The temperature of the slow solar wind electron, eV

$\boldsymbol{v}_{sw\perp}$ = Solar wind velocity perpendicular to tether, km/s

V = Tether potential, kV

V_s = Volume of central spacecraft, m^3

V_w = Solar wind electric potential, kV

α = Sail angle, rad

β = Coning angle, rad

γ = Thrust angle, rad

δ = Clock angle, rad

ε_0 = Vacuum permittivity, F/m

ε_k = Green-Lagrangian strain

ζ, η, Θ = Euler angles, rad

η_i = Convergence index

$\theta_{i,j}$ = Adjacent angle, rad

ϑ = Relative angle, rad

λ = Vector of the Lagrange multipliers

$\mu_{\square}$ = Standard gravitational parameter of the Sun, $m^3 \square s^{-2}$

ζ_i, w_i = Gaussian integration weight and abscissa

ρ = Linear density of the main tether, kg/m^3

ρ_k = Material density of the k_{th} element, kg/m^3

ρ_s = Material density of the central spacecraft, kg/m^3

σ_b = Tensile stress, N/m^2

ϕ = Ecliptic latitude angle, rad

φ = Nutation angle, rad

ψ = Ecliptic longitude angle, rad

$\hat{\omega}$ = Angular frequency of the coning motion, rad/s

ω_0 = Initial spin rate of the E-sail, rad/s

ω_c = Current spin rate of the E-sail, rad/s

ω_{des} = Desired spin rate of the E-sail, rad/s

$\boldsymbol{\omega}_s$ = Angular velocity of the central spacecraft, rad/s

$\mathbf{\Omega}$ = Angular velocity of the orbital coordinate system, rad/s

$\mathbf{\Omega}_0$ = Initial orbital angular velocity, rad/s

List of Abbreviations

2D = Two dimensional

au = astronomical unit

ANCF = Absolute Nodal Coordinate Formulation

CM = Center of Mass

CT = Center of Thrust

E-sail = Electric solar wind sail

FEM = Finite Element Method

NCF = Natural Coordinate Formulation

NPFEM = Nodal Position Finite Element Method

PD = Proportional-Derivative

PIC = Particle-In-Cell

RNCF = Referenced Nodal Coordinate Formulation

SMC = Sliding Mode Control

TSS = Tethered Spacecraft System

Chapter 1 INTRODUCTION AND JUSTIFICATION

Summary: In this chapter, the backgrounds and applications of the E-sail are introduced. Then, the research activities are justified, and the research objectives and methodologies of research are defined. At the end, the layout of this dissertation and a full list of publications out of the doctoral research are presented.

1.1 Backgrounds

Since the launch of the first artificial Earth orbiter, Sputnik I in 1957, thousands of spacecrafts have been launched to explore and expand human understanding of the solar system. However, most of them stayed in Earth orbits, and only Voyager 1 and 2 reached the edge of the solar system, which makes us still know little about the outer solar system. In order to improve our understanding of the outer solar system, many extraplanetary exploration concepts have been proposed. The first and most critical step to complete the extraplanetary exploration is to find an efficient interstellar propulsion system. This is because the extraplanetary exploration usually requires enormous energy for orbital transfer. However, it is uneconomical and unrealistic to complete it by using the conventional chemical propulsive system, which requires tremendous propellant mass. Therefore, the propellantless propulsion systems have received increased attention in the recent years. Electric solar wind sail (E-sail), one of the propellantless propulsion systems, stands out because of its unique advantages, as shown in Figure 1-1.

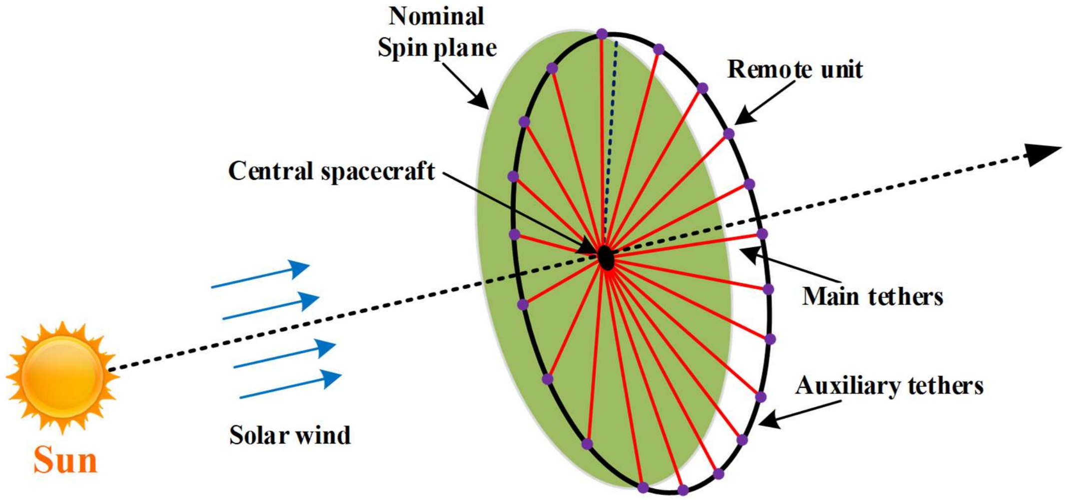

Figure 1-1 The Sketch of E-sail configuration.

1.1.1 E-sail Configurations

In 2004, the primitive E-sail concept was proposed by Janhunen as an alternative to magnetic sail, which harvests energy by repelling the protons in the solar wind [1]. The solar wind is a stream of charged particles consists of electrons, protons, and alpha particles, which is released from the upper atmosphere of the Sun (corona), as shown in Figure 1-2. However, this primeval E-sail concept is technically difficult to accomplish due to the use of a large squire wire grid. Later, it was improved in 2006 [2], which consists of a spinning central spacecraft connected with multiple kilometer-long, thin and positively charged tethers (main tethers) with remote units at the tips of each main tether as shown in Figure 1-3 [3]. The material of the main tether is a four-wire aluminium Hoytether, which is manufactured by using ultrasonic Al-wire bonding technology as presented in Figure 1-4(a) [4]. The main tethers are deployed by the spinning central spacecraft with the centrifugal force [5-6]. Up to now, there are two concepts to deploy the tethers: tangential and radial deployments [5-6], as shown in Figure 1-5. The radial deployment pulls out the tethers radially by the thruster at the remote units. Similar to the yo-yo despinner, the tangential deployment accelerates the end mass and deploys the tethers tangentially using a free deployment. The spinning main tethers form a spin plane (nominal spin plane), where the electrostatic field around each main tether deflects charged particles in the solar wind and results in a propulsive force. Meanwhile, the positively charged main tethers will attract electrons from the solar wind plasma and generate the electron currents. To maintain the positive potential of the main tethers, an onboard electron gun is used to remove the excess electrons to compensate for the arriving electric current. The energy loss of the electron gun is supplied by the solar panels mounted on the central spacecraft [3], see Figure 1-3(b). The direction of each main tether's propulsive force is along the component of the solar wind that is normal to the tether. The remote units are used to enhance the centrifugal forces acting on the main tethers to avoid the slack in the main tethers [3].

Meanwhile, the remote units can provide the thrusters that generating the initial spin rate of the E-sail or controlling the E-sail's spin rate to a desired value, see Figure 1-3.

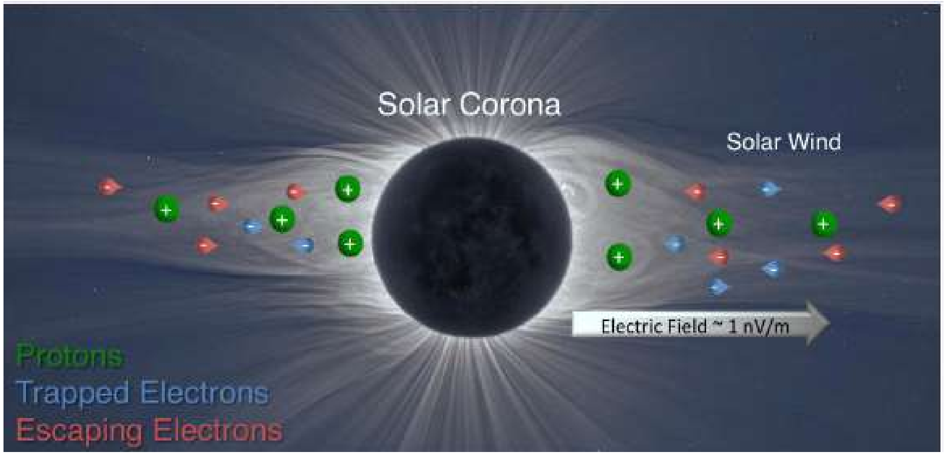

Figure 1-2 Sketch of the solar wind[1].

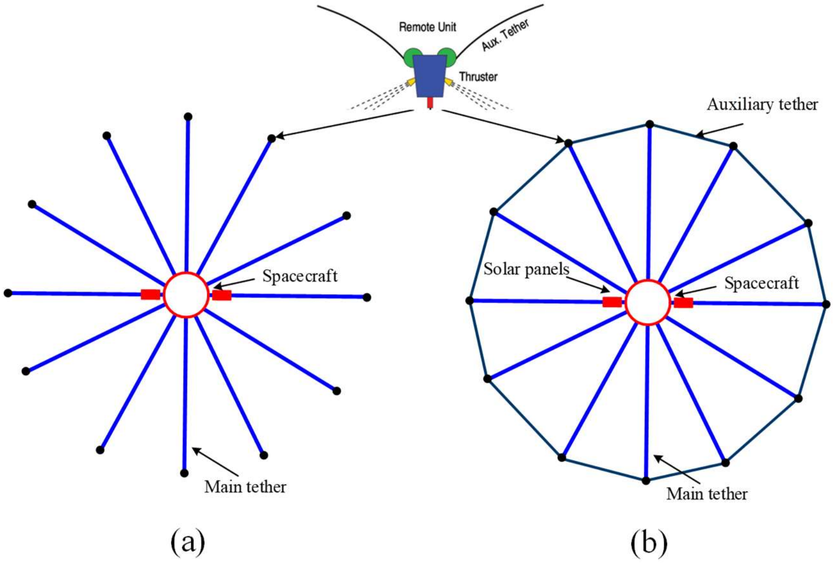

Figure 1-3 Two basic types of E-sail.

---

[1] https://now.uiowa.edu/2021/07/physicists-led-university-iowa-more-fully-describe-suns-electric-field.

This configuration is similar to the heliogyro solar sails [8-9] or the hub-spoke tethered satellite formation [10-11]. Even if this E-sail configuration is close to engineering achievable, it still has the drawback that cannot prevent the collisions between main tethers [3]. This is because the transverse propulsive force is produced in the spin plane when the solar wind is inclined with respect to the spin plane, which will lead to the main tethers' collision and must be avoided to ensure the proper operation of E-sail. Consequently, the nonconductive tethers (auxiliary tethers) are introduced to connect the remote units as shown in Figure 1-3(b), which are used as mechanism to increase the centrifugal forces acting on the main tethers to keep the main tethers equidistant. Kapton with a density of 1420kg/m^3 are used to manufacture the auxiliary tether, see Figure 1-4(b). It should be noted that the parameters of the E-sail are selected based on Ref. [12] in this dissertation.

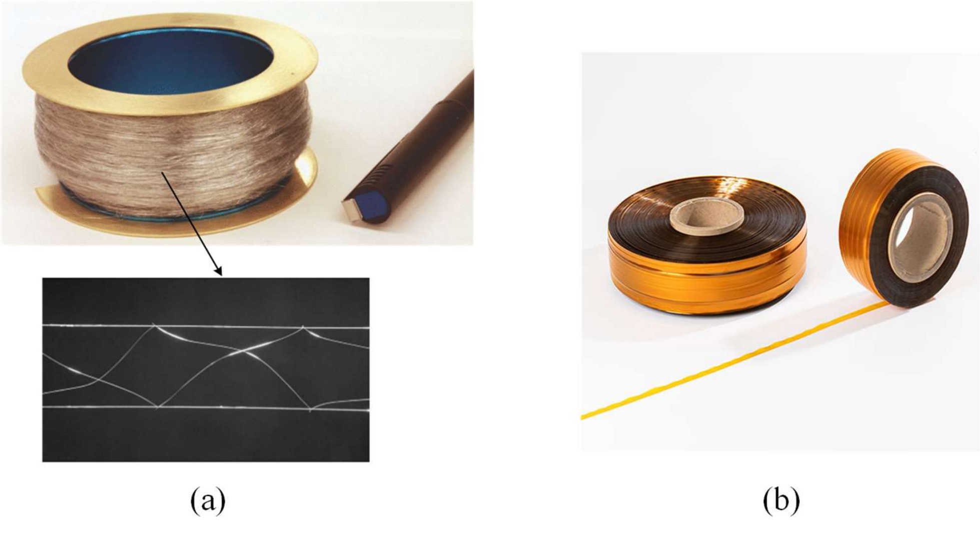
(a)
(b)

Figure 1-4 Material of the (a) main tether and (b) auxiliary tether [4] .

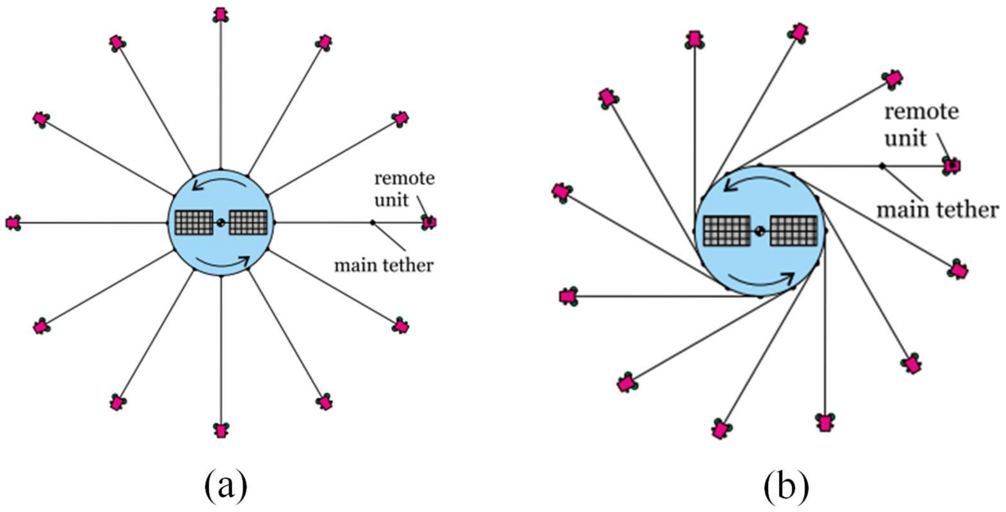

Figure 1-5 Deployment strategies of the E-sail (a) radial deployment and (b) tangential deployment [7].

1.1.2 Pros and Cons of the E-sail

Compared with the well-known solar sail, the E-sail has several advantages as follows. First and the foremost, the propulsive force of the E-sail is inversely proportional to $7/6$ power of the distance between the E-sail and the Sun, which makes the propulsive force of the E-sail decays slower than the solar sail [13]. This makes the propulsive force of the E-sail extends further into the solar system than the solar sail. Moreover, because the resultant propulsive force of each main tether is not always perpendicular to the E-sail spin plane [14], which makes it closely related to the E-sail orientation [15]. Thus, the attitude control of the E-sail in the space exploration can be easily accomplished by modulating the voltage of each main tether individually to generate the torques for attitude maneuvering of the E-sail [14, 16-20]. These peculiarity of the E-sail makes it appealing for various mission scenarios, such as the outer solar system exploration [21], interplanetary missions [22], missions toward asteroids [23], non-Keplerian orbits missions [24], generation of artificial equilibriums points [25], and asteroid tug [26].

Although the E-sail has many advantages, it still has some limitations and challenges. First and foremost, the E-sail does not operate inside the magnetosphere because there is no solar wind dynamic pressure inside the magnetosphere to generate the propulsive force [3]. Furthermore, the main tethers are maintained the high positive potential by an onboard electron gun, which is power by the solar panels mounted on the central spacecraft, as shown in Figure 1-3(b). However, it is a huge challenge to obtain too much power to supply the electron gun. Finally, the deployment of the tethers are the initial and key procedure of the E-sail operation. However, it is still a big challenge to deploy the E-sail with the auxiliary tethers.

1.2 Justification of Research

E-sail consists of the spinning central spacecraft that accounts for most of the mass of system connected by multiple kilometer-long lightweight tethers. This makes the dynamic characteristics of the E-sail very complex due to the elastic motions of the tethers, the coupling effects between the orbital and self-spinning motions of the E-sail, and the rigid-flexible coupling motions. The superposition of the various coupling effects and the high-order modes of flexible elastic tethers requires to establish a generalized model that can simulate these effects before the real E-sail space missions. Meanwhile, the key to successful execution of E-sail missions is to accurately achieve E-sail attitude control. However, its attitude control is different from the traditional spacecraft due to its huge structure. Therefore, this doctoral research focuses on the two main aspects (i) dynamic modeling of the E-sail, (ii) attitude control of E-sail and its application to the orbital maneuver.

1.2.1 Dynamic modeling of the E-sail

1.2.1.1 Challenges

Understanding the dynamics characteristics of the E-sail is the foundation of the success of the E-sail missions. The main technical challenges encountered can be summarized as follows:

(i) **Mathematical modeling of the E-sail.** The E-sail characterizes the coupled rigid-body motion of the central spacecraft, elastic deformation of the tethers, and the coupling effects of orbital and self-spinning motion. Therefore, it is necessary to develop a generalized high-fidelity E-sail model by integrating the rigid-body spacecraft attitude dynamics with the high-fidelity tether model.

(ii) **Unknown physics.** The application of the propulsive force on the main tethers will result in the coning motion of tethers [14, 27]. It was further revealed the coning angle of the E-sail changes periodically in the time domain. However, except showing the time history of the periodic coning motion, no attempt has been tried to explain in theory the mechanism behind the periodic motion. Moreover, the upper and lower spin rate bounds to ensure the proper operation of E-sail are still unclear.

(iii) **Configuration stability.** The magnitude and direction of the propulsive force depend on the magnitude and direction of the solar wind. The previous works assumed that magnitude of the solar wind velocity is constant. However, the solar wind velocity measurement of Voyager 2 mission [2] indicates that the magnitude of the solar wind velocity fluctuates in the range of 200 km/s and 1000 km/s as shown in Figure 1-6. Thus, the influence of the solar wind fluctuations on the E-sail configuration stability is still open to investigation.

(iv) **Rigid-flexible coupling effect.** The deflection of main tethers is directly coupled with the rigid-body dynamics of the central spacecraft. The influences of this nonlinear rigid-flexible coupling motion on the central spacecraft and the relative E-sail stability are less understood.

---

[2] ftp://space.mit.edu/pub/plasma/vgr/v2/ha/key.

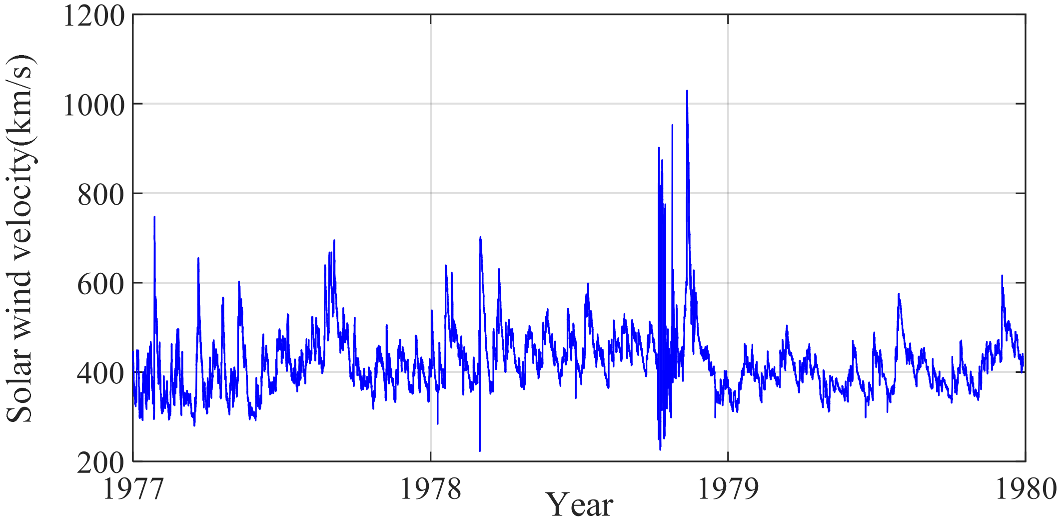

Figure 1-6 Time histories of solar wind velocity obtained from Voyager 2.

1.2.1.2 Limitations of Existing Treatments

Many effects have been devoted to the E-sail dynamics modeling in the literature, such as, the rigid tether model [28], the catenary tether model [29], and the flexible tether model [30]. However, the central spacecraft is assumed as a lumped mass and the nonlinear rigid-flexible coupling dynamics is ignored. The coupled motion between the central spacecraft attitude and the deflection of the main tethers is not considered. Meanwhile, the influence of the disturbance torques caused by the offset between of the central of mass (CM) and the center of thrust (CT) of the E-sail on the attitude dynamics of the E-sail have not been studied.

In addition, the deflection of main tethers, called the coning motion, has been showed numerically in the previous work [31-32]. Further, the numerical results of the rigid tether model [28], the catenary tether model [29, 33], and the flexible tether model [30] also revealed that the coning motion of the E-sail changes periodically in the time domain. However, no attempt has been tried to explain theoretically the mechanism behind the periodic motion, and whether the coning motion will affect the global dynamic behavior of the E-sail is still unknown.

Moreover, the upper and lower bounds of the spin rate are estimated with the assumption that the central spacecraft and main tethers are in the spin plane [28-29, 12]. The upper bound is determined intuitively by keeping the axial stress of main tether less than the tensile stress of tether material, while the lower bound is derived by assuming the centrifugal force in the main tether being five times of the propulsive force [3]. The latter is based on the assumption that the E-sail spin axis is parallel to the solar wind direction so that it is possible to obtain an analytical approximation of both the tether shape and the root force [32]. If the solar wind is inclined with respect to the spin plane, the explanation for the lower bound of the E-sail spin rate in Ref. [32] is not applicable. Thus, it is necessary to clearly investigate the physical meaning behind this lower bound if the E-sail spin axis is not parallel to the solar wind direction.

Finally, the magnitude and direction of the propulsive force depend on the density [13] and temperature of electrons and the direction of the solar wind [27, 30]. However, most previous literature assumed that the magnitude of the solar wind velocity is constant in the analysis although the velocity varies in the reality. While the influence of the solar wind fluctuations on the E-sail trajectory has been investigated in Refs. [34-36], the impact on the E-sail configuration is still open to investigation.

1.2.2 Attitude Control and Orbital Maneuver of the E-sail

1.2.2.1 Challenges

The attitude control of E-sail is essential to the E-sail orbital maneuvering missions. It experiences the following challenges [7]:

(i) **Attitude control of E-sail.** The key to successful execution of E-sail missions is to accurately achieve E-sail attitude control. However, the length of the main tether is usually kilometer-long, which makes the attitude dynamics of the E-sail sensitive to the disturbance torque.

(ii) **E-sail spin rate control.** It was noted that the spin rate of E-sail changes in the E-sail attitude maneuvering and deployment process because a transverse propulsive force is generated when the solar wind is inclined with respect to the spin plane. Thus, the spin rate should be maintained at a pre-defined or desired rate to maintain the stability of the E-sail.

(iii) **Trajectory design and tracking.** The flexible deformation of main tethers should be considered during the E-sail mission trajectory design. In addition, the shape of E-sail should be considered when dealing with the trajectory tracking problem.

1.2.2.2 Limitations of Existing Treatments

In the existing studies, the attitude control of E-sail was achieved by modulating the voltage of each individual main tether [17-18]. However, the voltage modulation strategy does not apply if the main tethers are not charged in certain periods of the E-sail orbital transfer missions [37]. Also, the exist control strategies are all the simple feedback control laws without the stability analysis.

Moreover, the investigation showed that the spin rate of E-sail changes if the E-sail is inclined with respect to the Sun-spacecraft direction. The spin rate control was achieved by controlling the auxiliary tether's voltage independently from the adjacent main tethers' voltages [17]. However, the attitude dynamics of the central spacecraft are not considered. To maintain the stability of the E-sail in the attitude maneuvering or the deployment of the E-sail, the spin rates of the central spacecraft and the E-sail should be simultaneously controlled to a pre-defined rate. Thus, a simple and efficient control strategy should be developed.

Finally, many efforts are dedicated to analyzing the trajectories of the

E-sail with different mission scenarios [38,39]. They focused on the trajectories design problem with a propulsive force model, which was obtained by assuming the tethers are in the same plane and ignoring the coning motion of tethers. In addition, they also ignored the shape of E-sail in the trajectory tracking problem and considered it as a lumped mass.

1.3 Objectives of Proposed Research

To address the existing challenges and limitations, this doctoral research focuses on the dynamic response and control of the E-sail and its application in different mission scenarios. Therefore, the objectives of this work are shown as follows:

(i) Develop the dynamic models of the E-sail in three different situations, that is, the high-fidelity E-sail model, the generalized E-sail model and the reduced order analytical model, respectively.

(ii) Reveal the unknown mechanism behind the periodic coning motion and the physics of the spin rate bounds and derive the analytic solution of the coning motion frequency and the spin rate bounds analytic expressions, respectively.

(iii) Investigate the configuration stability of E-sail under various conditions and the influence of parameters on the dynamic response of E-sail by applying the high-fidelity E-sail model.

(iv) Using the generalized E-sail model to study the rigid-flexible coupling effect and various conditions on the attitude dynamics and spin rate control problem of E-sail.

(v) Investigate the attitude control of the E-sail with different control strategies, which can be demonstrated by the parameter analysis.

(vi) Study the trajectory tracking problem of the E-sail with the reduced order model during the different deep space mission scenarios.

1.4 Methodology of Approach

The outline of the methodology of approach to achieve the objectives in this research is shown in Figure 1-7. It begins with the dynamic modeling of the E-sail, including the high-fidelity tether dynamic model developed by the nodal position finite element method (NPFEM), the generalized E-sail model considering the attitude dynamics of the central spacecraft using natural coordinate formulation (NCF) and the tether deformation using the nodal position finite element method, and the reduced-order analytical model. Lagrange equations of the first kind and Newton-Euler equations are utilized to derivate the mathematical formulations of the E-sail. The E-sail is assumed in the heliocentric ecliptic orbital plane at a distance of 1 au from the Sun. The environmental forces acting on the E-sail including the propulsive force based on the Coulomb's law and the gravitational force of the Sun.

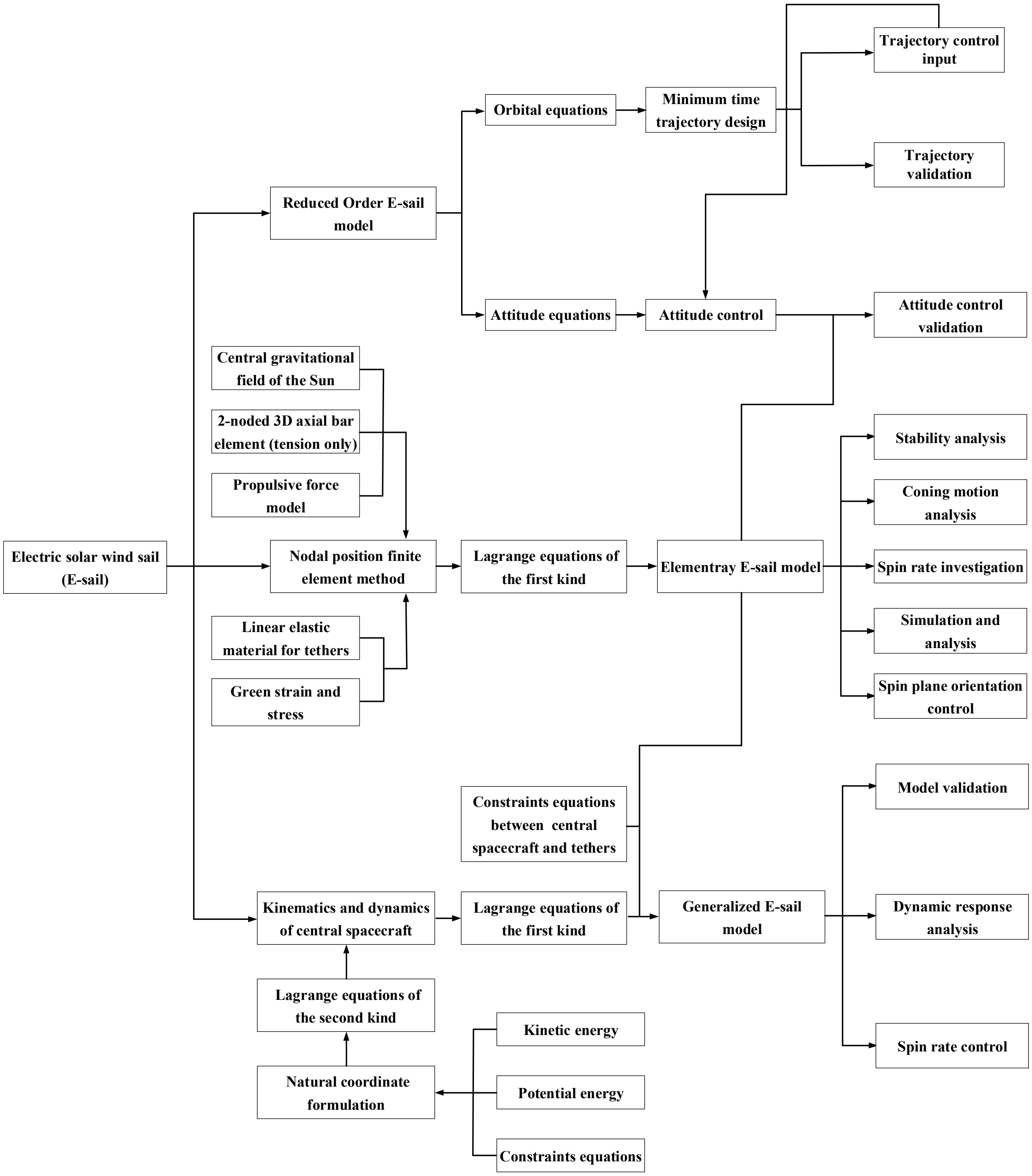

Figure 1-7 Methodology of approach.

To capture the tether dynamics with high-order modes, and the coupling effects of orbital and self-spinning motions of the E-sail, the tethers of the E-sail are discretized into inter-connected 2-noded tensile elements using the

NPFEM, where the displacement is replaced by the position as state variables. After development of the high-fidelity model, the configuration stability, spin rate bounds and the unknown mechanism behind the periodic coning motion are investigated and validated by theoretical and parametric analysis. Then, to achieve the spin plane orientation control, a simple proportional-derivative (PD) control strategy is proposed by applying control forces, where the control forces can be generated by the thrusters installed in the remote units.

Next, the translation and attitude dynamics of the central spacecraft is described non-singularly by the NCF, where the attitude angles are replaced by the Cartesian coordinates. The coupling between the rigid-body central spacecraft and the motion of the elastic tethers are described by Lagrange multipliers. Once the generalized E-sail model is established, the influence of the E-sail's geometrical configuration and disturbance torque on the E-sail dynamic characteristics are investigated. In real E-sail mission, the spin rate of the E-sail always perturbed by unknown disturbances. Thus, simple feedback torque control laws at the central spacecraft or at the central spacecraft and the remote units simultaneously are designed to investigate the control performance of the E-sail spin rate in the tether deployment or fully deployment processes.

Because the attitude information of the E-sail is implicit and must be calculated from the nodal positions in the NPFEM E-sail model, which makes it difficult to design an applicable attitude controller. To solve the problem, a reduced order analytical model is developed to describe the attitude dynamics of the E-sail. A sliding mode control (SMC) is proposed, and its stability is proved by the Lyapunov theory. Then, the control law is applied to the high-fidelity E-sail model to examine the control influence. Finally, with the help of attitude control, the trajectory tracking problems of E-sail in extraplanetary exploration missions are investigated by the reduced order analytical model.

1.5 Assumption of Dissertation

In this dissertation, the E-sail is assumed initially in the heliocentric ecliptic plane with its spin plane perpendicular to the ecliptic plane at a distance of 1 au from the Sun. The direction of the solar wind is assumed to be outward along the Sun-E-sail direction and the remote units are modeled as lumped masses. Unless noted otherwise, the solar wind velocity is assumed constant (400 km/s), the initial spin rate is $\omega_0 = 4 \times 10^{-3}\ rad/s$, the configuration of E-sail is symmetrical, and the electrical potential of all main tethers is assumed the same (20 kV). The following are special assumptions for the three E-sail models

(i) **High-fidelity E-sail model.** The central spacecraft is modeled as lumped masses, because of the extremely large ratio of the tether length over the dimensions of the central spacecraft.

(ii) **Generalized E-sail model.** The central spacecraft is assumed as a circular cylinder and its attitude and translation dynamic motions are considered.

(iii) **Reduced-order analytical model.** All tethers are assumed to be straight and belong to the same plane without consideration of coning motion. The spin rate of the E-sail and the orbital angular velocity are constant.

1.6 Layout of Dissertation

There are eight chapters in this dissertation. Following the introduction and justification in Chapter 1, Chapter 2 provides a detailed literature review of relevant work in the dynamics and attitude control of E-sail, and its application in deep space missions. Chapter 3 develops the three different mathematical formulations of the E-sail used in this dissertation for studying the dynamic characteristics, attitude control and orbit maneuvering in different mission scenarios. Chapter 4 focuses on the model validation without considering the influence of the propulsive force, which can be used as a benchmark for the rest of study. Meanwhile, the unknown physics behind the dynamic characteristics of the E-sail are reveal. Chapter 5 includes the parametric analysis of the E-sail dynamic characteristics by a high-fidelity tether dynamic model, while Chapter 6 investigates the rigid-flexible coupling effect on the attitude dynamics and spin control of E-sail with the rigid-flexible coupling high-fidelity model. Chapter 7 focuses on the attitude control problem of the E-sail, and the trajectory tracking problems in extraplanetary exploration missions. Finally, Chapter 8 concludes the work, identify the original contributions of this doctoral research, and outline the potential future research directions.

1.7 List of Publications

The contributions of this dissertation can be found in the following list of publications.

1. **C. Du**, Z.H. Zhu, G. Li, Analysis of thrust-induced sail plane coning and attitude motion of electric sail. *Acta Astronautica*, 178 (2021) 129-142. doi: 10.1016/j.actaastro.2020.09.001
2. **C. Du**, Z.H. Zhu, G. Li, Rigid-flexible coupling effect on attitude dynamics of electric solar wind sail. *Communications in Nonlinear Science and Numerical Simulation*, 95 (2021) 105663. doi: 10.1016/j.cnsns.2020.105663
3. **C. Du**, Z.H. Zhu, Dynamic characterization and sail angle control of electric solar wind sail by high-fidelity tether dynamics. *Acta Astronautica*, 189 (2021) 504-513. doi: 10.1016/j.actaastro.2021.09.019
4. **C. Du**, Z.H. Zhu, Parameters Influence on Attitude Dynamics of Electric Solar Wind Sail. *AIAA Scitech Forum*, 2022.

doi.org/10.2514/6.2022-2578

5. **C. Du**, Z.H. Zhu, J. Kang, Attitude Control and Stability Analysis of Electric Solar Wind Sail. (under review)

The publications associated with the candidate is given in the following list.

1. G. Li, Z.H. Zhu, **C. Du**, S.A. Meguid, Characteristics of coupled orbital-attitude dynamics of flexible electric solar wind sail. *Acta Astronautica*, 159 (2019) 593-608.

   doi.org/10.1016/j.actaastro.2019.02.009
2. G. Li, Z.H. Zhu, **C. Du**, Flight dynamics and control strategy of electric solar wind sails. *Journal of Guidance, Control, and Dynamics*, 43 (2020) 462-474.

   doi.org/10.2514/1.G004608
3. G. Li, Z.H. Zhu, **C. Du**, Stability and control of radial deployment of electric solar wind sail. *Nonlinear Dynamics*, 103 (2021) 481-501.

   doi.org/10.1007/s11071-020-06067-7

Chapter 2 LITERATURE REVIEW

Summary: In this chapter, the literature review covers the dynamics and control as well as orbital maneuver of E-sail. Based on the literature review, the objectives and methodology of the proposed research are suggested.

2.1 Propulsive Force

When protons from the Sun impinge on the electrostatic field produced by the positively charged main tethers, they are deflected and transfer some of their momentum. This momentum transfer is the propulsive force which accelerates an E-sail. The propulsive force as the only external force is significant to the E-sail because the application of E-sail requires precise knowledge of it. To date, many efforts have been devoted to measure the propulsive force, and there are several models of propulsive force that acts on the charged tethers. They are derived from either the particle-in-cell (PIC) simplified analytical model, or the empirical model. First, based on a two-dimensional (2D) PIC simulation of a positively charged tether, a simple model of the propulsive force was developed [13]. The influences of the solar wind density and velocity, physical properties of main tethers, and trapped shielding electrons were considered. Although effective, this propulsive force model was found to grossly underestimate the magnitude of the propulsive force due to consideration of the trapped shielding electrons [40]. By removing the consideration of the trapped shielding electrons, it was found the magnitude of the propulsive force increased roughly by five times from the 2D PIC model at 20 kV tether potential [40]. Consequently, a much-simplified form of the propulsive force model in Ref. [40] was proposed at a distance of 1 au from the Sun. It is worth emphasizing that the electron temperature and physical properties of main tethers are not included explicitly in this model, while the electron density in the undisturbed solar wind is assumed constant. However, the analysis showed that the influence of the electron temperature and density in the solar wind on the propulsive force is non-negligible [41]. The electron temperature and density measured from the real space can be obtained from Refs. [42-43]. Later, a new 2D PIC analysis with the explicit consideration of the trapped shielding electrons resulted a propulsive force roughly 3.8 times greater than that of the 2D PIC model at 20 kV tether potential [44]. The new result was confirmed by the similar result obtained by the analytic analysis [45] and the Boltzmann electron PIC model [46]. Recently, the NASA's experimental investigation [47] shown that the propulsive force at 20 kV tether potential and 1 au distance from the Sun is much greater than that of the new 2D PIC model in Ref. [44], and is even greater than that of the 2D PIC model in Ref. [13] by approximately 18 times.

2.2 Propulsive Acceleration and Sail Angle Models

The mathematic model of the E-sail propulsive acceleration and the relationship between propulsive acceleration and the E-sail orientation are significant to the preliminary E-sail analysis before the real space missions. In this section, the evolution history of these will be presented. Before starting, the definition of two angles, sail and thrust angles, are firstly introduced as shown in Figure 2-1, which are used to describe the relative orientation of E-sail. The positive sail angle α is measured in the counter-clockwise direction from the spin vector $\boldsymbol{n}$ to the Sun-E-sail direction $\boldsymbol{r}$, while the negative sail angle is in the opposite direction. The thrust angle γ is the angle between the $\boldsymbol{r}$ axis and the total propulsive acceleration $\boldsymbol{a}$.

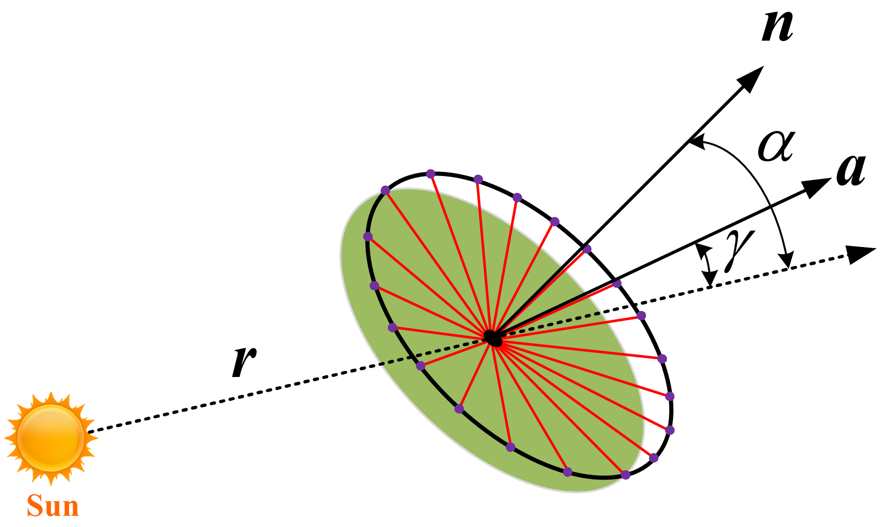

Figure 2-1 Sketch of E-sail sail and thrust angles.

As mentioned before, based on the propulsive force model obtained from Ref. [13], the first propulsive acceleration model was obtained as

$$\boldsymbol{a} = a_{\square}\,(1/r)^{7/6}\,\boldsymbol{r} \tag{2.1}$$

where $a_{\square}$ is the E-sail characteristic acceleration [48], and $r = |\boldsymbol{r}|$ is the Sun-spacecraft distance in au.

Then, a new mathematical model, which describe a more precise relationship between propulsive acceleration, thrust angle and sail angle, was obtained from the numerical curve-fitting [49-50], that is,

$$\gamma = \ell_1\alpha^6 + \ell_2\alpha^5 + \ell_3\alpha^4 + \ell_4\alpha^3 + \ell_5\alpha^2 + \ell_6\alpha + \ell_7 \tag{2.2}$$

$$\mathrm{a} = c_1\alpha^6 + c_2\alpha^5 + c_3\alpha^4 + c_4\alpha^3 + c_5\alpha^2 + c_6\alpha + c_7 \tag{2.3}$$

where the coefficients ℓ_i $(i = 1, 2, \cdots, 7)$ and c_i $(i = 1, 2, \cdots, 7)$ are listed in Table 2-1 and Table 2-2, respectively.

Table 2-1 Coefficients of the sail and thrust angles relationship.

ℓ_1	ℓ_2	ℓ_3	ℓ_4
3.681×10^{-10}	-8.295×10^{-8}	6.322×10^{-6}	-2.661×10^{-4}
ℓ_5	ℓ_6	ℓ_7	
3.652×10^{-3}	4.853×10^{-1}	0	

Table 2-2 Coefficients of dimensionless acceleration vs sail angle.

c_1	c_2	c_3	c_4
-5.896×10^{-13}	1.943×10^{-10}	-1.261×10^{-8}	7.027×10^{-7}
c_5	c_6	c_7	
-1.271×10^{-4}	6.904×10^{-5}	1.0	

Further, the refined mathematical models of propulsive force vector of a flat E-sail were derived by [15], where the simplified propulsive force model in Ref. [40] was used. The new models were

$$\gamma = \arccos\left(\frac{1+\cos^2\alpha}{\sqrt{1+3\cos^2\alpha}}\right) \tag{2.4}$$

$$\mathrm{a} = \kappa a_{\oplus}\sqrt{1+3\cos^2\alpha}\Big/2r \tag{2.5}$$

where $\kappa = \{0,\quad 1\}$ is the dimensionless switching parameter that is used to turn on/off the propulsive force.

It should be noted that the above two models are all derived from a flat E-sail assumption that is all the tethers belong to the same spin plane. To overcome this problem, a new propulsive force vector model based on a catenary tether model [31, 33] was obtained as

$$\gamma = \sqrt{(1-p)\sin^2\alpha + \frac{p^2\left(1+3\cos^2\alpha\right)}{4}} \tag{2.6}$$

$$p \approx \frac{1}{\lambda}\int_0^{x_t}\frac{dx}{\sqrt{1+\dot{s}^2}} \tag{2.7}$$

$$\lambda \approx \int_0^{x_t}\sqrt{1+\left(\dot{s}\right)^2}\,dx \tag{2.8}$$

where $p \in [0\quad 1]$ is a dimensionless coefficient related to the tether shaper s, x_t is the distance between the remote unit and central spacecraft, λ is the generic length of tether, respectively.

Consistent with Ref. [31], a refined best-fit polynomial equations of Ref.

[49] was proposed, which was numerically determined by considering the combined influences of propulsive and centrifugal forces [51].

2.3 Dynamic Modeling of the E-sail

Since the E-sail technology is still in its infancy, it is particularly important to develop a precise mathematical model to capture its dynamic characteristics. In the past decades, many efforts have been devoted to the E-sail dynamic modeling in the literature. Initially, the E-sail was assumed as a spherical rigid pendulum and the equations of motion of single tether were derived based on the variables sail angle, coning angle, and spin rate [14, 52]. A single straight main tether, which ignores the deformation of the tether, was used to understand the E-sail orientation manoeuvre. Similar to the tethered spacecraft system (TSS) [53-54], a reduced order E-sail model was developed by using the dumbbell tether model [55]. Also, the dumbbell model was used to model the E-sail attitude without singularity, where the tether was simplified as rigid bar and the mass was ignored [20]. The singularity problem can be avoided by using two vectors instead of two angular angles to develop the model. Furthermore, based on the rigid bar model, an E-sail model with multiple tethers was developed, where it was assumed that all the tethers belong to the same plane [15]. Based on this model, the coupled attitude-orbit dynamics of E-sail was modeled, and the flight control problem was investigated [56]. An analytical hub-spoke E-sail configuration model was also derived using Newton's Law based on this model [57]. The resultant natural frequencies and mode shapes were given to investigate the dynamics and stability of E-sail. At the same time, the other analytical hub-spoke E-sail configuration model during the tether bar deployment process was obtained based on Lagrange equations [58]. Both the radial and tangential deployment strategies were studied, and the deployment velocity was controlled though the central spacecraft speed.

However, the effect of spring influence of tether was not considered in the rigid bar tether models. It is significant important for E-sail deep space missions because the deformation of kilometer-long tether will have a significant impact on the dynamics of the E-sail. To address the challenge, many effects have been devoted to this. The tether was assumed as lumped masses connected by spring dampers [28, 59-62]. A single tether model [59] and a multiple-tether model [28] based on this single model were derived to analyze the dynamics of E-sail. Meanwhile, the braking control strategies [60] during the deployment process and flight dynamics [61] of a single tether model, and the eigenvalue analysis of a full-sate nonlinear E-sail model [62] were studied. Moreover, the elastic catenary theory was also used to address this challenge. The equation of a spinning tether shape was derived, and the shape was parameterized only by the coning angle and tether length [31]. Based on this model, a two-dimensional tether model was obtained with a given shape, and the equilibrium shape of the tether was derived [32]. Meanwhile, the attitude dynamics of an axially-symmetric E-sail based spacecraft was analyzed by using the propulsive force torque model [33]. It was found that the spacecraft motion is an undamped harmonic oscillation with a certain period at a small sail angle [29, 33]. This motion will lead to an external torque, which will in turn destabilizes the spacecraft.

Although effective, these methods are still limited because the slack phenomenon of the tether will happen under the dynamic response. To address this problem, the finite element method was used to develop the discretized model of tethers. The static structural response of the E-sail was investigated by using conventional finite element method (FEM) with three different beam models [63]. It showed that the full-dimensional E-sail model was necessary. The limitation of the conventional FEM is that it cannot describe the coupling of large rigid body rotation and displacement with small elastic deformation and singularity [64-65]. Thus, there are two approaches to address the problems: the absolute nodal coordinate formulation (ANCF) [66] and nodal position finite element method (NPFEM) [67]. The dynamic models of flexible tether were developed by using ANCF [68] and related referenced nodal coordinate formulation (RNCF) [69-70], the NPFEM [6, 18, 27, 30, 71]. The dynamics response and flight control of elastic tether model of E-sail were studied. However, all the models ignored the attitude of central spacecraft and coupling between rigid spacecraft and flexible tether. Thus, a generalized E-sail model was developed to investigate the coupling effect and spin rate control of E-sail [72].

2.4 Attitude Control of the E-sail

2.4.1 Orientation Control of the E-sail

The key to a successful application of the E-sail technology is the ability to accurately control the E-sail attitude, which includes the orientation and spin rate control of E-sail. The orientation control is achieved by the sail and clock angles of an E-sail that is dependent on the propulsive force vector [27, 38]. For instance, the E-sail should be kept Sun-facing (zero sail angle) to maximize the outward radial propulsive force [73]. However, to perform orbital maneuvering missions, a transverse component of propulsive force is required by tilting the spin plane of E-sail relative to the Sun-spacecraft direction at a non-zero sail angle [38]. Many efforts have been devoted to the study of attitude control of E-sail. The E-sail was first treated as a rigid-body spacecraft to study its attitude dynamics, where the spin plane of mail tethers were grossly simplified as a rigid disk with sail and clock angles expressed in the Euler angles [19, 29, 56]. By linearizing the nonlinear attitude dynamics of the simplified E-sail model, a feedback linearization control was proposed for the sail angle by controlling two Euler angles [56]. Later, the main tethers of E-sail were modeled as rigid pendulums or dumbbell models attached to the central hub and the E-sail attitude was controlled through the tether voltage modulation with the attitude feedback [14, 19, 74]. To avoid the singularity of Euler angles, the E-sail attitude was controlled by a proposed nonlinear model predictive controller [20].

Although effective, the disturbance caused by the dynamic coupling of axial and transverse elastic motion of main tethers was ignored in the pendulum model. To address the defect, the main tethers of E-sail were further modeled as flexible elastic wires by series of interconnected mass-spring models and the E-sail attitude was controlled by a more detailed voltage modulation scheme with six throttling control parameters [75]. It is noted someone argued that the dumbbell model in comparison with the mass-spring model is simpler and accurate enough to describe the tether motion of E-sail if the spin rate is greater than the lower bound that is required to keep main tethers taut [28]. However, it was found that the unsuppressed out-of-plane swing of main tethers, called coning motion, and the dynamic coupling between the local elastic tether deflection and the global orbital motion in the attitude maneuver may induce transverse vibration of tethers and then destabilize the E-sail spin rate [62]. A high-order multiphysics flexible E-sail model was built to better understand its dynamic characteristics, and a simplified attitude feedback control strategy was proposed with four throttling control parameters

[18]. Numerical analysis shows that the attitude of the E-sail has been controlled to the desired state. Unfortunately, the voltage modulation strategy does not apply if the main tethers are not charged in certain periods of transfer missions [37]. Accordingly, similar to the attitude control strategies for the tethered satellite formation [76] and the solar sails [8, 77], a complementary control strategy was proposed to control the E-sail attitude through injecting control forces at the remote units [71]. Parameter analysis by NPFEM shows this strategy is effective if all tethers are kept taut. Although effective, the stability of the control strategy by either voltage modulation at main tethers or thrust at remote units with mass-spring or NFFEM approach has not been investigated due to the difficulty in handling the high-order model under the Lyapunov framework.

2.4.2 Spin Rate Control of E-sail

To maintain the stability of the E-sail in the attitude maneuvering and the deployment of the E-sail, the E-sail's spin rate must be maintained at a pre-defined or desired rate to generate sufficient centrifugal force to keep tethers taut. First, a simple control law under the Lyapunov framework was proposed at the E-sail deployment process based on the lumped-mass model of E-sail [5]. It showed that the spin rate of E-sail can be controlled by controlling the spin rate of central hub. However, a different result was showed in [6] by using a simple PD controller, which was obtained by using NPFEM E-sail model. It showed that the spin rates of central hub and remote units must be controlled at the same time to maintain the stability of E-sail for the kilometer-long tethers at the deployment process. The results of [72] demonstrated the two different conclusions of [5-6], that was, the spin rates of the E-sail is not controllable by applying the control toque at the central spacecraft if the length of main is sufficiently long. Finally, the analysis demonstrated the tether vibration was suppressed, and the spin rate of the E-sail was stabilized by charging the auxiliary tether [16] at the fully deployment process.

2.5 E-sail Missions

The advantage mentioned at Chapter 1 makes the E-sail an attractive alternative to the solar sail for solar system missions. In this section, we will categorize most of the E-sail missions into groups. It should be noted that the "plasma brake" is not considered in current work, which uses the same working principle of E-sail but charging the main tethers with negative polarity. Also, all the interplanetary missions of E-sail should be started outside of Earth's magnetosphere, which the solar wind exists.

2.5.1 Non-Keplerian Orbit Missions

Non-Keplerian Orbit is the orbit whose plane does not pass through the CM of Sun [78]. To maintain the stability such a plane needs to continuously adjust the propulsive force direction to balance the gravitational and centrifugal forces components in the orbital plane, which is the advantage of E-sail [79]. Many new space applications have been proposed for such orbit, such as the continuous observation the Sun's polar region, which is lifted above the ecliptic plane as shown in Figure 2-2. The capabilities of E-sail to observe the Sun's polar region was firstly analyzed, and a comparison with solar sails was made to determine which system is more convenient for the displaced non-Keplerian orbit mission scenario [80]. The optimal (minimum time) transfer trajectories towards the displaced orbits were designed. The performance of E-sail in displaced non-Keplerian orbit was investigated by using a refined propulsive force [81]. And a control law was proposed to track a non-Keplerian orbit with a more accurate statistical model of solar wind dynamic pressure [82]. Further, the linearized relative motion and control of E-sail formation flight around a heliocentric displace orbit was investigated [83]. Finally, the feasibility of maintaining an E-sail based spacecraft in heliocentric displace orbit and orbit tracking problem were studied by using geometrical method and distributed coordinated control, respectively [84-85].

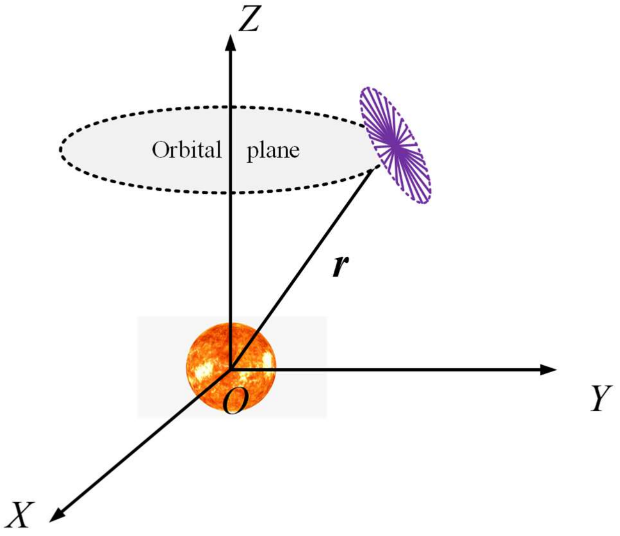

Figure 2-2 Sketch of non-Keplerian orbit.

2.5.2 Outer Solar System Missions

Outer solar system includes the giant planets, Kuiper belt objects, and beyond heliosphere interstellar space. E-sail is particularly suitable for outer solar system missions because it has the ability to provide continuous propellantless propulsion force and slower decay rate. First, the performance of E-sail reaching the heliosphere boundaries was studied in an optimal framework with minimum time [21]. It showed that a medium-performance E-sail has the potentialities to reach a distance of 100 au from the Sun in about 15 years, which is one-third the time of Voyager. Moreover, a mission scenario of delivering an atmospheric probe to Uranus and the comparison with traditional outer planet missions were preliminary analyzed [86].

2.5.3 Terrestrial Planets and Asteroids Missions

Terrestrial planets and asteroids missions gives an attractive choice for interplanetary mission transfers with E-sail. Many effects have been devoted to these missions. For instance, the performances of reaching the total 1025 currently known potentially hazardous asteroids was investigated by using optimal framework with minimum time [87]. The results showed the E-sail is a promising propulsion system. Meanwhile, the performances of E-sail for accomplishing flyby and return missions from a near-Earth asteroid was investigated by using the optimal framework [23, 88].

Venus and Mars are ideal terrestrial planets mission candidates because they do not have the magnetosphere. Thus, most of the attention was focused on them by using optimal framework with minimum time and trajectory tracking, which assumed the E-sail as an E-sail based spacecraft. For example, a locally-optimal control law by using the general approached was developed to study the performance of an E-sail based spacecraft [48]. Moreover, the finite Fourier series shape-based method [89], the indirect optimal approach [90], and the Bezier curve-based shaping approach [91] were used to design the mission trajectory. However, the E-sail based spacecraft can hardly follow the designed optimal trajectories to the target terrestrial planets or asteroids due to the uncertainty of solar wind. Thus, the trajectory tracking is necessary. A SMC law was proposed to overcome the propulsive force uncertainty and saturation problems [92]. Finally, a combined control was developed to counteract the influence of solar wind uncertainties by adjusting the voltage of main tethers [93].

2.5.4 Artificial Lagrangian Point Maintenance Missions

It is challenging to create and maintain artificial Lagrangian point in the restricted three-body problem. Because it is hard to continuously adjust thrust to balance the sum of gravitational and centrifugal force acting on the spacecraft. E-sail has the capability to deal with this issue. First, by assuming the constant orientation of E-sail, the existence and stability of artificial Lagrangian point for an E-sail based spacecraft were investigated with an elliptical restricted three-body problem [94]. Then, a proportional and a proportional derivative (PD) control strategies by modulating the voltage of main tethers were proposed to preliminarily analysis the dynamics of E-sail based spacecraft near an L1-type artificial Lagrangian point [95]. Finally, to deal with the unexpected E-sail actuator fault, a distributed fault-tolerant control framework was developed for E-sail based spacecraft at Sun-Earth artificial Lagrange points [95].

2.5.5 Mitigate Earth-threatening Asteroid Missions

There are around 100,000 objects near the Earth and one fifth of these are potentially dangerous to us [96]. To mitigate their threats, the trajectory of Earth-threatening asteroids must be deflected, which can be achieved by the E-sail. Currently, there are two ways to accomplish this: i) asteroid towing, ii) kinetic energy impactor. Asteroid towing is to connect the asteroid and E-sail with a tether. Through tilting the E-sail to continuously boosting the asteroids escape from the orbits that threat the Earth. The performances of using the E-Sail for deflecting the Earth-threatening asteroids was investigated, and its effectiveness and superiority were demonstrated [97]. The kinetic energy impactor is to use an E-sail based spacecraft to collide with the Earth-threatening asteroids with a high relative velocity. This collision will keep the asteroids' orbits away from the Earth. The mission scenario of orbital maneuvering by assuming the constant attitude E-sail was analyzed with the modulation of tethers' voltage [98]. It showed that the trajectory of asteroids with 1000 000 tons can be deflected to avoid the collision with Earth by using a 1000 kg E-sail. Finally, the effectiveness of this method was evaluated in comparison with solar sails.

Chapter 3 MATHEMATICAL FORMULATION OF E-SAIL

Summary: In this chapter, the mathematical formulation of the E-sail of three situations in this dissertation is presented. The first model is developed to investigate the influence of the elastic deformation motion of the tethers on the E-sail dynamic behaviors. The tethers are assumed elastic and discretized into inter-connected 2-noded tensile elements by using the NPFEM, while the central spacecraft and the remote units are simplified as lumped masses. Second, a rigid-flexible coupling dynamic model is obtained to study the modelling of rigid-flexible coupling influence on the attitude dynamics of the E-sail. This generalized model considers the attitude dynamics of the central spacecraft, the elastic deformation of the tethers and the rigid-flexible coupling between the spacecraft and the tethers. Finally, a reduced order analytical model is derived to approximately describe the flexible E-sail's attitude dynamics to design a stability control strategy for the E-sail attitude maneuver.

3.1 System Description

3.1.1 Coordinate Systems

In the $O_oX_oY_oZ_o$ coordinate system, the orbital motion of the E-sail is described. The origin O_o is located at the CM of the central spacecraft as shown in Figure 3-1(a). The Z_o axis is aligned with the direction pointing from the Sun to the CM of the spacecraft with the unit vector $\boldsymbol{a}_3$. The Y_o axis is aligned with the cross-product of $\boldsymbol{k}\times\boldsymbol{a}_3$ with the unit vector $\boldsymbol{a}_2$. The X_o axis completes the right-handed coordinate system with the unit vector $\boldsymbol{a}_1$.

In the $O_tX_tY_tZ_t$ coordinate system, the elastic elongation of the tether is described at the tether element level. The origin O_t is fixed at the node k of the k_{th} element, and the X_t axis and its unit vector $\boldsymbol{e}_x$ points from the node k to the node $k+1$. The Y_t axis is determined by the cross-product of $\boldsymbol{e}_x\times\boldsymbol{i}$ with the unit vector $\boldsymbol{e}_y$, and the Z_t axis forms a right-handed coordinate system with the unit vector $\boldsymbol{e}_z$, see Figure 3-1(b). If $\boldsymbol{e}_x\times\boldsymbol{i}=0$, the local tether element coordinate system $O_tX_tY_tZ_t$ will be set as $\boldsymbol{e}_x=\boldsymbol{i}$, $\boldsymbol{e}_y=\boldsymbol{j}$, $\boldsymbol{e}_z=\boldsymbol{e}_x\times\boldsymbol{e}_y$.

In the $O_{sp}X_{sp}Y_{sp}Z_{sp}$ coordinate system, the spin motion of the E-sail is described. The origin O_{sp} is also located at the CM of the central spacecraft as illustrated in Figure 3-1(c). The Z_{sp} axis is along the sail spin vector direction, the X_{sp} and the Y_{sp} axes are in the spin plane and complete a right-handed coordinate system. It should be noted that the X_{sp} and the Y_{sp} axes are decoupled from the self-spinning of the E-sail.

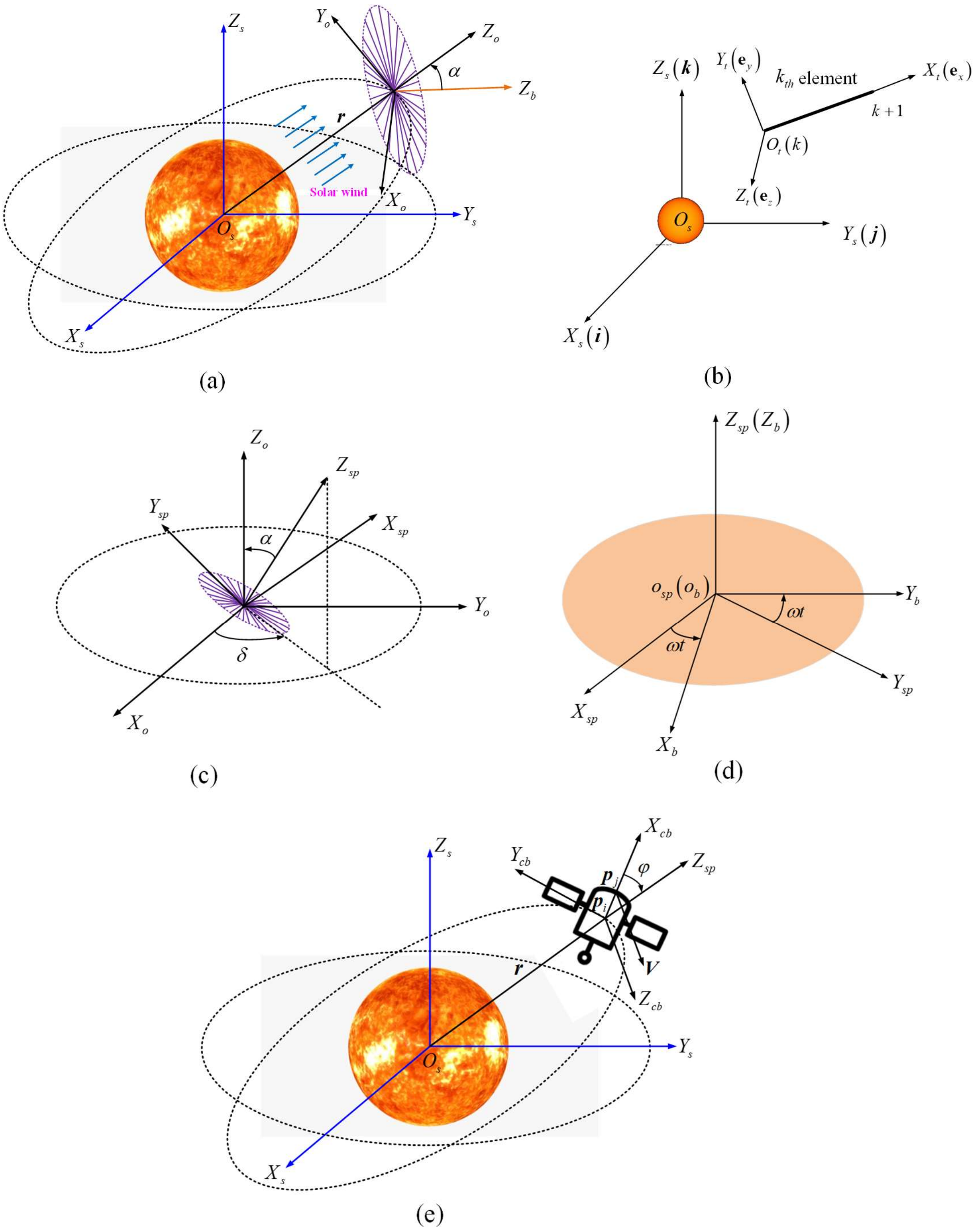

Figure 3-1 Schematic of E-sail coordinate systems.

In the $O_bX_bY_bZ_b$ coordinate system, the position information of the tethers and remote units is determined. The origin O_b is also at the CM of the central spacecraft as shown in Figure 3-1(d). The Z_b axis is aligned with the Z_{sp} axis. The X_b axis is aligned with the direction from the central spacecraft to the position of the 1st remote unit in the spin plane, and the Y_b axis forms a right-handed coordinate system.

Finally, the attitude dynamics of the central spacecraft is descried in the $O_{cb}X_{cb}Y_{cb}Z_{cb}$ coordinate system. The $O_{cb}X_{cb}Y_{cb}Z_{cb}$ coordinate system is defined by two basic points (p_i, p_j) and two non-coplanar unit vectors ($\mathbf{u}$, $\mathbf{v}$) of the central spacecraft as shown in Figure 3-1(e). The $\mathbf{u}$ and $\mathbf{v}$ are perpendicular to the axisymmetric axis and perpendicular to each other. The origin O_{cb} is at the CM of the central spacecraft (p_i),the X_{cb} axis is aligned with the vector pointing from p_i to p_j, the Y_{cb} axis is selected to be perpendicular to the X_{cb} axis and aligned with the direction of the unit vector $\mathbf{u}$, the Z_{cb} axis completes the right-handed coordinate system with the unit vector $\mathbf{v}$. The vector $\boldsymbol{r}$ is the position vector pointing from the center of Sun to the CM of the central spacecraft. The attitude velocity of the central spacecraft relative to the $O_sX_sY_sZ_s$ coordinate system $\left(\boldsymbol{\Omega}+\boldsymbol{\omega}_s\right)$ is the summation of the angular velocity of the $O_{cb}X_{cb}Y_{cb}Z_{cb}$ coordinate system relative to the $O_sX_sY_sZ_s$ coordinate system $\boldsymbol{\Omega}=\begin{bmatrix} 0 & 0 & \sqrt{\mu_{\square}/|\boldsymbol{r}|^3} \end{bmatrix}^T$ and the angular velocity of the central spacecraft in the

$O_s X_s Y_s Z_s$ coordinate system $\boldsymbol{\omega}_s$, where $\mu_{\odot}$ is the standard gravitational parameter of the Sun, the symbol $(\ )^T$ denotes the transpose matrix.

3.1.2 Relative Orientation of the Coordinate Systems

The relative orientation of the above coordinate systems can be described by the orbital and attitude angles of the E-sail and the transformation matrices, as shown in Figure 3-2.

First, the relative orientation of the $O_s X_s Y_s Z_s$ with respect to the $O_o X_o Y_o Z_o$ coordinate systems can be described by two angles $\phi \in \left[-\pi/2 \quad +\pi/2\right]$ and $\psi \in \left[0 \quad +2\pi\right]$ as shown in Figure 3-2(a), which are defined to measure the ecliptic latitude and longitude of the E-sail position as

$$\begin{cases} \phi = \arcsin\left(\sqrt{\left(r_x^2 + r_y^2\right)} \Big/ |\boldsymbol{r}|\right) \\ \psi = \begin{vmatrix} \arccos\left(r_x \Big/ \sqrt{\left(r_x^2 + r_y^2\right)}\right) & r_y \geq 0 \\ 2\pi - \arccos\left(r_x \Big/ \sqrt{\left(r_x^2 + r_y^2\right)}\right) & r_y < 0 \end{vmatrix} \end{cases} \tag{3.1}$$

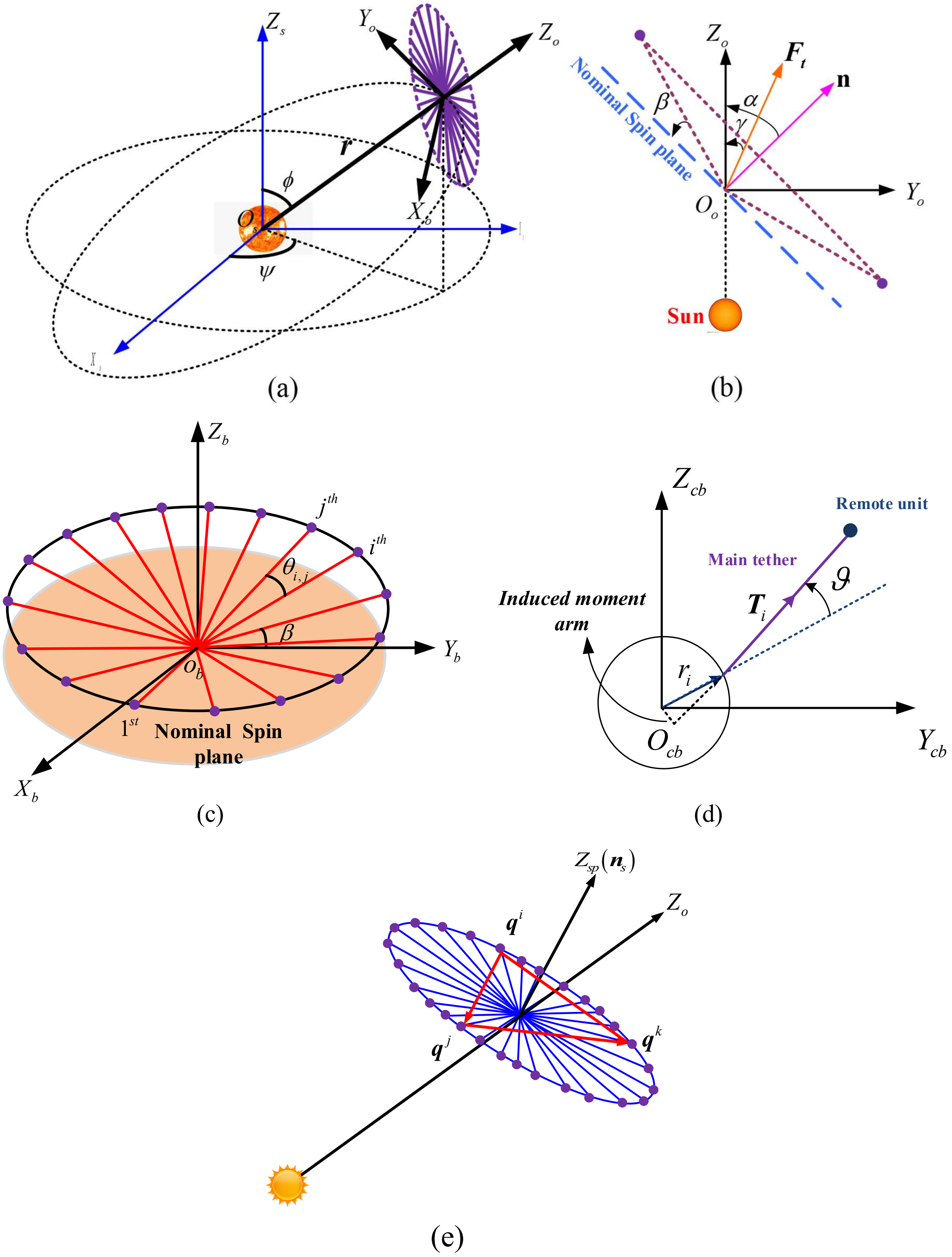

Figure 3-2 E-sail orientation and the related angles.

where arcsin and arccos represent the inverse of the sine cosine function, respectively, $\boldsymbol{r} = \begin{bmatrix} r_x & r_y & r_z \end{bmatrix}^T$ is the position vector of the central spacecraft in the $O_s X_s Y_s Z_s$ coordinate system.

The transformation matrices $\boldsymbol{A}_{s2o}$ and $\boldsymbol{T}_{s2o}$ are given to describe the relative orientation of the $O_s X_s Y_s Z_s$ with respect to the $O_o X_o Y_o Z_o$ coordinate systems in the form of vectors and angles as

$$\begin{aligned}\boldsymbol{A}_{s2o} &= \begin{bmatrix} \cos(\phi) & 0 & -\sin(\phi) \\ 0 & 1 & 0 \\ \sin(\phi) & 0 & \cos(\phi) \end{bmatrix} \begin{bmatrix} \cos(\psi) & \sin(\psi) & 0 \\ -\sin(\psi) & \cos(\psi) & 0 \\ 0 & 0 & 1 \end{bmatrix} \\ &= \begin{bmatrix} \cos(\phi)\cos(\psi) & \cos(\phi)\sin(\psi) & -\sin(\phi) \\ -\sin(\psi) & \cos(\psi) & 0 \\ \sin(\phi)\cos(\psi) & \sin(\phi)\sin(\psi) & \cos(\phi) \end{bmatrix}\end{aligned} \tag{3.2}$$

or

$$\boldsymbol{T}_{s2o} = \begin{bmatrix} \dfrac{O^s_{o\_x} O^s_{o\_z}}{\left|\boldsymbol{O}^s_o\right|^2} & \dfrac{O^s_{o\_y} O^s_{o\_z}}{\left|\boldsymbol{O}^s_o\right|^2} & -\dfrac{\left(O^s_{o\_x}\right)^2 + \left(O^s_{o\_y}\right)^2}{\left|\boldsymbol{O}^s_o\right|^2} \\ -\dfrac{O^s_{o\_y}}{\left|\boldsymbol{O}^s_o\right|} & \dfrac{O^s_{o\_x}}{\left|\boldsymbol{O}^s_o\right|} & 0 \\ \dfrac{O^s_{o\_x}}{\left|\boldsymbol{O}^s_o\right|} & \dfrac{O^s_{o\_y}}{\left|\boldsymbol{O}^s_o\right|} & \dfrac{O^s_{o\_z}}{\left|\boldsymbol{O}^s_o\right|} \end{bmatrix} \tag{3.3}$$

where the superscript s denotes the $O_s X_s Y_s Z_s$ coordinate system, $\boldsymbol{O}^s_o = \begin{bmatrix} O^s_{o\_x} & O^s_{o\_y} & O^s_{o\_z} \end{bmatrix}^T$ is the position vector of the origin O_o in the $O_s X_s Y_s Z_s$ coordinate system. It should be noted that the transformation matrices $\boldsymbol{A}_{s2o}$

and $\boldsymbol{T}_{s2o}$ are equivalent.

Then, the transformation matrix from the $O_tX_tY_tZ_t$ to the $O_sX_sY_sZ_s$ coordinate system can be written as

$$\boldsymbol{T}_{t2s}^{k} = \begin{bmatrix} \frac{X_{k+1}^s - X_k^s}{L_{e,k}} & 0 & -\frac{\left(Y_{k+1}^s - Y_k^s\right)^2 + \left(Z_{k+1}^s - Z_k^s\right)^2}{L_{e,k}^2} \\ \frac{Y_{k+1}^s - Y_k^s}{L_{e,k}} & \frac{Z_{k+1}^s - Z_k^s}{L_{e,k}} & \frac{\left(X_{k+1}^s - X_k^s\right)\left(Y_{k+1}^s - Y_k^s\right)}{L_{e,k}^2} \\ \frac{Z_{k+1}^s - Z_k^s}{L_{e,k}} & -\frac{Y_{k+1}^s - Y_k^s}{L_{e,k}} & \frac{\left(X_{k+1}^s - X_k^s\right)\left(Z_{k+1}^s - Z_k^s\right)}{L_{e,k}^2} \end{bmatrix} \tag{3.4}$$

where $\begin{pmatrix} X_k^s & Y_k^s & Z_k^s \end{pmatrix}^T$, $\begin{pmatrix} X_{k+1}^s & Y_{k+1}^s & Z_{k+1}^s \end{pmatrix}^T$, and $L_{e,k}$ are the position vectors of the k_{th} and $\left(k+1\right)_{th}$ nodes, and the instantaneous length of the k_{th} element, respectively. The instantaneous length of the k_{th} element is expressed as

$$L_{e,k} = \sqrt{\left(X_{k+1}^s - X_k^s\right)^2 + \left(Y_{k+1}^s - Y_k^s\right)^2 + \left(Z_{k+1}^s - Z_k^s\right)^2} \tag{3.5}$$

Furthermore, the sail and clocks angles $\alpha \in \left[-\pi, \quad +\pi\right]$ and $\delta \in \left[0, \quad +2\pi\right]$ are used to define the relative orientation of $O_oX_oY_oZ_o$ with respect to the $O_{sp}X_{sp}Y_{sp}Z_{sp}$ coordinate systems as shown in Figure 3-2(b). The positive sail angle α is measured in the counter-clockwise direction from the spin vector $\boldsymbol{n}_o$ to the O_oZ_o axis, while the negative sail angle is in the opposite direction. The clock angle δ is described by the angle between the positive X_o axis and the spin vector's projection onto the $O_oX_oY_o$ plane. These two angles are given by

$$\alpha = \begin{cases} \arccos\left(n_{o\_z}/\left|\boldsymbol{n}_o\right|\right) & if\ n_{o\_y} \geq 0 \\ -\arccos\left(n_{o\_z}/\left|\boldsymbol{n}_o\right|\right) & if\ n_{o\_y} < 0 \end{cases}$$

$$\delta = \begin{cases} \arccos\left(n_{o\_x}\Big/\sqrt{\left(n_{o\_x}\right)^2 + \left(n_{o\_y}\right)^2}\right) & if\ n_{o\_y} \geq 0 \\ 2\pi - \arccos\left(n_{o\_x}\Big/\sqrt{\left(n_{o\_x}\right)^2 + \left(n_{o\_y}\right)^2}\right) & if\ n_{o\_y} < 0 \end{cases} \tag{3.6}$$

where $\boldsymbol{n}_o = \begin{bmatrix} n_{o\_x} & n_{o\_y} & n_{o\_z} \end{bmatrix}^T = \boldsymbol{A}_{s2o}\boldsymbol{n}_s = \boldsymbol{T}_{s2o}\boldsymbol{n}_s$ is the unit vector of the E-sail spin axis direction in the $O_oX_oY_oZ_o$ coordinate system, and $\boldsymbol{n}_s$ is its expression in the $O_sX_sY_sZ_s$ coordinate system. The calculation of the unit spin vector $\boldsymbol{n}_s$ is introduced here, which is a dynamic state of the E-sail. It could be determined by solving a differential equation about the angular momentum of the E-sail [16]. To simplify the process, the current work proposes an alternative geometrical approach, where the spin vector $\boldsymbol{n}_s$ is defined by the positions of three remote units in the $O_sX_sY_sZ_s$ coordinate system, that is,

$$\boldsymbol{n}_s = \frac{\boldsymbol{P}_{i,j}^s \times \boldsymbol{P}_{j,k}^s}{\left\|\boldsymbol{P}_{i,j}^s \times \boldsymbol{P}_{j,k}^s\right\|} \tag{3.7}$$

where $\boldsymbol{P}_{i,j}^s = \boldsymbol{P}_j^s - \boldsymbol{P}_i^s$, $\boldsymbol{P}_{j,k}^s = \boldsymbol{P}_k^s - \boldsymbol{P}_j^s$, $\boldsymbol{P}_i^s$, $\boldsymbol{P}_j^s$ and $\boldsymbol{P}_k^s$ are the three selected remote units' position vectors, respectively.

In addition, attitude of the E-sail in the orbital coordinate system can also be described by three Euler angles: ζ, η and Θ, and the rotational sequence is $\boldsymbol{R}_1(\zeta)\rightarrow\boldsymbol{R}_2(\eta)\rightarrow\boldsymbol{R}_3(\Theta)$. The transformation matrices $\boldsymbol{A}_{o2sp}$ and $\boldsymbol{T}_{o2sp}$ are used to describe the relative orientation of the $O_oX_oY_oZ_o$ with respect to the $O_{sp}X_{sp}Y_{sp}Z_{sp}$ coordinate systems in both forms, respectively, that are,

$$\begin{aligned}\boldsymbol{A}_{o2sp} &= \begin{bmatrix} \cos\alpha & 0 & -\sin\alpha \\ 0 & 1 & 0 \\ \sin\alpha & 0 & \cos\alpha \end{bmatrix}\begin{bmatrix} \cos\delta & \sin\delta & 0 \\ -\sin\delta & \cos\delta & 0 \\ 0 & 0 & 1 \end{bmatrix} \\ &= \begin{bmatrix} \cos\alpha\cos\delta & \cos\alpha\sin\delta & -\sin\alpha \\ -\sin\delta & \cos\delta & 0 \\ \sin\alpha\cos\delta & \sin\alpha\sin\delta & \cos\alpha \end{bmatrix}\end{aligned} \tag{3.8}$$

or

$$\begin{aligned}\boldsymbol{T}_{o2sp} &= \begin{bmatrix} \cos\Theta & \sin\Theta & 0 \\ -\sin\Theta & \cos\Theta & 0 \\ 0 & 0 & 1 \end{bmatrix}\begin{bmatrix} \cos\eta & 0 & -\sin\eta \\ 0 & 1 & 0 \\ \sin\eta & 0 & \cos\eta \end{bmatrix}\begin{bmatrix} 1 & 0 & 0 \\ 0 & \cos\zeta & \sin\zeta \\ 0 & -\sin\zeta & \cos\zeta \end{bmatrix} \\ &= \begin{bmatrix} \cos\eta\cos\Theta & \cos\zeta\sin\Theta+\sin\zeta\sin\eta\cos\Theta & \sin\zeta\sin\Theta-\cos\zeta\sin\eta\cos\Theta \\ -\cos\eta\sin\Theta & \cos\zeta\cos\Theta-\sin\zeta\sin\eta\sin\Theta & \sin\zeta\cos\Theta+\cos\zeta\sin\eta\sin\Theta \\ \sin\eta & -\sin\zeta\cos\eta & \cos\zeta\cos\eta \end{bmatrix}\end{aligned} \tag{3.9}$$

where $\zeta\in[-\pi\quad\pi]$, $\eta\in\left[-\frac{\pi}{2}\quad\frac{\pi}{2}\right]$, $\Theta\in[-\pi\quad\pi]$ are the three Euler angles.

It was worth to mention that the transformation $\boldsymbol{A}_{o2sp}$ and $\boldsymbol{T}_{o2sp}$ are equivalent. Thus, comparing the Equations (3.8) with (3.9), the Euler angles can be expressed by the sail and clock angles, which can be obtain as

$$\eta = \arcsin(\sin\alpha\cos\delta)$$

$$\left|\begin{array}{l} \text{step 1}: \\ \zeta_{check} = \arccos\left(\cos\alpha/\cos\eta\right) \\ \mathit{step}\ 2: \\ \zeta = \begin{cases} \zeta_{check} & \mathit{if}\ \sin(\zeta_{check}) = -\sin\alpha\sin\delta/\cos\eta \\ -\zeta_{check} & \mathit{if}\ \sin(\zeta_{check}) \neq -\sin\alpha\sin\delta/\cos\eta \end{cases} \end{array}\right.$$

$$\left|\begin{array}{l} \text{step 1}: \\ \Theta_{check} = \arccos\left(\cos\alpha\cos\delta/\cos\eta\right) \\ \mathit{step}\ 2: \\ \Theta = \begin{cases} \Theta_{check} & \mathit{if}\ \sin(\Theta_{check}) = \sin\delta/\cos\eta \\ -\Theta_{check} & \mathit{if}\ \sin(\Theta_{check}) \neq \sin\delta/\cos\eta \end{cases} \end{array}\right. \tag{3.10}$$

It can be seen that the sail and clock angles can be controlled by controlling the three Euler angles.

The $O_{sp}X_{sp}Y_{sp}Z_{sp}$ with respect to the $O_bX_bY_bZ_b$ coordinate systems can be determined by a rotation angle along the Z_b axis, where the rotation angle is $\omega_0 t$, ω_0 is the spin rate of the E-sail and t is the current rotation time, see Figure 3-2(c). The transformation matrix $\boldsymbol{T}_{sp2b}$ from the $O_{sp}X_{sp}Y_{sp}Z_{sp}$ to the $O_bX_bY_bZ_b$ coordinate systems can be written as

$$\boldsymbol{T}_{sp2b} = \begin{bmatrix} \cos(\omega t) & \sin(\omega t) & 0 \\ -\sin(\omega t) & \cos(\omega t) & 0 \\ 0 & 0 & 1 \end{bmatrix} \tag{3.11}$$

Finally, the transformation matrix from the $O_{cb}X_{cb}Y_{cb}Z_{cb}$ to the $O_sX_sY_sZ_s$ coordinate systems is given by

$$\boldsymbol{T}_{cb2s} = \begin{bmatrix} \boldsymbol{p}_j - \boldsymbol{p}_i & \mathbf{u} & \mathbf{v} \end{bmatrix} \begin{bmatrix} \bar{\boldsymbol{p}}_j - \bar{\boldsymbol{p}}_i & \bar{\mathbf{u}} & \bar{\mathbf{v}} \end{bmatrix}^{-1} \tag{3.12}$$

where $\bar{\boldsymbol{p}}_i$, $\bar{\boldsymbol{p}}_j$, $\bar{\mathbf{u}}$ and $\bar{\mathbf{v}}$ are the projections of the vectors $\boldsymbol{p}_i$, $\boldsymbol{p}_j$, $\mathbf{u}$ and $\mathbf{v}$ in the $O_{cb}X_{cb}Y_{cb}Z_{cb}$ coordinate system, respectively. The symbol $(\ )^{-1}$ denotes the inverse of the matrix.

To describe the attitude motion and evaluate the dynamic performance of the E-sail, the system angles are defined and presented in this section, as shown in Figure 3-1 and Figure 3-2. They are the thrust angle $\gamma \in (-\pi/2,\ \ +\pi/2)$, the coning angle $\beta \in (-\pi/2,\ \ +\pi/2)$, the nutation angle $\varphi \in (-\pi/2,\ \ +\pi/2)$, the relative angle $\vartheta \in [-\pi/2,\ \ +\pi/2]$, and the adjacent angle $\theta_{i,j}$.

The thrust angle γ is the angle between the O_oZ_o axis and the total propulsive force $\boldsymbol{F}_t$. Because the main tether is always positively charged, the propulsive force is always in the positive side of the O_oZ_o axis. The coning angle β is defined by the angle between the nominal spin plane and each main tether. When the remote units are at the positive side of the spin plane, the angle is positive and vice versa. The coning motions of main tethers can be described by the same coning angle because the E-sail is an axisymmetric system, and the main tethers share the same spin plane. The positive nutation angle φ is measured counter-clockwise from the X_{cb} axis to the spin vector $\boldsymbol{n}$ and vice versa. The relative angle ϑ between the vectors $\boldsymbol{T}_i$ and $\boldsymbol{r}_i$ in the

$O_{cb}Y_{cb}Z_{cb}$ plane is the in-plane libration of main tether with respect to the radial direction. The positive ϑ is measured counter-clockwise from the vector $\boldsymbol{r}_i$ to the vector $\boldsymbol{T}_i$ and vice versa. The adjacent angle $\theta_{i,j}$ is the angle between the i^{th} and j^{th} main tethers.

Figure 3-3 shows three different configurations of the E-sail, which are named as Type I, Type II and Type III, respectively. These configurations represent three different designs of the E-sail with the sail plane aligned with the left edge, the CM, and the right edge of the central spacecraft, respectively.

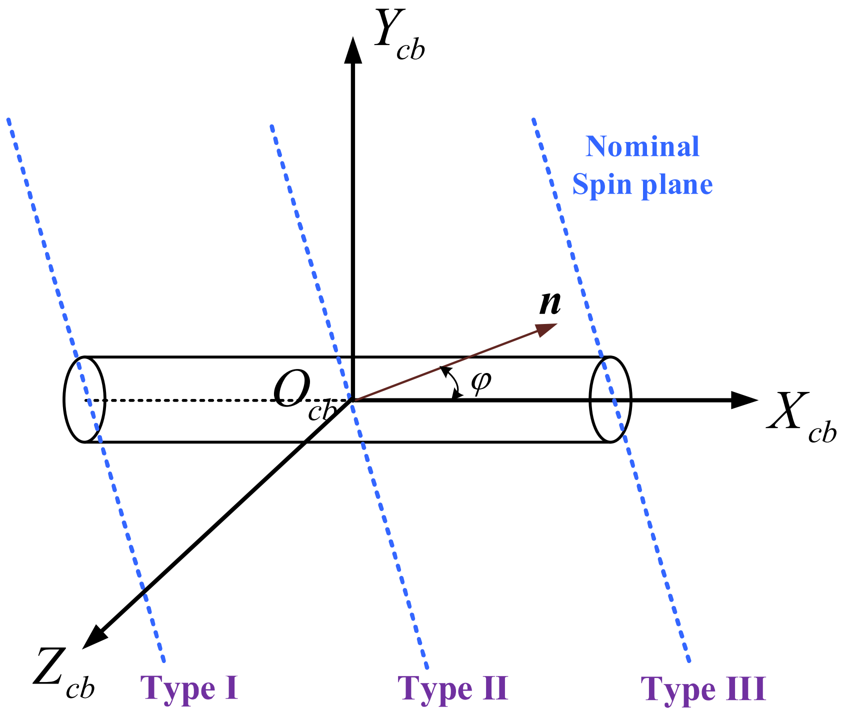

Figure 3-3 Three configurations of the E-sail.

3.2 Propulsive Force Formulation

The investigation of the E-sail requires precise knowledge of the propulsive force, which is generated by the positively charged main tethers. Many efforts have been devoted to the accurate analytic expression of the propulsive force in the literature. Currently, several models of propulsive force that acts on the charged tethers have been presented, which are derived from either the PIC simulation simplified analytical model, or the empirical model. Consider a long and positively charged tether in the solar wind. When the incident protons in the solar wind are in the close range (the Debye length) of the tether, they will be deflected due to the Coulomb effect and a propulsive force is generated accordingly. It should be noted that the propulsive force is calculated in the local tether element coordinate system. The propulsive force per unit length acting on the main tether was first derived from the 2D PIC model as described in Ref. [13]

$$\boldsymbol{f}_{dl} = K \frac{m_p n \left|\boldsymbol{v}_{sw\perp}\right| r_0 \boldsymbol{v}_{sw\perp}}{\sqrt{exp\left[\dfrac{m_p \boldsymbol{v}_{sw\perp}^2}{eV} \ln\left(\dfrac{r_0}{r_w}\right)\right] - 1}} \tag{3.13}$$

$$n \approx 7.2\times10^{6}\left(\frac{1}{r}\right)^{2} + 1.95\times10^{3}\left(\frac{1}{r}\right)^{4} + 8.1\times10^{-1}\left(\frac{1}{r}\right)^{6} \tag{3.14}$$

$$r_0 = 2\sqrt{\varepsilon_0 T_e / \left(ne^2\right)} \quad T_e \approx 3.8e\left[1 + 1.5\left(\frac{1}{r}\right)^{4/3}\right] \tag{3.15}$$

where $\boldsymbol{f}_{dl}$ is the propulsive force per unit tether length in N/m, $K \approx 3.09$ is the coefficient of the propulsive force determined by numerical simulations [13], $m_p = 1.67262 \times 10^{-27} kg$ is the solar wind proton mass, n is the undisturbed solar wind electron density [6], $\boldsymbol{v}_{sw\perp}$ is the solar wind velocity perpendicular to the direction of the tether and the magnitude is denoted by $|\boldsymbol{v}_{sw\perp}|$, r_0 is the two times of electron Debye length, $e = 1.60218 \times 10^{-19} C$ is the elementary charge, V is the tether potential, r_w is the tether effective radius, r is the Sun-spacecraft distance in au, $\varepsilon_0 = 8.85419 \times 10^{-12} F/m$ is the vacuum permittivity, T_e is the temperature of the slow solar wind electron [43]. Here, the fast solar wind component, which usually exists in the polar orbit, is neglected because the E-sail is in the ecliptic plane.

Furthermore, it can be seen that the propulsive force depends on how many electrons are trapped by the electric field of the positively charged tethers. By removing the trapped electrons completely, it was found that the magnitude of propulsive force per unit length is increased roughly by five times from Equation (3.13). It can be further simplified if the E-sail is near 1 au distance from the Sun [3] as

$$\boldsymbol{f}_{dl} = \sigma \, \boldsymbol{v}_{sw\perp} \tag{3.16}$$

$$\sigma = 0.18 \, max(0, V - V_w) \sqrt{\varepsilon_0 m_p n} \tag{3.17}$$

where V_w is the solar wind electric potential (usually 1kV). Here, 0.18 is the coefficient of the propulsive force, which is determined by numerical simulations.

Different from the PIC modeling approach, NASA derived an empirical propulsive force model near 1 au distance from the Sun [47] as follows:

$$\boldsymbol{f}_{dl} = 2.58 n m_p \left|\boldsymbol{v}_{sw\perp}\right| r_0 \sqrt{V} \boldsymbol{v}_{sw\perp} \tag{3.18}$$

Although the prediction of propulsive force models in Equation (3.16) and (3.18) is closer to experimental measurements, the models do not include the distance effect explicitly and thus can not be used in the region far away from 1 au. On the contrary, the model in Equation (3.13) provides a physical insight of the propulsive force by considering the influences of the solar wind, E-sail location relative to the Sun, and properties of the main tether, even though it grossly underestimates the magnitude of the propulsive force. Therefore, the model in Equation (3.13) is modified by a factor K in the current work to investigate the impact of different propulsive force model on the dynamic response of the E-sail. The value of K is determined based on Equations (3.16) and (3.18) for the parametric analysis to account for the impacts of the solar wind conditions, E-sail location and properties of the main tether. The modified model of the propulsive force unit length is expressed as

$$\boldsymbol{f}_{dl} = K_i \frac{m_p n \left|\boldsymbol{v}_{sw\perp}\right| r_0 \boldsymbol{v}_{sw\perp}}{\sqrt{exp\left[\frac{m_p \boldsymbol{v}_{sw\perp}^2}{eV} \ln\left(\frac{r_0}{r_w}\right)\right] - 1}} \tag{3.19}$$

where $K_i\left(i=1,2,3\right)$ is the coefficient that represents these three propulsive force models, where $K_1=3.09$ [13], $K_2=11.74$ [44], and $K_3=56.36$ [47].

3.3 Modeling of E-sail by Nodal Position Finite Element Method

The dynamics of elastic tethers of the E-sail has been modeled by beam [63, 69-70] and bar [67, 99-100] models. Among them, the bar model [67] by the Nodal Position Finite Element method (NPFEM) provides a good balance in terms of accuracy and computational efficiency and is adopted in this dissertation. The dynamics of main and auxiliary tethers are described by the NPFEM due to its advantage in dealing with the coupled elastic and rigid nonlinear motion of flexible tethers. The influence of the flexible elastic deformation of the tethers on the dynamic characteristics of E-sail is studied by using this high-fidelity model. All tethers are assumed as elastic inter-connected 2-noded tensile elements, which obey the Hooke's law. The central spacecraft and the remote units are simplified as lumped masses.

Considering the k_{th} tether element in the Figure 3-1(b), the arbitrary point in the $O_tX_tY_tZ_t$ coordinate system can be described by the coordinate $\boldsymbol{q}=\left[x \quad y \quad z\right]^T$, and the coordinates can be expressed in the $O_sX_sY_sZ_s$ coordinate system as

$$\boldsymbol{q}=\boldsymbol{S}_k\boldsymbol{q}_k \tag{3.20}$$

where $\boldsymbol{q}$ is the position vector of the arbitrary point in the $O_sX_sY_sZ_s$ coordinate system, $\boldsymbol{q}_k = \left\{X_k^s, Y_k^s, Z_k^s, X_{k+1}^s, Y_{k+1}^s, Z_{k+1}^s\right\}^T$ is the position vector of the k_{th} element, and $\boldsymbol{S}_k$ is the element shape function, which is defined as

$$\boldsymbol{S}_k = \begin{bmatrix} 1-\xi & 0 & 0 & \xi & 0 & 0 \\ 0 & 1-\xi & 0 & 0 & \xi & 0 \\ 0 & 0 & 1-\xi & 0 & 0 & \xi \end{bmatrix} \tag{3.21}$$

where $\xi = x/L_{e,k}$.

Taking the first and second order derivatives of Equation (3.20) with respect to time t yields the velocity $\dot{\boldsymbol{q}}$ and the acceleration $\ddot{\boldsymbol{q}}$ of the arbitrary point in the $O_sX_sY_sZ_s$ coordinate system as follows:

$$\begin{aligned} \dot{\boldsymbol{q}} &= \frac{d\boldsymbol{q}}{dt} = \boldsymbol{S}_k\dot{\boldsymbol{q}}_k \\ \ddot{\boldsymbol{q}} &= \frac{d^2\boldsymbol{q}}{dt^2} = \boldsymbol{S}_k\ddot{\boldsymbol{q}}_k \end{aligned} \tag{3.22}$$

Then, the Green-Lagrangian strain of the k_{th} element is defined by

$$\varepsilon_k = L_{0,k}/L_{e,k} - 1 = \boldsymbol{\varepsilon}\boldsymbol{q}_k - 1 \tag{3.23}$$

where $L_{0,k}$ is the undeformed length of the k_{th} element, $\boldsymbol{\varepsilon}$ is the strain matrix, such that,

$$\boldsymbol{\varepsilon} = \begin{bmatrix} -\frac{\cos\theta_x}{L_{0,k}} & -\frac{\cos\theta_y}{L_{0,k}} & -\frac{\cos\theta_z}{L_{0,k}} & \frac{\cos\theta_x}{L_{0,k}} & \frac{\cos\theta_y}{L_{0,k}} & \frac{\cos\theta_z}{L_{0,k}} \end{bmatrix} \tag{3.24}$$

where $\cos\theta_x$, $\cos\theta_y$ and $\cos\theta_z$ are the directional cosines, which can be written as

$$\cos\theta_x = \frac{X^s_{k+1} - X^s_k}{L_{e,k}} \quad \cos\theta_y = \frac{Y^s_{k+1} - Y^s_k}{L_{e,k}} \quad \cos\theta_z = \frac{Z^s_{k+1} - Z^s_k}{L_{e,k}} \tag{3.25}$$

Furthermore, the strain matrix $\boldsymbol{\varepsilon}$ can be decomposed into the product of the strain matrix in $O_t X_t Y_t Z_t$ coordinate system and the coordinate transformation matrix as

$$\boldsymbol{\varepsilon} = \boldsymbol{\varepsilon}_0 \boldsymbol{T}_k \tag{3.26}$$

where

$$\boldsymbol{\varepsilon}_0 = \left\lfloor -1/L_{0,k} \quad 0 \quad 0 \quad 1/L_{0,k} \quad 0 \quad 0 \right\rfloor \tag{3.27}$$

$$\boldsymbol{T}_k = \left\lfloor \begin{array}{cccccc} \cos\theta_x & \cos\theta_y & \cos\theta_z & 0 & 0 & 0 \\ 0 & 0 & 0 & 0 & 0 & 0 \\ 0 & 0 & 0 & 0 & 0 & 0 \\ 0 & 0 & 0 & \cos\theta_x & \cos\theta_y & \cos\theta_z \\ 0 & 0 & 0 & 0 & 0 & 0 \\ 0 & 0 & 0 & 0 & 0 & 0 \end{array} \right\rfloor \tag{3.28}$$

With the definition of the strain ε_k, the elastic stress in the element using the Hooke's law can be written as

$$\sigma_k = E_k \varepsilon_x = \boldsymbol{D}\boldsymbol{q}_k - E_k \tag{3.29}$$

where E_k and $\boldsymbol{D} = E_k \boldsymbol{\varepsilon}$ are the Young's modulus and elastic matrix of the k_{th} element.

3.3.1 Kinetic Energy

The kinetic energy of the k_{th} element can be written as

$$T_{e,k} = \frac{1}{2}\int_0^{L_{e,k}} \rho_k A_k \dot{\boldsymbol{q}}^T \dot{\boldsymbol{q}} dl = \frac{1}{2}\int_0^{L_{e,k}} \rho_k A_k \boldsymbol{S}_k^T \dot{\boldsymbol{q}}_k^T \dot{\boldsymbol{q}}_k \boldsymbol{S}_k dl = \frac{1}{2}\dot{\boldsymbol{q}}_k^T \boldsymbol{M}_{e,k} \dot{\boldsymbol{q}}_k \tag{3.30}$$

where $T_{e,k}$, ρ_k and A_k are the kinetic energy, material density and the cross-section area of the element, respectively. $\boldsymbol{M}_{e,k}$ is the mass matrix of the element, which can be expressed as

$$\boldsymbol{M}_{e,k} = \frac{\rho_k A_k L_{0,k}}{6}\begin{bmatrix} 2 & 0 & 0 & 1 & 0 & 0 \\ 0 & 2 & 0 & 0 & 1 & 0 \\ 0 & 0 & 2 & 0 & 0 & 1 \\ 1 & 0 & 0 & 2 & 0 & 0 \\ 0 & 1 & 0 & 0 & 2 & 0 \\ 0 & 0 & 1 & 0 & 0 & 2 \end{bmatrix} \tag{3.31}$$

It should be noticed that the mass matrix of the element is constant in the $O_s X_s Y_s Z_s$ coordinate system.

The kinetic energy of the i^{th} lumped mass can be written as

$$T_i = \frac{1}{2} m_i \sum_{i=1}^{M} \boldsymbol{v}_i^T \boldsymbol{v}_i \tag{3.32}$$

T_i, m_i and $\boldsymbol{v}_i$ are the kinetic energy, mass, and the velocity of the mass point, respectively.

Thus, the mass matrix of the k_{th} element including the mass of the lumped mass is

$$\boldsymbol{M}_{e,k} = \frac{\rho_k A_k L_{0,k}}{6} \begin{bmatrix} 2 & 0 & 0 & 1 & 0 & 0 \\ 0 & 2 & 0 & 0 & 1 & 0 \\ 0 & 0 & 2 & 0 & 0 & 1 \\ 1 & 0 & 0 & 2 & 0 & 0 \\ 0 & 1 & 0 & 0 & 2 & 0 \\ 0 & 0 & 1 & 0 & 0 & 2 \end{bmatrix} + \begin{bmatrix} 0 & 0 & 0 & 0 & 0 & 0 \\ 0 & 0 & 0 & 0 & 0 & 0 \\ 0 & 0 & 0 & 0 & 0 & 0 \\ 0 & 0 & 0 & m_i & 0 & 0 \\ 0 & 0 & 0 & 0 & m_i & 0 \\ 0 & 0 & 0 & 0 & 0 & m_i \end{bmatrix} \tag{3.33}$$

3.3.2 Strain Energy

The strain energy of the k_{th} element can be obtained as

$$U_{e,k} = \frac{1}{2}\int_0^{L_{e,k}} E_k A_k \varepsilon_x^2 dl = \frac{1}{2}\boldsymbol{q}_k^T \boldsymbol{K}_{e,k} \boldsymbol{q}_k - \boldsymbol{q}_k^T \boldsymbol{F}_{e,k} + \frac{1}{2} E_k A_k L_{e,k} \tag{3.34}$$

where $\boldsymbol{K}_{e,k}$ is the stiffness matrix of the element and $\boldsymbol{F}_{e,k}$ is the generalized nodal force vector resulting from the elasticity of the element, which can be written as

$$\boldsymbol{K}_{e,k} = E_k A_k L_{e,k} \boldsymbol{\varepsilon}^T \boldsymbol{\varepsilon} = \boldsymbol{T}_k^T \boldsymbol{K}_{e,k}^0 \boldsymbol{T}_k \tag{3.35}$$

$$\boldsymbol{F}_{e,k} = E_k A_k L_{e,k} \boldsymbol{\varepsilon}^T = E_k A_k L_{e,k} \boldsymbol{T}_k^T \boldsymbol{\varepsilon}_0 \tag{3.36}$$

$$\boldsymbol{K}_{e,k}^0 = \frac{E_k A_k L_{e,k}}{L_{0,k}^2} \begin{bmatrix} 1 & 0 & 0 & -1 & 0 & 0 \\ 0 & 0 & 0 & 0 & 0 & 0 \\ 0 & 0 & 0 & 0 & 0 & 0 \\ -1 & 0 & 0 & 1 & 0 & 0 \\ 0 & 0 & 0 & 0 & 0 & 0 \\ 0 & 0 & 0 & 0 & 0 & 0 \end{bmatrix} \tag{3.37}$$

3.3.3 Potential Energy and the External Forces

The potential energy of the k_{th} element can be obtained as

$$V_{e,k} = -\int_0^{L_{e,k}} \frac{\mu_\odot \rho_k A_k}{r_k} dl \tag{3.38}$$

where $\mu_\odot$ is the Sun's gravitational parameter, $V_{e,k}$ and r_k are the potential energy and distance from the CM of Sun to the element, respectively.

The potential energy of the i^{th} lumped mass can be written as

$$V_i = -\frac{\mu_\odot m_i}{r_i} \tag{3.39}$$

where r_i is the distance between the center of Sun and the i^{th} lumped mass.

The nodal force vectors, resulting from the gravity force $\boldsymbol{F}_{g,k}$ and the propulsive force $\boldsymbol{F}_{t,k}$ acting on the k_{th} tether element, are derived based on the principle of virtual work, that is,

$$\delta \boldsymbol{W}_{g,k} = \int_0^{L_{e,k}} \boldsymbol{S}_k^T \rho_k A_k \delta \boldsymbol{q}_{e,k}^T \mathbf{g}_\odot \, dl = \delta \boldsymbol{q}_{e,k}^T \boldsymbol{F}_{g,k} \tag{3.40}$$

$$\delta \boldsymbol{W}_{t,k} = \int_0^{L_{e,k}} \delta \boldsymbol{q}_{e,k}^T \boldsymbol{S}_k^T \boldsymbol{T}_{t2s}^k \boldsymbol{f}_{dl} dl = \delta \boldsymbol{q}_{e,k}^T \boldsymbol{F}_{t,k} \tag{3.41}$$

where $\boldsymbol{g}_\odot$ is the gravitational acceleration.

Equations (3.40) and (3.41) are evaluated by the Gaussian quadrature,

$$\boldsymbol{F}_{g,k} = \int_0^{L_{e,k}} \boldsymbol{S}_k^T \rho_k A_k \mathbf{g}_\odot \, dl = \frac{\rho_k A_k L_{e,k}}{2} \sum_{i=1}^{GI} w_i \boldsymbol{S}_k^T \left[\frac{L_{e,k}}{2}(1+\zeta_i) \right] \mathbf{g}_\odot \left[\frac{L_{e,k}}{2}(1+\zeta_i) \right] \tag{3.42}$$

$$\boldsymbol{F}_{t,k} = \int_0^{L_{e,k}} \boldsymbol{S}_k^T \boldsymbol{T}_{t2s}^k \boldsymbol{f}_{dl} dl = \frac{L_{e,k}}{2} \sum_{i=1}^{GI} w_i \boldsymbol{S}_k^T \left[L_{e,k}(1+\zeta_i)/2 \right] \boldsymbol{T}_{t2s}^k \boldsymbol{f}_{dl} \left[L_{e,k}(1+\zeta_i)/2 \right] \tag{3.43}$$

where GI is the point number of the Gaussian-Legendre quadrature, w_i and ζ_i are the Gaussian integration weight and abscissa, respectively. It should be noted that the variables in this section are all defined in the $O_sX_sY_sZ_s$ coordinate system.

3.3.4 Equations of motion of the E-sail

The equation of motion of the k_{th} element can be derived by utilizing the Lagrange equation of the second kind in the following form:

$$\frac{d}{dt}\left(\frac{\partial T_{e,k}}{\partial \dot{\boldsymbol{q}}_k}\right)-\frac{\partial T_{e,k}}{\partial \boldsymbol{q}_k}+\frac{\partial\left(V_{e,k}+U_{e,k}\right)}{\partial \boldsymbol{q}_k}=\boldsymbol{Q}_{e,k} \tag{3.44}$$

Thus, the discrete equation of motion of the k_{th} tether element can be obtained as

$$\boldsymbol{M}_{e,k}\ddot{\boldsymbol{q}}_k+\boldsymbol{K}_{e,k}\boldsymbol{q}_k=\boldsymbol{F}_{e,k}+\boldsymbol{F}_{g,k}+\boldsymbol{F}_{t,k} \tag{3.45}$$

where $\boldsymbol{M}_{e,i}$ and $\boldsymbol{K}_{e,i}$ are the mass and stiffness matrices of the k_{th} element, $\boldsymbol{F}_{e,k}$, $\boldsymbol{F}_{g,k}$ and $\boldsymbol{F}_{t,k}$ are the generalized elastic force resulting from NPFEM, gravity force and propulsive force of the k_{th} element, respectively. It is worth noting that that the tethers' material damping is not introduced in Equation (3.45) because of the lack of material damping data in space. Moreover, it should be emphasized that the propulsive force only acts on the main tethers, because only the main tethers are positively charged to form the electrostatic field and the auxiliary tethers are uncharged.

Assembling Equation (3.45) with the standard procedure in the finite element method leads to the discrete equations of motion of the E-sail,

$$\boldsymbol{M}_e\ddot{\boldsymbol{q}}_e + \boldsymbol{K}_e\boldsymbol{q}_e = \boldsymbol{F}_e + \boldsymbol{F}_g + \boldsymbol{F}_t \tag{3.46}$$

where $\boldsymbol{M}_e$ is the global mass matrix including the masses of the tethers and the remote units that are modelled as lumped masses and attached to the ends of the main tethers, $\boldsymbol{K}_e$ is the global stiffness matrix, $\boldsymbol{q}_e$ and $\ddot{\boldsymbol{q}}_e$ are the vectors of global position and acceleration of E-sail, $\boldsymbol{F}_e$, $\boldsymbol{F}_g$ and $\boldsymbol{F}_t$ are the vectors of global elastic, gravitational and propulsive forces, respectively. It should noted that the discrete equations of motion of auxiliary tethers are also included in Equation (3.46) and obtained by using the same procedure. The only difference is that the propulsive force produced by the auxiliary tethers are zero due to the nonconductive property.

3.4 Mathematic Formulation of the Generalized E-sail Model

The influence of the rigid-flexible coupling between the spacecraft and the tethers on the dynamic response of E-sail is studied with a generalized model. The attitude and translation dynamics of the central spacecraft is described by the NCF, while the tether deformation is described by the NPFEM. The remote units are simplified as lumped masses. The central spacecraft is modeled as a circular cylinder with a symmetrical axis by the NCF in the global Cartesian coordinate system $O_sX_sY_sZ_s$. Two basic points and two non-coplanar unit vectors are defined to describe the translational and rotational motions with 12 generalized global coordinates of the central spacecraft as shown in

Figure 3-1(e), such that,

$$\boldsymbol{p} = \begin{bmatrix} \boldsymbol{p}_i^T & \boldsymbol{p}_j^T & \mathbf{u}^T & \mathbf{v}^T \end{bmatrix}^T \tag{3.47}$$

where the superscript T denotes the transpose matrix.

The position vector of an arbitrary point p_a of the central spacecraft in the $O_sX_sY_sZ_s$ coordinate system can be written as

$$\begin{aligned} \boldsymbol{p}_a &= \boldsymbol{p}_i + c_1\left(\boldsymbol{p}_j - \boldsymbol{p}_i\right) + c_2\mathbf{u} + c_3\mathbf{v} \\ &= \begin{bmatrix} \left(1-c_1\right)\boldsymbol{I}_3 & c_1\boldsymbol{I}_3 & c_2\boldsymbol{I}_3 & c_3\boldsymbol{I}_3 \end{bmatrix} \boldsymbol{p} = \boldsymbol{C}\boldsymbol{p} \end{aligned} \tag{3.48}$$

where $\boldsymbol{C} = \begin{bmatrix} \left(1-c_1\right)\boldsymbol{I}_3 & c_1\boldsymbol{I}_3 & c_2\boldsymbol{I}_3 & c_3\boldsymbol{I}_3 \end{bmatrix}$ is a constant matrix, $\boldsymbol{I}_3$ is the 3×3 identity matrix, c_1, c_2 and c_3 are the constants. These constants obey the following equation

$$\overline{\boldsymbol{p}}_a = c_1\left(\overline{\boldsymbol{p}}_j - \overline{\boldsymbol{p}}_i\right) + c_2\overline{\mathbf{u}} + c_3\overline{\mathbf{v}} \tag{3.49}$$

where $\overline{\boldsymbol{p}}_a$, $\overline{\boldsymbol{p}}_i$, $\overline{\boldsymbol{p}}_j$, $\overline{\mathbf{u}}$ and $\overline{\mathbf{v}}$ are the projections of the vectors $\boldsymbol{p}_a$, $\boldsymbol{p}_i$, $\boldsymbol{p}_j$, $\mathbf{u}$ and $\mathbf{v}$ in the $O_bX_bY_bZ_b$ coordinate system, respectively.

Equation (3.49) can be expressed in a matrix form as

$$\overline{\boldsymbol{p}}_a = \begin{bmatrix} \overline{\boldsymbol{p}}_j - \overline{\boldsymbol{p}}_i & \overline{\mathbf{u}} & \overline{\mathbf{v}} \end{bmatrix} \begin{bmatrix} c_1 \\ c_2 \\ c_3 \end{bmatrix} = \overline{\boldsymbol{X}}\mathbf{c} \tag{3.50}$$

where $\overline{\boldsymbol{X}} = \begin{bmatrix} \overline{\boldsymbol{p}}_j - \overline{\boldsymbol{p}}_i & \overline{\mathbf{u}} & \overline{\mathbf{v}} \end{bmatrix}$, $\mathbf{c} = \begin{bmatrix} c_1 & c_2 & c_3 \end{bmatrix}^T$.

Thus, these constants c_1, c_2 and c_3 can be obtained by

$$\mathbf{c} = \overline{\boldsymbol{X}}^{-1}\overline{\boldsymbol{p}}_a \tag{3.51}$$

where the symbol $(\ )^{-1}$ denotes the inverse of the matrix.

Taking the first and second order derivatives of Equation (3.48) with respect to time t yields the velocity $\dot{\boldsymbol{p}}_a$ and the acceleration $\ddot{\boldsymbol{p}}_a$ of the point p_a as follow:

$$\begin{aligned} \dot{\boldsymbol{p}}_a &= \frac{d\boldsymbol{p}_a}{dt} = \boldsymbol{C}\dot{\boldsymbol{p}} \\ \ddot{\boldsymbol{p}}_a &= \frac{d^2\boldsymbol{p}_a}{dt^2} = \boldsymbol{C}\ddot{\boldsymbol{p}} \end{aligned} \tag{3.52}$$

3.4.1 Kinetic Energy of Central Spacecraft

The kinetic energy of the central spacecraft can be written as

$$T_s = \frac{1}{2}\int_{V_s} \rho_s \dot{\boldsymbol{p}}_a^T \dot{\boldsymbol{p}}_a dV_s = \frac{1}{2}\dot{\boldsymbol{p}}^T \boldsymbol{M}_s \dot{\boldsymbol{p}} \tag{3.53}$$

where ρ_s and V_s are the density and the volume of the central spacecraft. $\boldsymbol{M}_s$ is the mass matrix of the spacecraft, which can be obtained by

$$\begin{aligned} \boldsymbol{M}_s &= \rho_s \int_V \boldsymbol{C}^T \boldsymbol{C} dV_s \\ &= \rho_s \int_{V_s} \begin{bmatrix} (1-c_1)^2 \boldsymbol{I}_3 & (1-c_1)c_1\boldsymbol{I}_3 & (1-c_1)c_2\boldsymbol{I}_3 & (1-c_1)c_3\boldsymbol{I}_3 \\ (1-c_1)c_1\boldsymbol{I}_3 & c_1^2\boldsymbol{I}_3 & c_1c_2\boldsymbol{I}_3 & c_1c_3\boldsymbol{I}_3 \\ (1-c_1)c_2\boldsymbol{I}_3 & c_1c_2\boldsymbol{I}_3 & c_2^2\boldsymbol{I}_3 & c_2c_3\boldsymbol{I}_3 \\ (1-c_1)c_3\boldsymbol{I}_3 & c_1c_3\boldsymbol{I}_3 & c_2c_3\boldsymbol{I}_3 & c_3^2\boldsymbol{I}_3 \end{bmatrix} dV_s \end{aligned} \tag{3.54}$$

where

$$\int_{V_s} \rho_s dV_s = m_s \tag{3.55}$$

$$\int_{V_s} \rho_s \mathbf{c} dV_s = \bar{\boldsymbol{X}}^{-1} \int_{V_s} \rho_s \bar{\boldsymbol{p}}_a dV_s = m_s \bar{\boldsymbol{X}}^{-1} \bar{\boldsymbol{p}}_{CM} \tag{3.56}$$

$$\int_{V_s} \rho_s \mathbf{c}\mathbf{c}^T dV_s = \bar{\boldsymbol{X}}^{-1}\left(\int_{V_s} \rho_s \bar{\boldsymbol{p}}_a \bar{\boldsymbol{p}}_a^T dV_s\right)\left(\bar{\boldsymbol{X}}^{-1}\right)^T$$
$$= \begin{bmatrix} \bar{I}_x/H^2 & \bar{I}_{xy}/H & \bar{I}_{xz}/H \\ \bar{I}_{xy}/H & \bar{I}_y & \bar{I}_{yz} \\ \bar{I}_{xz}/H & \bar{I}_{yz} & \bar{I}_z \end{bmatrix} \tag{3.57}$$

where m_s is the mass of central spacecraft, $\bar{\boldsymbol{p}}_{CM} = \begin{bmatrix} \bar{p}_{CM\_x} & \bar{p}_{CM\_y} & \bar{p}_{CM\_z} \end{bmatrix}^T$ is the position of spacecraft CM in the $O_{cb}X_{cb}Y_{cb}Z_{cb}$ coordinate system, H is the height of central spacecraft. $\bar{I}_x = \int_{V_s} \rho_s \bar{p}_{a\_x}^2 dV_s$, $\bar{I}_y = \int_{V_s} \rho_s \bar{p}_{a\_y}^2 dV_s$, $\bar{I}_z = \int_{V_s} \rho_s \bar{p}_{a\_z}^2 dV_s$, $\bar{I}_{xy} = \int_{V_s} \rho_s \bar{p}_{a\_x} \bar{p}_{a\_y} dV_s$, $\bar{I}_{xz} = \int_{V_s} \rho_s \bar{p}_{a\_x} \bar{p}_{a\_z} dV_s$, $\bar{I}_{yz} = \int_{V_s} \rho_s \bar{p}_{a\_y} \bar{p}_{a\_z} dV_s$, $\bar{\boldsymbol{p}}_a = \begin{bmatrix} \bar{p}_{a\_x} & \bar{p}_{a\_y} & \bar{p}_{a\_z} \end{bmatrix}^T$.

Substituting Equations (3.55)-(3.57) into Equation (3.54) yields

$$\boldsymbol{M}_s = \begin{bmatrix} \left(m_s + \frac{\bar{I}_x}{H^2} - \frac{2m_s\bar{p}_{CM\_x}}{H}\right)\boldsymbol{I}_3 & \left(\frac{m_s\bar{p}_{CM\_x}}{H} - \frac{\bar{I}_x}{H^2}\right)\boldsymbol{I}_3 & \left(m_s\bar{p}_{CM\_y} - \frac{\bar{I}_{xy}}{H}\right)\boldsymbol{I}_3 & \left(m_s\bar{p}_{CM\_z} - \frac{\bar{I}_{xz}}{H}\right)\boldsymbol{I}_3 \\ \left(\frac{m_s\bar{p}_{CM\_x}}{H} - \frac{\bar{I}_x}{H^2}\right)\boldsymbol{I}_3 & \left(\frac{\bar{I}_x}{H^2}\right)\boldsymbol{I}_3 & \left(\frac{\bar{I}_{xy}}{H}\right)\boldsymbol{I}_3 & \left(\frac{\bar{I}_{xz}}{H}\right)\boldsymbol{I}_3 \\ \left(m_s\bar{p}_{CM\_y} - \frac{\bar{I}_{xy}}{H}\right)\boldsymbol{I}_3 & \left(\frac{\bar{I}_{xy}}{H}\right)\boldsymbol{I}_3 & \left(\bar{I}_y\right)\boldsymbol{I}_3 & \left(\bar{I}_{yz}\right)\boldsymbol{I}_3 \\ \left(m_s\bar{p}_{CM\_z} - \frac{\bar{I}_{xz}}{H}\right)\boldsymbol{I}_3 & \left(\frac{\bar{I}_{xz}}{H}\right)\boldsymbol{I}_3 & \left(\bar{I}_{yz}\right)\boldsymbol{I}_3 & \left(\bar{I}_z\right)\boldsymbol{I}_3 \end{bmatrix} \tag{3.58}$$

Equation (3.57) can be formed from the moments of inertia in the $O_{cb}X_{cb}Y_{cb}Z_{cb}$ coordinate system, that is,

$$\bar{\boldsymbol{I}} = \int_{V_s} \rho_s \left[\left(\bar{\boldsymbol{p}}_a \cdot \bar{\boldsymbol{p}}_a \right) \boldsymbol{I}_3 - \bar{\boldsymbol{p}}_a \bar{\boldsymbol{p}}_a \right] dV_s = \begin{bmatrix} I_{xx} & -I_{xy} & -I_{xz} \\ -I_{xy} & I_{yy} & -I_{yz} \\ -I_{xz} & -I_{yz} & I_{zz} \end{bmatrix} \tag{3.59}$$

where $I_{xx} = \int_{V_s} \rho_s \left(\bar{p}^2_{a\_y} + \bar{p}^2_{a\_z} \right) dV_s = \bar{I}_y + \bar{I}_z$, $I_{yy} = \int_{V_s} \rho_s \left(\bar{p}^2_{a\_x} + \bar{p}^2_{a\_z} \right) dV_s = \bar{I}_x + \bar{I}_z$, $I_{zz} = \int_{V_s} \rho_s \left(\bar{p}^2_{a\_x} + \bar{p}^2_{a\_y} \right) dV_s = \bar{I}_x + \bar{I}_y$, $I_{xy} = \bar{I}_{xy}$, $I_{xz} = \bar{I}_{xz}$, $I_{yz} = \bar{I}_{yz}$.

Comparing Equation (3.57) with Equation (3.59), the relationship between them can be expressed as

$$\begin{bmatrix} \bar{I}_x \\ \bar{I}_y \\ \bar{I}_z \end{bmatrix} = \begin{bmatrix} 0 & 1 & 1 \\ 1 & 0 & 1 \\ 1 & 1 & 0 \end{bmatrix}^{-1} \begin{bmatrix} I_{xx} \\ I_{yy} \\ I_{zz} \end{bmatrix} \tag{3.60}$$

Finally, the mass matrix of the cylindrical central spacecraft with an axisymmetric axis is obtained by

$$\begin{aligned} \boldsymbol{M}_s &= \rho_s \int_V \boldsymbol{C}^T \boldsymbol{C} dV_s \\ &= m_s \begin{bmatrix} \frac{13}{12}\boldsymbol{I}_3 & -\frac{1}{12}\boldsymbol{I}_3 & \boldsymbol{0}_3 & \boldsymbol{0}_3 \\ -\frac{1}{12}\boldsymbol{I}_3 & \frac{1}{12}\boldsymbol{I}_3 & \boldsymbol{0}_3 & \boldsymbol{0}_3 \\ \boldsymbol{0}_3 & \boldsymbol{0}_3 & \frac{1}{4}\boldsymbol{I}_3 R_s^2 & \boldsymbol{0}_3 \\ \boldsymbol{0}_3 & \boldsymbol{0}_3 & \boldsymbol{0}_3 & \frac{1}{4}\boldsymbol{I}_3 R_s^2 \end{bmatrix} \end{aligned} \tag{3.61}$$

where R_s is the radius of the central spacecraft, $\boldsymbol{0}_3$ is the 3×3 zero matrix. It is noted that the mass matrix is a constant matrix.

3.4.2 Potential Energy of the Central Spacecraft

The gravitational potential energy of the central spacecraft in the $O_s X_s Y_s Z_s$ coordinate system can be written as

$$V_f = -\int \boldsymbol{f} d\boldsymbol{p}_a^T = -\int d\boldsymbol{p}^T \boldsymbol{C}^T \boldsymbol{f} \tag{3.62}$$

where V_f is the central spacecraft potential energy, $\boldsymbol{f}$ is the gravitational force of the infinitesimal volume dm at the point p_a,

$$\boldsymbol{f} = -dm\boldsymbol{g}_{\square} = -\frac{\mu_{\square}}{\left|\boldsymbol{r} + \boldsymbol{r}_a\right|^3}\left(\boldsymbol{r} + \boldsymbol{r}_a\right) dm \tag{3.63}$$

where $\boldsymbol{r}_a$ is the position vector of p_a from the origin O_{cb} , $\boldsymbol{g}_{\square}$ is the gravitational acceleration of the central spacecraft.

The partial derivative of Equation (3.62) with respect to $\boldsymbol{p}$ leads to the equivalent gravitational force $\boldsymbol{f}_{g\_s}$ as

$$\boldsymbol{f}_{g\_s} = \frac{\partial V_f}{\partial \boldsymbol{p}} = -\boldsymbol{C}^T \boldsymbol{f} \tag{3.64}$$

and the total gravitational forces acting on the central spacecraft are calculated by $\boldsymbol{F}_{g\_s} = \int \boldsymbol{f}_{g\_s}$.

Moreover, the gravity gradient torque about the origin O_{cb} is calculated as

$$\tau_g = \int \boldsymbol{r}_a \times \boldsymbol{f} = -\mu_{\square} \int \frac{\boldsymbol{r}_a \times \boldsymbol{r}}{\left|\boldsymbol{r} + \boldsymbol{r}_a\right|^3} dm \tag{3.65}$$

Expanding $|\boldsymbol{r}+\boldsymbol{r}_a|^{-3}$ into Taylor series and neglecting the higher order terms yield the following approximation,

$$|\boldsymbol{r}+\boldsymbol{r}_a|^{-3} \cong \frac{1}{|\boldsymbol{r}|^3}\left(1-3\frac{\boldsymbol{r}\boldsymbol{r}_a}{|\boldsymbol{r}|^2}\right) \tag{3.66}$$

Substituting Equation (3.66) into Equation (3.65) yields

$$\boldsymbol{\tau}_g = 3\frac{\mu_{\square}}{|\boldsymbol{r}|^5}\int \boldsymbol{r}\boldsymbol{r}_a\left(\boldsymbol{r}_a \times \boldsymbol{r}\right)dm \tag{3.67}$$

Since the rotation of the central spacecraft is described by the Cartesian coordinates instead of the angular parameters, the external torque $\boldsymbol{\tau}$ applied to the central spacecraft should be replaced by an equivalent pair of forces accordingly. The generalized forces corresponding to the external torque $\boldsymbol{\tau}$ can be expressed as [101-102]

$$\boldsymbol{F}_\tau = \begin{bmatrix} \mathbf{0}_{3\times1}^T & \mathbf{0}_{3\times1}^T & \boldsymbol{f}_{\mathbf{u}}^T & \boldsymbol{f}_{\mathbf{v}}^T \end{bmatrix}^T \tag{3.68}$$

where $\boldsymbol{f}_{\mathbf{u}}$ and $\boldsymbol{f}_{\mathbf{v}}$ are the forces associate with the NCF unit vectors $\mathbf{u}$ and $\mathbf{v}$, respectively.

In order to obtain this generalized force, the external torque $\boldsymbol{\tau}$ is decomposed into components in the direction aligned and perpendicular to the unit vector $\mathbf{u}$, respectively,

$$\begin{cases} \boldsymbol{\tau}_{\mathbf{u}} = (\boldsymbol{\tau}\cdot\ \mathbf{u})\mathbf{u} \\ \boldsymbol{\tau}_{\mathbf{u}_\perp} = \boldsymbol{\tau} - (\boldsymbol{\tau}\cdot\ \mathbf{u})\mathbf{u} \end{cases} \tag{3.69}$$

where $\tau_{\mathbf{u}}$ and $\tau_{\mathbf{u}_\perp}$ are the torque components aligned and perpendicular to the direction of the unit vector $\mathbf{u}$, respectively.

Thus, the equivalent pair of forces $\boldsymbol{f}_{\mathbf{u}}$ and $\boldsymbol{f}_{\mathbf{v}}$ perpendicular to the directions of unit vectors $\mathbf{u}$ and $\mathbf{v}$, respectively, can be obtained as,

$$\begin{cases} \boldsymbol{f}_{\mathbf{u}} = \tau_{\mathbf{u}_\perp} \times \mathbf{u} \\ \boldsymbol{f}_{\mathbf{v}} = \tau_{\mathbf{u}} \times \mathbf{v} \end{cases} \tag{3.70}$$

Substituting Equation (3.67) into Equations (3.68)-(3.70) yields

$$\boldsymbol{F}_{\tau\_g} = \begin{bmatrix} \mathbf{0}_{3\times1}^T & \mathbf{0}_{3\times1}^T & \boldsymbol{f}_{\mathbf{u}\_g}^T & \boldsymbol{f}_{\mathbf{v}\_g}^T \end{bmatrix}^T \tag{3.71}$$

where $\boldsymbol{F}_{\tau\_g}$ is the generalized force represent the gravity gradient torque.

3.4.3 Angular Velocity and Acceleration of Central Spacecraft

Because the attitude motion of the central spacecraft is described by the NCF in the Cartesian coordinates instead of the Euler angles, the angular velocity and angular acceleration of the central spacecraft cannot be obtained directly. They are obtained by solving the following kinematic equations,

$$\begin{cases} \dot{\boldsymbol{p}}_j - \dot{\boldsymbol{p}}_i + \left(\boldsymbol{p}_j - \boldsymbol{p}_i\right) \times \left(\boldsymbol{\Omega} + \boldsymbol{\omega}_s\right) = 0 \\ \dot{\mathbf{u}} + \mathbf{u} \times \left(\boldsymbol{\Omega} + \boldsymbol{\omega}_s\right) = 0 \\ \dot{\mathbf{v}} + \mathbf{v} \times \left(\boldsymbol{\Omega} + \boldsymbol{\omega}_s\right) = 0 \end{cases} \tag{3.72}$$

$$\begin{cases} \ddot{\boldsymbol{p}}_j - \ddot{\boldsymbol{p}}_i + \left(\dot{\boldsymbol{p}}_j - \dot{\boldsymbol{p}}_i\right) \times \left(\boldsymbol{\Omega} + \boldsymbol{\omega}_s\right) + \left(\boldsymbol{p}_j - \boldsymbol{p}_i\right) \times \left(\dot{\boldsymbol{\Omega}} + \dot{\boldsymbol{\omega}}_s\right) = 0 \\ \ddot{\mathbf{u}} + \dot{\mathbf{u}} \times \left(\boldsymbol{\Omega} + \boldsymbol{\omega}_s\right) + \mathbf{u} \times \left(\dot{\boldsymbol{\Omega}} + \dot{\boldsymbol{\omega}}_s\right) = 0 \\ \ddot{\mathbf{v}} + \dot{\mathbf{v}} \times \left(\boldsymbol{\Omega} + \boldsymbol{\omega}_s\right) + \mathbf{v} \times \left(\dot{\boldsymbol{\Omega}} + \dot{\boldsymbol{\omega}}_s\right) = 0 \end{cases} \tag{3.73}$$

where $\boldsymbol{\omega}_s$ and $\dot{\boldsymbol{\omega}}_s$ are the angular velocity and acceleration of the central spacecraft in the $O_sX_sY_sZ_s$ coordinate system, respectively.

Thus, the angular velocity and acceleration in the $O_{cb}X_{cb}Y_{cb}Z_{cb}$ coordinate system are expressed as

$$\begin{cases} \boldsymbol{\omega}_{cb} = \boldsymbol{T}_{cb2s}^T \boldsymbol{\omega}_s \\ \dot{\boldsymbol{\omega}}_{cb} = \boldsymbol{T}_{cb2s}^T \dot{\boldsymbol{\omega}}_s \end{cases} \tag{3.74}$$

3.4.4 Constraint Equations of the Central spacecraft

As shown in Equation (3.47), the six degrees of freedom of the central spacecraft are described by the 12 generalized coordinates, which means the 12 generalized coordinates of the central spacecraft are not independent. Therefore, six constraint equations are introduced to eliminate the extra redundant degrees of freedom, that is,

$$\boldsymbol{\Phi}_s = \begin{cases} \left|\boldsymbol{p}_j - \boldsymbol{p}_i\right| - H^2/4 = 0 \\ \left|\mathbf{u}\right| - 1 = 0 \\ \left|\mathbf{v}\right| - 1 = 0 \\ \left(\boldsymbol{p}_j - \boldsymbol{p}_i\right)^T \mathbf{u} = 0 \\ \left(\boldsymbol{p}_j - \boldsymbol{p}_i\right)^T \mathbf{v} = 0 \\ \mathbf{u}^T \mathbf{v} = 0 \end{cases} \tag{3.75}$$

where the first three equations represent the equidistant constraint of the central spacecraft, and the last three equations express the vertical constraint.

3.4.5 Equations of motion of the E-sail

The equations of motion of the generalized E-sail can be derived by utilizing the Lagrange equation of the first kind as following:

$$\begin{cases} \dfrac{d}{dt}\left(\dfrac{\partial L}{\partial \dot{\boldsymbol{q}}}\right) - \dfrac{\partial L}{\partial \boldsymbol{q}} + \boldsymbol{\Phi}_{\boldsymbol{q}}^{T}\boldsymbol{\lambda} = \boldsymbol{Q} \\ \boldsymbol{\Phi} = 0 \end{cases} \tag{3.76}$$

where $L = T - (U + V)$ is the Lagrangian of the E-sail, $\boldsymbol{q} = \begin{bmatrix} \boldsymbol{p}^T & \boldsymbol{q}_e^T \end{bmatrix}^T$ is the position vector of the E-sail, $\boldsymbol{\lambda}$ is the vector of the Lagrange multipliers, $\boldsymbol{Q}$ is the generalized force, $\boldsymbol{\Phi}$ and $\boldsymbol{\Phi}_q = \partial\boldsymbol{\Phi}/\partial\boldsymbol{q}$ are the constraint equation and the corresponding Jacobian matrix, respectively. The detailed expression of the kinetic, strain and potential energy of the E-sail T, U and V are written as

$$\begin{cases} T = T_s + \sum_{k=1}^{N} T_{e,k} + \sum_{i=1}^{M} T_i \\ U = \sum_{k=1}^{N} U_{e,k} \\ V = V_f + \sum_{k=1}^{N} V_{e,k} + \sum_{i=1}^{M} V_i \end{cases} \tag{3.77}$$

where N is the total number of the elements, M is the total number of the remote units. $T_{e,k}$, T_i, $U_{e,k}$, $V_{e,k}$, and V_i are the kinetic, strain and potential energy of the k_{th} tether element and i^{th} remote unit, which can be obtained in the previous section, respectively.

Accordingly, the equations of motion of the E-sail can be obtained as

$$\begin{cases} \boldsymbol{M}\ddot{\boldsymbol{q}} + \Phi_q^T \lambda = \boldsymbol{F} \\ \Phi = 0 \end{cases} \tag{3.78}$$

where $\boldsymbol{M}$, $\ddot{\boldsymbol{q}}$ and $\boldsymbol{F}$ are the mass matrix, acceleration vector and external force vector of the E-sail, respectively. The detailed expressions of the matrix and vectors are expressed by

$$\boldsymbol{M} = \begin{bmatrix} \boldsymbol{M}_s & \boldsymbol{0} \\ \boldsymbol{0} & \boldsymbol{M}_e \end{bmatrix}, \quad \Phi = \begin{bmatrix} \Phi_s \\ \Phi_{s\_t} \end{bmatrix}, \quad \boldsymbol{F} = \begin{bmatrix} \boldsymbol{F}_{g\_s} + \boldsymbol{F}_{\tau\_g} \\ \boldsymbol{F}_e + \boldsymbol{F}_t + \boldsymbol{F}_g - \boldsymbol{K}_e \boldsymbol{q}_e \end{bmatrix} \tag{3.79}$$

where $\boldsymbol{M}_s$ is the mass matrix of the central spacecraft in Equation (3.61), Φ_{s_t} is the constraint equation of spherical joints on the central spacecraft, which joins the central spacecraft with the elastic tethers. The constraint equations of spherical joints can be written as

$$\Phi_{s\_t} = \begin{cases} \Phi_{x\_i} = p_{e\_x\_i} - q_{e\_x\_i} = 0 \\ \Phi_{y\_i} = p_{e\_y\_i} - q_{e\_y\_i} = 0 \quad i = 1,2...m \\ \Phi_{z\_i} = p_{e\_z\_i} - q_{e\_z\_i} = 0 \end{cases} \tag{3.80}$$

where m is the number of the joints, $\boldsymbol{p}_{e\_i} = \begin{bmatrix} p_{e\_x\_i} & p_{e\_y\_i} & p_{e\_z\_i} \end{bmatrix}^T$ and $\boldsymbol{q}_{e\_i} = \begin{bmatrix} q_{e\_i\_x} & q_{e\_i\_y} & q_{e\_i\_z} \end{bmatrix}^T$ are the position of the interconnected points on the central spacecraft to connect the tethers.

It should be noted that Equation (3.78) is highly nonlinear due to including the rigid-flexible coupling influence by the Lagrange multiplier approach. Thus, it must be solved iteratively by the Runge-Kutta type method for differential-algebraic equations. The control influence is transmitted from the central spacecraft to the main tethers via the rigid-flexible coupling constraint and the coupling is reflected in the tension fluctuation in the main tethers.

3.4.6 Disturbance Torques

As shown in Figure 3-4, a disturbance torque of the resultant propulsive force will be generated by the E-sail if the CM of the E-sail is not coincided with its CT (center of thrust). Moreover, a disturbance torque of tether tension will be generated on the central spacecraft if the main tethers swing relative to the radial direction as illustrated in Figure 3-2(c). It must be recognized that the CM and CT of the E-sail and tether tension can be influenced by the nonlinear elastic deformations of the tethers as well as the large deflection/bending of the main tethers. In addition, the fluctuation of tensions in the main tethers leads to fluctuation of disturbance torque, which in turn influences the attitude dynamics of the central spacecraft via the rigid-flexible coupling constraints.

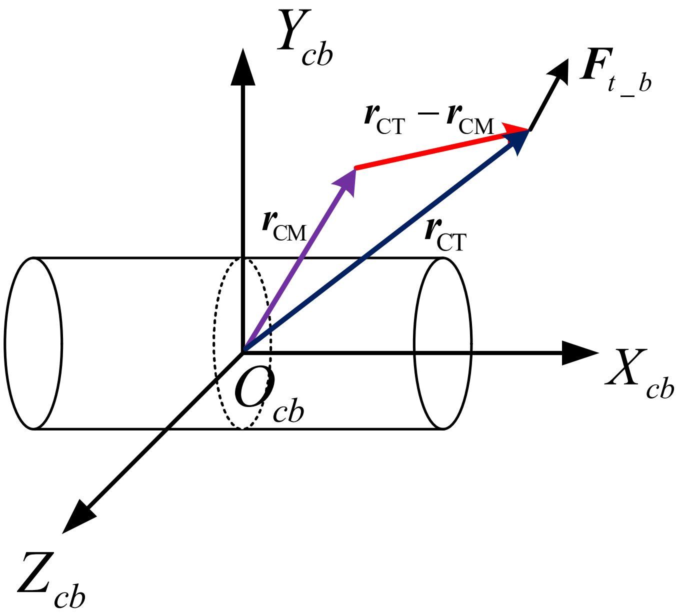

Figure 3-4 Schematic of the disturbance torque.

These torques will result in the fluctuation of spin rates of the E-sail and the central spacecraft. The following illustrates how to include these influences into the model.

The position vectors of CM and CT of the E-sail are defined in the $O_{cb}X_{cb}Y_{cb}Z_{cb}$ coordinate system, which can be written as

$$\begin{cases} \boldsymbol{r}_{\text{CM}} = \left(\sum_{i=1}^{nn} m_i \boldsymbol{X}_i \right) \Big/ \left(\sum_{i=1}^{nn} m_i \right) \\ \boldsymbol{r}_{\text{CT}} = \left(\tilde{\boldsymbol{F}}_{t\_cb}^{T} \right)^{-1} \left(\sum_{i=1}^{nn} \boldsymbol{X}_i \times \boldsymbol{f}_i \right) \end{cases} \quad i = 1, 2 \ldots nn \tag{3.81}$$

where nn is the number of the nodes, $\boldsymbol{X}_i$ is the position vector from the i_{th} node to the origin O_{cb} of the $O_{cb}X_{cb}Y_{cb}Z_{cb}$ coordinate, m_i , $\boldsymbol{f}_i$, $\boldsymbol{r}_{\text{CM}} = \begin{bmatrix} r_{\text{CM}_x} & r_{\text{CM}_y} & r_{\text{CM}_z} \end{bmatrix}^T$ and $\boldsymbol{r}_{\text{CT}} = \begin{bmatrix} r_{\text{CT}_x} & r_{\text{CT}_y} & r_{\text{CT}_z} \end{bmatrix}^T$ are the mass components, propulsive force components, and position vectors of the CM and CT of the E-sail, respectively. Then, the skew-symmetric cross-product matrix associated the propulsive force $\boldsymbol{F}_{t\_cb} = \begin{bmatrix} F_{cb_x} & F_{cb_y} & F_{cb_z} \end{bmatrix}^T$ in the $O_{cb}X_{cb}Y_{cb}Z_{cb}$ coordinate system is defined by

$$\tilde{\boldsymbol{F}}_{t\_cb} = \begin{bmatrix} 0 & -F_{cb_z} & F_{cb_y} \\ F_{cb_z} & 0 & -F_{cb_x} \\ -F_{cb_y} & F_{cb_x} & 0 \end{bmatrix} \tag{3.82}$$

Therefore, the disturbance torque of the resultant propulsive force $\boldsymbol{F}_{t\_cb}$ caused by the offset between the CM and CT of E-sail as presented in Figure 3-4 is obtained as

$$\boldsymbol{\tau}_{t\_t} = \left(\boldsymbol{r}_{\mathrm{CT}} - \boldsymbol{r}_{\mathrm{CM}}\right) \times \boldsymbol{F}_{t\_cb} \tag{3.83}$$

It will be transmitted to the central spacecraft via the rigid-flexible coupling, which is the tensions in the main tethers. The disturbance torque on the central spacecraft due to the tension of each main tether as shown in Figure 3-2(d), which can be written as

$$\boldsymbol{\tau}_T = \boldsymbol{r}_i \times \boldsymbol{T}_i \tag{3.84}$$

where $\boldsymbol{r}_i$ is the position vector from the origin O_{cb} to the i_{th} interconnected point and $\boldsymbol{T}_i$ is the tension of the i_{th} tether.

3.5 Reduced Order Model of Attitude Equations of E-sail

In the previous section, the elastic deformation of the tethers, the orbital and attitude motions of the E-sail are described by the NPFEM, while the attitude equations of motion of the E-sail are implicit and must be calculated from the states of nodal positions by Equations (3.1)-(3.10), which makes it difficult to design a feedback law for the attitude control. Although the high-fidelity dynamic model accurately describes the dynamic characteristics of the E-sail, it also brings inconvenience to the attitude stability control of the E-sail. To solve the problem, a reduced order analytical E-sail model is established to capture the attitude dynamics of the E-sail in order to design the attitude controller in current work. It should be noted that all the following equations and the relative terms are obtained in the $O_{sp}X_{sp}Y_{sp}Z_{sp}$ coordinate system.

To simplify the problem of dynamics and control, it is assumed that

(i) The central spacecraft is orbiting on the heliocentric ecliptic plane, which is $\phi = \pi/2$,

(ii) The spin rate of the E-sail and the orbital angular velocity are constant, and

(iii) All tethers are straight and belong to the same plane without consideration of coning motion.

Based on the above assumptions, the angular momentum of the E-sail can be written as

$$\boldsymbol{H} = \boldsymbol{I}\boldsymbol{\omega} \tag{3.85}$$

where $\boldsymbol{H}$ is the angular momentum of the E-sail, $\boldsymbol{I}$ is the moment of inertia tensor of the E-sail, and $\boldsymbol{\omega} = \begin{bmatrix} \omega_x & \omega_y & \omega_z \end{bmatrix}^T$ is the angular velocity of the E-sail about the principal axes. The detailed derivation of these terms are presented in the following.

3.5.1 Moment of Inertia of Reduced Order Model of E-sail

Because the E-sail is symmetric with respect to the $Z_{sp}\left(Z_b\right)$ axis, the principal axes of inertia are the same with the axes of the $O_{sp}X_{sp}Y_{sp}Z_{sp}$ coordinate system. Therefore, the moment of inertia tensor of the E-sail $\boldsymbol{I}$ in the $O_{sp}X_{sp}Y_{sp}Z_{sp}$ coordinate system can be expressed by

$$\boldsymbol{I} = \begin{bmatrix} I_x & 0 & 0 \\ 0 & I_y & 0 \\ 0 & 0 & I_z \end{bmatrix} \tag{3.86}$$

where I_x, I_y and I_z are the moments of inertia along the principal axes of inertia, that is,

$$\begin{aligned} I_x &= I_{x\_mt} + I_{x\_at} + I_{x\_ru} \\ I_y &= I_{y\_mt} + I_{y\_at} + I_{y\_ru} \\ I_z &= I_{z\_mt} + I_{z\_at} + I_{z\_ru} \end{aligned} \tag{3.87}$$

where $\left(I_{x\_mt} \quad I_{y\_mt} \quad I_{z\_mt}\right)$, $\left(I_{x\_at} \quad I_{y\_at} \quad I_{z\_at}\right)$ and $\left(I_{x\_ru} \quad I_{y\_ru} \quad I_{z\_ru}\right)$ are the moments of inertia of the main tethers, auxiliary tethers, and the remote units along the three axes, respectively.

The moments of inertia of the main tethers can be written as

$$\begin{aligned} I_{x\_mt} &= \sum_{i=1}^{N}\int \left(\left(y_i^{sp}\right)^2 + \left(z_i^{sp}\right)^2 \right) dm \\ I_{y\_mt} &= \sum_{i=1}^{N}\int \left(\left(x_i^{sp}\right)^2 + \left(z_i^{sp}\right)^2 \right) dm \\ I_{z\_mt} &= \sum_{i=1}^{N}\int \left(\left(x_i^{sp}\right)^2 + \left(y_i^{sp}\right)^2 \right) dm \end{aligned} \tag{3.88}$$

where $\boldsymbol{l}_i^{sp} = \begin{bmatrix} x_i^{sp} & y_i^{sp} & z_i^{sp} \end{bmatrix}^T$ is the position vector of the infinitesimal mass point dm along the i^{th} main tether, $i = 1, \cdots N$, N is the total number of the main tethers(remote units), $dm = \rho dl$, ρ is the linear mass density, dl is the infinitesimal tether length.

The position vector of dm in the $O_b X_b Y_b Z_b$ coordinate system can be written as

$$\boldsymbol{l}_i^{b} = \begin{bmatrix} l\cos\left(2\pi(i-1)/N\right) & l\sin\left(2\pi(i-1)/N\right) & 0 \end{bmatrix}^T \tag{3.89}$$

where $l \in \begin{bmatrix} 0 & L \end{bmatrix}$ is the distance from the CM of the central spacecraft to the mass point dm, L is the length of the main tethers.

Thus, the position of the mass point dm in the $O_{sp} X_{sp} Y_{sp} Z_{sp}$ coordinate system can be written as

$$\boldsymbol{l}_i^{sp} = \left(\boldsymbol{T}_{sp2b}\right)^T \boldsymbol{l}_i^{b} = \begin{bmatrix} l\cos\left(2\pi(i-1)/N + \omega_0 t\right) & l\sin\left(2\pi(i-1)/N + \omega_0 t\right) & 0 \end{bmatrix}^T \tag{3.90}$$

Substituting Equation (3.90) into Equation (3.88) yields the moment of inertia of the main tethers as

$$
\begin{aligned}
I_{x\_mt} &= \sum_{i=1}^{N}\int_0^L \rho l^2 \sin^2\left(2\pi(i-1)/N+\omega_0 t\right)dl = \frac{1}{6}N\rho L^3 \\
I_{y\_mt} &= \sum_{i=1}^{N}\int_0^L \rho l^2 \cos^2\left(2\pi(i-1)/N+\omega_0 t\right)dl = \frac{1}{6}N\rho L^3 \\
I_{z\_mt} &= \sum_{i=1}^{N}\int_0^L \rho l^2 dl = \frac{1}{3}N\rho L^3
\end{aligned}
\tag{3.91}
$$

where

$$
\begin{aligned}
\sum_{i=1}^{N}\sin^2\left(2\pi(i-1)/N+\omega_0 t\right) &= \sum_{i=1}^{N}\frac{1-\cos\left(2\left(2\pi(i-1)/N+\omega_0 t\right)\right)}{2} = \frac{N}{2} \\
\sum_{i=1}^{N}\cos^2\left(2\pi(i-1)/N+\omega_0 t\right) &= \sum_{i=1}^{N}\frac{1+\cos\left(2\left(2\pi(i-1)/N+\omega_0 t\right)\right)}{2} = \frac{N}{2}
\end{aligned}
\tag{3.92}
$$

Similarly, the moment of inertia of the auxiliary tethers and the remote units are given by

$$
\begin{aligned}
I_{x\_at} + I_{x\_ru} &= \frac{1}{2}N\left(m_{re}+m_{au}\right)L^2 \\
I_{y\_at} + I_{y\_ru} &= \frac{1}{2}N\left(m_{re}+m_{au}\right)L^2 \\
I_{z\_at} + I_{z\_ru} &= N\left(m_{re}+m_{au}\right)L^2
\end{aligned}
\tag{3.93}
$$

where m_{re} and m_{au} are the masses of the i^{th} remote unit and the connected auxiliary tethers, respectively.

Substituting Equations (3.91) and (3.93) into Equation (3.87) yields

$$
\begin{aligned}
I_x &= \frac{1}{2}\left(\frac{1}{3}\rho L + m_{re} + m_{au}\right)NL^2 \\
I_y &= \frac{1}{2}\left(\frac{1}{3}\rho L + m_{re} + m_{au}\right)NL^2 \\
I_z &= \left(\frac{1}{3}\rho L + m_{re} + m_{au}\right)NL^2
\end{aligned}
\tag{3.94}
$$

Obviously, there exist $I_z = 2I_x = 2I_y$. For the sake of convenience, let $I_x = I_y = J$ and $I_z = 2J$.

3.5.2 Derivation of Kinematic Differential Equations of E-sail

The angular velocity of the E-sail $\boldsymbol{\omega}$ in the $O_{sp}X_{sp}Y_{sp}Z_{sp}$ coordinate system can be written as

$$\boldsymbol{\omega} = \boldsymbol{\omega}_{o2i}^{sp} + \boldsymbol{\omega}_{sp2o}^{sp} + \boldsymbol{\omega}_{b2sp}^{sp} \tag{3.95}$$

where $\boldsymbol{\omega}_{o2i}^{sp}$ is the angular velocity of the $O_oX_oY_oZ_o$ with respect to the $O_sX_sY_sZ_s$ coordinate systems, $\boldsymbol{\omega}_{sp2o}^{sp}$ is the angular velocity of the $O_{sp}X_{sp}Y_{sp}Z_{sp}$ with respect to the $O_oX_oY_oZ_o$ coordinate systems, and $\boldsymbol{\omega}_{b2sp}^{sp}$ is the angular velocity of the $O_bX_bY_bZ_b$ with respect to the $O_{sp}X_{sp}Y_{sp}Z_{sp}$ coordinate systems, respectively.

The detailed expressions of the terms in Equation (3.95) are given by

$$\boldsymbol{\omega}_{o2i}^{sp} = \boldsymbol{T}_{o2sp}\boldsymbol{\omega}_{o2i} = \begin{bmatrix} -\Omega\cos\eta\cos\Theta \\ \Omega\cos\eta\sin\Theta \\ -\Omega\sin\eta \end{bmatrix} \tag{3.96}$$

$$\begin{aligned}\boldsymbol{\omega}_{sp2o}^{sp} = & \begin{bmatrix} 0 \\ 0 \\ \dot{\Theta} \end{bmatrix} + \begin{bmatrix} \cos\Theta & \sin\Theta & 0 \\ -\sin\Theta & \cos\Theta & 0 \\ 0 & 0 & 1 \end{bmatrix} \begin{bmatrix} 0 \\ \dot{\eta} \\ 0 \end{bmatrix} + \\ & \begin{bmatrix} \cos\Theta & \sin\Theta & 0 \\ -\sin\Theta & \cos\Theta & 0 \\ 0 & 0 & 1 \end{bmatrix} \begin{bmatrix} \cos\eta & 0 & -\sin\eta \\ 0 & 1 & 0 \\ \sin\eta & 0 & \cos\eta \end{bmatrix} \begin{bmatrix} \dot{\zeta} \\ 0 \\ 0 \end{bmatrix} \\ = & \begin{bmatrix} \cos\eta\cos\Theta & \sin\Theta & 0 \\ -\cos\eta\sin\Theta & \cos\Theta & 0 \\ \sin\eta & 0 & 1 \end{bmatrix} \begin{bmatrix} \dot{\zeta} \\ \dot{\eta} \\ \dot{\Theta} \end{bmatrix}\end{aligned} \tag{3.97}$$

$$\boldsymbol{\omega}_{b2sp}^{sp} = \left(\boldsymbol{T}_{sp2b}\right)^{T} \boldsymbol{\omega}_{b2sp} = \begin{bmatrix} 0 \\ 0 \\ \omega_0 \end{bmatrix} \tag{3.98}$$

Substituting Equations (3.96)-(3.98) into Equation (3.95) yields

$$\boldsymbol{\omega} = \begin{bmatrix} \omega_x \\ \omega_y \\ \omega_z \end{bmatrix} = \begin{bmatrix} -\Omega\cos\eta\cos\Theta + \cos\eta\cos\Theta\dot{\zeta} + \sin\Theta\dot{\eta} \\ \Omega\cos\eta\sin\Theta - \cos\eta\sin\Theta\dot{\zeta} + \cos\Theta\dot{\eta} \\ -\Omega\sin\eta + \sin\eta\dot{\zeta} + \dot{\Theta} + \omega_0 \end{bmatrix} \tag{3.99}$$

3.5.3 Attitude Dynamical Equations of E-sail

Taking the first derivative of Equation (3.85) with respect to time t yields the Euler's attitude dynamical equations of the E-sail as

$$\begin{aligned} &\dot{\omega}_x + \omega_y\omega_z = \tau_x / J \\ &\dot{\omega}_y - \omega_x\omega_z = \tau_y / J \\ &\dot{\omega}_z = \tau_z / (2J) \end{aligned} \tag{3.100}$$

where τ_x, τ_y and τ_z are the three-axis external torques.

Moreover, substituting Equations (3.94) and (3.99) into Equation (3.85) yields the kinematic differential equations of the E-sail as

$$\begin{aligned}
\dot{\zeta} &= \Omega + \frac{1}{\cos\eta}\left(\omega_x \cos\Theta - \omega_y \sin\Theta\right) \\
\dot{\eta} &= \omega_x \sin\Theta + \omega_y \cos\Theta \\
\dot{\Theta} &= \omega_z - \omega_0 + \tan\eta(\omega_y \sin\Theta - \omega_x \cos\Theta)
\end{aligned} \tag{3.101}$$

It should be noted that the singularity condition of the Euler angle η will never happen because the maximum sail angle is assumed to be approximately 70° in order to ensure the mechanical stability of the E-sail [3].

Chapter 4 RESEARCH ON MODEL VALIDATION AND DYNAMIC CHARACTERISTICS OF THE E-SAIL

Summary: In this chapter, the model validation and dynamic characteristics of the E-sail are investigated. Frist, a proper trade-off between the accuracy and the computational efficiency is conducted before the numerical investigation, and the appropriate tether element is given. The aim of the second section is to verify the two E-sail models without considering the influence of the propulsive force. Third, the unknown mechanism behind the periodic coning motion of the E-sail is revealed and the analytic solution of its frequency is derived under the assumption of small coning angle and verified by the numerical simulation. Finally, an analytic expression of the upper and lower spin rate bounds is derived to guarantee the normal operation of the E-sail, which can be utilized to select the initial spin rate of the E-sail and evaluate whether the spin rate requires to be controlled.

4.1 Convergence of Tether Element Mesh

In this dissertation, the main objective is to find the dynamic behaviors of the E-sail. As shown in Chapter 3, the E-sail model is developed by considering high-order modes of the flexible elastic tethers. The tethers of E-sail are assumed elastic and discretized into inter-connected 2-noded tensile elements using the nodal position finite element method. Because the accuracy of the finite element E-sail model depends on the total number of tether elements used in the model. The more elements, the higher the accuracy of solution, and the higher the computational loads. Therefore, in order to minimize the modeling error in the analysis with reasonable computational loads, an appropriate trade-off between the accuracy and the computational efficiency is conducted before the numerical investigation. Let the main and auxiliary tethers be discretized into 1 to 6 and 1 to 4 elements, respectively. The convergence of the numerical solution is measured by an index η_i, that is,

$$\eta_i = \frac{\varepsilon_{i,k}}{\varepsilon_{1,k}} \tag{4.1}$$

where $\varepsilon_{i,k}$ is the strain of the k_{th} tether in the i_{th} element where the tether is discretized into i elements, and $\varepsilon_{1,k}$ is in the 1_{st} element where the tether is modeled with only one element, respectively. Accordingly, the η_i describes the longitudinal deformation of the tethers. If the ratio maintains the constant, the accuracy of the tether' elastic deformation motion will be guaranteed.

Figure 4-1 shows the convergence results. It can be seen that the solution starts to converge after the main and auxiliary tethers are discretized into two elements. As the number of the elements per tether increases beyond two elements, the solutions are converged in both cases of the main and auxiliary tethers. The ratio becomes almost constant after each main tether is discretized into five elements and each auxiliary tether is discretized into three elements. For the coning motion that represents out-of-plane deflection of the main tether, five elements in main tether and three elements in the auxiliary tether can describe up to the second mode and the first mode, respectively. These modes are sufficient to describe the coning motion because they are the main deflection modes of the E-sail's tethers. Furthermore, one element per tether is sufficient to describe the tension mode. Therefore, the main and auxiliary tethers are discretized into five and three elements, respectively, in the following analyses.

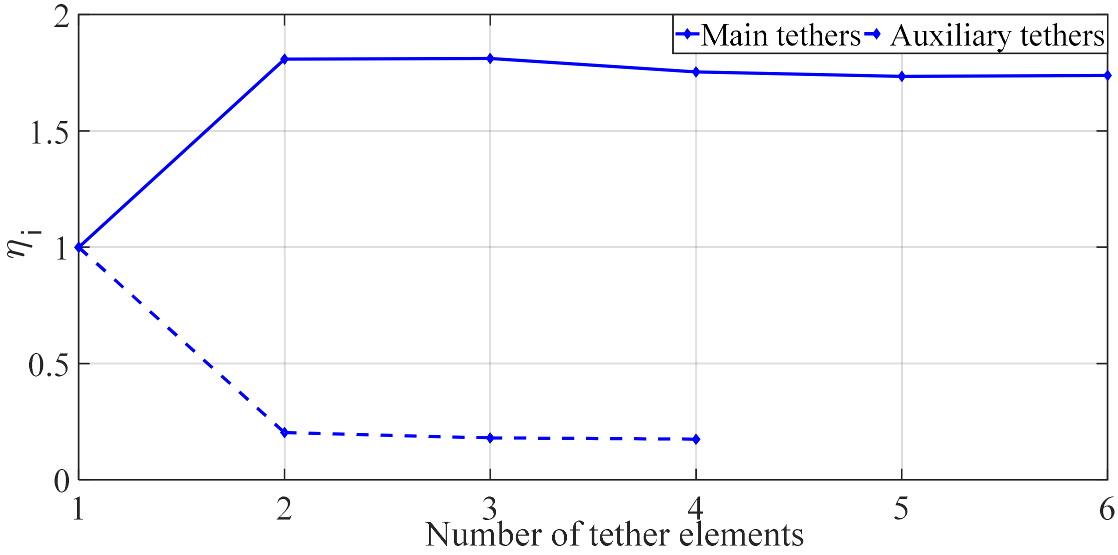

Figure 4-1 Convergence of the E-sail with different numbers of the tether elements.

4.2 Dynamic Performance of the E-sail without Propulsive Force

The aim of this section is to verify the validity of the two high-fidelity dynamic E-sail models by considering the influence of only gravitational force and the accuracy of the integration method. Because the E-sail models in the current work are new type of models, which are not able to compare with the results in the literature. Thus, the stability of E-sail under the orbital motion is used to evaluate the validity of the models. Here, the propulsive force is not introduced, which means the main tethers are not charged and $\boldsymbol{F}_t = 0$ in Equation (3.46). The E-sail is assumed initially in the heliocentric ecliptic plane with its spin plane perpendicular to the ecliptic plane at a distance of 1 au from the Sun. It is further assumed that the E-sail consists of 12 main tethers with 12 connected auxiliary tethers, as shown in Figure 4-2. The configuration of the E-sail is initially maintained by spinning the central spacecraft and the remote units with a spin rate ω_0. The initial orbital angular velocity $\boldsymbol{\Omega}_0$ of the E-sail is assumed to be $\begin{bmatrix} 0 & 0 & \sqrt{\mu_{\odot}/r^3} \end{bmatrix}^T$ and initial sail angle is set as zero.

Furthermore, the stability of E-sail, analyzed by the numerical simulation of the dynamic models derived in Chapter 3 is assessed by evaluating the evolution of the geometrical features of E-sail configuration. Two evaluation criteria are defined in particular:

a) Adjacent angle $\theta_{i,j}$, which is a parameter to measure if the main tethers collide with each other. If the adjacent angle keeps the constant, the E-sail configuration is stable and vice versa.

b) The coplanarity of the remote units, which is a necessary condition to evaluate the stability of E-sail configuration. If the remote units remain on the same plane, the E-sail configuration stability is preserved. The coplanarity is evaluated by randomly selecting remote units to form a plane and calculating the distances d_i from the i^{th} remote unit to this plane. As a reference, four remote units (1st, 4th, 7th, and 10th) are selected to form the plane.

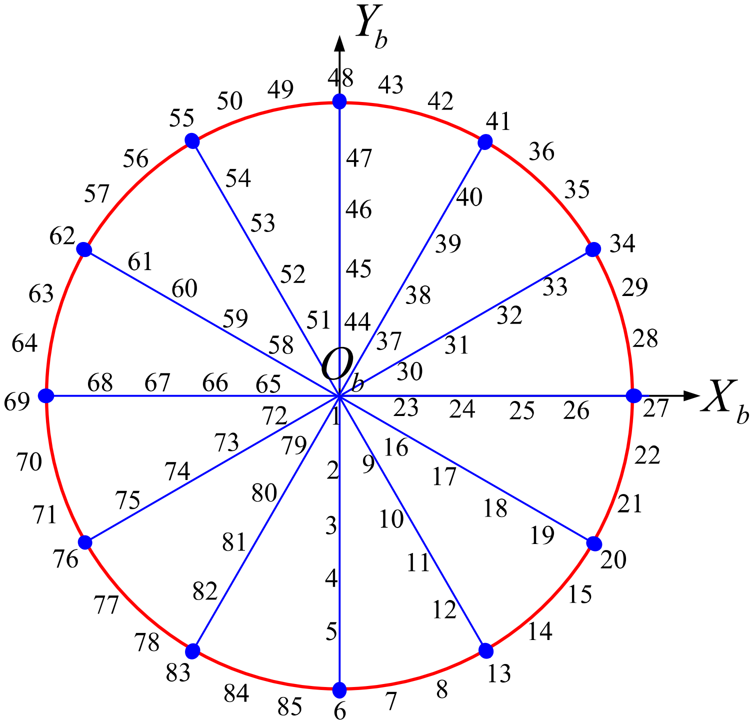

Figure 4-2 E-Sail initial configuration on $O_bX_bY_b$ plane.

4.2.1 NPFEM E-sail Model

The aim of this section is to verify the high-fidelity E-sail model developed in section 3.3 by analyzing the numerical simulation results. The central spacecraft and the remote units are modeled as lumped masses, because of the extremely large ratio of the tether length over the dimensions of the central spacecraft and the remote units. The initial position vector of the i^{th} remote unit $\boldsymbol{p}_{re\_i}^{b}$ in the $O_bX_bY_bZ_b$ coordinate system can be written as

$$\boldsymbol{p}_{re\_i}^{b}=\left[\begin{array}{ccc} L\cos\left(2\pi\left(i-1\right)/12\right) & L\sin\left(2\pi\left(i-1\right)/12\right) & 0 \end{array}\right]^{T} \quad i=1,\ldots 12 \tag{4.2}$$

The parameters of the E-sail are presented in Table 4-1, where the material properties of the tethers are from the Refs. [12, 103]. The equations of motion of the E-sail are solved by the Runge-Kutta type method, and the total simulation period is 24 hours with a time step size of 0.01s, where the simulation time is not the physical time. The resulting dynamic responses of the E-sail are shown in Figure 4-3 to Figure 4-6.

Table 4-1 Parameters of the E-sail system.

Parameters	Values
Mass of the central spacecraft (*kg*)	1,000
Mass of the remote unit (*kg*)	1.5
Initial spin rate ω_0 (*rad/s*)	0.004
Young's modulus of the main tether (*GPa*)	70
Young's modulus of the auxiliary tether (*GPa*)	2.5
Linear density of the main tether (*kgm*$^{-1}$)	1.155×10^{-5}

Linear density of the auxiliary tether (kgm^{-1})	2.705×10^{-4}
Radius of the main tether (m)	3.690×10^{-5}
Radius of the auxiliary tether (m)	2.462×10^{-5}
Length of the main tether (km)	10
Length of the auxiliary tether (km)	5.176
Initial orbital radius (au)	1.0

Figure 4-3(a) shows the Sun-E-sail distance is constant in the duration of simulation as expected due to the zero propulsive force. Thus, the accuracy of the integration method and the E-sail model are validated. However, Figure 4-3(b) illustrates that the sail angle increases by one degree in the negative direction, which is consistent with results of the tethered satellite formations in Refs. [10-11]. This can be explained by the coupling between the in-plane and out-of-orbital-plane dynamics of the E-sail, which makes the orientation between the spin plane and the Sun-spacecraft direction not constant. Thus, the orientation control strategy should be considered to maintain the constant sail angle. The E-sail in the current dissertation consists of 12 main tethers. Accordingly, there are 12 adjacent angles, and each adjacent angle is 30°. If all the adjacent angles are kept at 30°, the E-sail configuration is stable. As shown in Figure 4-4 and Figure 4-5, it indicates that all the twelve remote units remain on the same spin plane with the same constant 30° adjacent angle. It illustrates that the E-sail is in a steady state as expected. Moreover, the lengths, tensions of the main and auxiliary tethers, and the spin rate of E-sail are constant during the simulation duration, as presented in Figure 4-6. Therefore, it also verifies the steady state of E-sail. In summary, the validity of the E-sail model by considering the central spacecraft as a lumped mass and the accuracy of the integration method are validated. The results in this section are used as a benchmark for the rest of study of the NPFEM E-sail model, where the main tethers are positively charged, and the propulsive force is considered.

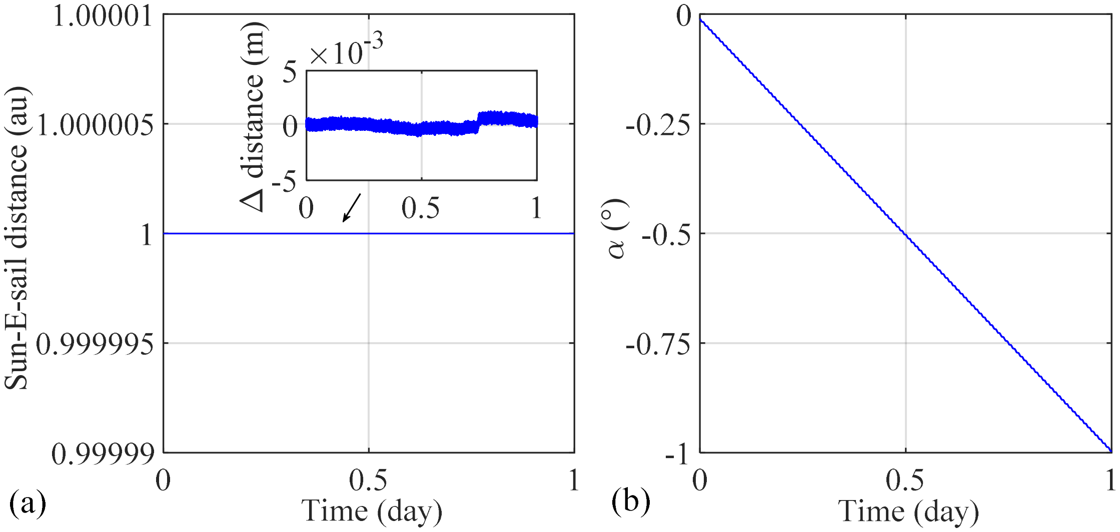

Figure 4-3 Time histories of (a) the Sun/E-sail distance and (b) the sail angle with zero propulsive force.

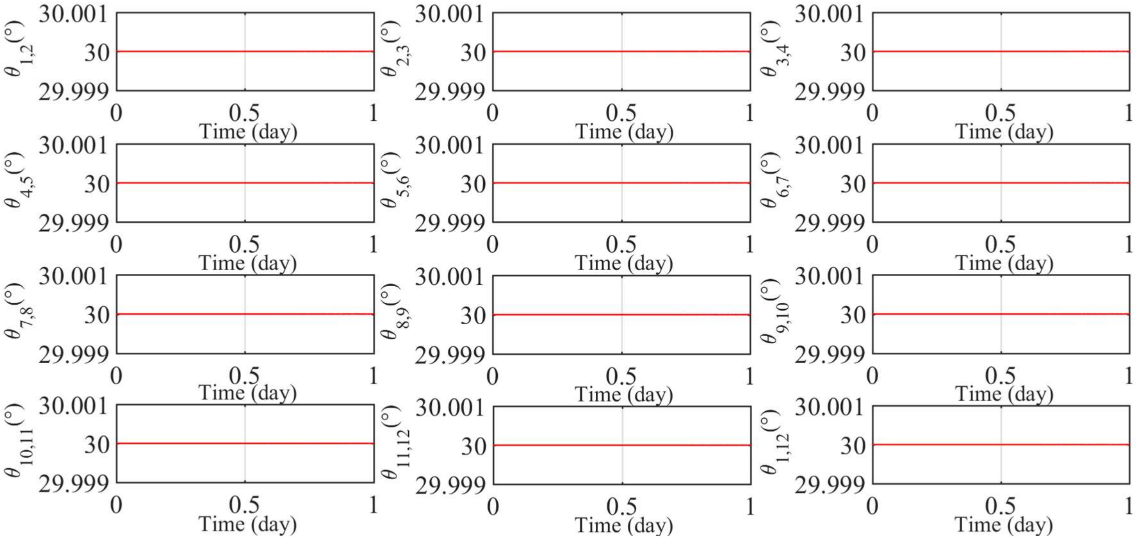

Figure 4-4 Time histories of the adjacent angles with zero propulsive force.

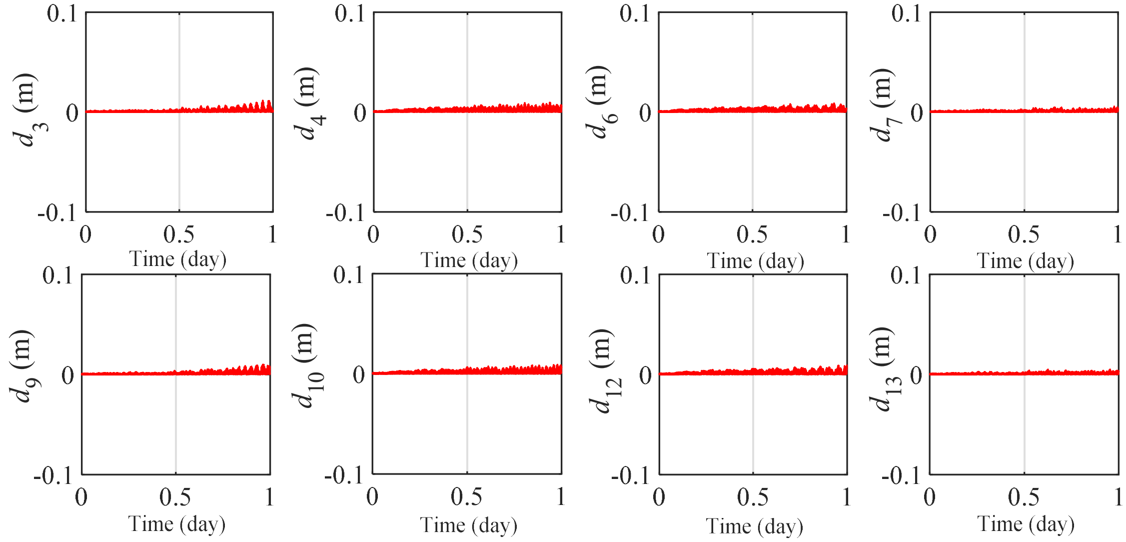

Figure 4-5 Time histories of distances of remote unit to the reference plane with zero propulsive force.

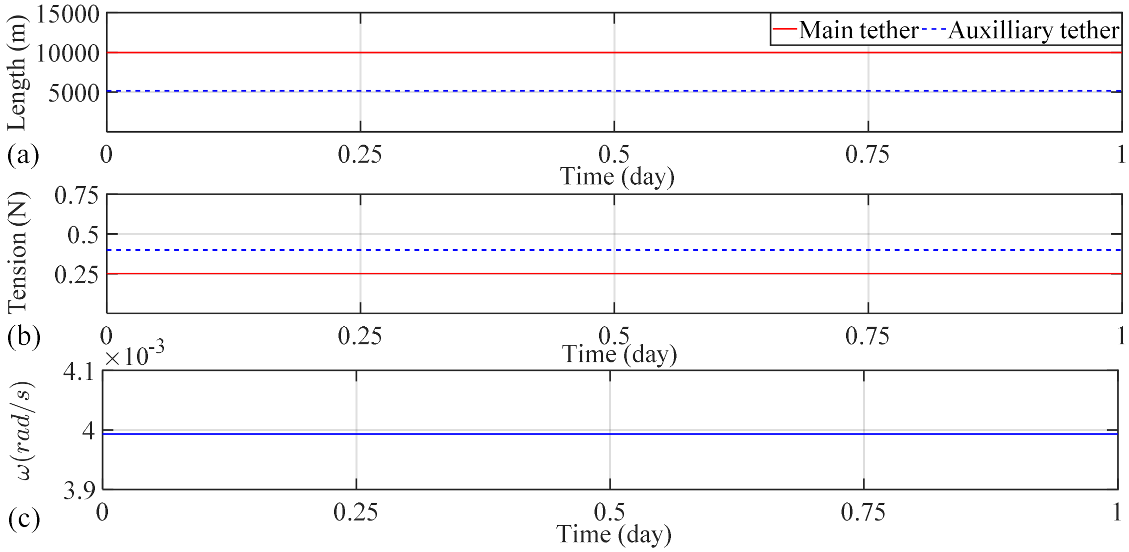

Figure 4-6 Time histories of (a) the length of 1st main and auxiliary tethers (b) tensions in the main and auxiliary tethers and (c) spin rate of the E-sail with zero propulsive force.

4.2.2 Generalized E-sail Model

The aim of this section is to verify the validity of the generalized E-sail model developed in Section 3.4 by examining the dynamic response of the E-sail with zero propulsive force (no positively charge applied to the main tethers), zero initial sail angle and Type II configuration. Therefore, it is expected that the E-sail will be in a steady condition and its spin plane will be perpendicular to its spin axis with zero coning angle. Also, the CM and CT of the E-sail are expected to be the same and coincide with the CM of the central spacecraft. Thus, the resulting disturbance torques on the E-sail is zero as indicated in Equation (3.83).

In the simulation, the E-sail is assumed initially in the heliocentric ecliptic plane with its spin plane perpendicular to the ecliptic plane at a distance of 1 au from the Sun. The E-sail also consists of 12 main tethers and 12 connected auxiliary tethers. The initial nutation angle φ_0 is assumed zero. The position vector of the i^{th} interconnected point between the i^{th} main tether and central spacecraft in the $O_bX_bY_bZ_b$ coordinate system is given by

$$\boldsymbol{p}^b_{cm\_i} = \begin{bmatrix} R_s\cos\left(2\pi\left(i-1\right)/12\right) & R_s\sin\left(2\pi\left(i-1\right)/12\right) & 0 \end{bmatrix}^T \quad i=1,\ldots 12 \tag{4.3}$$

The position vector of the i^{th} remote unit in the $O_bX_bY_bZ_b$ coordinate system can be written as

$$\boldsymbol{p}^b_{re\_i} = \begin{bmatrix} \left(L+R_s\right)\cos\left(2\pi\left(i-1\right)/12\right) & \left(L+R_s\right)\sin\left(2\pi\left(i-1\right)/12\right) & 0 \end{bmatrix}^T \quad i=1,\ldots 12 \tag{4.4}$$

Table 4-2 shows the parameters of the E-sail used in simulation, where the material properties of tethers are also kept the same with Table 4-1. The equations of motion of the E-sail are solved by the 5th order Runge-Kutta type method for differential-algebraic equations. The maximum iteration number and the absolute error tolerance at each time step are defined as 10 and 10^{-10}, respectively. The total simulation period is 15 hours with a time step of 0.01s.

Table 4-2 Properties of the generalized E-sail model.

Parameters	Values
Mass of the central spacecraft (*kg*)	1,000

Mass of the Remote Unit (*kg*)	1.5
Radius of the central spacecraft (*m*)	1.0
Height of the central spacecraft (*m*)	1.0
Initial spin rate of the central spacecraft (*rad/s*)	$[0.004 \quad 0 \quad 0]^T$

The simulation results are shown in Figure 4-7 to Figure 4-9. Figure 4-7(a) shows that the Sun-E-sail distance is constant in the duration of simulation as expected due to the zero propulsive force. Moreover, the accuracy of the integration method is also validated due to the trivial error. Figure 4-7(b) shows the in-plane libration angle of the main tether is oscillating around the radial direction of the central spacecraft. Although very small, it results in a disturbance torque in the X_{cb} -axis as indicated by Equation (3.84). Accordingly, the spin angular velocity and accelerations of the central spacecraft in the $O_{cb}X_{cb}Y_{cb}Z_{cb}$ coordinate system are illustrated in the X_{cb} axis, as presented in Figure 4-8. These small oscillations are caused by the transient influence at the beginning of the numerical simulation, where we started the simulation with nominal tether length and zero tension. The elasticity of the main tethers allows the tether being elongated and then oscillated back and forth about the radial direction due to the Coriolis force effect. The components of the angular velocities ω_{cb_y}, ω_{cb_z} and the angular accelerations $\dot{\omega}_{cb_y}$, $\dot{\omega}_{cb_z}$ in the Y_{cb} and Z_{cb} axes are basically zero because the coning angle is zero as shown in Figure 4-9(c), and there is no component of the disturbance torque in these two axes.

Furthermore, the tensions in the main and auxiliary tethers, spin rate, nutation angle, coning angle, and CM and CT of the E-sail are illustrated in Figure 4-9. It indicates that the E-sail is in a steady state as expected. Its spin rate is equal to the mean spin rate of the central spacecraft. Also, the CM and CT of the E-sail are the same and coincide with the CM of the central spacecraft. This also confirms the stability of the E-sail. Thus, the results in this section are used as a benchmark for the rest of study of the generalized E-sail model, where the main tethers are positively charged, and the propulsive force is considered. The attitude dynamic of the central spacecraft is also considered.

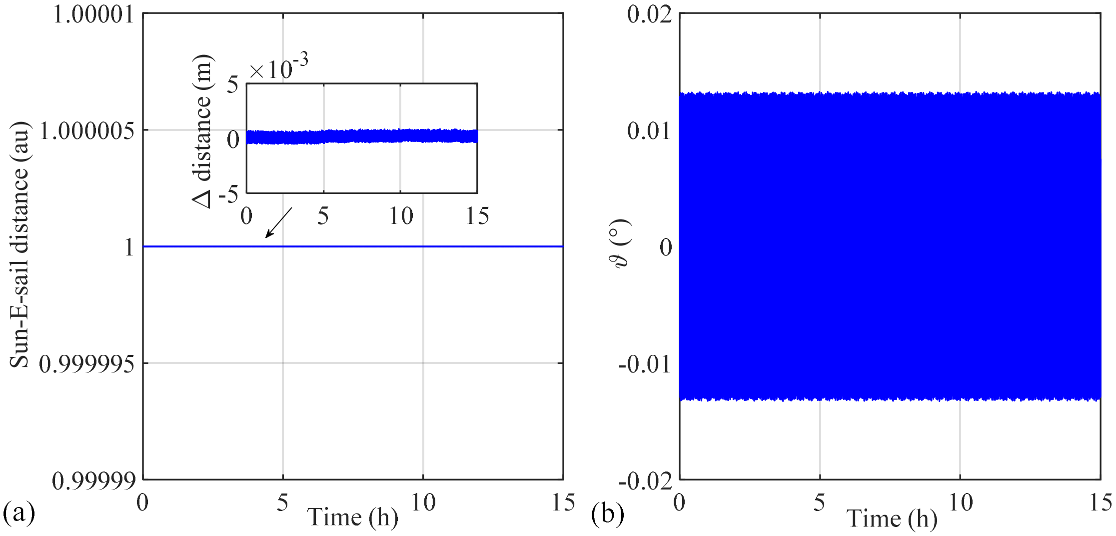

Figure 4-7 Time histories of (a) the Sun-E-sail distance (b) in-plane libration angle with zero propulsive force.

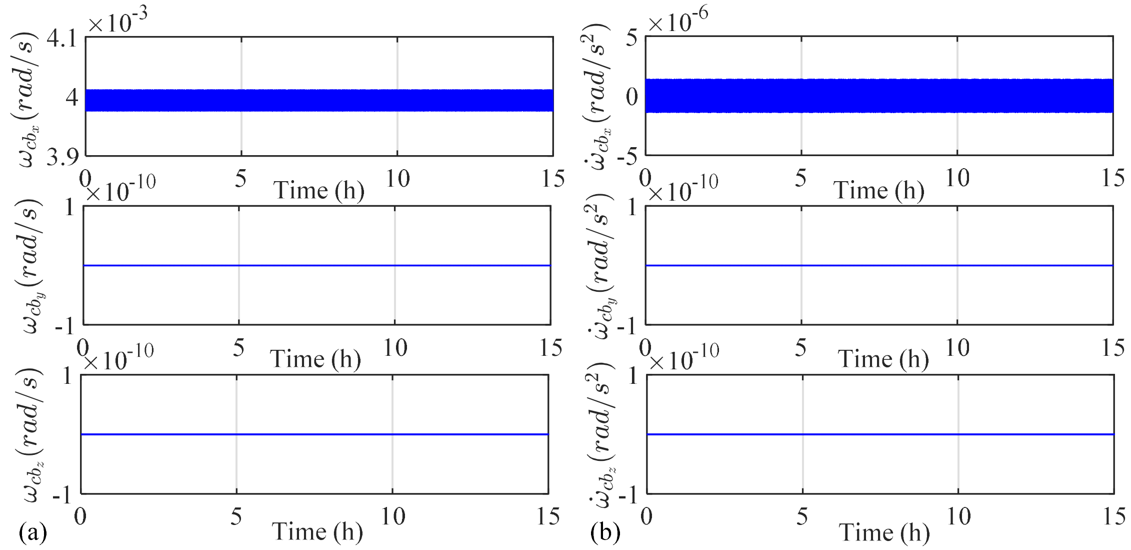

Figure 4-8 Time histories of (a) the spin rate and (b) accelerations of the central spacecraft in the $O_{cb}X_{cb}Y_{cb}Z_{cb}$ coordinate system.

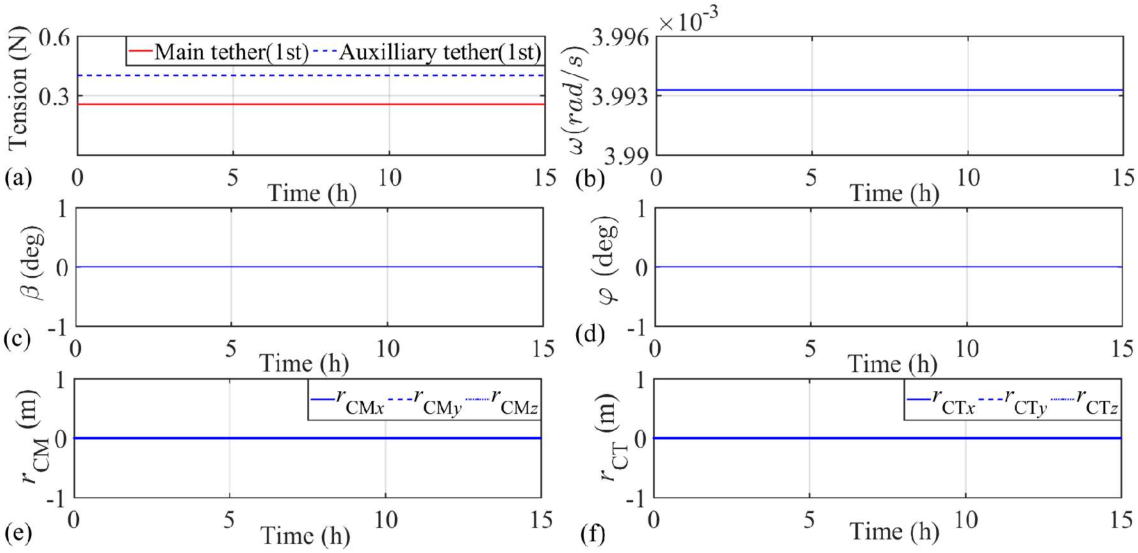

Figure 4-9 Time histories of (a) the tensions in the main and auxiliary tethers (b) the spin rate (c) the coning angle (d) the nutation angle (e) CM and (f) CT of the E-sail, respectively.

4.3 Coning Motion of the E-sail

The aim of the current section is to reveal the unknown mechanism behind the periodic coning motion of the tethers and derive an analytic expression of the coning motion frequency under the assumption of small coning angle. Moreover, it is interesting to know if the coning motion of the tethers will affect the global dynamic behavior of the E-sail. In particular, the equilibrium shape of the main tethers of the E-sail is estimated. The numerical simulation results verify the correctness of the coning motion analysis.

4.3.1 Mechanism of Periodic Coning Motion

The previous works [27-28, 31-33] showed numerically the coning motion of the E-sail vs the magnitude of propulsive force. Furthermore, it was revealed that the coning motion of the E-sail changes periodically under the propulsive force, which can be seen from the works by the rigid tether model [14, 28], the catenary tether model, and flexible tether model [30]. However, the mechanism behind the phenomenon is less understood.

Consider the i^{th} main tether as a sample as shown in Figure 4-10(a) in the $O_oX_oY_oZ_o$ coordinate system, it is assumed stretched and straight and the gravitational force is neglected. The E-sail is spinning in a plane perpendicular to the heliocentric ecliptic plane and the sail angle is set as zero degree. Thus, the propulsive force will generate a torque τ_t that pushes the tether rotating out of the nominal spin plane with respect to the central spacecraft. The analytical expression of the torque with the arbitrary sail angle was given in Ref. [32]. With the above assumption, a simplified expression of the i^{th} main tether torque τ_t can be obtained as

$$\tau_t = \left| \int_0^L \boldsymbol{l} \times \boldsymbol{f}_{dl} dl \right| \tag{4.5}$$

where L is the length of the i^{th} main tether and $\boldsymbol{l}$ is the position vector of the infinitesimal tether length dl of the i^{th} main tether measured from the central spacecraft.

At the same time, the centrifugal forces due to the inertia of the i^{th} main tether and remote unit will generate a restoring torque to push the i^{th} main tether rotating back to the nominal spin plane, as shown in Figure 4-10(a). Meanwhile, if there are auxiliary tethers connected to the i^{th} remote unit, the tension T_a acting on the auxiliary tethers has a resultant force in the i^{th} main tether that partially cancels the centrifugal forces as illustrated in Figure 4-10(b). The tension T_a is given by

$$T_a = \left(T_{a_1} + T_{a_2}\right)\cos\left(\left(\pi - 2\pi/M\right)/2\right) \tag{4.6}$$

$$T_{a_1} = T_{a_2} = \frac{E_{au} A_{au} \Delta L_{au}}{L_{au}} \tag{4.7}$$

where T_{a_1} and T_{a_2} are the tensions generated by the connected auxiliary tethers of the i^{th} main tether, E_{au}, L_{au} and ΔL_{au} are the Young's modulus, undeformed length, elongation of the auxiliary tether, respectively.

Thus, the total restoring torque caused by the resultant of centrifugal force and tensions of auxiliary tethers acting on the i^{th} main tether can be expressed as

$$\tau_c = \tau_{c\_t} + \tau_{c\_r} - \tau_{c\_f} \tag{4.8}$$

where τ_{c_t} and τ_{c_r} are the torques of the centrifugal forces F_{c_t} and F_{c_r} resulting from the masses of the main tether and remote unit including the auxiliary tethers respectively, τ_{c_f} is the resultant force of the tension T_a acting on the auxiliary tethers, respectively. The detailed expressions of these terms are written as

$$\tau_{c\_t} = F_{c\_t} l \sin\beta = \int_0^L \rho l^2 \sin\beta \cos\beta \omega^2 dl = \left(m_t L^2 \cos\beta \sin\beta \omega^2\right)/3 \tag{4.9}$$

$$\tau_{c\_r} = F_{c\_r} L \sin\beta = \left(m_{re} + m_{au}\right) L^2 \cos\beta \sin\beta \omega^2 \tag{4.10}$$

$$\tau_{c\_f} = T_a L \sin\beta \tag{4.11}$$

where ω is the E-sail spin rate, m_{re}, m_{au} and m_t are the masses of the i^{th} remote unit, the connected auxiliary tethers, and the i^{th} main tether, respectively.

Obviously, the velocity of coning motion and the relative coning angle will increase if $\tau_t > \tau_c$ and vice versa.

From the free-body diagram in Figure 4-10(c), the equation of the coning motion is derived from the moment balance about the central spacecraft, that is,

$$\left(m_{re}+m_{au}+m_t/3\right)L^2\ddot{\beta}=-\tau_c \tag{4.12}$$

where $\ddot{\beta}$ is the angular acceleration of the coning motion.

For a small β, $\cos\beta\approx 1$, $\sin\beta\approx\beta$ and Equation (4.12) is simplified as

$$\ddot{\beta}+\left\{\omega^2-T_a\Big/\left[\left(m_{re}+m_{au}+m_t/3\right)L\right]\right\}\beta=0 \tag{4.13}$$

Accordingly, it can be seen that the velocity of the coning motion reaches its maximum at $\tau_t=\tau_c$ when the acceleration is zero. Also, it should be noted that Equation (4.13) indicates the coning motion is harmonic. The similar phenomenon can be found from the pendulum motion.

Thus, the angular frequency of the coning motion is obtained as

$$\widehat{\omega}=\sqrt{\omega^2-T_a\Big/\left[\left(m_{re}+m_{au}+m_t/3\right)L\right]} \tag{4.14}$$

where $\widehat{\omega}$ is the angular frequency of the coning motion.

Accordingly, the period of the coning motion can be written as

$$T_{cm}=\frac{2\pi}{\widehat{\omega}}=\frac{2\pi}{\sqrt{\omega^2-T_a\Big/\left[\left(m_{re}+m_{au}+m_t/3\right)L\right]}} \tag{4.15}$$

It should be noted that the period of the coning motion depends on the length of the i^{th} main tether, the masses of the i^{th} remote unit, main and auxiliary tethers, the spin rate of the E-sail, and the resultant tension component of adjacent auxiliary tethers in the i^{th} main tether direction. As the spin rate increases, the length of the main tether increases due to the tether elongation under the higher centrifugal force. Accordingly, the tension acting on the auxiliary tethers increases, leading to a higher T_a as shown in Equation (4.7). Furthermore, the period of the coning motion will be reduced based on Equation (4.15). Finally, if there are no auxiliary tethers ($T_a = 0$), the angular frequency of the coning motion $\hat{\omega}$ will be the same as the spin rate of the E-sail, as illustrated in Equation (4.14).

Recalling Equations (4.5) and (4.8), the dynamic equilibrium of the coning motion will be reached at $\tau_t = \tau_c$, and the corresponding coning angle can be obtained with the assumption of a small coning angle, which can be written as

$$\beta = \frac{\tau_t}{\left(m_{re} + m_{au} + m_t/3\right) L^2 \omega^2 - T_a L} \tag{4.16}$$

Equation (4.16) illustrates that the magnitude of the equilibrium coning angle is proportional to the torque due to the propulsive force and inversely proportional to the masses of the main and auxiliary tethers, and the remote unit, the length of the main tether, the resultant tension of the adjacent auxiliary tethers, and the spin rate of the E-sail, respectively. However, the equilibrium state of the E-sail is influenced by a small disturbance from the coupling between the orbital and the spin motions, that is,

$$F_C = -2\left(m_{re} + m_{au} + m_t/3\right) \boldsymbol{\Omega} \times \left(\boldsymbol{\omega} \times \boldsymbol{L}\right) \tag{4.17}$$

where $\boldsymbol{\omega}$ is the spin rate vector of the E-sail, $\boldsymbol{L}$ is the position vector of the i^{th} main tether, and $\boldsymbol{\Omega}$ is the angular velocity of the E-sail orbiting around the Sun.

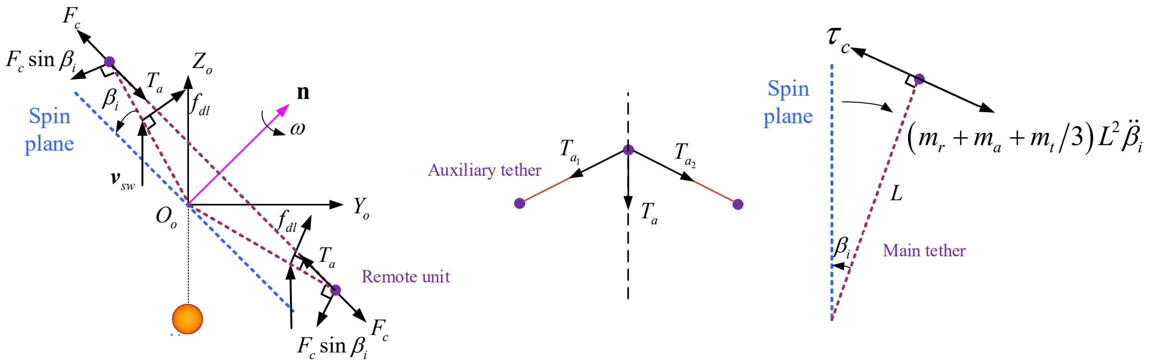

(a) (b) (c)

Figure 4-10 Free-body diagram of E-sail.

4.3.2 Influence of the E-sail Parameters on Coning Motion

The aim of this section is to verify the correctness of the coning motion analysis in the previous section and investigate the influence of the E-sail parameters on the coning motion. The NPFEM E-sail model is used, and the E-sail consist of 12 main tethers with 12 connected auxiliary tethers. The physical properties of the E-sail are the same as these in Table 4-1, while the propulsive force is introduced. It is assumed that the potential bias of all main tethers is the same (20 kV) and the solar wind velocity is constant (400km/s), which can be obtained from Ref. [13]. The propulsive force coefficient $K_2 = 11.74$ in Equation (3.19) is utilized with the zero initial sail angle. The total simulation period is 6 hours with a time step size of 0.01s.

Equation (4.15) shows that the period of the coning motion depends on the spin rate of the E-sail, and the masses of the remote units and tethers. For the given lengths of the main and auxiliary tethers, the masses of main and auxiliary tether are constant. Thus, the only parameters that can affect the coning motion are the spin rate and the mass of remote unit. In this section, the influences of the variations of mass of the remote unit m_{re} and the initial spin rate ω_0 are investigated, as presented in Table 4-3. Here, Case A to F are used to verify the correctness of Equation (4.15), while Case G and H are utilized to confirm the analysis of the E-sail's initial equilibrium configuration. The rest of the E-sail parameters are the same as before. The simulation results are shown in Table 4-4 and Figure 4-11 to Figure 4-14.

Table 4-3 Parameters of the parametric investigation.

Label	$m_{re}(kg)$	$\omega_0(rad/s)$	E-sail configuration	Initial coning angle (*degree*)
Case A	0.5	0.004	No auxiliary tether	0
Case B	1.5	0.004	No auxiliary tether	0
Case C	0.5	0.004	Auxiliary tether	0
Case D	1.5	0.004	Auxiliary tether	0
Case E	1.5	0.003	No auxiliary tether	0
Case F	1.5	0.003	Auxiliary tether	0
Case G	1.5	0.004	No auxiliary tether	0.36
Case H	1.5	0.004	Auxiliary tether	0.36

Table 4-4 Periods of the coning motion.

Label	Case A	Case B	Case C	Case D	Case E	Case F
Periods by Equation (4.15), (s)	2079	1571	1571	2672	2036	2096
Periods from simulation, (s)	2076	1565	1565	2624	2027	2077

First, Table 4-4 shows that the period of the coning motion predicted by Equation (4.15) is approximately identical to the simulation results. This proves that the coning motion is caused by the combination of the propulsive force, the tensions acting on the auxiliary tethers, and the centrifugal force acting on the main tether as revealed in Section 4.3.1. It should be pointed out that the error between the calculated and simulation values has nothing to do with the variation of the E-sail's spin rate. In addition, Figure 4-11(a) shows that the period of the coning motion is the same as the spin period of the E-sail configuration without the auxiliary tethers, while is different with that of the E-sail configuration with the auxiliary tethers due to the tensions acting on the auxiliary tethers. This verifies the finding in Equation (4.15).

Second, Figure 4-11 also illustrates that the magnitude of the coning angle is inversely proportional to the mass of the remote unit without (Figure 4-11(a)) and with (Figure 4-11(b)) the auxiliary tethers. This is because the greater the mass of the remote unit, the greater the centrifugal force that leads to a higher restoring torque, as shown in Equation (4.10). Figure 4-11 also shows that the E-sail with auxiliary tethers has a smaller magnitude of the coning angle than the E-sail without auxiliary tethers. This also verifies the finding in Equation (4.15). Next, Figure 4-12 shows that the period and magnitude of the coning motion are influenced by the different initial spin rates both without (Figure 4-12(a)) and with (Figure 4-12(b)) the auxiliary tethers. It can be seen that the higher the initial spin rate, the smaller magnitude of the coning motion. This is because a higher initial spin rate leads to the greater centrifugal force and, therefore, to the greater restoring torques. Figure 4-11(b) and Figure 4-12(b) also indicate that the period of the coning motion reduces if the tension acting on the auxiliary tethers is higher due to the higher initial spin rate and greater mass of remote unit. This is consistent with the prediction of Equation (4.15). As presented in Figure 4-13, the variation trends of tensions acting on the main and auxiliary tethers are also consistent with the coning motion, which also verifies the analysis in Section 4.3.1. It should be noticed that the tension acting on the auxiliary tether is out of phase of the tension acting on the main tether. As the propulsive force increases, the tension in the auxiliary tether decreases and vice versa.

Third, Figure 4-14(a) shows that the propulsive force torque is approximately constant, as expected, because of the small coning motion. However, the variation trend of the restoring torque due to the centrifugal force is approximately in phase with the coning motion, and the maximum value is approximately twice of the propulsive force torque. This indicates that there is a dynamic equilibrium state in the coning motion. This is consistent with the prediction of Equation (4.16) and will be analyzed in the following.

Finally, the equilibrium state of the E-sail configuration without the auxiliary tether is approximated by assuming the propulsive force torque equal to the restoring torque as shown in Equation (4.16). The corresponding coning angle is obtained from Equation (4.16) and is 0.36 degree for the case without the auxiliary tether. Using this coning angle as an initial condition for the E-sail configurations with and without the auxiliary tethers, Figure 4-14(b) shows that the coning angle of the E-sail without the auxiliary tethers is approximately constant, as expected. The small periodic oscillation is due to the orbital-spin disturbance as presented in Equation (4.17) and the approximation in getting the equilibrium state of the coning angle. For an E-sail with the auxiliary tethers, the coning angle oscillates periodically as predicted by Equation (4.15). In summary, the correctness of the analytical coning motion angular frequency expression is validated.

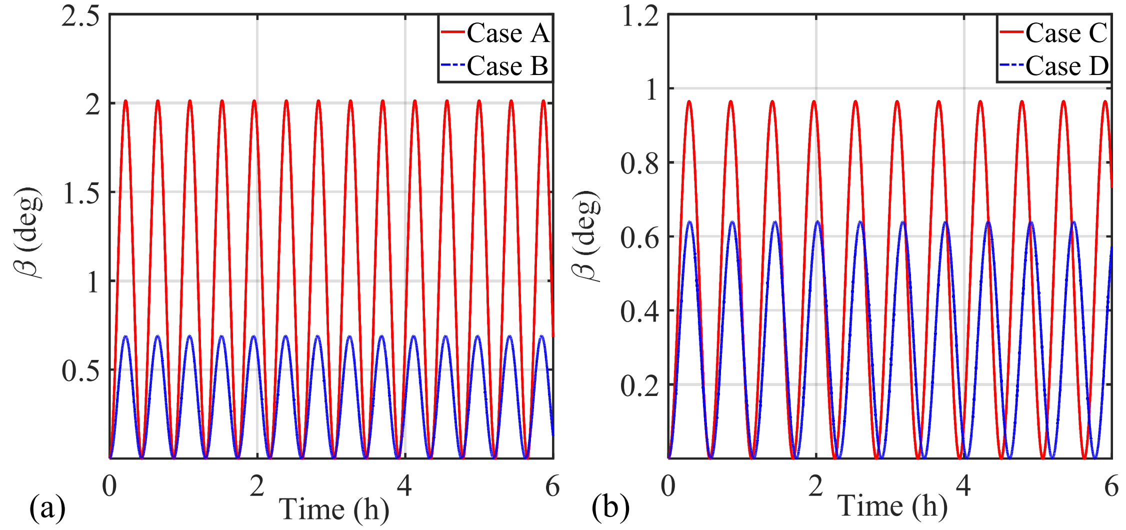

Figure 4-11 Time histories of the coning motion of different masses m_{re} without (a) and with (b) the auxiliary tethers.

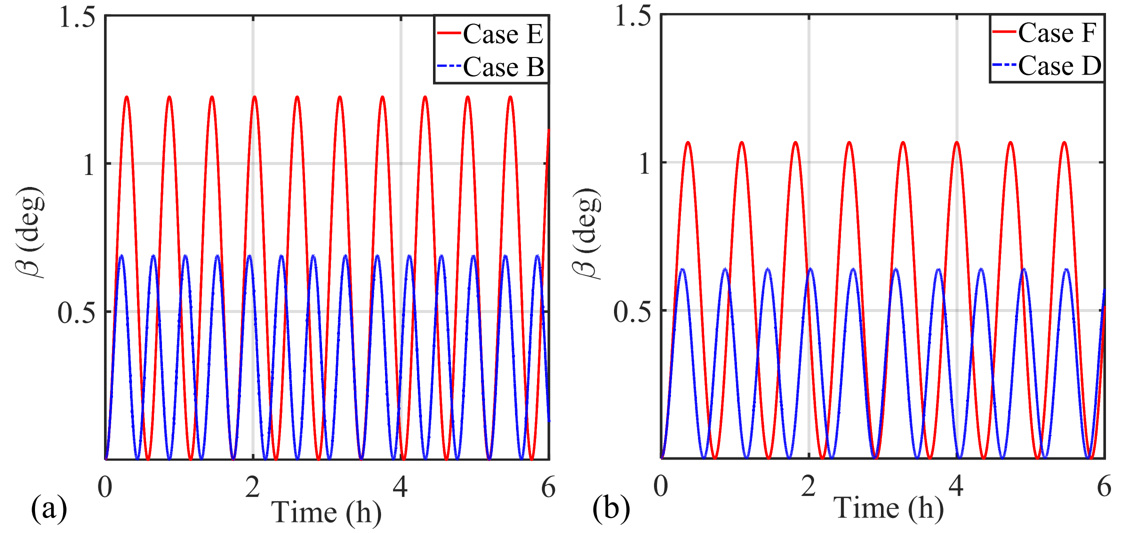

Figure 4-12 Time histories of the coning motion of different initial spin rates ω_0 without (a) and with (b) the auxiliary tethers.

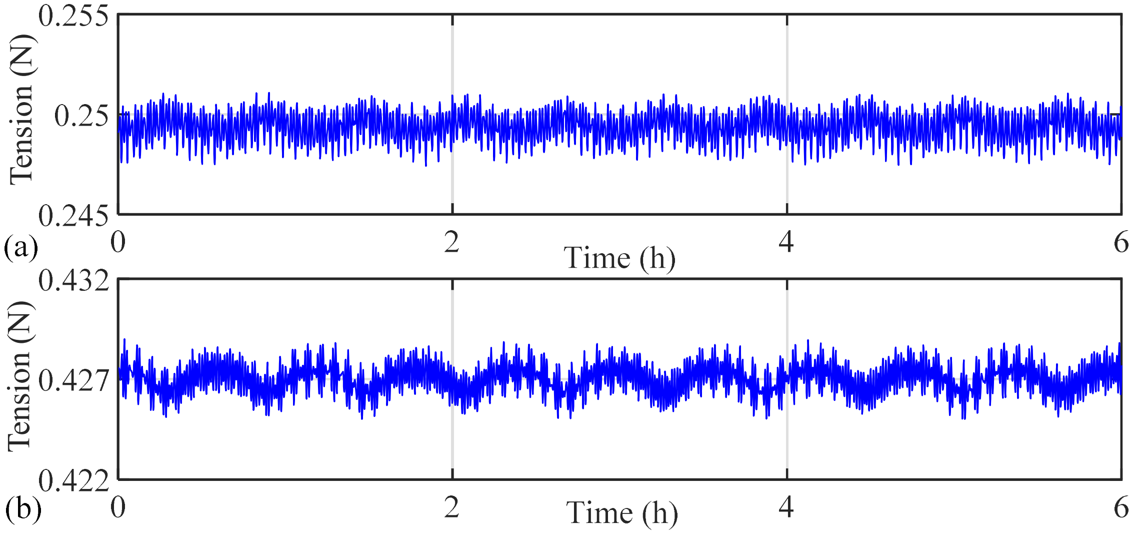

Figure 4-13 Tensions acting on the (a) main and (b) auxiliary tethers with Case D.

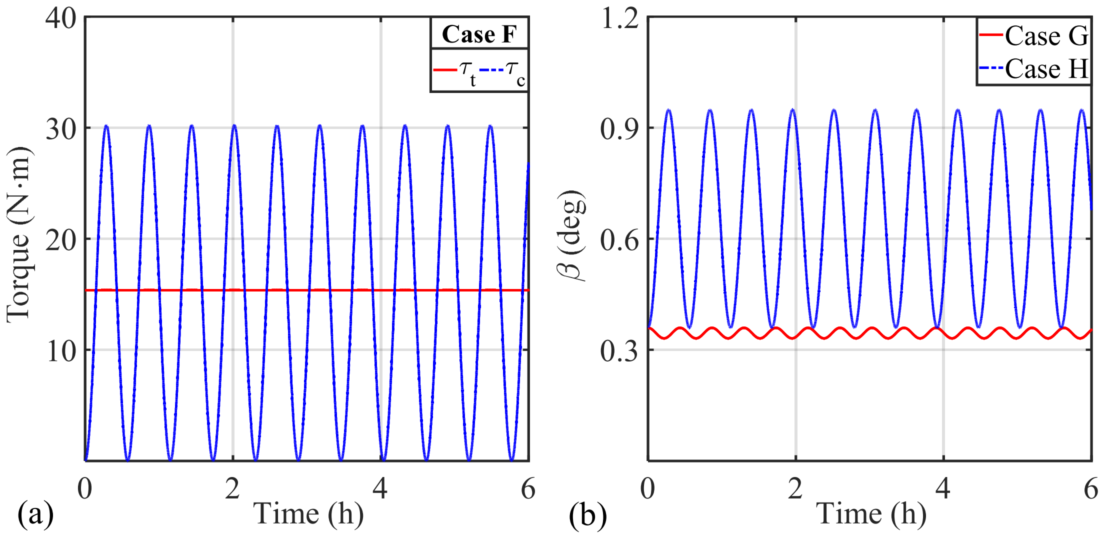

Figure 4-14 Comparisons of (a) the torques and (b) the coning angles with different cases.

4.4 Spin Rate of the E-sail

To guarantee the proper operation of the E-sail, the spin rate should be selected with a certain range. The previous work [3] has presented a rough criterion for selecting the spin rate of E-sail. Accordingly, the upper and lower bounds of the spin rate have been estimated based on the guideline with the assumption that the central spacecraft and tethers are in the same plane [28, 12]. In addition, it was revealed that the coning motion of the E-sail will impact the magnitude of the centrifugal and propulsive forces [27], and further affect the upper and lower bounds of the spin rate. The influence of the coning motion on the spin rate bounds is less understood. Additionally, the upper bound of the spin rate is well understood from the perspective of material properties, which is determined intuitively by keeping the axis stress of the main tether less than the tensile stress of the tether material. However, there is no clear physical meaning behind the lower spin rate bound.

In this section, the upper and lower spin rate bounds of the axisymmetric E-sail with auxiliary tethers are revisited to reveal the physics that dictates these bounds and analytical expression are provided to ensure the proper operation of the E-sail. In the analysis, it is assumed that the central spacecraft is orbiting in the heliocentric ecliptic plane, and the E-sail is spinning in a plane perpendicular to the heliocentric ecliptic plane. This assumption is based on the fact that most of the terrestrial planets are orbiting the sun approximately in the same ecliptic plane, which means the in-plane angle $\delta = \frac{\pi}{2}$. It is further assumed that the main and auxiliary tethers are stretched and straight without any slack, and the coupling between the orbital and spin motions is neglected.

4.4.1 Upper Bound of Spin Rate

As shown in Figure 4-15, the criterion to derive the upper bound of the spin rate is the same with the previous works [28-29, 33], that is, the upper bound of the spin rate should be limited to ensure the centrifugal force F_{c_i} in the main tether produced by the spinning motion of the E-sail cannot exceed the maximum tensile strength $T_m^{\max}$ of the main tethers as

$$F_{c\_i} \le T_m^{\max} \cos\beta \tag{4.18}$$

$$T_m^{\max} = \sigma_b A_m \tag{4.19}$$

where σ_b and A_m are the ultimate tensile strength and the cross-sectional area of the main tether.

Considering the i^{th} main tether as a sample as shown in Figure 4-15(a) in the $O_b X_b Y_b Z_b$ coordinate system, F_{c_i} can be written as

$$F_{c\_i} = (m_{re} + m_{au}) L \cos\beta\omega^2 + \int_0^L \rho l \cos\beta\omega^2 dl = m_{eff}\omega^2 L\cos\beta \tag{4.20}$$

where ω is the spin rate, $m_{eff} = \left(m_{re} + m_{au} + L\rho/2\right)$ is the effective mass, l is the distance measured from the infinitesimal tether length dl to the central spacecraft, m_{re} and m_{au} are the masses of the i^{th} remote unit and the connected auxiliary tethers, L and ρ are the length and linear density of the main tether, respectively.

Substituting Equations (4.19) and (4.20) into Equation (4.18) yields the upper bound of the spin rate as

$$\omega \leq \omega_{\max} = \sqrt{\frac{\sigma_b A_m}{(m_{re} + m_{au} + \frac{\rho L}{2})L}} = \sqrt{\frac{\sigma_b A_m}{m_{eff} L}} \tag{4.21}$$

Equation (4.21) indicates that the upper bound of the E-sail spin rate depends only on the physical properties of the main/auxiliary tethers and remote units. Once the configuration of an E-sail is determined, the upper bound is a design constant.

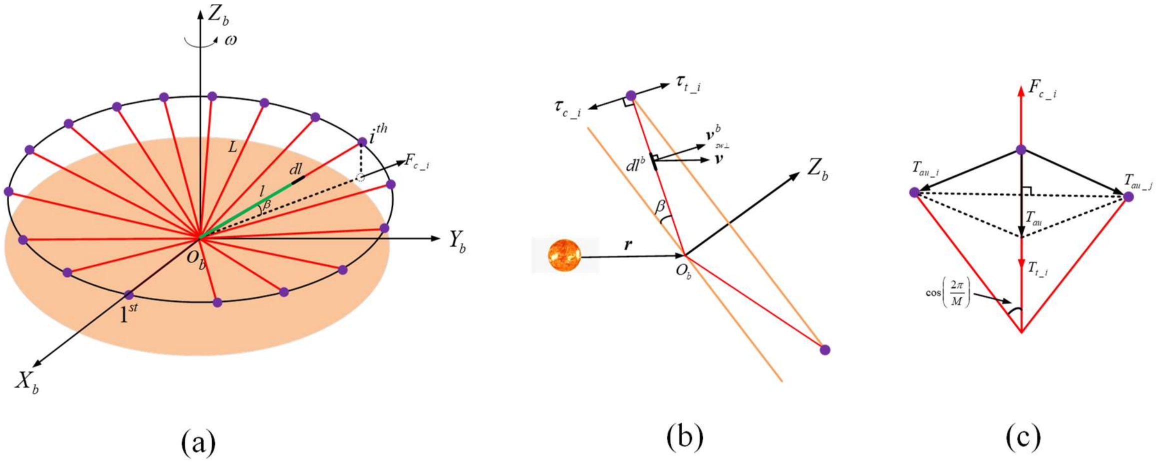

Figure 4-15 Free-body diagram of the tether.

4.4.2 Lower Bound of Spin Rate

Next, the current work tries to explain analytically the criterion of lower spin rate bound from the perspective of E-sail stability. Unlike the derivation of the upper bound spin rate, the lower bound of spin rate was given in the literature by assuming the centrifugal force in the main tether being five times greater than the propulsion force [3, 28-29, 12] without explanation. Although the explanation of the lower bound of E-sail spin rate criterion was given in Ref. [32], it assumed that there are not the auxiliary tethers and sail angle is zero degree. Moreover, the inclination of the solar wind velocity with respect to the E-sail spin axis (non-zero sail angle) may result in the collisions of main tethers and make the E-sail instability [3]. Therefore, the E-sail with auxiliary tethers under any sail angle is investigated in current dissertation. The following reveals the physics behind this lower bound of spin rate criterion.

Recall the role of auxiliary tethers is to prevent the collision of adjacent main tethers [3, 14, 27, 31], which is caused by the coning motion of the E-sail. This can be done by the tension forces acting on the stretched auxiliary tethers, which tends to maintain the stability of the E-sail. Thus, all auxiliary tethers must be kept taut. However, as shown in Figure 4-15, the torques of propulsion force and tensions in the connected auxiliary tethers with respect to the central spacecraft will push the main tethers away from the spin plane [27]. Consequently, the distance between two remote units connected by the auxiliary tether is reduced, leading to the relaxation of tension in the auxiliary tether. At the same time, the torque of centrifugal forces of the main tether, remote unit and auxiliary tethers will pull the main tether back to the spin plane. Thus, the spin rate must be sufficiently large to prevent the auxiliary tether from slacking. Accordingly, the spin rate of the E-sail corresponding to zero tension in the auxiliary tether will be the lower bound.

Let L_{au} and L_0 be the unstretched lengths of the auxiliary and main tethers. From Figure 4-15, the geometric relationship between the elongations of auxiliary and main tethers is

$$\Delta L_{au} = 2\left\lfloor \left(L_0 + \Delta L_0\right)\cos\beta - L_0 \right\rfloor \sin(\pi/M) \tag{4.22}$$

where ΔL_{au} and ΔL_0 are the elongations of the auxiliary and main tethers, and M is the total number of auxiliary tethers.

The tension in the auxiliary tether becomes zero when $\Delta L_{au} = 0$. Then, the corresponding coning angle is

$$\cos\beta = \frac{L_0}{\left(L_0 + \Delta L_0\right)} = \frac{1}{\left(1+\varepsilon\right)} \tag{4.23}$$

$$\sin\beta = \frac{\sqrt{2\varepsilon + \varepsilon^2}}{\left(1+\varepsilon\right)} \tag{4.24}$$

where $\varepsilon = \Delta L_0 / L_0$ is the strain of the main tether.

The lower bound of spin rate can be obtained from the torque balance of the i^{th} main tether with respect to the central spacecraft. The torque balance can be written as,

$$\tau_{t\_i} = \tau_{c\_i} \tag{4.25}$$

where τ_{c_i} and τ_{t_i} are the centrifugal force torque and the propulsion force torque acting on the i^{th} main tether with respect to the central spacecraft, respectively.

According to Figure 4-15(a), the torque τ_{c_i} produced by the centrifugal force acting on the i^{th} main tether can be written as

$$\begin{aligned} \tau_{c\_i} &= (m_{re} + m_{au})L^2 \sin\beta \cos\beta\omega^2 + \int_0^L \rho l^2 \sin\beta \cos\beta\omega^2 dl \\ &= (m_{re} + m_{au} + \rho L/3)L^2\omega^2 \sin\beta \cos\beta \end{aligned} \tag{4.26}$$

The derivation of the torque produced by the propulsion force is similar to Refs. [31-32]. Therefore, as shown in Figure 4-15(b), the infinitesimal propulsion torque $d\boldsymbol{\tau}_{t\_i}$ of the i^{th} main tether in the $O_bX_bY_bZ_b$ coordinate system is given by

$$d\boldsymbol{\tau}_{t\_i} = \boldsymbol{l}_i^b l \times \boldsymbol{f}_{dl}^b dl \tag{4.27}$$

where $\boldsymbol{l}_i^b$ is the unit vector of the i^{th} main tether, dl is the infinitesimal tether length at the distance of l from the central spacecraft, $\boldsymbol{f}_{dl}^b$ is the propulsive force per unit tether length in the $O_bX_bY_bZ_b$ coordinate system, respectively.

The unit vector $\boldsymbol{l}_i^b$ in the $O_bX_bY_bZ_b$ coordinate system can be written as

$$\boldsymbol{l}_i^b = \begin{bmatrix} \cos\beta\cos\left(2\pi(i-1)/M\right) & \cos\beta\sin\left(2\pi(i-1)/M\right) & \sin\beta \end{bmatrix}^T \tag{4.28}$$

and the propulsion force of the infinitesimal tether length dl is

$$\boldsymbol{f}_{dl}^{b} = \boldsymbol{T}_{sp2b}\boldsymbol{T}_{o2sp}\boldsymbol{T}_{s2o}\boldsymbol{T}_{t2s}^{k}\boldsymbol{f}_{dl}dl = \sigma\boldsymbol{v}_{sw\perp}^{b}dl \tag{4.29}$$

where $\boldsymbol{v}_{sw\perp}^{b}$ is the component of the solar wind velocity perpendicular to the direction of the i^{th} main tether in Equation (3.16), which is defined in the $O_bX_bY_bZ_b$ coordinate system as

$$\boldsymbol{v}_{sw\perp}^{b} = \nu\left(\boldsymbol{l}_{i}^{b} \times \boldsymbol{r}^{b}\right) \times \boldsymbol{l}_{i}^{b} \tag{4.30}$$

where $\nu = \left\|\boldsymbol{v}_{sw}\right\|$ is the solar wind velocity modulus, $\boldsymbol{r}^{b}$ is the sun-spacecraft unit vector in the $O_bX_bY_bZ_b$ coordinate system, that is,

$$\boldsymbol{r}^{b} = \boldsymbol{T}_{sp2b}\boldsymbol{T}_{o2sp}\boldsymbol{r}^{o} \tag{4.31}$$

where $\boldsymbol{r}^{o} = \begin{bmatrix} 0 & 0 & 1 \end{bmatrix}^{T}$ is the sun-spacecraft unit vector in the $O_oX_oY_oZ_o$ coordinate system.

Thus,

$$\boldsymbol{r}^{b} = \begin{bmatrix} -\sin\alpha\cos\left(\omega t\right) & \sin\alpha\sin\left(\omega t\right) & \cos\alpha \end{bmatrix}^{T} \tag{4.32}$$

Accordingly, the $\boldsymbol{v}_{sw\perp}^{b}$ is obtained as

$$\boldsymbol{v}^{b}_{sw\perp} = \nu \begin{bmatrix} \begin{array}{l} \sin\alpha\cos\left(\omega t\right)\cos^{2}\beta\cos^{2}\left(\dfrac{2\pi\left(i-1\right)}{M}\right) - \sin\alpha\cos\left(\omega t\right) \\ -\cos\alpha\sin\beta\cos\beta\cos\left(\dfrac{2\pi\left(i-1\right)}{M}\right) \\ -\sin\alpha\sin\left(\omega t\right)\cos^{2}\beta\sin\left(\dfrac{2\pi\left(i-1\right)}{M}\right)\cos\left(\dfrac{2\pi\left(i-1\right)}{M}\right) \end{array} \\ \begin{array}{l} \sin\alpha\sin\left(\omega t\right)\sin^{2}\beta + \sin\alpha\sin\left(\omega t\right)\cos^{2}\beta\cos^{2}\left(\dfrac{2\pi\left(i-1\right)}{M}\right) \\ -\cos\alpha\sin\beta\cos\beta\sin\left(\dfrac{2\pi\left(i-1\right)}{M}\right) \\ +\sin\alpha\cos\left(\omega t\right)\cos^{2}\beta\sin\left(\dfrac{2\pi\left(i-1\right)}{M}\right)\cos\left(\dfrac{2\pi\left(i-1\right)}{M}\right) \end{array} \\ \\ \begin{array}{l} \cos\alpha\cos^{2}\beta + \sin\alpha\cos\left(\omega t\right)\sin\beta\cos\beta\cos\left(\dfrac{2\pi\left(i-1\right)}{M}\right) \\ -\sin\alpha\sin\left(\omega t\right)\sin\beta\cos\beta\sin\left(\dfrac{2\pi\left(i-1\right)}{M}\right) \end{array} \end{bmatrix} \tag{4.33}$$

Substituting Equations (4.32) and (4.33) into Equation (4.27) yields the detailed expression of the infinitesimal propulsion torque $d\tau_{t\_i}$ as

$$d\tau_{t\_i} = \sigma v l dl \begin{bmatrix} \cos\alpha\cos\beta\sin\left(\dfrac{2\pi\left(i-1\right)}{M}\right) - \sin\alpha\sin\beta\sin\left(\omega t\right) \\ -\sin\alpha\sin\beta\cos\left(\omega t\right) - \cos\alpha\cos\beta\cos\left(\dfrac{2\pi\left(i-1\right)}{M}\right) \\ \sin\alpha\cos\beta\sin\left(\left(\dfrac{2\pi\left(i-1\right)}{M}\right) + \omega t\right) \end{bmatrix} \tag{4.34}$$

Thus, integrating Equation (4.34) over the length of the i^{th} main tether results the propulsion force torque τ_{t_i} as

$$\begin{aligned}\tau_{t\_i} &= \int_0^L d\tau_{t\_i} \\ &= \frac{1}{2}\sigma v L^2 \begin{bmatrix} \cos\alpha\cos\beta\sin\left(\dfrac{2\pi(i-1)}{M}\right) - \sin\alpha\sin\beta\sin(\omega t) \\ -\sin\alpha\sin\beta\cos(\omega t) - \cos\alpha\cos\beta\cos\left(\dfrac{2\pi(i-1)}{M}\right) \\ \sin\alpha\cos\beta\sin\left(\left(\dfrac{2\pi(i-1)}{M}\right) + \omega t\right) \end{bmatrix}\end{aligned} \tag{4.35}$$

The modulus of the τ_{t_i} is defined as $\tau_{t\_i} = |\tau_{t\_i}|$ and can be written as

$$\tau_{t\_i} = \frac{1}{2}\sigma v L^2 \sqrt{\begin{matrix} \cos^2\alpha\cos^2\beta + \sin^2\alpha\cos^2\beta\cos^2\left(\dfrac{2\pi(i-1)}{M} + \omega t\right) \\ +\sin^2\alpha\sin^2\beta + \dfrac{1}{2}\sin 2\alpha\sin 2\beta\sin\left(\dfrac{2\pi(i-1)}{M} + \omega t\right) \end{matrix}} \tag{4.36}$$

Without the loss of generality, simplifying Equation (4.36) by $t=0$ and $i=1$ leads to

$$\tau_{t\_1} = \frac{1}{2}\sigma v L^2 \sqrt{\cos^2\alpha\cos^2\beta + \sin^2\alpha} = \frac{L}{2}F_{t\_1} \tag{4.37}$$

$$F_{t\_1} = \sigma v L \sqrt{\cos^2\alpha\cos^2\beta + \sin^2\alpha} \tag{4.38}$$

where F_{t_1} is the total propulsive force acting on the 1^{st} main tether.

Substituting Equations (4.26) and (4.37) into (4.25) yields the lower bound of the spin rate as

$$\omega_{\min} = \sqrt{\frac{F_{t\_1}}{(m_{re} + m_{au} + \rho L/3)L\sin 2\beta}} \tag{4.39}$$

Equation (4.39) shows that the lower bound of spin rate depends not only on the physical properties of the main/auxiliary tethers and the remote units, but also on the coning angle and the propulsive force.

Combining Equations (4.21) and (4.39), the upper and lower bounds of the spin rate are presented as

$$\sqrt{\frac{F_{t\_1}}{(m_{re}+m_{au}+\rho L/3)L\sin 2\beta}} \le \omega \le \sqrt{\frac{\sigma_b A_m}{m_{eff} L}} \tag{4.40}$$

Substituting Equation (4.23) into Equation (4.39) yields

$$\begin{aligned} F_{t\_1} &= \left(m_{re}+m_{au}+\rho L/3\right) L\omega_{\min}^2 \sin 2\beta \\ &< \left(m_{re}+m_{au}+\rho L/2\right) L\omega_{\min}^2\, 2\sqrt{2\varepsilon+\varepsilon^2}\Big/\left(\left(1+\varepsilon\right)^2\right) \\ &\approx 2\sqrt{2\varepsilon}F_{c\_1} \end{aligned} \tag{4.41}$$

or

$$\frac{F_{c\_1}}{F_{t\_1}} \ge \frac{1}{2\sqrt{2\varepsilon}} \tag{4.42}$$

The relationship in Equation (4.42) at the lower bound of spin rate is shown in Figure 4-16. The fivefold of the rate F_{c_1}/F_{t_1}, suggested in Ref. [3], corresponds to a strain of $\varepsilon = 0.005$. For the Kevlar yarns, the strain at break is between 0.024 and 0.036. Thus, the design value of $\varepsilon = 0.005$ represents a safety factor of strain around 6. For high strength metals such as Titanium Alloys - Ti6Al4V Grade 5, the strain at break is about 0.01, which represents a safety factor of 2.

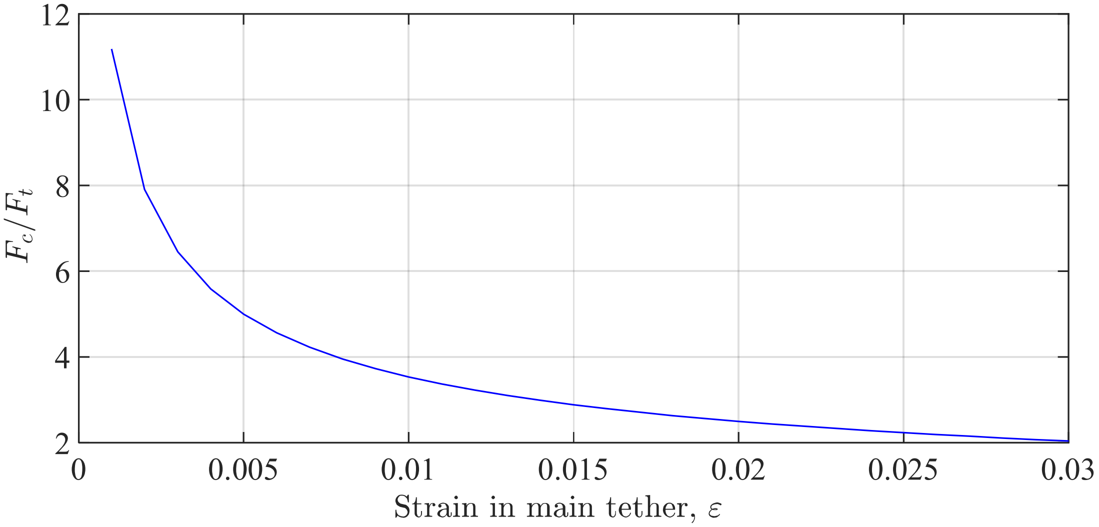

Figure 4-16 Ratio of centrifugal force over propulsive force vs the strain in main tether.

Thus, the minimum spin rate is determined by two factors: (i) no slack in the auxiliary tethers and (ii) a proper strain safety factor of the main tether for a given tether material.

4.4.3 Influence of the E-sail Parameters on Spin Rate

Consider an E-sail is in the heliocentric ecliptic orbital plane at a distance of 1 au from the Sun with the material properties shown in Table 4-1, where the properties of the tether material are from Ref. [12]. The voltage of all main tethers is assumed the same (20kV) and the solar wind velocity is constant (400km/s). The coefficient of Equation (3.19) $K_2 = 11.74$ is used. Assume the allowable strain for the main tether at the lower bound of spin rate as $\varepsilon = 0.005$. When the sail angle $\alpha = 0^{\circ}$, the upper and lower bounds of the spin rate can be obtained from Ref. [12] and the current work in Equation (4.40) can be written as

$$8.720\times10^{-4}\,rad/s \le \omega \le 6.696\times10^{-3}\,rad/s \tag{4.43}$$

$$9.371\times10^{-4}\,rad/s \le \omega \le 6.709\times10^{-3}\,rad/s \tag{4.44}$$

where Equations (4.43) and (4.44) represent the previous and current upper and lower bounds of the E-sail spin rate, respectively.

Table 4-5 Parameters of the spin rate bounds investigation.

Label	$m_{re}\,(kg)$	$\alpha\,(degree)$	$\beta\,(degree)$
Case A	1.5	NA	$[0\quad 5]$
Case B	$[0\quad 3]$	NA	5
Case C	1.5	0	$(0\quad 5]$
Case D	$[0\quad 3]$	0	5
Case E	1.5	$[0\quad 75]$	5

It should be noted that the E-sail spin rate bounds are approximately the same in both cases, and the slight difference is caused by the coning motion of tethers. Thus, it can be concluded that the theoretical analysis in current work can explain the criterion of the lower spin rate bound and can be utilized for the selection of the initial spin rate and the evaluation criteria for whether to control the spin rate.

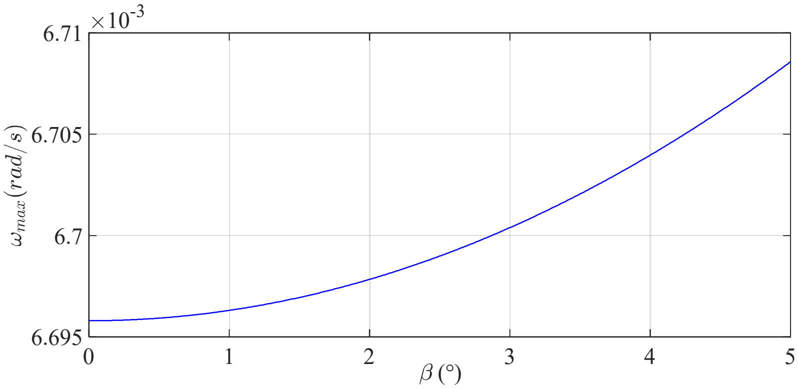

(a) Case A

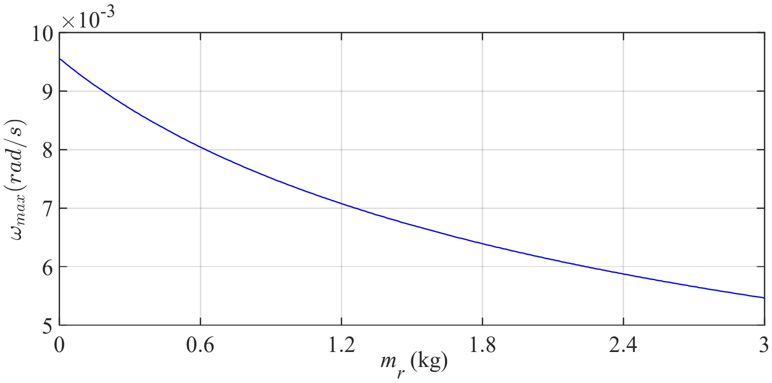

(b) Case B

Figure 4-17 Upper bound of the spin rate as the functions of (a) the coning angle and (b) the mass of remote unit.

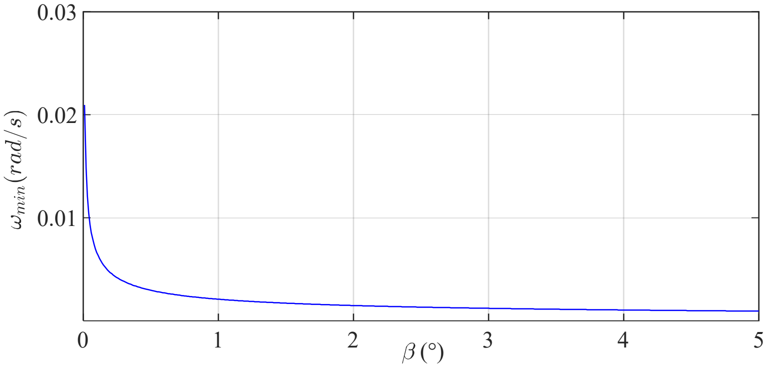

(a) Case C

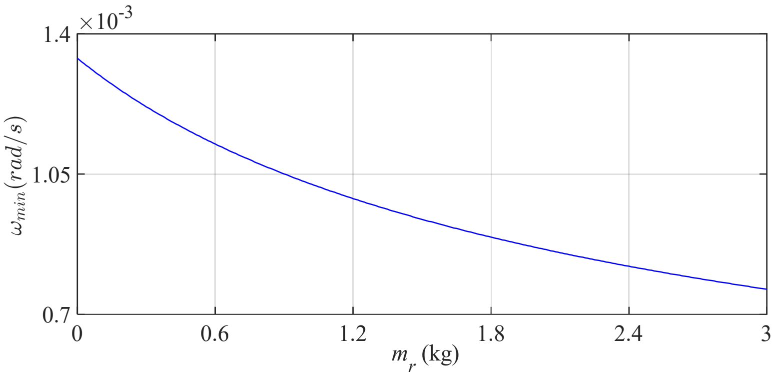

(b) Case D

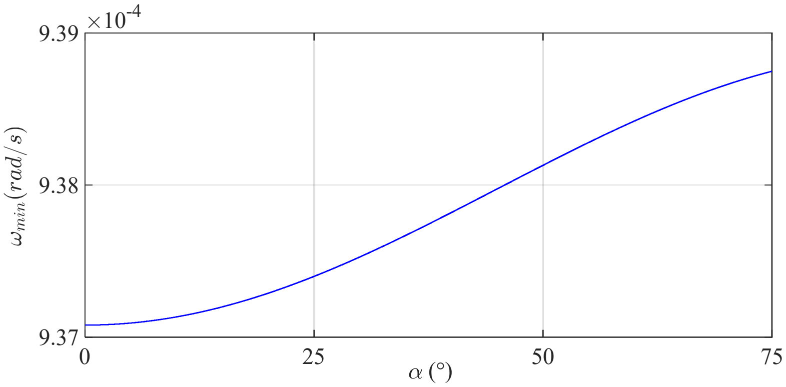

(c) Case E

Figure 4-18 Lower bound of the spin rate as the functions of (a) the coning angle (b) the mass of remote unit and (c) the sail angle.

Furthermore, Equation (4.40) indicates the dependence of spin rate on the coning and sail angles, the material properties of tethers, and the mass of remote unit. For the given length of main tether, the only parameters that can influence the upper and lower bounds of the E-sail spin rate are the coning and sail angles, and the mass of remote unit, see Table 4-5. Therefore, the impacts of the variations of the coning angle β, the sail angle α, and the mass of remote unit m_r are studied. The simulation results are presented in Figure

4-17 and Figure 4-18.

Figure 4-17(a) shows that the upper bound of the spin rate increases over coning angle with a small coning angle assumption, and the minimum value $6.696\times10^{-3}\,rad/s$ is obtained at $\beta=0^\circ$. However, the magnitude of the variation is negligible. In addition, the variation of the remote unit has a significant effect on the upper bound of the spin rate, as shown in Figure 4-17(b). Moreover, it can be concluded that the influence of sail angle on the lower bound of spin rate is negligible with the given five-degree coning angle, while the coning angle and mass of remote unit have significant effect on the lower bound of spin rate, as illustrated in Figure 4-18.

Thus, an initial spin rate $\omega_0 = 4\times10^{-3}\,rad/s$ is adopted in the rest of the study. It is worth noting that the obtained theoretical spin rate bounds are applicable to any sail angle value. Through the parametric analysis by the numerical simulation, the results show the new lower bound of the E-sail with auxiliary tethers depends on the strain of the main tethers. At the zero-sail angle, the new theoretical lower bound of spin rate gives the similar result of the existing estimation that is constrained for the zero-sail angle condition but applicable for the E-sail without auxiliary tethers.

Chapter 5 PARAMETRIC ANALYSES OF THE NPFEM E-SAIL MODEL

Summary: In this chapter, the dynamic characteristics of the E-sail is investigated by a high-fidelity tether dynamic model developed in Section 3.3. First, the influences of the solar wind fluctuations on the configuration stability of the E-sail are investigated by parametric analysis with different E-sail configurations, sail angles, and spin rates. Then, the influences of the propulsive force models and the initial E-sail orientation on the dynamic characteristics of the sail plane coning and attitude motion of E-sail are analyzed. Through parametric analyses, some significant conclusions are presented in current chapter.

5.1 Stability of the E-sail Configuration Subject to Solar Wind Speed Fluctuations

The aim of this section is to investigate the influence of the solar wind fluctuations on the stability of the axisymmetric E-sail. Consider an E-sail with 12 main tethers and 12 connected auxiliary tethers. The electric potential of all main tethers is assumed the same (20 kV) and constant over the time [12] and the rest of parameters of the E-sail are given in Table 4-1. The main and auxiliary tethers are modelled by NPFEM and are discretized into five and two 2-noted tensile elements in accordance with the Section 4.1, respectively. Initially, the E-sail spin plane is perpendicular to the heliocentric ecliptic plane at a distance of 1 au from the Sun, and the initial position vectors of the remote units and nodes of elements are determined by Equation (4.2). The solar wind velocity is assumed to be 400 *km/s* in the first day, 800 *km/s* in the second day, and 400 *km/s* again in the third day. The total simulation period is three days with a time step of 0.01s. The stability of E-sail configuration subject to the solar wind speed fluctuations is evaluated by examining two geometrical features: (i) the adjacent angle $\theta_{i,j}$ and (ii) the coplanarity of remote units as shown in Section 4.2.

5.1.1 Stability of the E-sail Configuration with and without Auxiliary Tethers

Although the E-sail with auxiliary tethers has been widely adopted, it is still interesting to know the necessity and effectiveness of auxiliary tethers. Thus, the stability of the E-sail configuration with and without the auxiliary tethers is investigated from the perspective of torque balance of main tethers in this section. As discussed in Section 4.4.2, the propulsive torque pushes the main tethers out of the spin plane, while the centrifugal torque counterbalances the propulsive torque by pulling the main tethers back to the spin plane. For a pair of symmetrical main tethers, such as the 1st and 7th main tethers, the centrifugal and propulsive torques are

$$\tau_{c\_1} = \tau_{c\_7} = (m_{re} + m_{au} + \rho L/3) L^2 \omega^2 \sin\beta \cos\beta \tag{5.1}$$

$$\begin{aligned}
\tau_{t\_1} &= \frac{1}{2}\sigma v L^2 \sqrt{\begin{aligned}&\cos^2\alpha\cos^2\beta + \sin^2\alpha\sin^2\beta + \sin^2\alpha\cos^2\beta\cos^2(\omega t)\\ &+\frac{1}{2}\sin 2\alpha \sin 2\beta \sin(\omega t)\end{aligned}}\\
\tau_{t\_7} &= \frac{1}{2}\sigma v L^2 \sqrt{\begin{aligned}&\cos^2\alpha\cos^2\beta + \sin^2\alpha\sin^2\beta + \sin^2\alpha\cos^2\beta\cos^2(\omega t)\\ &-\frac{1}{2}\sin 2\alpha \sin 2\beta \sin(\omega t)\end{aligned}}
\end{aligned} \tag{5.2}$$

It shows the centrifugal torque is independent of the sail angle, while the propulsive torque is dependent on the sail angle. Thus, the torque balance changes as the sail angle varies, which will lead to different coning angles for each main tether based on Equation (5.2). Consequently, the remote units will not be on the same plane. It will result in a difference in the spin rate of each main tether, causing potential collisions of main tethers if no auxiliary tethers are introduced. This will be verified by the following numerical simulations.

The parameters for numerical simulation are listed in Table 5-1, where three cases are considered. In cases A and B, no auxiliary tethers are employed. The dynamic responses of E-sail are studied for two sail angles (0 and 30 degrees) to demonstrate the influence of sail angle and auxiliary tethers on the stability of E-sail's configuration. In case C, auxiliary tethers are introduced for a non-zero (30°) sail angle to demonstrate the effectiveness of auxiliary tethers in maintaining the stable configuration of E-sail. As a reference, four remote units (1st, 4th, 7th, and 10th) are selected to form a plane. The resulting dynamic responses of the E-sail are shown in Figure 5-1 and Figure 5-2.

Table 5-1 Parameters of the E-sail configuration.

Label	$m_{re}(kg)$	$\omega_0(rad/s)$	Auxiliary tether	Sail angle (*degree*)
Case A	1.5	0.004	No	0
Case B	1.5	0.004	No	30
Case C	1.5	0.004	Yes	30

Because the E-sail in the current work consists of 12 main tethers and 12 connected auxiliary tethers as shown in Figure 4-2. Accordingly, there are 12 adjacent angles, and each adjacent angle is 30°. If all the adjacent angles maintain the constant 30°, the E-sail configuration will be stable. Figure 5-1 shows the time histories of all adjacent angles over a 3-day period. The adjacent angles in the case A maintain constant with very slight variation as shown in the insert as expected in Equation (5.2), no matter how the solar wind velocity varies. Although the daily fluctuation of solar wind velocity causes the daily fluctuation of propulsion torques, the torques acting on all main tethers are the same and axisymmetric. Thus, the temporal fluctuation of propulsion torques does not affect the circumferential distribution of main tethers. In the case B, the adjacent angles vary significantly over the 3-day period due the fluctuation of the solar wind velocity, eventually resulting in the collision of main tethers and remote units. The fluctuation in solar wind velocity causes variation of the propulsion torques not only in the temporal scale but also in the circumferential direction. This causes the main tethers coning out of plane at different rates as the E-sail spins and then as moving radially. Accordingly, it can be concluded that the E-sail without auxiliary tethers under a non-zero sail angle is unstable even if the spin rate of E-sail meets the requirements. On the contrary, Figure 5-1 also shows that the adjacent angles are kept constant even when the sail angle in not zero in the case C. This demonstrates that the auxiliary tethers are effective in maintaining the E-sail configuration to avoid the collision among main tethers, even if the propulsive force torques of the symmetrical main tethers are inequivalent.

The condition of constant adjacent angles is only one of two conditions of the stable E-sail configuration. The other is the co-plane condition of remote units, which will be examined by measuring the distances of remote units to the reference plane formed by randomly selected four remote units. If the distances between the other eight remote units and the reference plane maintain zero, the E-sail configuration will be stable. The measured distances are shown in Figure 5-2. Similarly, all remote units of the E-sail without auxiliary tethers in case A are coplanar as expected when the sail angle is zero. This is because the propulsion torques acting on all main tethers are the same and axisymmetric, see Equation (5.2). However, when the sail angle is not zero in case B, these remote units without auxiliary tethers are not coplanar, where the propulsion torques of each main tether are no longer the same and axisymmetric. This also verifies that the E-sail will be unstable under a non-zero sail angle if the auxiliary tethers are not considered. Finally, in case C, all remote units of the E-sail with auxiliary tethers are coplanar even if the sail angle is not zero. This demonstrates again that the auxiliary tethers are effective in keeping the E-sail configuration stable.

In summary, the parametric analysis shows that the configuration of E-sail without auxiliary tethers is stable only at the zero-sail angle condition. The auxiliary tethers are essential for a stable configuration of E-sail at non-zero sail angle, which provides a capacity of orbit maneuvering.

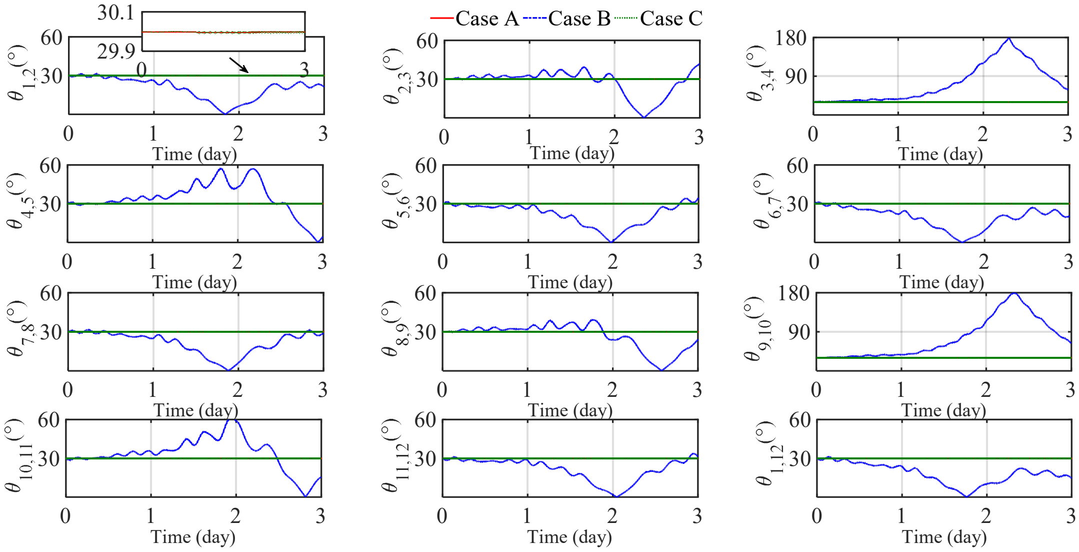

Figure 5-1 Time histories of the adjacent angles with the solar wind fluctuations.

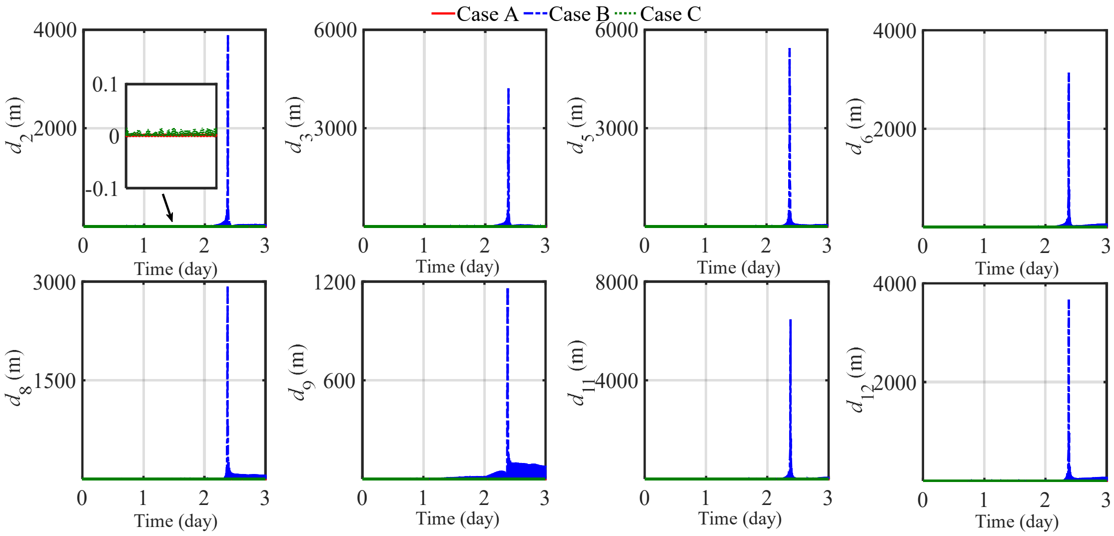

Figure 5-2 Time histories of the distances of remote units to the reference plane with the solar wind fluctuations.

5.1.2 Dynamic Responses of the E-sail with Auxiliary Tethers

In this section, the dynamic responses of an E-sail with auxiliary tethers under the solar wind speed fluctuations are investigated by varying the mass of remote units and the spin rates. Equation (5.2) shows the dependence of the propulsive torque on the spin rate, the masses of remote unit and tethers, and the material properties of tethers. For the given length and material properties of tethers, the only parameters that can affect the E-sail dynamics are the mass of the remote unit and the spin rate. Thus, the influences of the variations of the spin rate and the mass of the remote unit on the E-sail configuration with the auxiliary tethers are investigated, as shown in Table 5-2. It is worth noting that all spin rates are greater than the minimum spin rate defined in Section

4.4.2. The sail angle $\alpha = 30^{\circ}$ is used in the analysis and the E-sail parameters are the same as before. The simulation results are presented in Figure 5-3 and Figure 5-4.

In all cases, the fluctuations of the solar wind velocity cause significant variation of coning angles as indicated by Equation (5.2). Accordingly, the tensions in the main tethers fluctuate accordingly. However, the adjacent angles between two main tethers are almost constant and the coplanarity of all remote units in maintained, which means the E-sail is stable as mentioned in Section 5.1.1. These results demonstrate that the auxiliary tethers are necessary to keep the E-sail configuration stable.

In summary, the study also verifies that the stability of E-sail with auxiliary tethers is maintained even if the parameters change, if the spin rate meets the newly proposed spin rate bound.

Table 5-2 Parameters of the parametric investigation of E-sail.

Label	$m_{re}(kg)$	$\omega(rad/s)$
Case D	0.0	0.004
Case E	1.5	0.004
Case F	3.0	0.004
Case G	1.5	0.003
Case H	1.5	0.005

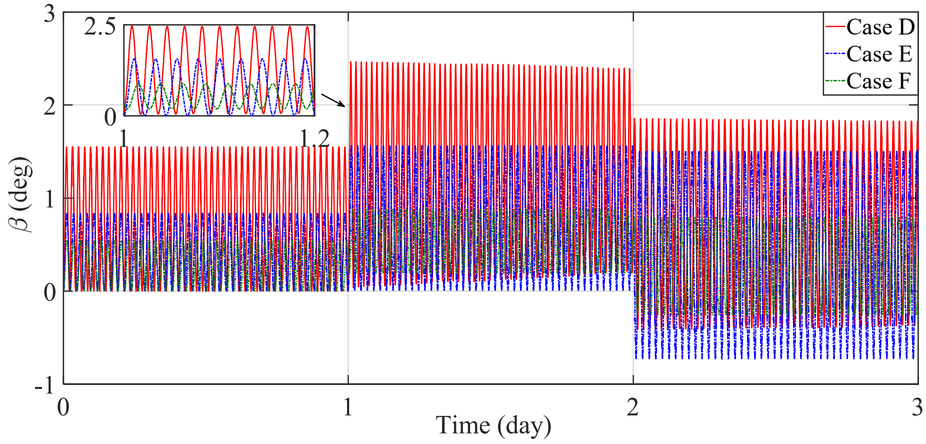

(a) Coning angle

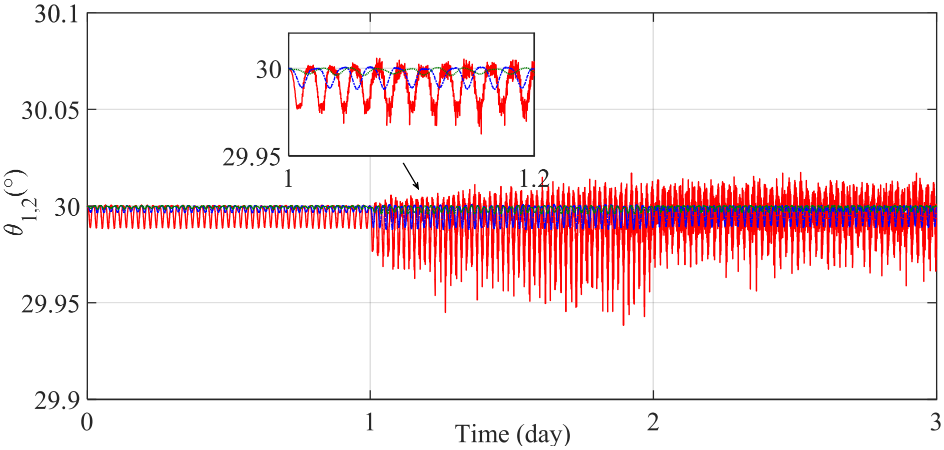

(b) Adjacent angle

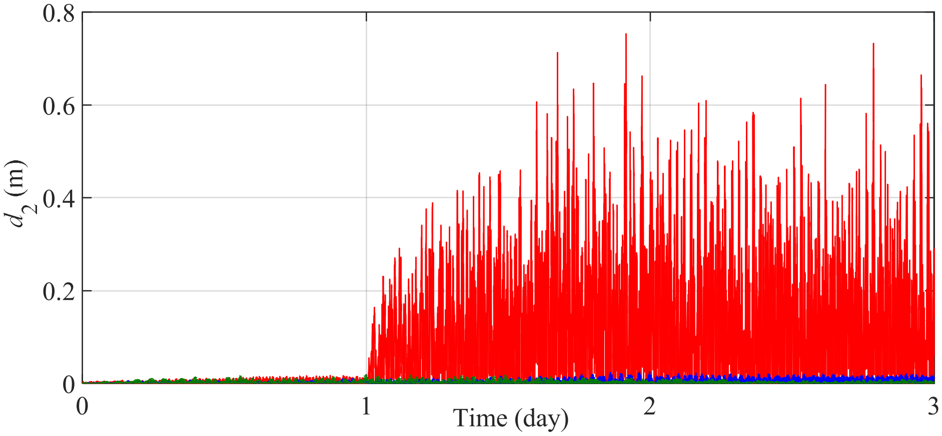

(c) Coplanarity measure for the remote unit

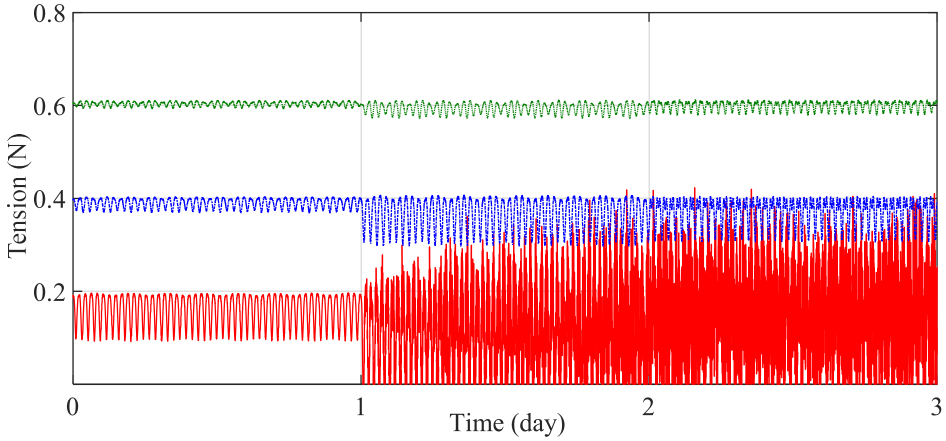

(d) Auxiliary tether tension

Figure 5-3 Time histories of E-sail responses with different masses m_{re} subject to solar wind velocity fluctuations.

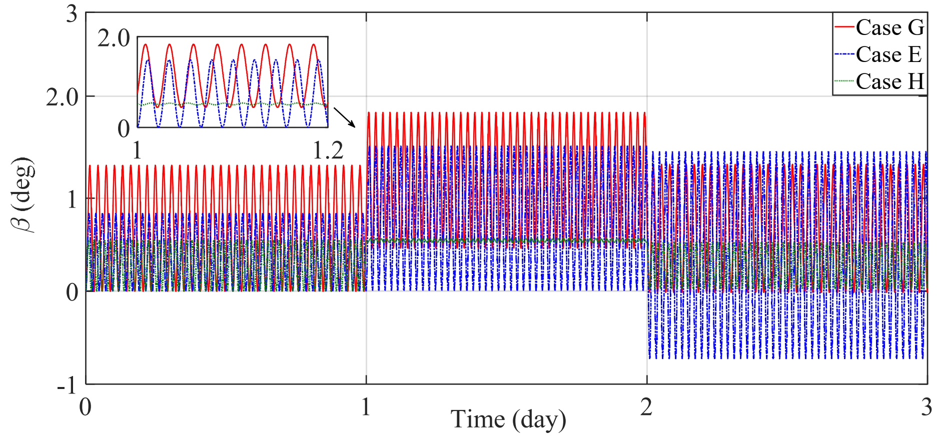

(a) Coning angle

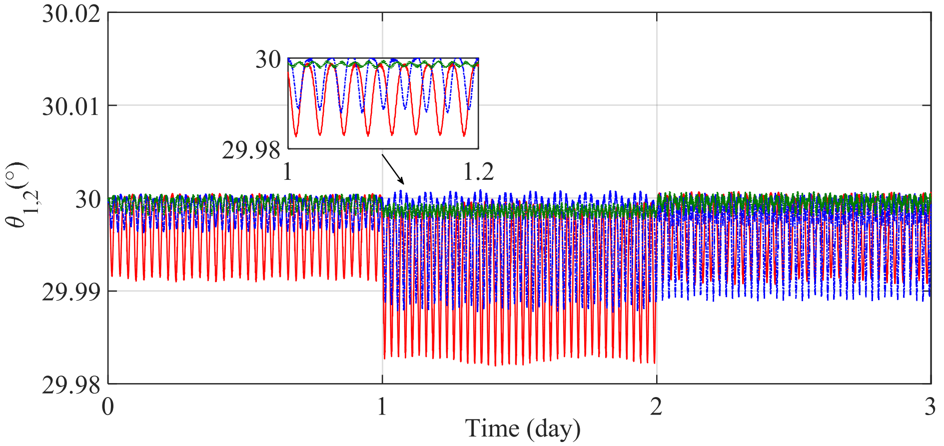

(b) Adjacent angle

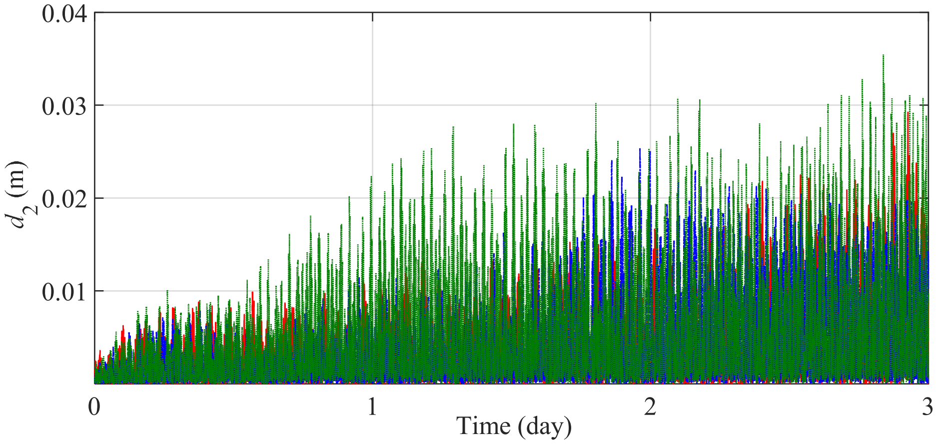

(c) Coplanarity measure for the remote unit

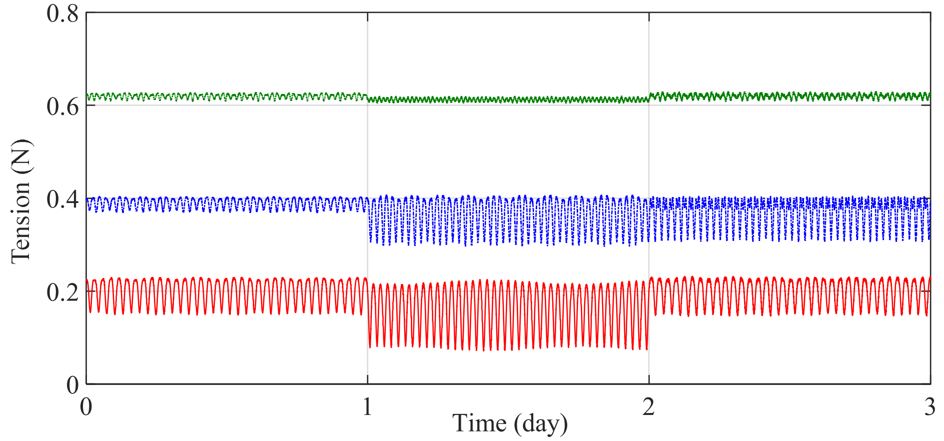

(d) Auxiliary tether tension

Figure 5-4 Time histories of E-sail responses with different spin rate ω subject to solar wind velocity fluctuations.

5.2 Influence of Propulsive Force Magnitude on E-sail Response

As shown in Equation (3.19), three models of propulsive force derived from the PIC simplified analytical model or the empirical model are presented. The application of E-sail requires precise knowledge of external loading and corresponding response. Thus, in this section, the influences of the propulsive force magnitude on the dynamic characteristics of the sail plane coning and attitude motion of E-sail are investigated by varying the coefficient K_i in Equation (3.19) that is, $K_1 = 3.09$ [13], $K_2 = 11.74$ [44], and $K_3 = 56.36$ [47] with the zero initial sail angle. The parameters of the E-sail are kept the same as Table 4-1, and the solar wind velocity (400 km/s) and the main tether voltages (20 kV) are constant. The initial spin rate $\omega_0 = 4 \times 10^{-3}\ rad/s$ is adopted, which is obtained from Section 4.4.2. The total simulation period is 24 h with a time step of 0.01s. The resulting dynamic responses of the E-sail are shown in Figure 5-5 to Figure 5-8.

First of all, Figure 5-5 shows that the magnitude of the propulsive force is directly proportional to the coefficient K_i, while the resulting propulsive force is approximately constant in the short duration of simulation as shown in Figure 5-5(b). This is because the orbital change of the E-sail's CM is negligible compared with the absolute orbital radius. However, the change rate of the E-sail's CM orbital radius is directly proportional to the coefficient K_i, and increases over time as illustrated in Figure 5-5(a). Next, Figure 5-6 shows the influence of the propulsive force magnitude on the sail and thrust angles, which is not noticeable unlike the incremental rate of the orbital radius. Overall, the predicted sail angle increases only by one degree in the negative direction with the three different magnitudes of the propulsive force. This phenomenon is consistent with the result in Figure 4-3(b), which indicates that the variation trend of the sail angle and the propulsive force is independent. At the same time, the variation of the thrust angle is approximately the half of the sail angle under the three different magnitudes of the propulsive force, which is consistent with the results in [14-15, 37] even if their magnitudes of the propulsive force are different. Moreover, the variation trends of the coning angles are qualitatively identical for the three different coefficients K_i as shown in Figure 5-7, although the absolute values of the coning angle are different. Therefore, it can be concluded that the different force magnitudes have a noticeable effect on the radial deformation of the E-sail, but their effects on its attitude are approximately the same.

As mentioned before, the collisions between the main tethers are prevented by the tensions generated by the auxiliary tethers. This means the capability of the auxiliary tethers to maintain the E-sail stability is limited. When the tensions of the auxiliary tethers are zero, the capability will disappear, and the E-sail may be unstable. Meanwhile, Figure 5-7 shows that the coning angle is dependent on the magnitude of the propulsive force. Thus, it is interesting to obtain the maximum allowable coning angle. Recalling Equation (4.23), when the initial spin rate is given, the elongations of the main tether ΔL_0 can be derived from the force balance of between the centrifugal force and the tensions generated by the main and adjacent auxiliary tethers after the E-sail fully deployed, that is,

$$F_{c\_i} = (m_{re} + m_{au})\left(L_0 + \Delta L_0\right)\omega^2 + \int_0^{L_0+\Delta L_0} \rho l \frac{L_0}{L_0 + \Delta L_0}\omega^2 dl \tag{5.3}$$

$$T_i = T_{t\_i} + \left(T_{au\_i} + T_{au\_j}\right)\sin\left(\left(\frac{\pi}{M}\right)\right) \tag{5.4}$$

$$T_{t\_i} = E_k A_m \frac{\Delta L_0}{L_0} \tag{5.5}$$

$$T_{au\_i} = T_{au\_j} = E_{au} A_{au} \frac{\Delta L_{au}}{L_{au}} \tag{5.6}$$

where T_{t_i}, T_{au_i} and T_{au_j} are the tensions generated by the main and adjacent auxiliary tethers, respectively.

Thus, the elongations of the main tether ΔL_0 can be obtained as

$$\Delta L_0 = \frac{m_{eff} L_0 \omega^2}{E_k A_m / L_0 + 4\sin^2\left(\pi/M\right) E_{au} A_{au} / L_{au} - m_{eff}\omega^2} \tag{5.7}$$

Substituting Equation (5.7) into Equation (4.23) yields the maximum coning angle as

$$\beta_{\max} = \arccos\left(L_0 \middle/ \left(L_0 + \frac{m_{eff} L_0 \omega^2}{E_{mt} A_{mt} / L_0 + 4\sin^2\left(\pi/M\right) E_{au} A_{au} / L_{au} - m_{eff}\omega^2} \right) \right) \tag{5.8}$$

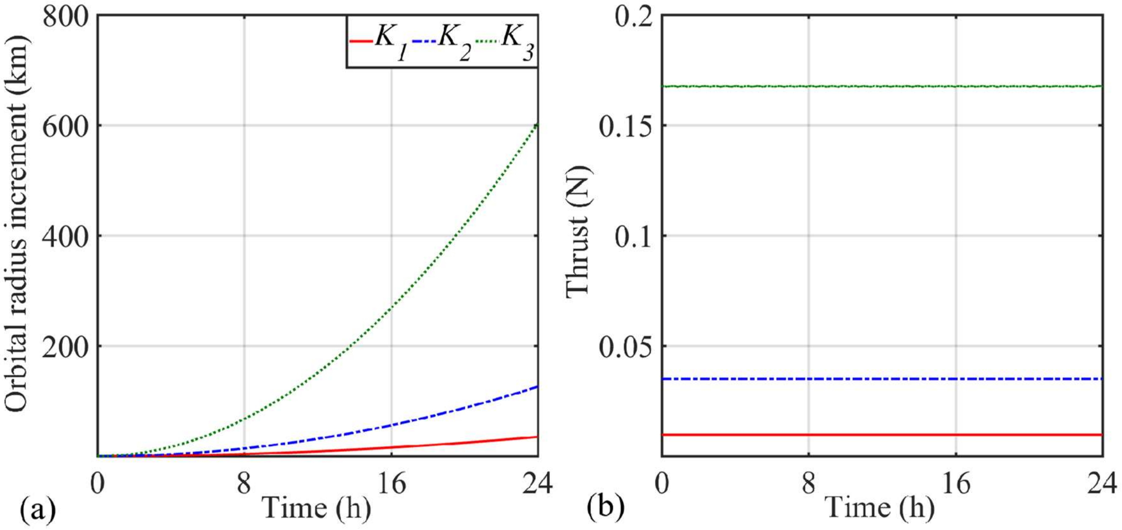

Figure 5-5 Time histories of (a) the increment of orbit radius of the central spacecraft and (b) the E-sail thrust with different coefficients K_i.

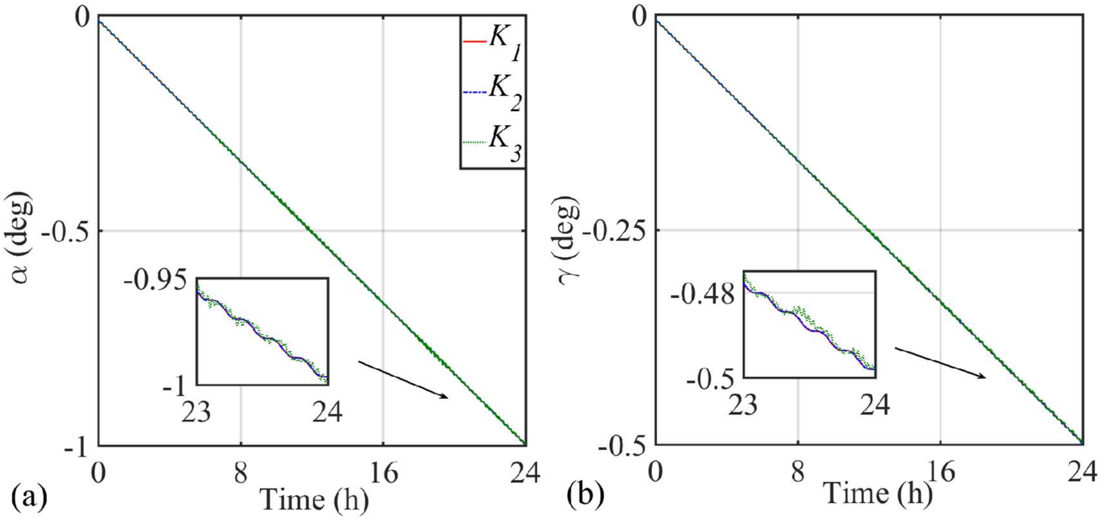

Figure 5-6 Time histories of (a) the sail angle and (b) the thrust angle with different coefficients K_i.

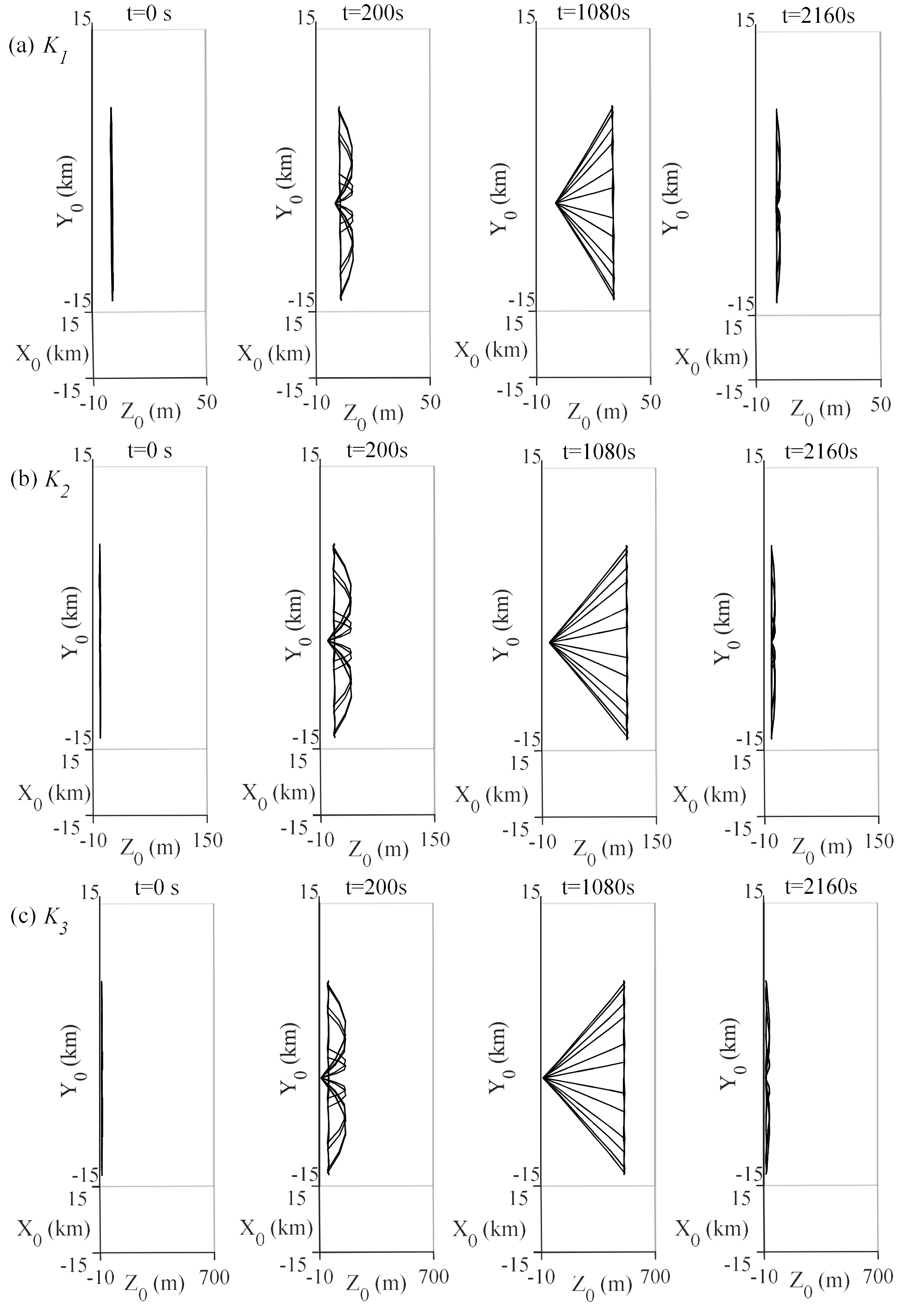

Figure 5-7 Variation trends of the E-sail configuration with different coefficients K_i (a) K_1=3.09 [13] (b) K_2=11.74 [44] and (c) K_3=56.36 [47].

Finally, the influence of the propulsive force magnitude on the geometrical configuration and the E-sail spin rate are investigated. Figure 5-8 shows that the variations of the coning angle and the E-sail spin rate with the three different coefficients K_i. The variation trend of the coning angle in Figure 5-8(a) is similar to the work in Ref. [28], and the difference of the coning motion periods can be explained by Equation (5.8) due to the different magnitudes of the tension acting on the auxiliary tethers. Thus, the assumption of the small coning motion is acceptable because the coning angles shown in Figure 5-8 are very small. It was worth noting that these three coning angles are all less than the maximum coning angle, which means the E-sail configuration is stable. Moreover, the time history of the spin rate ratio (ω/ω_0) under the three different coefficients is depicted in Figure 5-8(b). It shows that the spin ratio is almost the same for all three different coefficients with a variation less than 0.2%, which is caused by the variation of the E-sail coning angle. Therefore, it can be concluded that the influence of the propulsive force magnitude on the E-sail spin rate is negligible. Accordingly, the assumptions of the constant electron density and constant solar wind velocity are acceptable because they only affect the magnitude of the propulsive force.

In summary, the parametric investigation shows that the magnitude of the propulsive force only influences the increment of the orbital radius of the central spacecraft. Its influence on the sail and thrust angles, the coning motion and the E-sail spin rate is negligible. Accordingly, it can be concluded that the variation of the propulsive force model has a negligible effect on the E-sail attitude motion. This offers the convenience for the future E-sail mission analysis. Therefore, the moderate propulsive force coefficient K_2 has been adopted in the rest of study instead of using two extreme values.

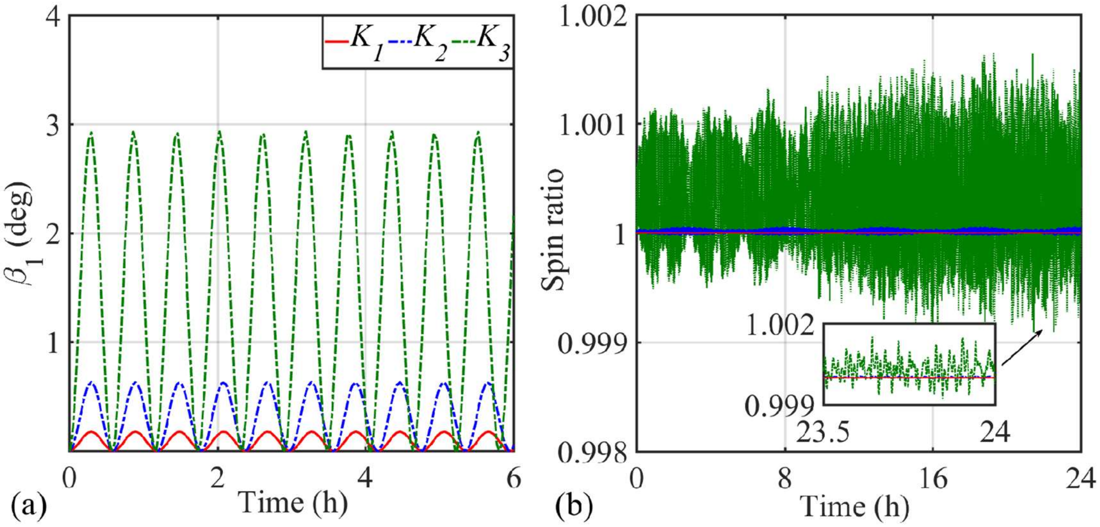

Figure 5-8 Time histories of (a) coning angle and (b) spin rate ratio with different coefficients K_i.

5.3 Influence of the Sail Angle on E-sail Response

The aim of this section is to explore the influence of the change of the E-sail orientation on its dynamics by considering the coning motion. This is done by varying the sail angle at the beginning of the simulation. The sail angle at the beginning of the simulation is referred as the initial sail angle in the following. Three initial sail angles are used to represent these E-sail orientations, that is, $\alpha_0 = 30$, $\alpha_0 = -30$, and $\alpha_0 = -150$ degrees, as illustrated in Figure 5-9. Based on the definition of the sail angle in Section 3.1.2, the sail angles of 30 and -150 degrees represent the same spin plane but in the opposite direction, while the sail angles of 30 and -30 degrees are symmetric with respect to the O_oZ_o direction. The solar wind velocity is assumed constant (400 km/s), and the electrical potential of all main tethers is assumed the same (20 kV) and constant over time. The initial spin rate is $\omega_0 = 4 \times 10^{-3}\ rad/s$ and the rest of the E-sail parameters is the same as Table 4-1. The total simulation period is 24 h with a time step of 0.01s. The responses of the E-sail are presented in Figure 5-10 and Figure 5-11.

Figure 5-10(a) shows that the orbital radius of the central spacecraft increases over time at an increased rate. However, the increments of the orbital radius are different between -30 degree and the other two initial sail angles. The difference increases over time. This can be explained by the circumferential thrust component $\boldsymbol{F}_t \sin\gamma$, which will decrease or increase the tangential velocity of the orbital motion. Moreover, the difference of the thrust in Figure 5-10(b) can also explain the difference of the increments of the orbital radius. Then, the effect of the initial sail angle on the sail and thrust angles is shown in Figure 5-11. The sail angle increases by one degree in the negative direction with the -30 and -150 degrees initial sail angles, while decreases by one degree in the positive direction with the 30 degree initial sail angle. The variation of the thrust angle is approximately the half of the sail angle, while the variation trends are the same with the sail angle.

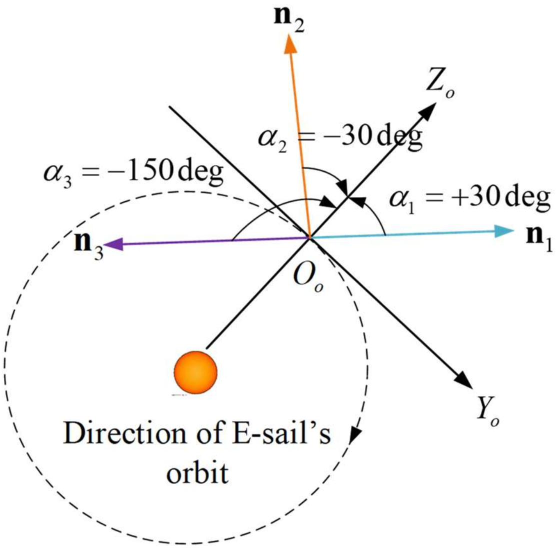

Figure 5-9 E-sail orientation in the orbital plane $O_oY_oZ_o$.

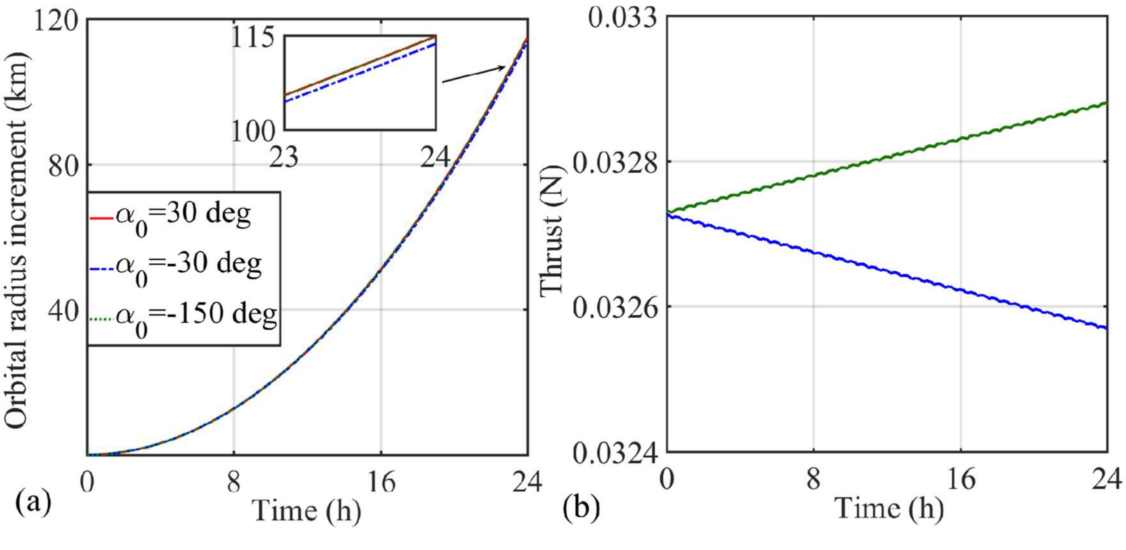

Figure 5-10 Time histories of (a) the increment of orbital radius of the central spacecraft and (b) the E-sail thrust with the different initial sail angles.

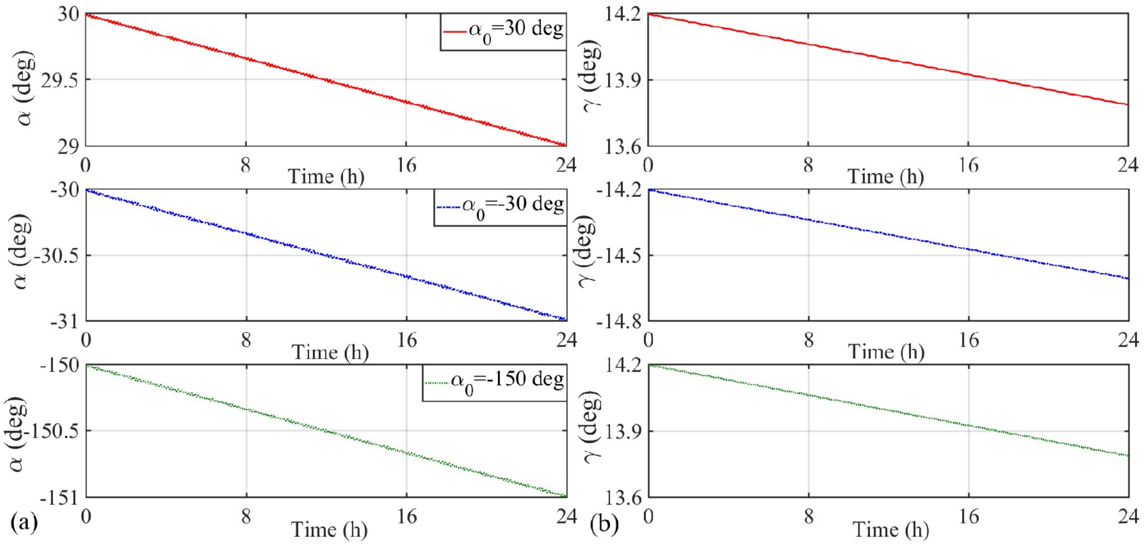

Figure 5-11 Time histories of (a) the sail angle and (b) the thrust angle with the different initial E-sail sail angles.

Furthermore, the impact of the initial sail angle on the thrust vector is evaluated with respect to the selected initial sail angles ranging from 0 to 75 degrees at an increment of 5 degrees. The resulting dynamic responses of the E-sail are shown in Figure 5-12 and Figure 5-13.

Figure 5-12 shows that, as the initial sail angle increases, the orbital radius of the central spacecraft increases over time at a decreased rate. This is because the radial component of the thrust decreases as the initial sail angle increases. The trend of the increment rate is more obvious as the initial sail angle increases. The influences of the initial sail angle on the sail and thrust angles are shown in Figure 5-13. The sail angle decreases over time at a decreased rate by approximately one degree, and the variation trend is approximately the same for different initial sail angles. Unlike the influence of the propulsive force magnitude seen in the previous section, the influence of the initial sail angle on the thrust angle is significant. The trend of the thrust angle decreases first and then increases after the initial sail angle is greater than 55 degrees as the initial sail angle increases.

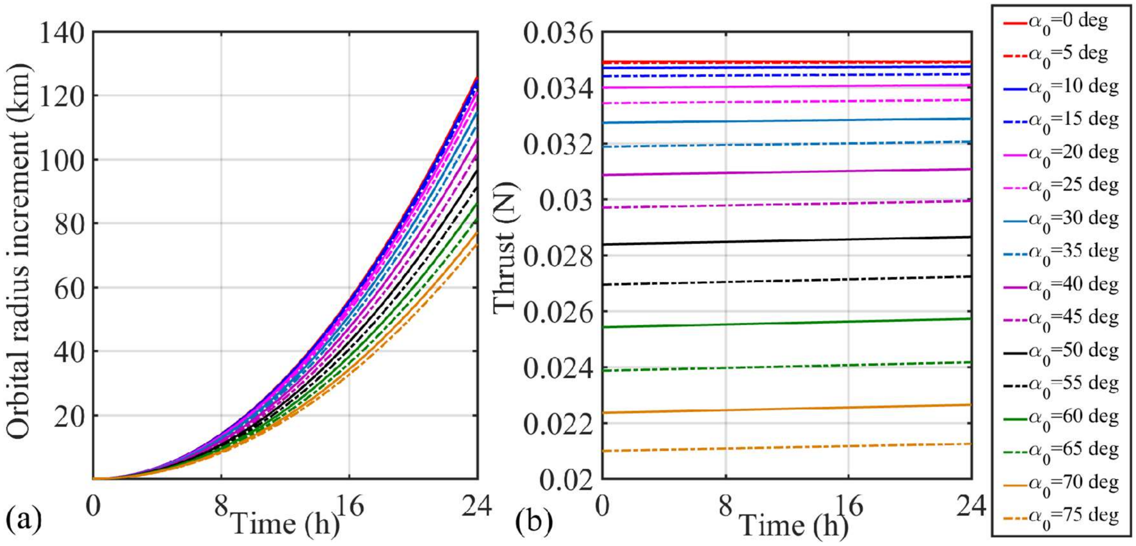

Figure 5-12 Time histories of (a) the increment of orbital radius of the central spacecraft and (b) the E-sail thrust with the different initial sail angles.

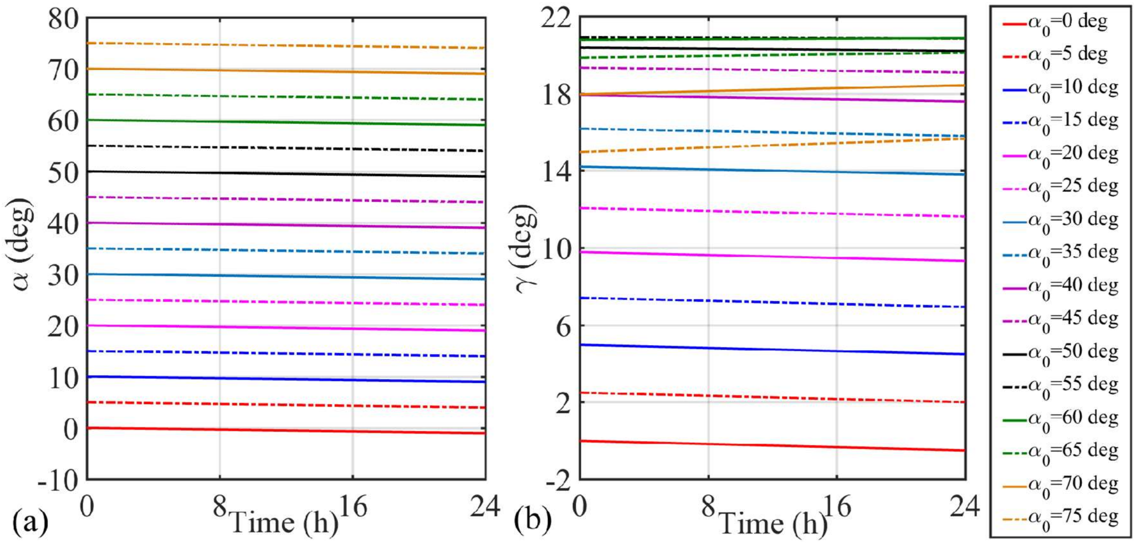

Figure 5-13 Time history of (a) the sail angle and (b) the thrust angle with the different initial sail angles.

In addition, the relationship over time between the sail and thrust angles is derived by a curve-fitting, similar to Ref. [49], that is,

$$\gamma(\mathrm{t}) = \ell_1\alpha^6(\mathrm{t}) + \ell_2\alpha^5(\mathrm{t}) + \ell_3\alpha^4(\mathrm{t}) + \ell_4\alpha^3(\mathrm{t}) + \ell_5\alpha^2(\mathrm{t}) + \ell_6\alpha(\mathrm{t}) + \ell_7 \tag{5.9}$$

where the coefficients ℓ_i $(i = 1, 2, \cdots, 7)$ are listed in Table 5-3.

Table 5-3 Coefficients of the sail and thrust angles relationship.

ℓ_1	ℓ_2	ℓ_3	ℓ_4
8.561×10^{-11}	-2.367×10^{-8}	1.432×10^{-6}	-7.204×10^{-5}

ℓ_5	ℓ_6	ℓ_7
6.573×10^{-4}	4.968×10^{-1}	1.433×10^{-4}

Similarly, the relationship over time between the dimensionless acceleration of the E-sail and the sail angle is derived by a curve-fitting as,

$$\mathrm{a}^{\circ}(\mathrm{t}) = c_1\alpha^6(\mathrm{t}) + c_2\alpha^5(\mathrm{t}) + c_3\alpha^4(\mathrm{t}) + c_4\alpha^3(\mathrm{t}) + c_5\alpha^2(\mathrm{t}) + c_6\alpha(\mathrm{t}) + c_7 \tag{5.10}$$

where the coefficients c_i $(i = 1, 2, \cdots, 7)$ are listed in Table 5-4. Here, a° is the dimensionless acceleration of the E-sail, that is,

$$\mathrm{a}^{\circ}(\mathrm{t}) = \frac{\boldsymbol{F}_t / m_E}{\mathrm{a}_{\square}} \tag{5.11}$$

where m_E is the total mass of the E-sail. Thus, the dimensionless acceleration is independent on the propulsive force model.

Table 5-4 Coefficients of dimensionless acceleration vs sail angle.

c_1	c_2	c_3	c_4
-1.631×10^{-12}	3.693×10^{-10}	-1.908×10^{-8}	4.956×10^{-7}

c_5	c_6	c_7
-1.189×10^{-4}	2.573×10^{-5}	1.0

Finally, Figure 5-14 shows the comparisons between the Equations (5.9) -(5.10) and the results in the Refs. [15, 49], which are derived from the different E-sail models. Figure 5-14(a) shows that the thrust angles predicted by the different models are almost the same, and approximately equal to one-half of the sail angle when the sail angle is less than 30 degrees. As the sail angle increases, the magnitudes of thrust angle predicted by the different models start to deviate but with the same trends, such as increases and then decrease after the sail angle is greater than 55 degrees. The current model gives the different magnitude among the three models. This is because the directions of the normal incident solar wind acting on the tether vary along the tether length due to the coning motion and deformation of the tether in current model, while the directions are the same for an ideally flat E-sail model.

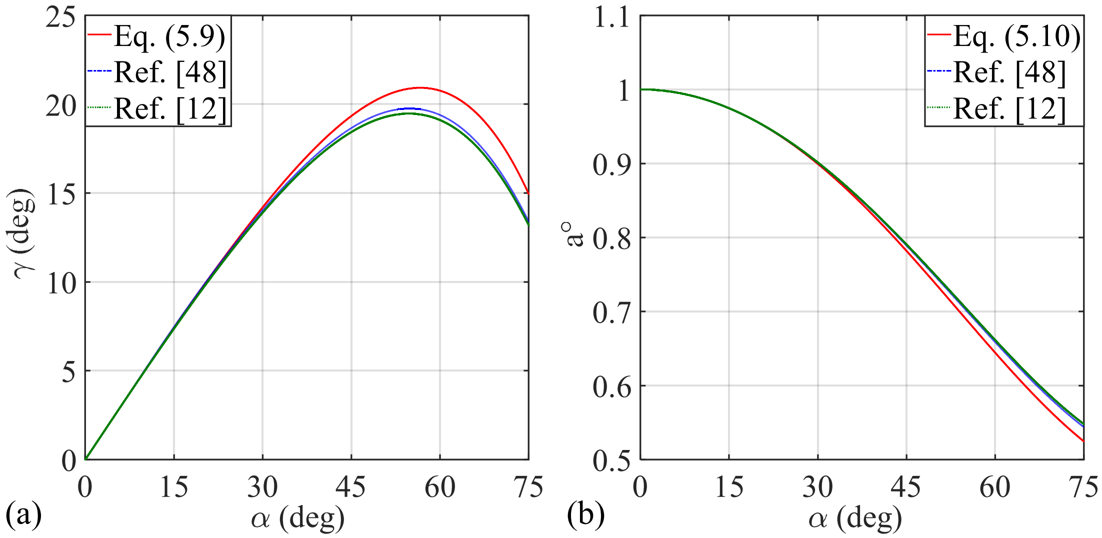

Figure 5-14 (a) Thrust angle vs sail angle, (b) dimensionless acceleration vs the sail angle.

The other reason is that these three models use different propulsive force models, where the current work uses the generalized model (3.19) while the other two use the simplified model as shown in Equation (3.16). Therefore, the resultant thrust vectors are different among the three models. The difference in magnitudes among the three models is exceedingly small, due to the small coning angle, deformation of the tether, and propulsive force around 1 au. The comparison of the dimensionless acceleration has the similar trends as presented in Figure 5-14(b) without the consideration of coning motion, which indicates the coning motion has insignificant impact on the macro dynamic behaviors.

In summary, the parametric analysis shows that the change of sail angle has significant influences on both the thrust vector and the sail angle variation, while has negligible effect on the macro dynamic behaviors of E-sail.

Chapter 6 PARAMETRIC ANALYSES OF THE GENERALIZED E-SAIL MODEL

Summary: In this chapter, the rigid-flexible coupling effect on the attitude dynamics and spin control of E-sail is investigated by using the rigid-flexible coupling high-fidelity model developed in Section 3.4. Based on the generalized E-sail model, the influence of the E-sail orientation, solar wind fluctuations, and geometrical configuration on the dynamic characteristics of the E-sail is investigated by a parametric analysis. Furthermore, the spin rate of the E-sail can be controlled to the desired value with finite time by a simple control law, even in the tether deployment process, with finite control input mainly at the remote units. Finally, some conclusions are given in this chapter.

6.1 Dynamic Response of E-sail with Different Attitudes

In this section, the influence of the E-sail attitude with respect to the solar wind direction on its dynamics is investigated by varying the sail angle. As shown in Figure 6-1, two sail angles, $\alpha = 0\,\text{deg}$ and $\alpha = 30\,\text{deg}$ are adopted in the analysis. The E-sail parameters are consistent with Table 4-2, and the E-sail configuration is Type II. The electric potential of all main tethers and the solar wind velocity are also the same as in Ref. [13], and the coefficient of

$K_2 = 11.74$ is used. The simulation results are presented in Figure 6-2 to Figure 6-7.

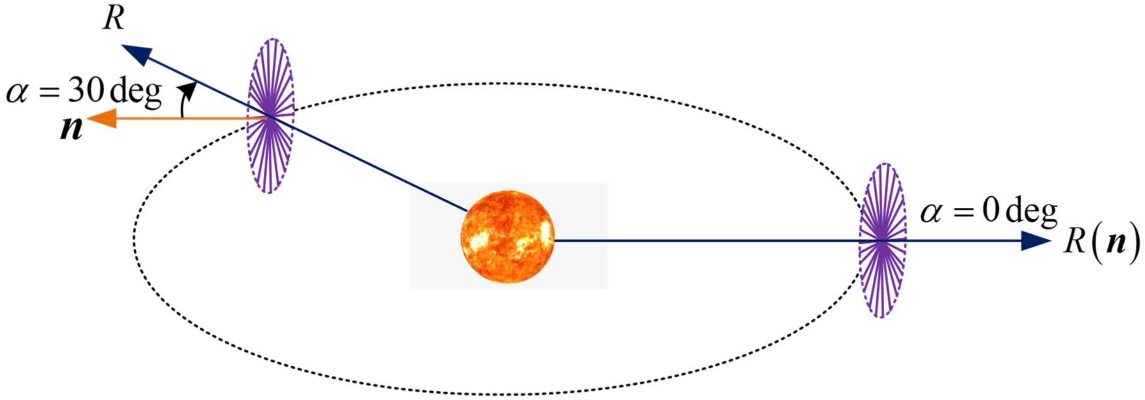

Figure 6-1 E-sail attitude with different sail angles.

First, Figure 6-2(a) indicates that the Sun-E-sail distance increases over time in both cases but at different rates. The higher increase rate leads to the larger deformation of main tethers. This is because the zero sail angle generates the greater propulsive force than the 30-degree sail angle, and this is the same as the phenomenon in Ref. [27]. Figure 6-2(b) shows the in-plane periodic libration of main tethers, where the libration in zero sail angle is greater than the 30-degree sail angle. The smaller in-plane libration angle, the better stability of the E-sail system. At the same time, the angular velocities of the central spacecraft are affected by the fluctuation of tensions caused by the deformation of tethers as indicated by Equation (3.84). Because the central spacecraft rotates coaxially with the E-sail system, the E-sail will be stable if the central spacecraft only rotates on the X_{cb} axis and the angular velocities of the other two axes are zero. Accordingly, Figure 6-3 shows the component of spin rate in X_{cb}-axis ω_{cb_x} of the central spacecraft fluctuates periodically in the same phase, where the magnitude of zero sail angle is greater than that of 30 degree sail angle. Comparing with Ref. [28], it should be noted that the variation trend of the ω_{cb_x} is different, where the tether of the E-sail was modeled as a dumbbell model and did not catch the high mode of tether libration relative to the radial direction. However, unlike the variation trend of the ω_{cb_x}, the variation trends of the ω_{cb_y} and the ω_{cb_z} in the two cases are different because the non-zero sail angle generates a small offset between the CM and CT of the E-sail.

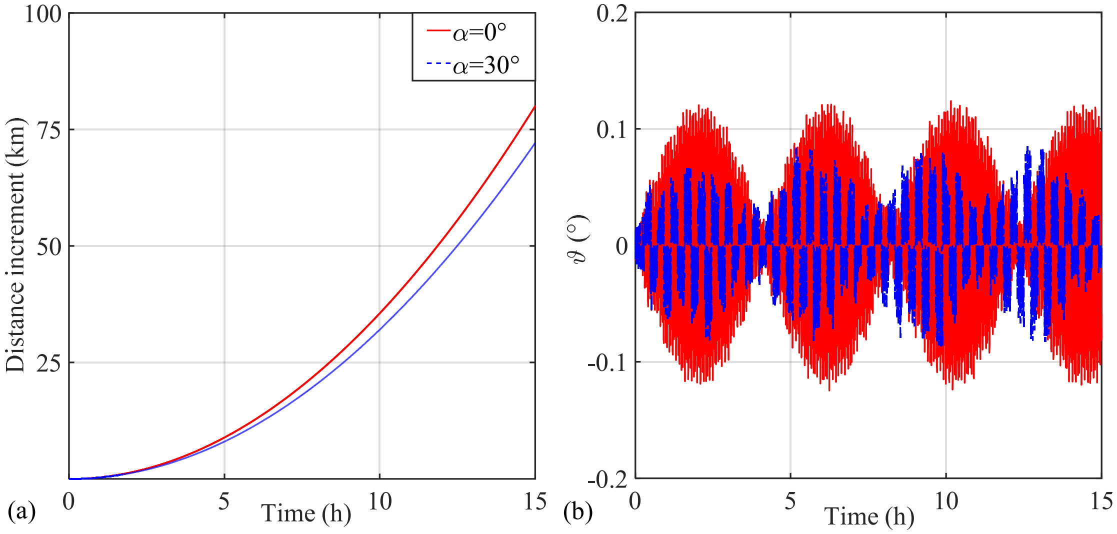

Figure 6-2 Time histories of (a) the Sun/E-sail distance increment (b) in-plane libration angle with different sail angles.

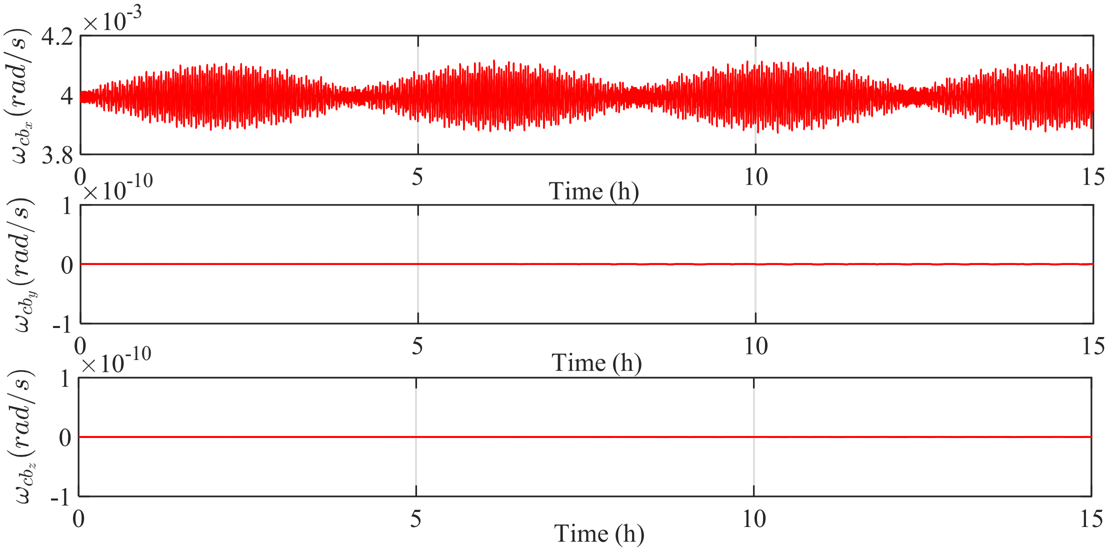

(a) $\alpha = 0^{\circ}$

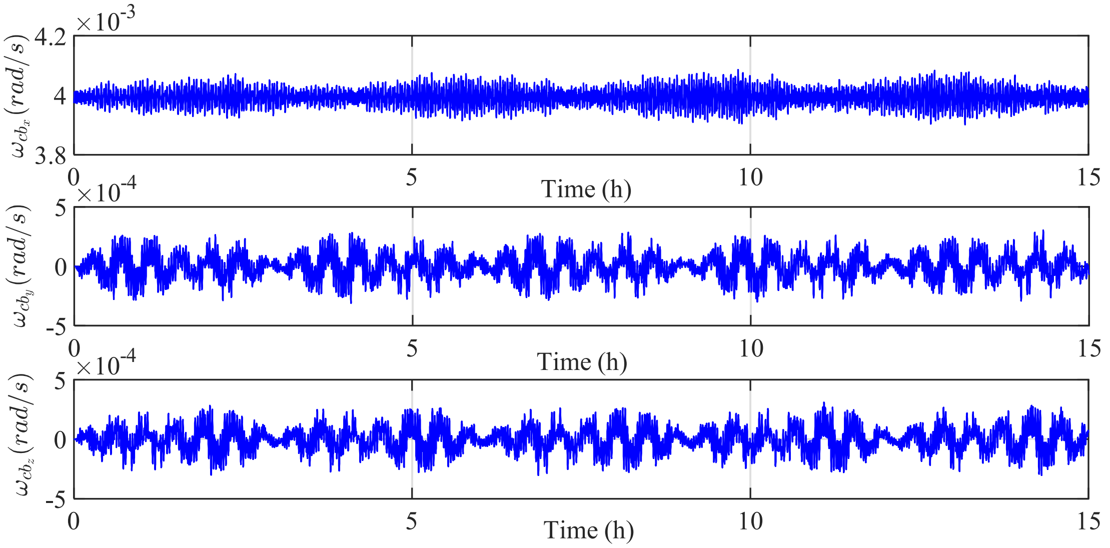

(b) $\alpha = 30^{\circ}$

Figure 6-3 Time histories of angular velocities of the central spacecraft in the $O_{cb}X_{cb}Y_{cb}Z_{cb}$ coordinate system with different sail angles.

Next, the variation of the angular velocities of the central spacecraft is further explained by examining the resultant propulsive force generated by the positively charged main tethers. Figure 6-4 shows that the resultant propulsive force components F_{cb_x} in two cases maintain the periodic oscillation due to the influence of the coning motion of tethers. The analytical expression of the periodic coning motion oscillation has been derived in the previous work [27]. The different magnitudes are mainly caused by the non-zero sail angle, where the resultant propulsive force components F_{cb_x} decreases as the sail angle increases. Meanwhile, the resultant propulsive force components F_{cb_y} and F_{cb_z} in the case of zero sail angle are zero as expected, while periodically oscillates in the case of 30 degrees sail angle.

Furthermore, Figure 6-5 illustrates the variation trends of the CM and the CT of the E-sail. It indicates that the CM oscillates in the X_{cb} axis due to the coning motion of the E-sail. The CT of the E-sail varies within the $O_{cb}X_{cb}Y_{cb}$ plane with the 30 degrees sail angle, while maintains zero with the zero sail angle, respectively. Compared with Refs. [8-9], the variation magnitudes of the E-sail's CM and CT are much greater than that of solar sail due to the much larger structure, which leads to the precession and nutation motions of the E-sail much greater.

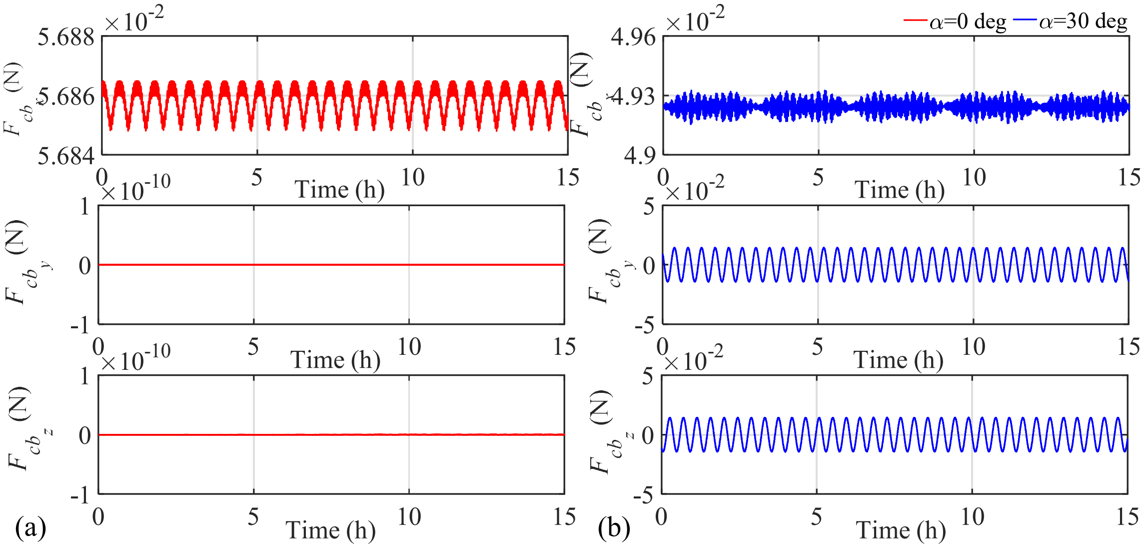

Figure 6-4 Time histories of (a) and (b) the E-sail resultant propulsive force components in the $O_{cb}X_{cb}Y_{cb}Z_{cb}$ coordinate system with different sail angles.

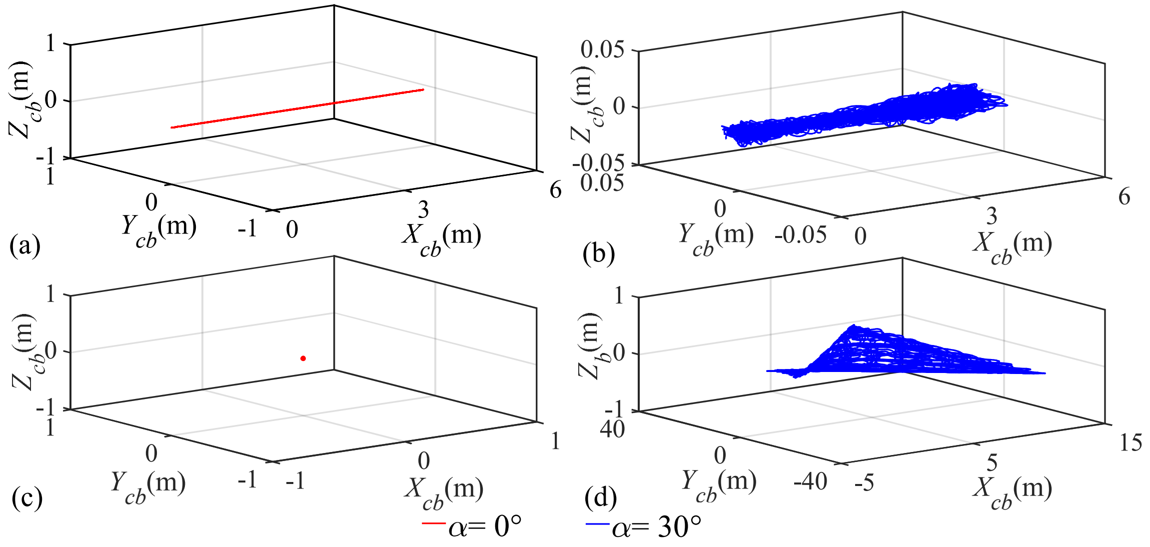

Figure 6-5 Time histories of the CM (a) and (b) and the CT (c) and (d) of the E-sail in the $O_{cb}X_{cb}Y_{cb}Z_{cb}$ coordinate system with different sail angles.

Finally, Figure 6-6(a) and (d) show the variation trends of tensions in the main and auxiliary tethers and the periodic oscillation of coning angle, respectively. This is because the propulsive force generates a torque that pushes the main tether rotating out of the nominal spin plane with respect to the central spacecraft, and the centrifugal forces due to the inertia of the main tether and the remote unit generates a restoring torque to pull the main tether back to the spin plane, see Section 4.3.1. Moreover, Figure 6-7 shows the variation trends of the E-sail geometrical configuration related to the coning motion. Through the simulation results of Figure 6-2 and Figure 6-7, it can be concluded that the nonlinear rigid-flexible coupling motions of E-sail have a prominent impact on the attitude of the central spacecraft. Figure 6-6(b) illustrates that the variation trends of the E-sail spin rates in the two cases are within a small scale. The variation of the spin rate can be explained by the changing of the E-sail CM along the X_{cb} axis. The magnitudes of the spin rate in the two cases are approximately the same because the dominant moment of inertia of the E-sail is along the principal spin axis, which aligns with the unit spin vector direction. Thus, we can conclude that the E-sail spin rate is robust against the disturbance torques if it is sufficient large. Moreover, Figure 6-6(c) shows the variation trend of the nutation angle, which can also be explained by Equation (3.83) due to the effect of the disturbance torque. If the nutation angle maintain zero, the E-sail configuration will be stable. Thus, it means that the E-sail configuration that considers the attitude motion of the central spacecraft may unstable at a non-zero sail angle.

In summary, it is found that the deformation motion of flexible tethers will cause the offset of CM and thrust of E-sail, which generates disturbance torques on the central spacecraft. Through the nonlinear rigid-flexible coupling, the disturbance causes the tension fluctuations and the undesired fluctuations of the E-sail's attitude and spin rate.

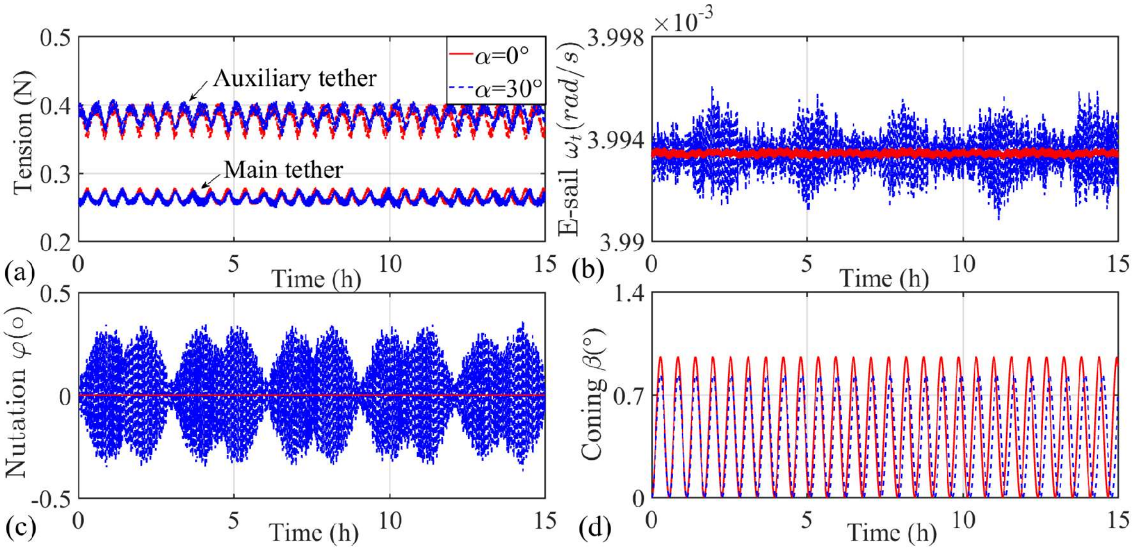

Figure 6-6 Time histories of (a) tension in the main and auxiliary tethers (b) E-sail spin rate (c) nutation angle and (d) coning angle with different sail angles.

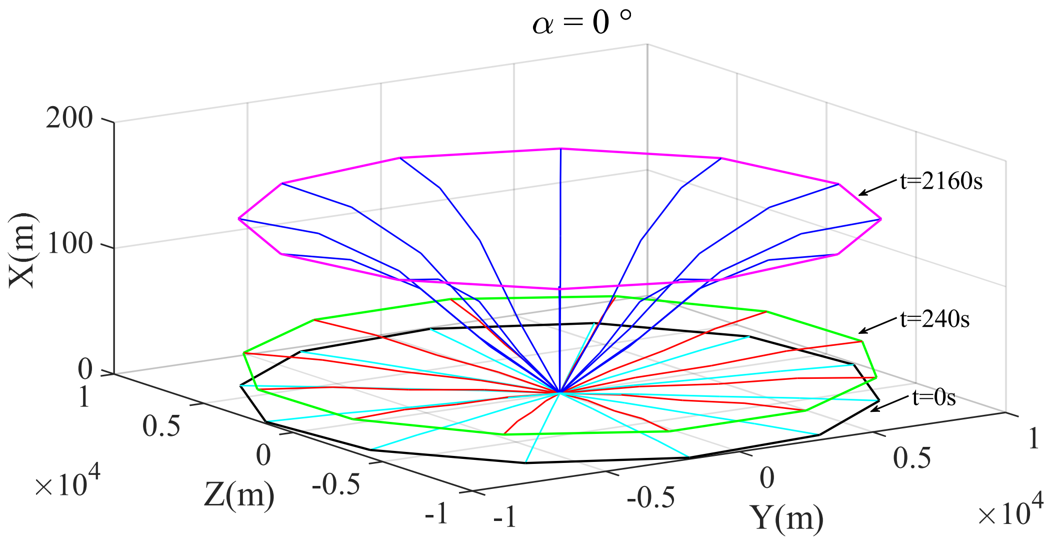

Figure 6-7 Variation trends of the E-sail configuration.

6.2 Dynamic Response of E-sail with Different Configurations

The aim of this section is to further investigate the influence of the offset between the CM and CT of the E-sail by varying the position of the spin plane with respective to the CM of the central spacecraft. As shown in Figure 3-3, three different E-sail configurations are considered here, that is, Type I, Type II and Type III with the sail angle being $\alpha = 30^\circ$. The E-sail parameters are kept the same as shown in Table 4-2, The electric potential of all main tethers and the solar wind velocity are also the same as in Ref. [12], and the coefficient of $K_2 = 11.74$ is used. In such configurations, it is important to understand the effect of the nonlinear coupling between the central spacecraft attitude dynamics and coning motion oscillation of tethers on the stability of the E-sail. Then, the useful standards for designing a spinning E-sail are introduced. The resulting dynamic responses of the E-sail are shown in Figure 6-8 to Figure 6-12.

Figure 6-8 shows that the influences of the different E-sail configurations on the increment of the Sun-E-sail distance and the in-plane periodic libration of main tethers are negligible. The same phenomenon is also presented in the spin rate component ω_{cb_x} of central spacecraft as shown in Figure 6-9, and the resultant propulsive force components F_{cb_y} and F_{cb_z} as illustrated in Figure 6-10, respectively. However, the magnitudes of the spin rate components ω_{cb_y}, ω_{cb_z} and the resultant propulsive force component F_{cb_z} of Type I and Type III configurations are much greater than that of Type II configuration. This difference can be explained by the different magnitude of the E-sail's CM along the Y_{cb} and Z_{cb} axes, while the variation of the CT is approximately the same for all three configurations as shown in Figure 6-11. It should be noted that the angular velocities of the central spacecraft in the Y_{cb} and Z_{cb} may make the E-sail unstable, as presented in Section 6.1. Accordingly, it can be concluded that the Type II configuration of the E-sail is more stable than the other two configurations. Furthermore, Figure 6-12 shows that the influence of the different configurations on the tensions of the main and auxiliary tethers, the E-sail spin rate, and the coning motion of tethers is negligible. The only difference is the magnitude of the nutation angle, which is caused by the difference of the CM of the E-sail configuration. The smallest nutation angle occurs at the Type II compared with the other two configurations, which indicates the Type II is more stable among three configurations. Because if the nutation angle is non-zero, the main tether may wrap around the central spacecraft and destabilize the E-sail configuration.

In summary, it is suggested that the spin plane of the E-sail should pass through the CM of central spacecraft for better stability to avoid the potential tether wrapping around the central spacecraft. The best E-sail configuration among the three configurations is the Type II configuration.

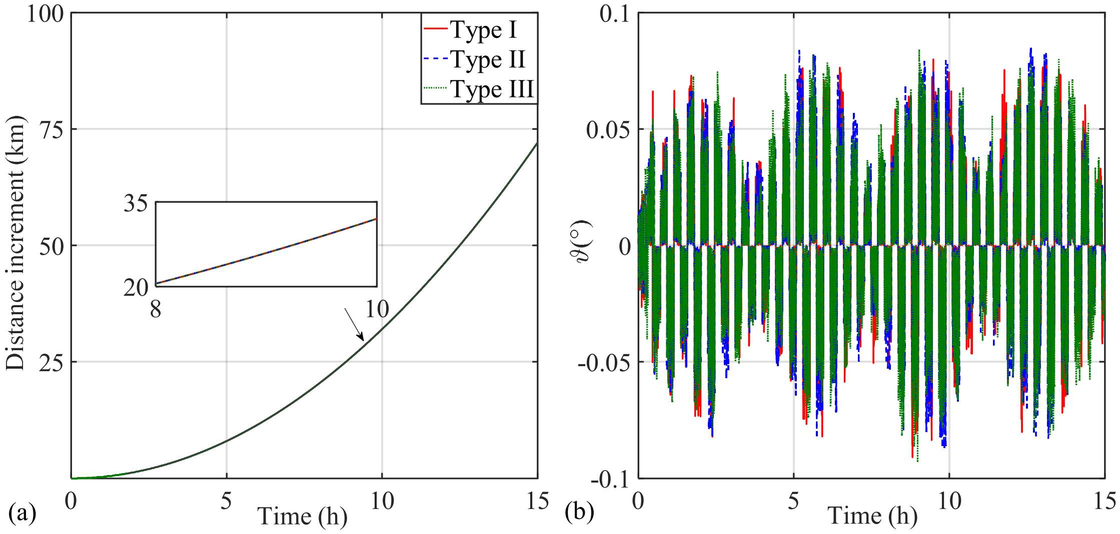

Figure 6-8 Time histories of (a) the Sun/E-sail distance increment (b) in-plane libration angle with different configurations.

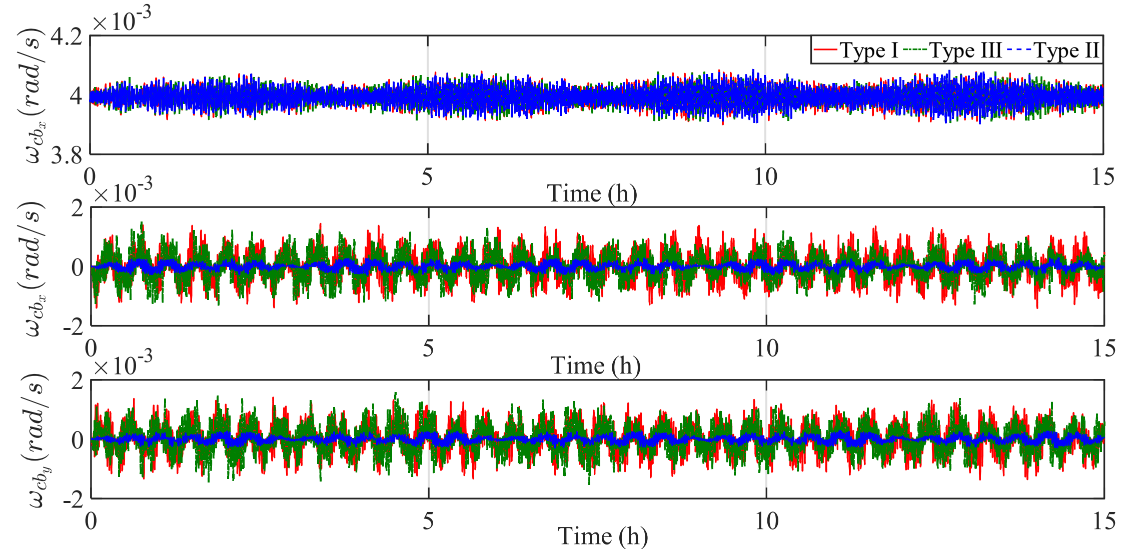

Figure 6-9 Time histories of angular velocities of the central spacecraft in the $O_{cb}X_{cb}Y_{cb}Z_{cb}$ coordinate system with different configurations.

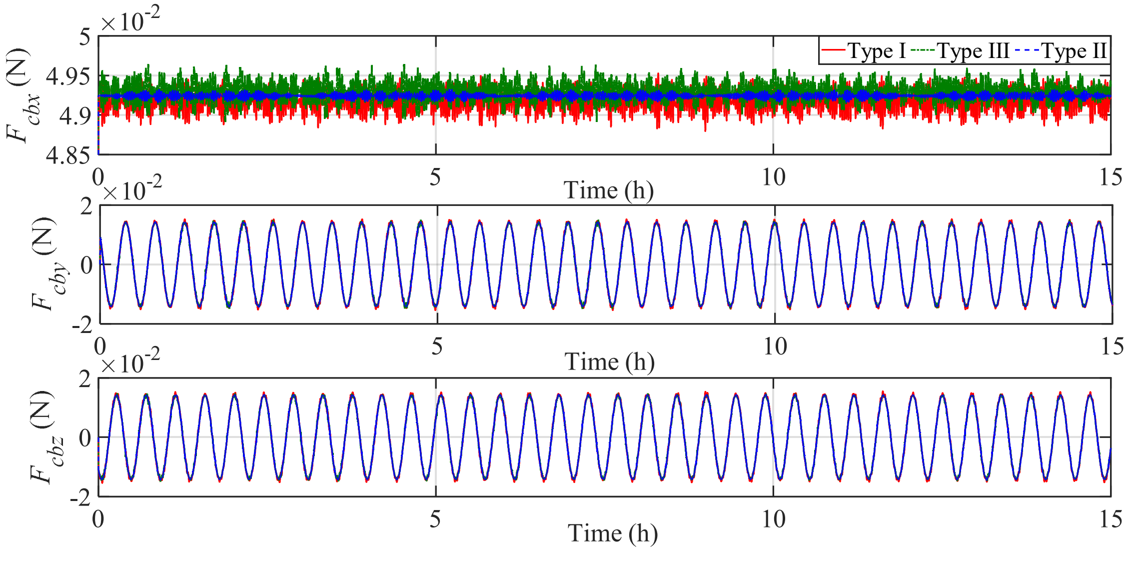

Figure 6-10 Time histories of the E-sail resultant propulsive force components in the $O_{cb}X_{cb}Y_{cb}Z_{cb}$ frame with different configurations.

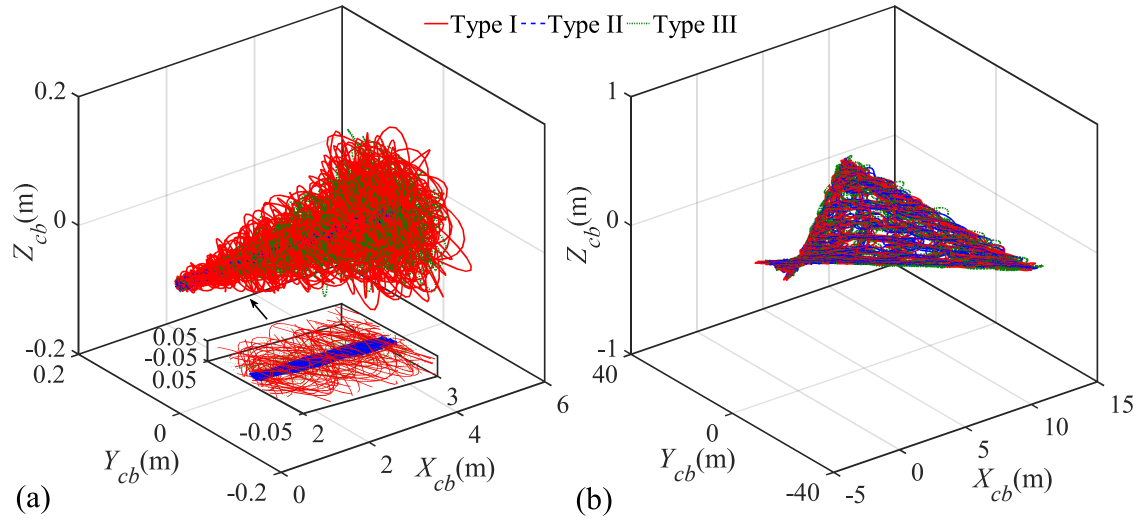

Figure 6-11 Time histories of (a) CM and (b) CT of the E-sail in the $O_{cb}X_{cb}Y_{cb}Z_{cb}$ coordinate system with different configurations.

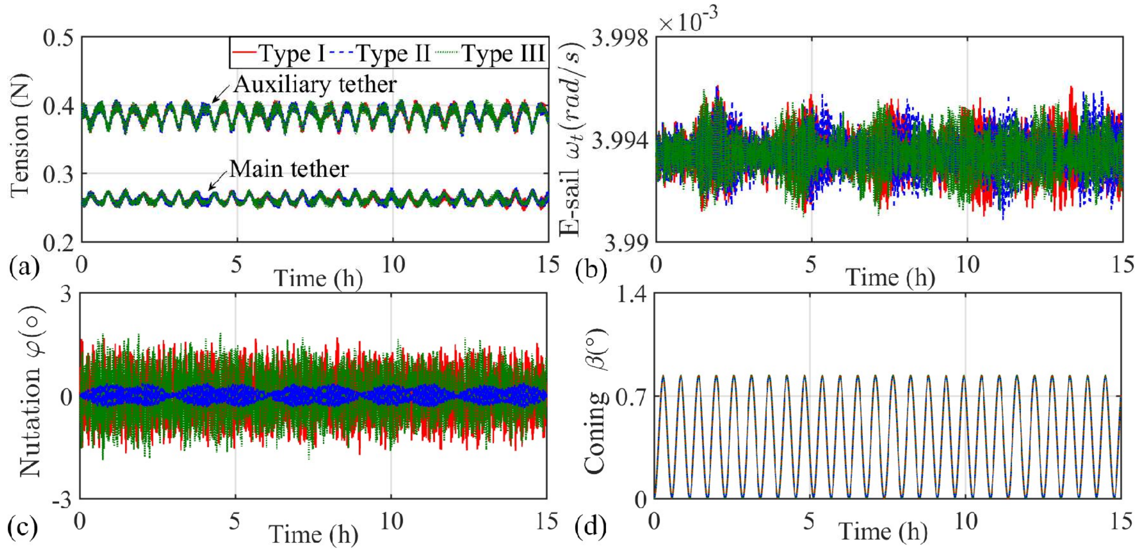

Figure 6-12 Time histories of (a) tension in main and auxiliary tethers (b) spin rate (c) nutation angle and (d) coning angle of the E-sail with different configurations.

6.3 Dynamic Response of E-sail with Solar Wind Fluctuations

The aim of this section is to investigate the influence of the solar wind fluctuations on the stability of the E-sail. This can be done by varying the solar wind velocity during the simulation period based on the solar wind velocity measurement of Voyager 2, as presented in Figure 1-6. The E-sail parameters are consistent with the Section 6.2. Type II configuration of the E-sail is considered. The only difference is that the magnitude of the solar wind velocity is no longer a constant value, see Table 6-1. Here, the influence of the symmetric/asymmetric configuration of the E-sail on the E-sail's stability is studied. The solar wind velocity is assumed to be 400 km/s on the first 5 hours, 800 km/s on the second 5 hours, and 400 km/s again on the third 5 hours. The total simulation period is three days with a time step of 0.01s.

Table 6-1 Parameters of the parametric investigation.

Label	Solar wind velocity (*km/s*)	Number of main(auxiliary) tethers
Case A	400	12(12)
Case B	400-800-400	12(12)
Case C	400	11(11)

6.3.1 Influence of Solar Wind Fluctuations on E-sail Dynamic Performance

The aim of this section is to investigate the influence of the solar wind fluctuations on the dynamic responses of E-sail. The simulation results are shown in Figure 6-13 to Figure 6-17. Figure 6-13(a) shows that the Sun-E-sail distance increases over time in both cases but at different rates. This can be explained by the fact that the case B generates the greater propulsive force than the case A in the second 5 hours, as shown in Figure 6-14, which leads to higher increase rate and larger coning motion of main tethers. The increment of the resultant propulsive force can be explained by Equation (3.19) due to the increase of the solar wind velocity. Meanwhile, the periodic oscillation of the resultant propulsive force components F_{cb_y} and F_{cb_z} in the second 5 hours can be explained by the influence of the coning motion. The fluctuation of the propulsive force caused by the solar wind fluctuations in case B will affect the angular velocity of the central spacecraft as presented in Equation (3.83). At the same time, the greater tensions due to the larger deformation of main tethers will result in the greater in-plane libration of main tethers based on Equation (3.84), as shown in Figure 6-13(b). As mentioned before, the E-sail may unstable if the in-plane libration angle is non-zero. Accordingly, the angular velocity of the central spacecraft in the three axes have greater amplitude of the oscillation as shown in Figure 6-15. Greater angular velocities of the Y_{cb_y} and Z_{cb_z} axes mean that the E-sail is more unstable. This can also be explained by the offset between the CM and CT of the E-sail as presented in Figure 6-16, where the variation magnitudes of the E-sail's CM and CT in case B are much greater than that of case A due to the solar wind fluctuations. It will also lead to the greater precession and nutation motions of the E-sail.

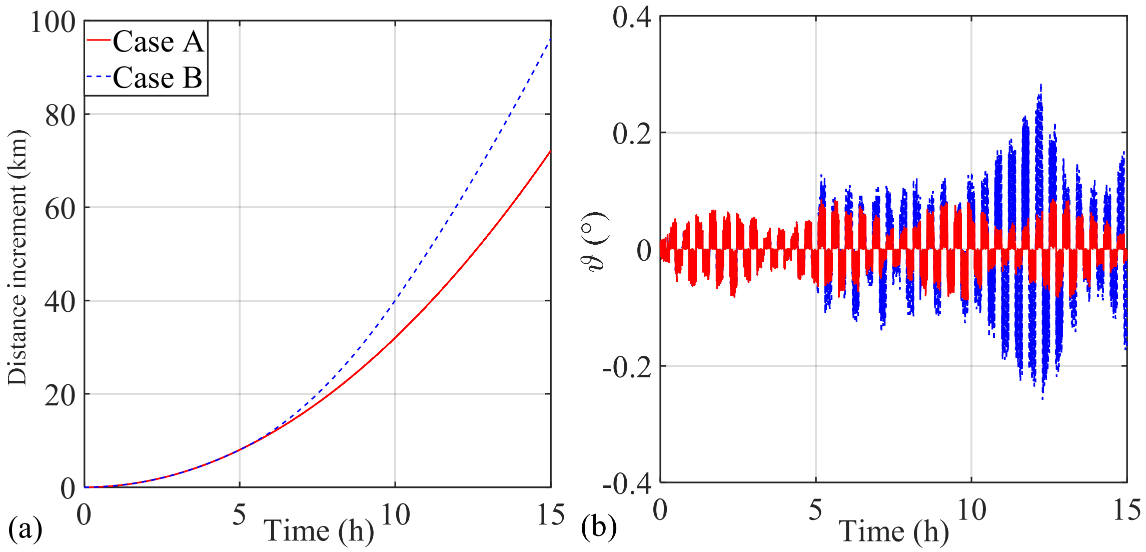

Figure 6-13 Time histories of (a) the Sun/E-sail distance increment (b) in-plane libration angle with the solar wind fluctuations.

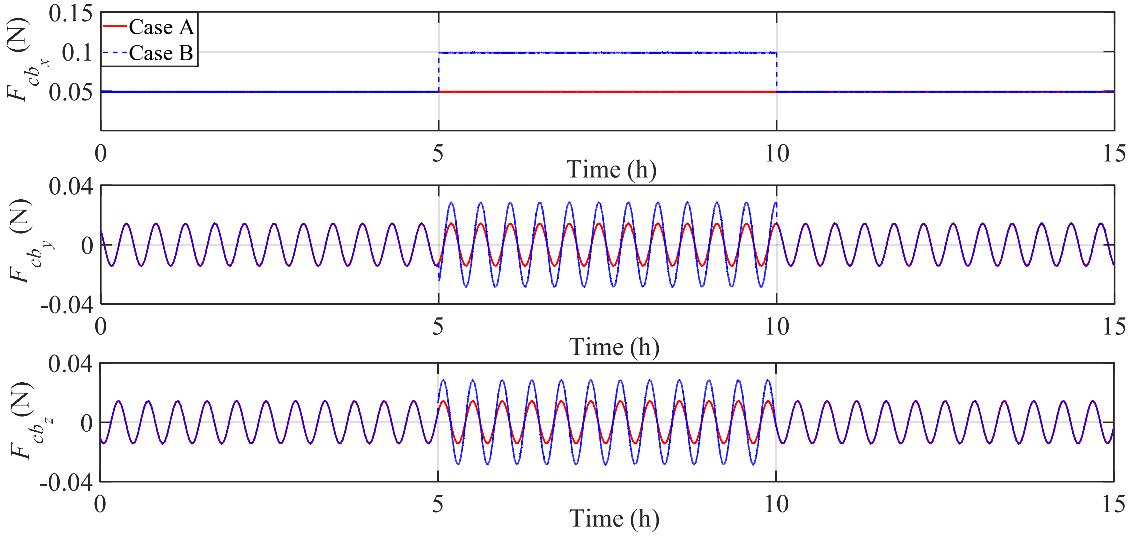

Figure 6-14 Time histories of the E-sail resultant propulsive force components in the $O_{cb}X_{cb}Y_{cb}Z_{cb}$ frame with the solar wind fluctuations.

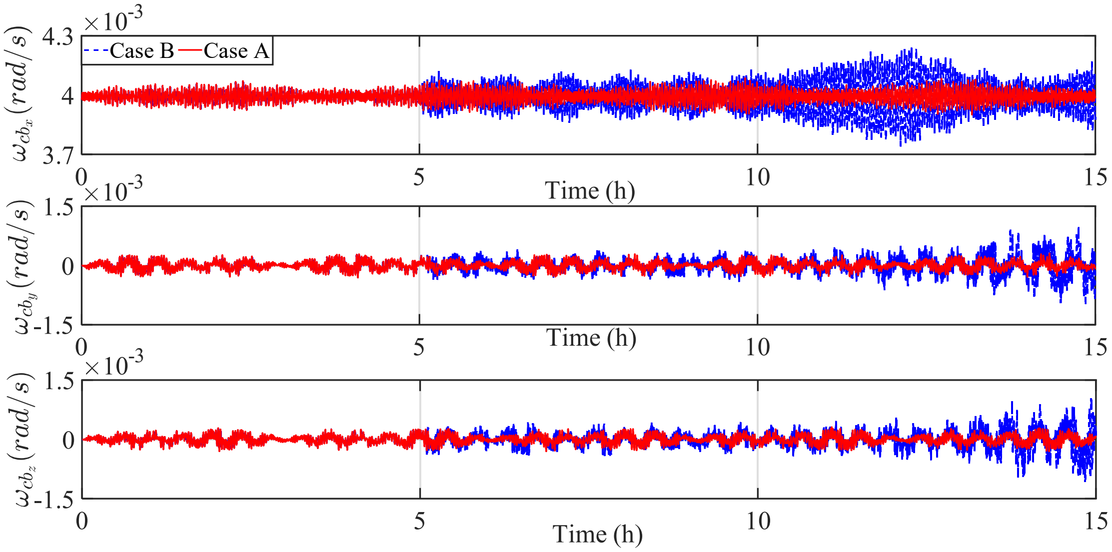

Figure 6-15 Time histories of angular velocity of the central spacecraft in the $O_{cb}X_{cb}Y_{cb}Z_{cb}$ frame with the solar wind fluctuations.

Furthermore, Figure 6-17(a) and (d) show the variation trends of tensions in the main and auxiliary tethers and the periodic oscillation of coning angle, respectively. This is because the greater resultant propulsive force of case B shown in Figure 6-14 generates a greater torque to push the main tethers rotating out the spin plane with respect to the central spacecraft, which leads to the greater elongation and coning motion of tethers. As shown in Figure 6-17(b), the small variation of the E-sail spin rate can also be explained by the changing of the E-sail CM along the X_{cb} axis. The magnitude of the spin rate in case B is slightly larger than that of case A, which can also demonstrate that the E-sail with axisymmetric configuration is robust against the solar wind fluctuations. Moreover, Figure 6-17(c) shows the variation trends of the nutation angles as indicated in Equation (3.84) due to the influence of the disturbance torque. Through the simulation results, it can be concluded that the influence of the solar wind fluctuations on the attitude of the central spacecraft is noticeable, while the influence on the E-sail spin rate is negligible. Thus, the spin rate of the central spacecraft should be controlled to be consistent with the E-sail spin rate to maintain stability of the E-sail.

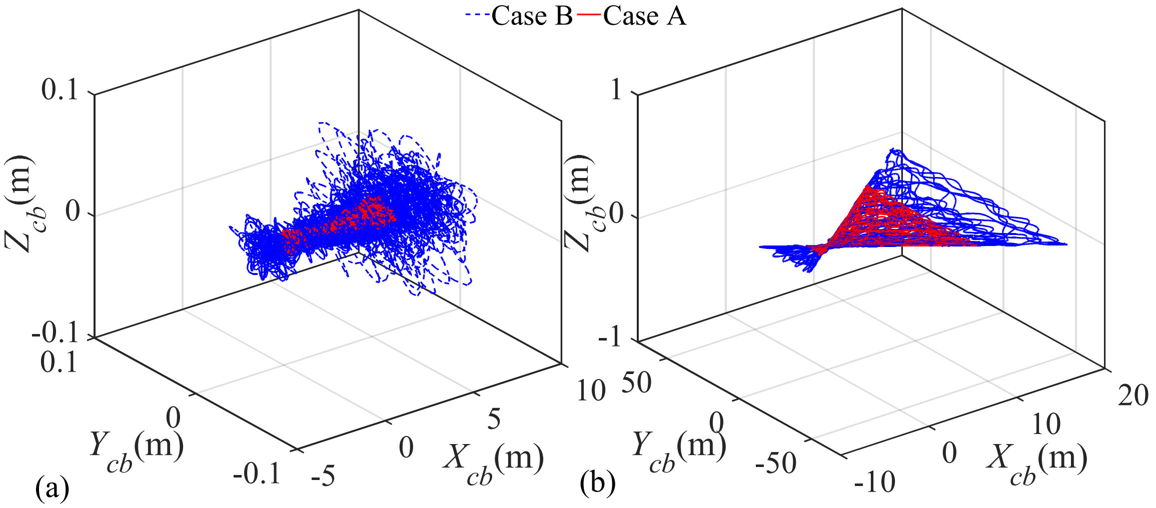

Figure 6-16 Time histories of (a) CM and (b) CT of the E-sail in the $O_{cb}X_{cb}Y_{cb}Z_{cb}$ frame with the solar wind fluctuations.

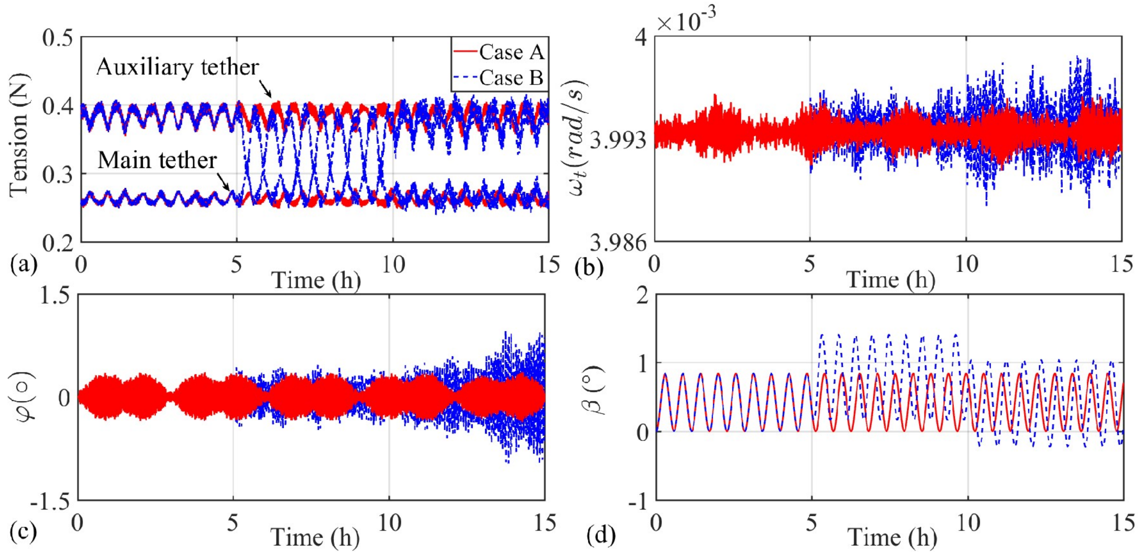

Figure 6-17 Time histories of (a) tension in main and auxiliary tethers (b) spin rate (c) nutation angle and (d) coning angle of the E-sail with the solar wind fluctuations.

6.3.2 Influence of Geometrical Configuration on E-sail Dynamic Performance

The aim of this section is to further study the effect of the offset between the CM and CT of the E-sail by setting the E-sail to an asymmetric configuration. This can be achieved by removing one main tether. Two cases are considered here to investigate the dynamic responses of E-sail, that is, Cases A and C. In such configurations, the E-sail is a symmetric configuration that consists of 12 main tethers with 12 connected auxiliary tethers, while the E-sail is an asymmetric configuration that consists of 11 main tethers with 11 connected auxiliary tethers. The solar wind velocity is assumed constant, and the rest of the E-sail parameters are kept the same as presented in Table 4-2. The resulting dynamic responses are shown in Figure 6-18 to Figure 6-22.

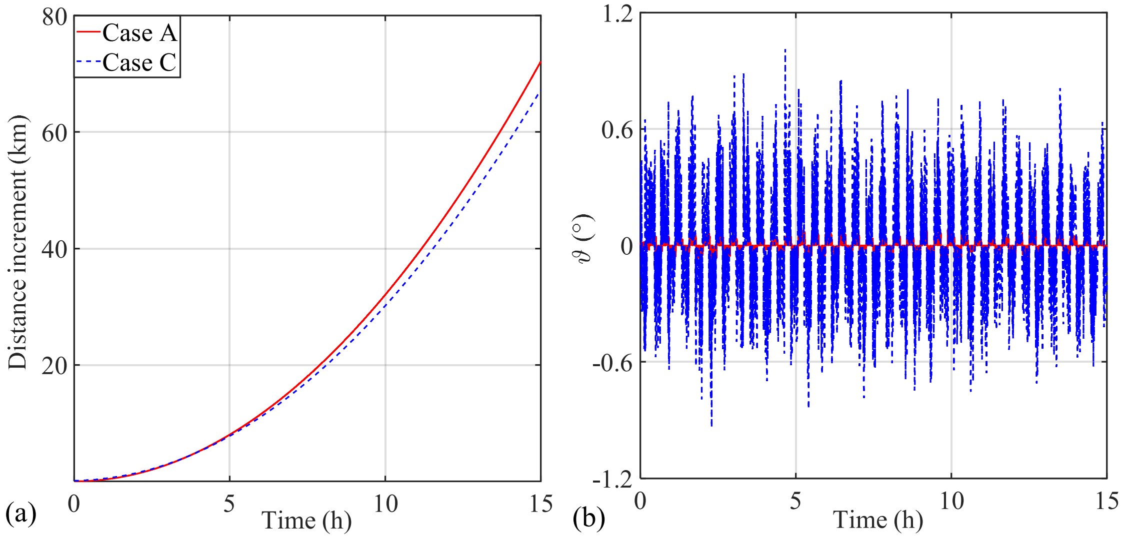

Figure 6-18 Time histories of (a) the Sun/E-sail distance increment (b) in-plane libration angle with different configurations.

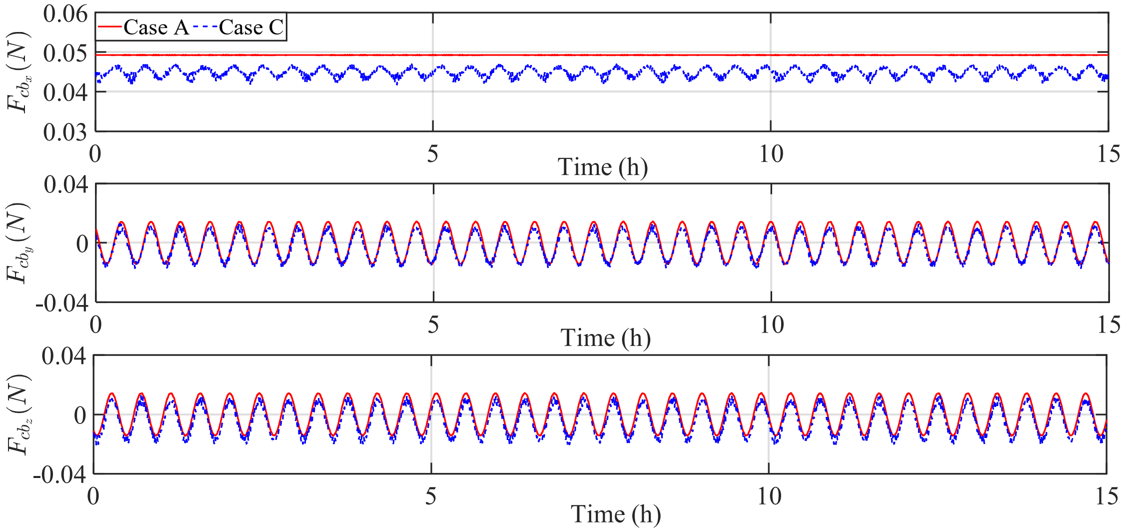

Figure 6-19 Time histories of the E-sail resultant propulsive force components in the $O_{cb}X_{cb}Y_{cb}Z_{cb}$ frame with different configurations.

Compared with Case A, the propulsive force generated by Case C is slightly smaller due to the lack of one main tether, which in turn makes the

Sun-E-sail distance increment slightly smaller, as shown in Figure 6-18(a) and Figure 6-19. Therefore, the influence of the resultant propulsive force on the coning motions and in-plane libration of main tethers, and the angular velocity of the central in both cases should be very small. However, Figure 6-18(b) shows the variation of the libration of main tethers is particularly significant in Case C about two degrees compared with that of in Case A about 0.2 degrees. It indicates that the E-sail in Case C is more unstable because the smaller in-plane libration angle and the better stability of the E-sail system. The similar condition can be seen in Figure 6-20, where the three-axis angular velocity of the central spacecraft oscillates in a relatively large scale. It also suggested that the E-sail in Case C is more unstable due to the greater angular velocities of the Y_{cb_y} and Z_{cb_z} axes. The significant difference between the angular velocity of central spacecraft and the E-sail spin rate leads to a greater in-plane libration of main tether with respect to the radial direction of central spacecraft, as presented in Figure 6-18(b). Moreover, this angular velocity oscillation may cause the instability of the central spacecraft, which in turn will result in the instability of E-sail. The difference of the central spacecraft angular velocity can be explained by the offset between the CM and CT of the E-sail as shown in Figure 6-21, where the variation magnitudes of the E-sail's CM and CT in case C are much greater than that of case A due to the lack of one main tether. This also verifies the influence of the disturbance torques in Equations (3.83) and (3.84) on the attitude dynamics of E-sail.

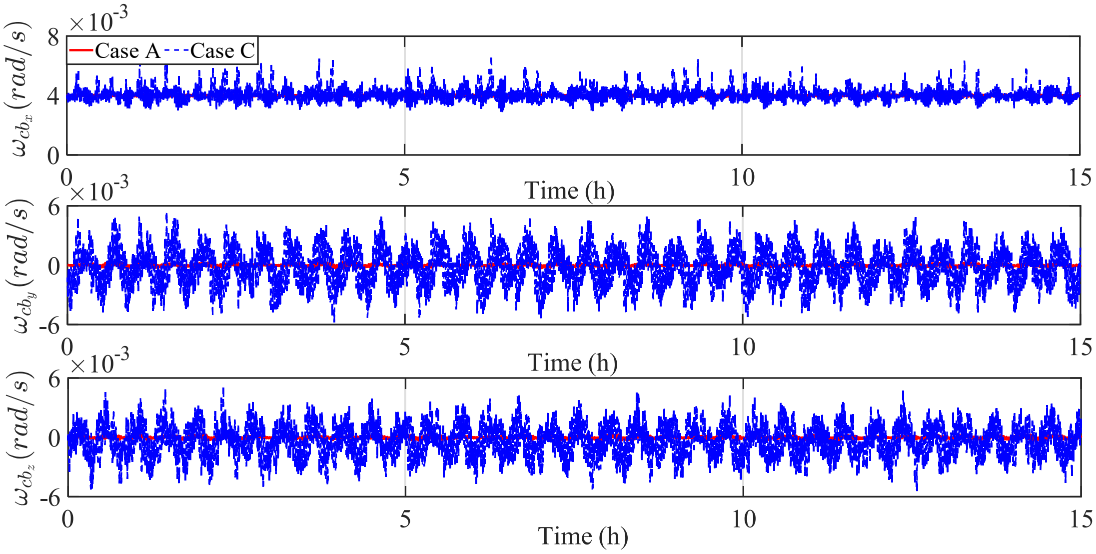

Figure 6-20 Time histories of angular velocity of the central spacecraft in the

$O_{cb}X_{cb}Y_{cb}Z_{cb}$ frame with different configurations.

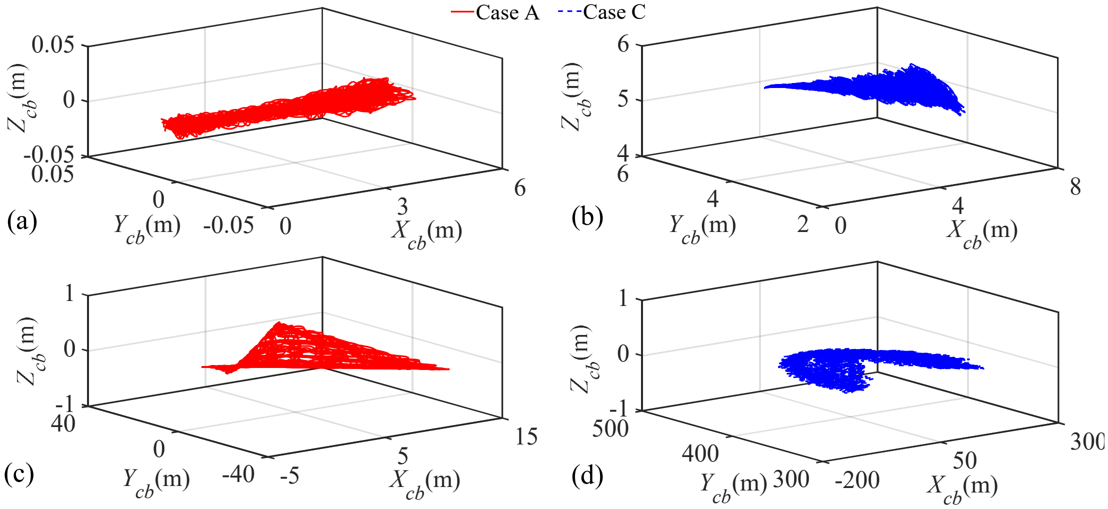

Figure 6-21 Time histories of CM (a) and (b) and CT (c) and (d) of the E-sail in the

$O_{cb}X_{cb}Y_{cb}Z_{cb}$ frame with different configurations.

Finally, the variation trends of tensions in the main and auxiliary tethers, the periodic oscillation of coning angle, and the variation of the E-sail spin rate in both cases are not noticeable, as shown in Figure 6-22. This is because the dominate moment of inertia of the E-sail is along the principal spin axis (the unit spin vector direction $\boldsymbol{n}$). Moreover, the violent oscillation of the central spacecraft angular velocity leads to the deviation between the principal spin axes of central spacecraft and E-sail, which is measured by the nutation angle, as illustrated in Figure 6-22(c). The greater nutation angle also verifies that the E-sail in Case C is more unstable.

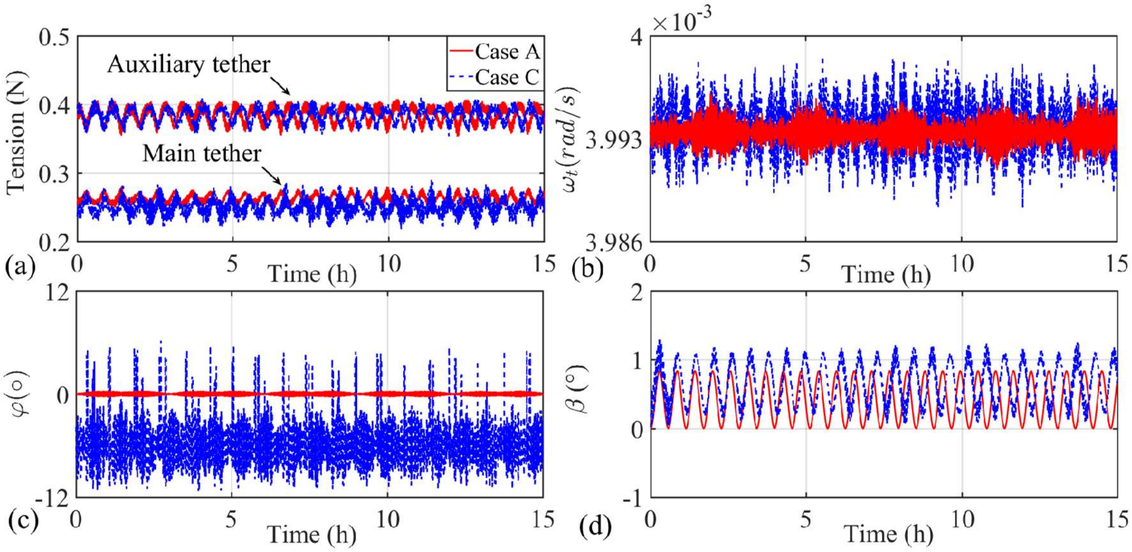

Figure 6-22 Time histories of (a) tension in main and auxiliary tethers (b) spin rate (c) nutation angle and (d) coning angle of the E-sail with different configurations.

In summary, the parametric analysis indicates that the E-sail's stability has a strong dependence on the geometrical configuration, and the E-sail with asymmetric configuration should be avoided. The nutation angle and the angular velocity of the central spacecraft should be actively controlled if the E-sail becomes asymmetrical.

6.4 Spin Rate Control of E-sail

The previous section results indicate that the spin rate of the central spacecraft can be influenced by the nonlinear rigid-flexible coupling dynamics. To maintain stability of the E-sail, the spin rates of the central spacecraft and E-sail should be controlled to a desired value. In this section, the spin rate of the E-sail is controlled by a simple feedback law to maintain the stability of the E-sail in the tether deployment process and the E-sail operation period, respectively.

6.4.1 Spin Rate Control Strategy

To maintain the stability of the E-sail in the attitude maneuvering and the deployment of the E-sail, it requires constant management of the spin rate of the E-sail. The E-sail spin rate must be maintained at a desired rate to generate sufficient centrifugal force to keep tethers taut and E-sail stiffness. Furthermore, it is assumed that the angular velocities around the Y_{cb} and Z_{cb} axes are negligible. Thus, the attitude dynamic of the spinning E-sail around the X_{cb} axis can be simplified as

$$I_{cb\_x}\dot{\omega}_c = \tau_{cb\_x} \tag{6.1}$$

where I_{cb_x} is the E-sail moment of inertia around the X_{cb} axis, ω_c is the current spin rate and $\dot{\omega}_c$ is the first order derivative of ω_c with respect to time t, which can be obtained from Equation (3.73). τ_{cb_x} is the required control torque applied to E-sail.

The control can be applied at the remote units and/or the central spacecraft. A simple feedback controller is implemented to stabilize the spin rate as shown in Figure 6-23, that is,

$$\tau_c = \kappa_c \left(\omega_{des} - \omega_c \right) \tag{6.2}$$

$$\boldsymbol{F}_r = \sum_{i=1}^{M} \boldsymbol{F}_{r\_i} = \sum_{i=1}^{M} \left(\kappa_t \left(\omega_{des} - \omega_t \right) \frac{\boldsymbol{n} \times \mathbf{b}_i}{\left| \boldsymbol{n} \times \mathbf{b}_i \right|} \right) \tag{6.3}$$

where τ_c is the control torque applied to the central spacecraft, κ_c and κ_t are the feedback control gains, ω_{des} and ω_t are the desired and current spin rates of the central spacecraft and E-sail around the X_{cb}-axis, respectively. $\boldsymbol{F}_r$ is the total control force applied to the remote units, and $\boldsymbol{F}_{r\_i}$ is the control force applied to the i_{th} remote unit, as shown in Figure 6-24, $\mathbf{b}_i$ is the position vector from the origin O_{cb} to the i^{th} remote unit. The simple feedback controller is adopted because the E-sail is stable, and the spin rate of E-sail is very small.

Figure 6-23 shows the principles of how the feedback controller are generated and applied. The block diagram indicates only the torque τ_c is applied to control the central spacecraft if the ω_c and ω_t can reach the desired value ω_{des}. According to the description in Section 3.4.2, the control torque τ_c should be replaced by an equivalent pair of forces in order to utilize by the NCF. Therefore, the τ_c is firstly decomposed into components in the direction aligned and perpendicular to the unit vector $\mathbf{u}$ as

$$\begin{cases} \tau_{\mathbf{u}} = \mathbf{0} \\ \tau_{\mathbf{u}_\perp} = |\tau_c| \dfrac{(\boldsymbol{p}_j - \boldsymbol{p}_i)}{|\boldsymbol{p}_j - \boldsymbol{p}_i|} \end{cases} \tag{6.4}$$

Substituting Equation (6.4) into Equation (3.70) yields the equivalent pair of the control forces as

$$\boldsymbol{F}_{\tau\_c} = \begin{bmatrix} \mathbf{0}_3^T & \mathbf{0}_3^T & |\tau_c|\mathbf{v}^T & \mathbf{0}_3^T \end{bmatrix}^T \tag{6.5}$$

Figure 6-23 also indicates if the ω_c and ω_t can not reach the desired value ω_{des} by only controlling the central spacecraft, the control forces $\boldsymbol{F}_r$ should be applied simultaneously to the remote units. The aim of controlling both the central spacecraft and remote units simultaneously is to avoid the generation of disturbance torque as presented in Equation (3.84).

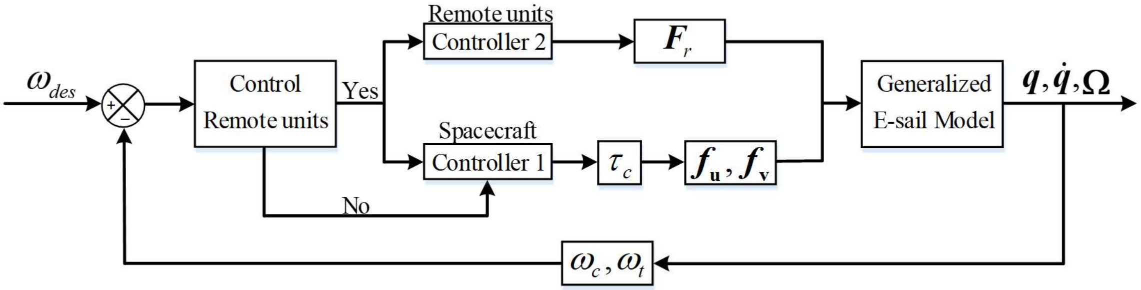

Figure 6-23 Block diagram of the E-sail control system.

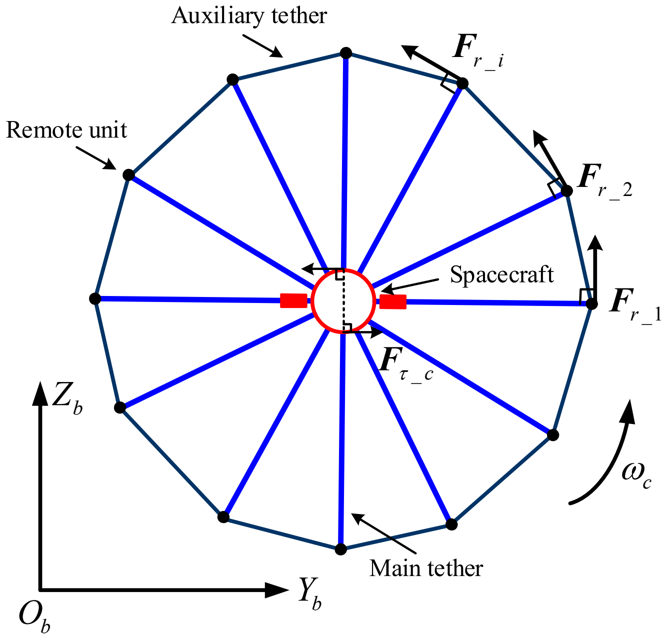

Figure 6-24 Control forces acting on the E-sail.

6.4.2 Spin Rate Control of the Fully Deployment E-sail

The aim of this section is to investigate the control performance of the E-sail's spin rate. The Type II configuration of the E-sail is considered with 12 main and connected auxiliary tethers. The tethers are assumed fully deployed and spin steadily in the same spin plane. The main tethers are positively charged with the constant solar wind velocity. The rest of the E-sail parameters are consistent with Table 4-2, except the tether length. Four different lengths of the main tethers are considered, i.e., 10m, 100m, 1km and 10km to evaluate the control performance of the E-sail's spin rate by controlling the central spacecraft or/and the remote units, respectively. The desired spin rate ω_{des} is set as 0.0045 rad/s. The maximum control torque/force and the duration of control are assumed to be 0.01N·m/0.01N and 10 hours, respectively. The time step size is 0.01s. The simulation results are presented in Figure 6-25 and Figure 6-26.

First, only the spin rate of the central spacecraft is controlled to investigate the control performance of the E-sail spin rate. The maximum feedback control gain is assumed as 20 due to the limitation on the maximum available control torque [12]. Figure 6-25 shows that the control performance of the E-sail spin rate is directly inversely proportional to the lengths of the main tether. Figure 6-25(a) shows the spin rate of E-sail can be controlled to the desired value in less than 2 hours with the control gain of 2 when the length of the main tether is 10m. As a comparison, it takes approximately 10 hours with the maximum gain of 20 to reach the same desire spin rate for 100m long tether, see Figure 6-25(b). Unlike these two lengths of the main tether, Figure 6-25(a) and (d) indicate the spin rate of E-sail is very hard to reach the desired value in the cases of long main tethers (1km and 10km) even with the maximum gain 20. In summary, it can be concluded that the spin rate of E-sail is not controllable by only applying the control torque at the central spacecraft if the length of main is sufficiently long.

Furthermore, to control the spin rate of long tether E-sail to reach the desired value, the control torque and forces need to be simultaneously applied at the central spacecraft and the remote units, as presented in Figure 6-23.

Only one main tether length, 10km, is considered. The feedback control gains for the central spacecraft κ_c and the remote units κ_t are set to 10. Figure 6-26 shows that the spin rate of the E-sail can reach the desired value in less than 5 hours with small control torque and forces applied to the central spacecraft and the remote units simultaneously. Meanwhile, the E-sail maintains stable because there is no tether slacking occurs in the control process, which can be demonstrated by the increased tensions of the main and auxiliary tethers to keep the tethers taut.

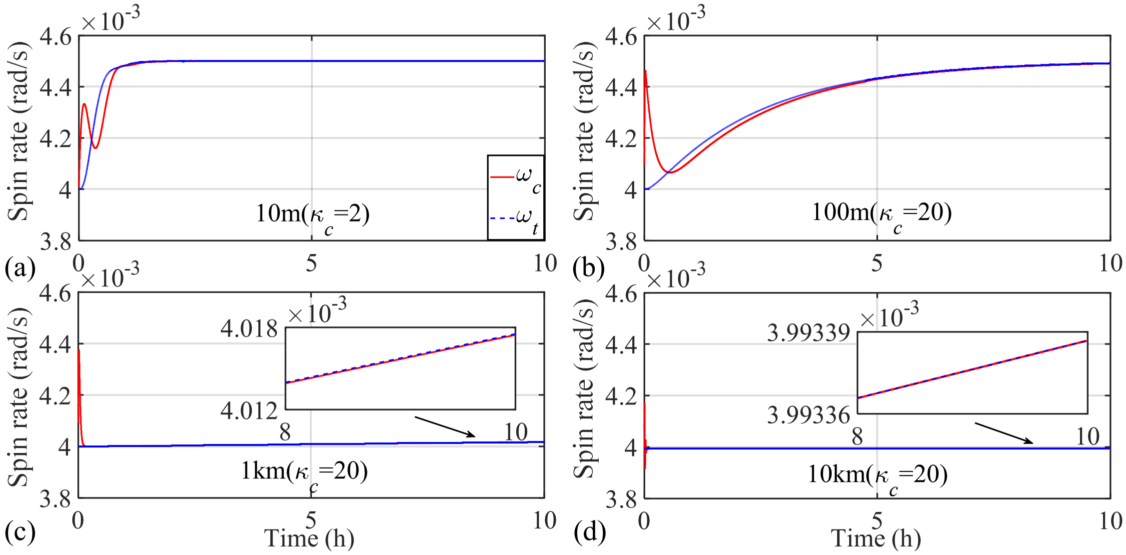

Figure 6-25 Time histories of E-sail's spin rate by controlling the spin rate of the central spacecraft with different lengths of main tethers.

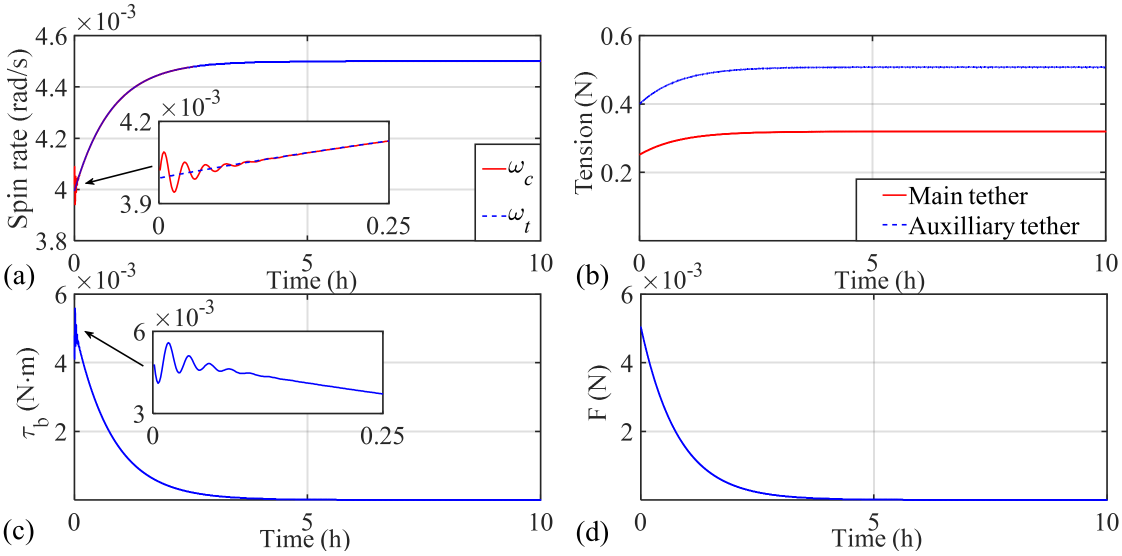

Figure 6-26 Time histories of (a) the E-sail's spin rate (b) tensions in the main and auxiliary tethers (c) the control torque at the central spacecraft (d) the control force at the remote units with 10km long main tethers.

6.4.3 Spin Rate Control of E-sail in Tether Deployment Process

The primary challenge of the E-sail is to generate sufficient momentum to maintain the spin-stabilize of the E-sail deployment. Thus, the control performance of the spin rate of E-sail in the tether deployment is explored in this section. Type II configuration of the E-sail is considered. The parameters of the E-sail in Table 4-2 are used, except the main tether length. The propulsive force is introduced.

First, the main tethers are assumed deployed from 0 to 1km in radial direction without spin rate control. Then, the main tethers are deployed from 1 km to 10 km at a constant velocity 0.5m/s while a spin rate control is applied to keep the E-sail spinning at a desired rate. The desired spin rate ω_{des} is still 0.0045 rad/s. The maximum control torque/force and the duration of control are also assumed to be 0.01N·m/0.01N and 10 hours, respectively. The feedback control gains for the central spacecraft κ_c and the remote units κ_t are set to 10. The results are shown in Figure 6-27.

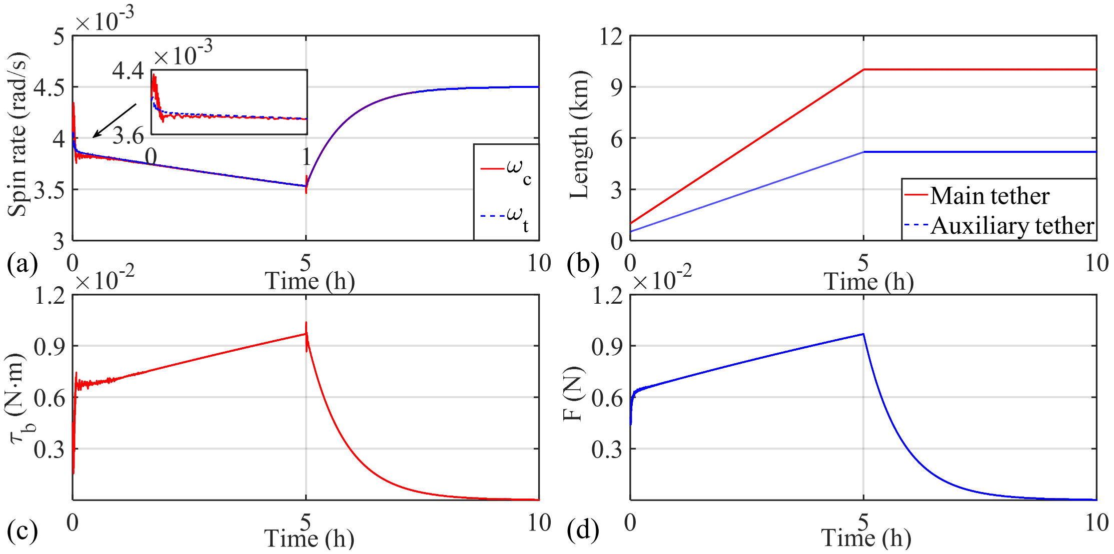

Figure 6-27 Time histories of (a) spin rates of the E-sail and central spacecraft (b) lengths of main and auxiliary tethers (c) control torque and (d) control forces at the central spacecraft and remote units in the tether deployment process.

Figure 6-27 shows that the main tethers are successfully deployed to the target length (10km), like the Ref. [104]. However, Figure 6-27(a) shows the spin rate of E-sail reduces as the main tether length increases due to the conservation of momentum. Because of the finite control input torque and forces at the central spacecraft and the remote units, the spin rate of the E-sail are not able to reach the desired value. However, the finite control input torque and forces can still keep the spin rate of the E-sail equal to that of the central spacecraft to prevent the main tethers wrapping around the central spacecraft in the tether deployment process. Accordingly, the stability of the E-sail is guaranteed. Once the tether deployment completed, the spin rates of the E-sail and the central spacecraft can be quickly reached to the desired value simultaneously by the control torque and forces. As the spin rates approach to the desired value, Figure 6-27(c)-(d) show the control input quickly diminishes to zero, which also demonstrates the effective of the controller.

In conclusion, the spin rate of E-sail can be controlled by a simple control law mainly by the finite control input at the remote units even in the tether deployment process.

Chapter 7 ATTITUDE CONTROL AND TRAJECTORY TRACKING OF E-SAIL

Summary: In this chapter, the attitude control and stability analysis of E-sail, and trajectory design and tracking problem of E-sail are studied. First, a simple feedback control law was proposed and verified by using the high-fidelity E-sail model developed in Section 3.3. Then, a SMC controller is designed for the reduced order analytical E-sail model in Section 3.5 and its stability is proved. Later, the control torque is mapped to the control thrust at remote units or the voltage modulation of main tethers in the flexible E-sail model, respectively. Further, the potential E-sail mission trajectory is designed and tracked by using the reduced-order model. Finally, some conclusions are presented.

7.1 E-sail Sail Angle Control with a Simple PD Control Strategy

In this section, the thrust vectoring of an E-sail can be controlled by tilting its sail angle to the desired value with respect to the solar wind velocity. Different from some literature that proposed to regulate the voltages of each main tether individually to generate a control torque, which is sensitive to the environment fluctuations such as the velocity and electron density of solar wind, the current work proposes to apply control forces at remote units to generate the control torque as shown in Figure 7-1. The main tethers are not charged to separate the influence of the propulsive force in the sail angle control. The parameters of the E-sail are the same as Table 4-1. The total simulation period is two days with a time step of 0.01s.

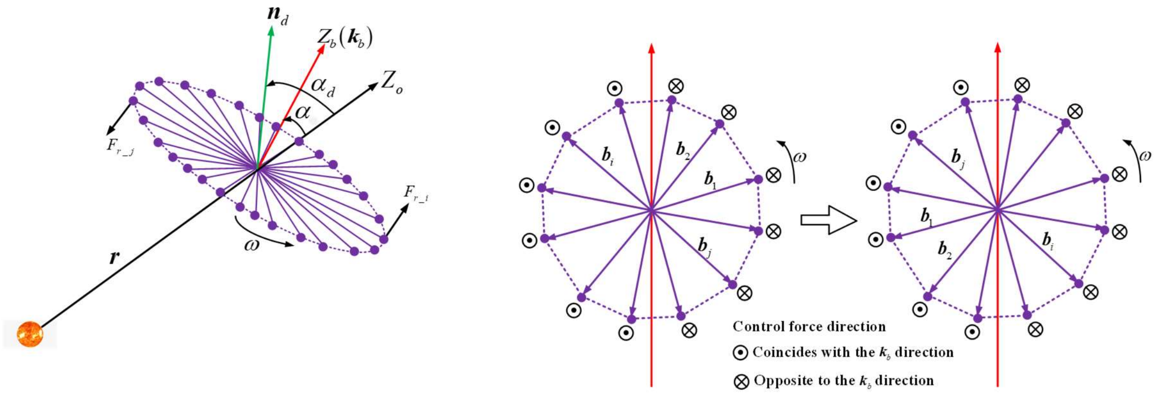

(a) (b)

Figure 7-1 Control forces applied to the remote units.

As shown Figure 7-1, let $\boldsymbol{F}_{r\_i}^{b}$ be the control force applied by the i^{th} remote unit and normal to the spin plane in the body-fixed coordinate system $O_bX_bY_bZ_b$. Thus, a simple proportional-derivative (PD) feedback force control law is proposed as

$$\boldsymbol{F}_{r\_i}^{b} = -\xi_i\left(\kappa_p e + \kappa_d \dot{e}\right)\boldsymbol{k}_b \tag{7.1}$$

where κ_p and κ_d are the control gains, $e = \alpha - \alpha_d$ is the control error, α_d is the desired sail angle, $\dot{e}$ is the derivative of e with respective to time, $\boldsymbol{k}_b$ is the unit vector aligned with the Z_b axis, and ξ_i is the directional index of the control forces

$$\xi_i = \begin{cases} -1 & \boldsymbol{l}_i^b \cdot \boldsymbol{n}_d > 0 \\ 0 & \boldsymbol{l}_i^b \cdot \boldsymbol{n}_d = 0 \\ 1 & \boldsymbol{l}_i^b \cdot \boldsymbol{n}_d < 0 \end{cases} \tag{7.2}$$

Here, $\boldsymbol{l}_i^b$ is the unit position vector of the i^{th} main tether or remote unit relative to the central spacecraft, defined in Equation (4.28), and $\boldsymbol{n}_d$ is the desired unit spin vector. Both are defined in the $O_b X_b Y_b Z_b$ coordinate system.

Then, the total control torque $\boldsymbol{\tau}$ can be written as

$$\begin{aligned} \boldsymbol{\tau} &= \sum_{i=1}^{M} \boldsymbol{\tau}_i = \sum_{i=1}^{M} L\boldsymbol{l}_i^b \times \boldsymbol{F}_{r\_i}^b \\ &= -\left(\kappa_p e + \kappa_d \dot{e}\right) \sum_{i=1}^{M} L\xi_i \begin{bmatrix} \cos\beta \sin\left(\dfrac{2\pi(i-1)}{M}\right) & -\cos\beta\cos\left(\dfrac{2\pi(i-1)}{M}\right) & \sin\beta \end{bmatrix}^T \\ &= -\left(\kappa_p e + \kappa_d \dot{e}\right) \boldsymbol{f}(L, \beta) \end{aligned} \tag{7.3}$$

Thus, the sail angle error $e = \alpha - \alpha_d$ obeys the following error dynamics

$$\left\lfloor M\left(m_{re} + m_{au} + \rho L/3\right) L^2 \right\rfloor \ddot{e} = \left|\boldsymbol{\tau}\right| = -\left(\kappa_p e + \kappa_d \dot{e}\right) \left|\boldsymbol{f}(L, \beta)\right| \tag{7.4}$$

Obviously, the PD controller is exponentially stable if the control gains $\kappa_d > 0$ and $\kappa_p > 0$. If $\kappa_d = 0$ and $\kappa_p > 0$, the controller is asymptotically stable.

Furthermore, the effectiveness of the control law is examined by numerical simulation. The initial and desired sail angles are set to ($0^\circ \mapsto 30^\circ$) and ($0^\circ \mapsto 10^\circ$), while the control gains are selected as ($\kappa_p = 0.01$, $\kappa_d = 0.015$) and

($\kappa_p = 0.015$, $\kappa_d = 0.015$), respectively. The simulation results are shown in Figure 7-2 and Figure 7-3.

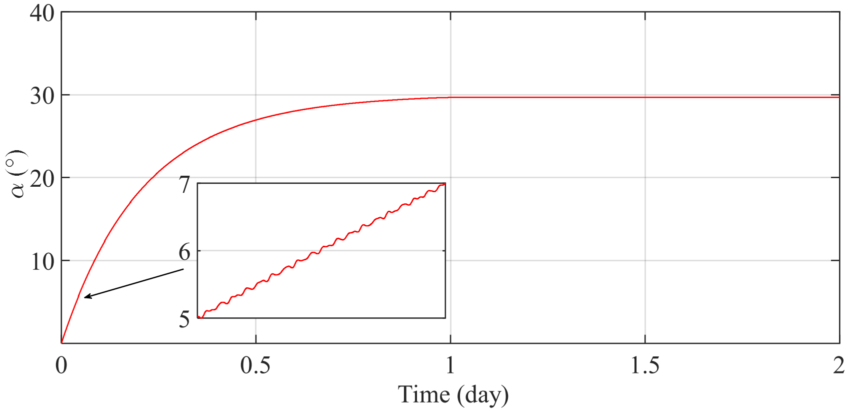

(a) Sail angle

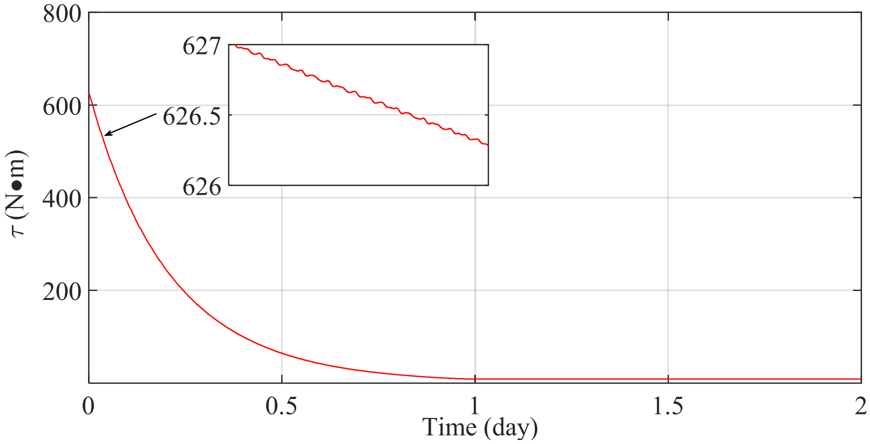

(b) Total control torque

Figure 7-2 Time histories of the sail angle control with the desired 30° sail angle.

Intuitively, Figure 7-2(a) and Figure 7-3(a) show that the sail angle is quickly approaching to the desired value in about one day, compared to eight days by regulating the voltages of each main tether individually in Ref. [18]. Accordingly, Figure 7-2(b) and Figure 7-3(b) show the control torque, which diminishes quickly as the sail angle approaches to the desired value. Similar to the solar wind sails, the control forces can be applied by the control vanes at the tips of the main tethers [8-9].

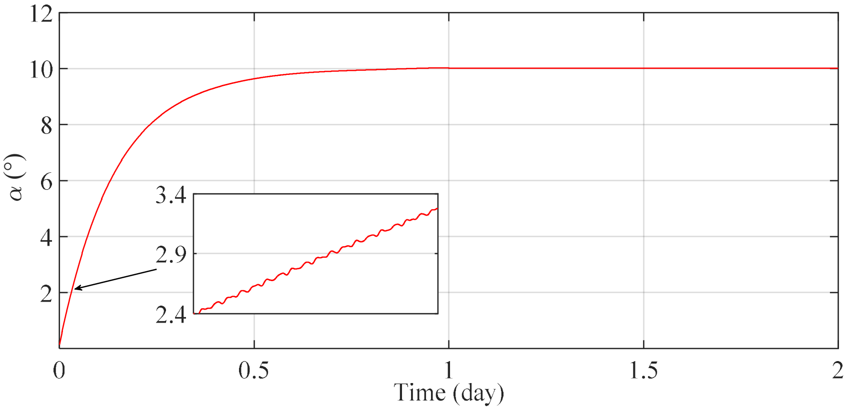

(a) Sail angle

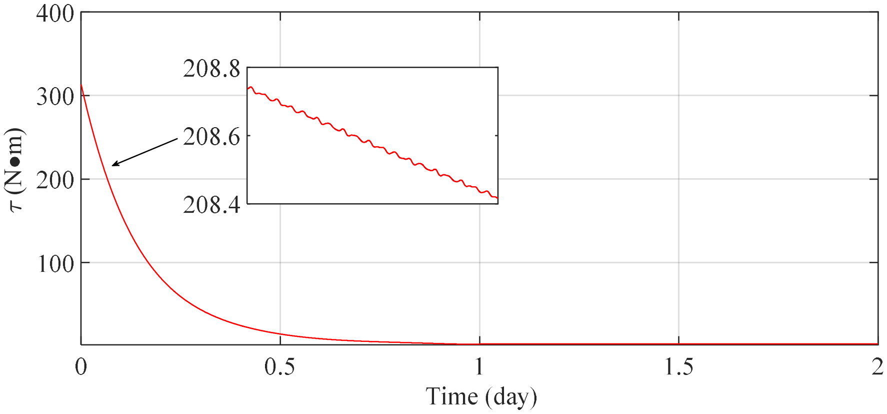

(b) Total control torque

Figure 7-3 Time histories of the sail angle control with the desired 10° sail angle.

In summary, the proposed control strategy can be combined with the voltage modulation strategy in Ref. [16] to quickly control and maintain the desired sail angle for the attitude maneuvering of the E-sail mission. The current work can be applied for the orbital transfer or asteroid flyby missions.

7.2 Attitude Control and Stability Analysis of E-sail

Although many effects have been devoted to the attitude control of E-sail, which can be achieved by voltage modulation at main tethers or thrust at remote units with mass-spring or NFFEM approach. The stability of the control strategy has not been investigated due to the difficulty in handling the high-order model under the Lyapunov framework. Therefore, the aim of this section is to thoroughly investigate the stability control of the E-sail in attitude maneuver with the high-order flexible tether model based on NPFEM. The control strategy is derived by using a simplified reduced order, but equivalent, analytical model under the Lyapunov framework. Then, it is applied to the high-fidelity model like a virtual experiment to demonstrate its effectiveness. Noting that the attitudes of the E-sail, such as the sail and clock angles expressed in Euler angles, are not the state in the high-fidelity E-sail, a mapping scheme has been developed to map the control torques derived from the reduced-order analytical model to the control forces acting on the remote units in the high-fidelity E-sail model. The effect of the control gains on the control performance is investigated in both the analytical and high-fidelity models. Finally, the versatility of the proposed control strategy is investigated by modulating the voltage of each individual main tether in E-sail attitude maneuver.

7.2.1 Attitude Control Law

Inspired by previous work [105-106] in space tether system, reduce order modeling approaches are applied in current work, where the control strategy was developed based on a grossly simplified analytical model and then applied to the finite element model. As shown in Figure 7-4, the sail and clock angles must be controlled to reach the desired values to accomplish the E-sail's attitude maneuver. First, the desired Euler angles are calculated by Equation (3.10) with the input of desired sail and clock angles. Then, the attitude controller is developed with the reduced order analytical E-sail model. Finally, the designed control torques will be mapped to the control forces at nodes of remote units in the high-fidelity model of the E-sail.

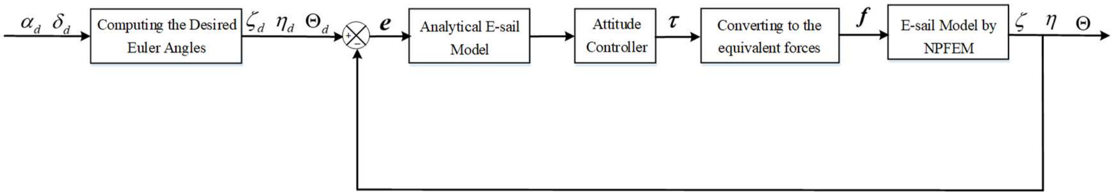

Figure 7-4 Block diagram of the E-sail attitude control strategy.

7.2.1.1 Derivation of Control Strategy

The acceleration of the Euler angles can be obtained by deriving Equation (3.101) with respect to time t as

$$\begin{aligned}
\ddot{\zeta} &= \frac{\left(\cos\eta\left(\cos\Theta(\dot{\omega}_x-\omega_y\dot{\Theta})-\sin\Theta(\omega_x\dot{\Theta}+\dot{\omega}_y)\right)+\dot{\eta}\sin\eta\left(\omega_x\cos\Theta-\omega_y\sin\Theta\right)\right)}{\cos^2\eta}\\
\ddot{\eta} &= \sin\Theta\left(\dot{\omega}_x-\omega_y\dot{\Theta}\right)+\cos\Theta\left(\omega_x\dot{\Theta}+\dot{\omega}_y\right)\\
\ddot{\Theta} &= \dot{\omega}_z+\tan\eta\left(\sin\Theta\left(\dot{\omega}_y+\omega_x\dot{\Theta}\right)+\cos\Theta\left(\omega_y\dot{\Theta}-\dot{\omega}_x\right)\right)-\frac{\dot{\eta}\left(\omega_x\cos\Theta-\omega_y\sin\Theta\right)}{\cos^2\eta}
\end{aligned} \tag{7.5}$$

Substituting the attitude dynamics equations in Equation (3.100) and kinematic equations in Equation (3.99) into (7.5) yields

$$\begin{aligned}
\ddot{\zeta} &= \frac{\left(\tau_x\cos\Theta-\tau_y\sin\Theta\right)}{J\cos\eta}-\frac{\dot{\eta}\left(2\dot{\Theta}+\omega_0\right)}{\cos\eta}\\
\ddot{\eta} &= \left(\dot{\zeta}-\Omega\right)^2\sin\eta\cos\eta+\frac{\left(\tau_x\sin\Theta+\tau_y\cos\Theta\right)}{J}+\left(2\dot{\Theta}+\omega_0\right)\left(\dot{\zeta}-\Omega\right)\cos\eta\\
\ddot{\Theta} &= \dot{\eta}\left(2\dot{\Theta}+\omega_0\right)\tan\eta-\dot{\eta}\left(\dot{\zeta}-\Omega\right)\cos\eta-\frac{\left(\tau_x\tan\eta\cos\Theta-\tau_y\tan\eta\sin\Theta-\tau_z/2\right)}{J}
\end{aligned} \tag{7.6}$$

or in the vector form

$$\ddot{\boldsymbol{\varpi}} = \boldsymbol{D}\left(\boldsymbol{\varpi}\right)\left(\boldsymbol{U}-\boldsymbol{C}\left(\boldsymbol{\varpi},\dot{\boldsymbol{\varpi}}\right)\right) \tag{7.7}$$

where $\boldsymbol{\varpi}=\left[\zeta \quad \eta \quad \Theta\right]^T$ represents the vector of Euler angles, $\dot{\boldsymbol{\varpi}}=\left[\dot{\zeta} \quad \dot{\eta} \quad \dot{\Theta}\right]^T$ and $\ddot{\boldsymbol{\varpi}}=\left[\ddot{\zeta} \quad \ddot{\eta} \quad \ddot{\Theta}\right]^T$ are the angular velocity and acceleration, $\boldsymbol{U}=\boldsymbol{B\tau}$, $\boldsymbol{B}$, $\boldsymbol{D}\left(\boldsymbol{\varpi}\right)$ and $\boldsymbol{C}\left(\boldsymbol{\varpi},\dot{\boldsymbol{\varpi}}\right)$ are given by

$$\boldsymbol{B}=\begin{bmatrix} \frac{1}{J} & 0 & 0 \\ 0 & \frac{1}{J} & 0 \\ 0 & 0 & \frac{1}{2J} \end{bmatrix} \qquad \boldsymbol{D}(\boldsymbol{\varpi})=\begin{bmatrix} \frac{\cos\Theta}{\cos\eta} & -\frac{\sin\Theta}{\cos\eta} & 0 \\ \sin\Theta & \cos\Theta & 0 \\ -\cos\Theta\tan\eta & \sin\Theta\tan\eta & 1 \end{bmatrix}$$

$$\boldsymbol{C}(\boldsymbol{\varpi},\dot{\boldsymbol{\varpi}})=\begin{bmatrix} \dot\eta\left(2\dot\Theta+\omega_0\right)\cos\Theta-\left(\dot\zeta-\Omega\right)\sin\Theta\cos\eta\left(\left(2\dot\Theta+\omega_0\right)+\sin\eta\left(\dot\zeta-\Omega\right)\right) \\ -\dot\eta\left(2\dot\Theta+\omega_0\right)\sin\Theta-\left(\dot\zeta-\Omega\right)\cos\eta\cos\Theta\left(\left(2\dot\Theta+\omega_0\right)+\sin\eta\left(\dot\zeta-\Omega\right)\right) \\ \cos\eta\dot\eta\left(\dot\zeta-\Omega\right) \end{bmatrix} \tag{7.8}$$

It should be emphasized that the attitude control of the E-sail is a nonlinear control problem due to the nonlinearity of Equation (7.7). The E-sail is generally subjected to many uncertainties like model uncertainty, solar wind fluctuation and gravity disturbances. Therefore, the Sliding Mode Control (SMC) is adopted due to its strong robustness and simplicity in dealing with parametric uncertainties and disturbances of a nonlinear system [107]. Further, the SMC can suppress the excitation generated by the high frequency on-off control of the main tether voltage. It should be noted that the aim of this section is to investigate the feasibility of applying a control strategy developed from the reduced order analytical E-sail model to the high-fidelity E-sail model. Once the feasibility is validated, any nonlinear attitude control strategy can be evaluated by using the high-fidelity E-sail model. The simple sliding mode control is used to demonstrate the feasibility of this concept, rather than comparing control performance with the existing E-sail attitude controller.

First, define a sliding surface vector as

$$\boldsymbol{S} = \dot{\boldsymbol{\varpi}} + \boldsymbol{\lambda}\boldsymbol{\varpi}_e \tag{7.9}$$

$$\boldsymbol{S} = \begin{bmatrix} S_1 \\ S_2 \\ S_3 \end{bmatrix} \quad \boldsymbol{\varpi}_d = \begin{bmatrix} \zeta_d \\ \eta_d \\ \Theta_d \end{bmatrix} \quad \boldsymbol{\lambda} = \begin{bmatrix} \lambda_1 & 0 & 0 \\ 0 & \lambda_2 & 0 \\ 0 & 0 & \lambda_3 \end{bmatrix} \tag{7.10}$$

where $\boldsymbol{\varpi}_e = \boldsymbol{\varpi} - \boldsymbol{\varpi}_d$ is the error vector of the Euler angles, $\boldsymbol{\varpi}_d$ is the vector of the desired Euler angles, and $\boldsymbol{\lambda}$ is a positive definite constant matrix of control parameters, which determine the convergence rate of the sliding surface.

Taking the derivative of Equation (7.9) with respect to time t yields the error dynamics of the Euler angles as

$$\dot{\boldsymbol{S}} = \ddot{\boldsymbol{\varpi}} + \boldsymbol{\lambda}\dot{\boldsymbol{\varpi}}_e = \boldsymbol{D}(\boldsymbol{\varpi})\left(\boldsymbol{U} - \boldsymbol{C}(\boldsymbol{\varpi}, \dot{\boldsymbol{\varpi}})\right) + \boldsymbol{\lambda}\dot{\boldsymbol{\varpi}}_e \tag{7.11}$$

Define an exponential control law as,

$$\dot{\boldsymbol{S}} = -\boldsymbol{k}_1 \operatorname{sgn}(\boldsymbol{S}) - \boldsymbol{k}_2 \boldsymbol{S} \tag{7.12}$$

where sgn is the sign function, $-\boldsymbol{k}_2\boldsymbol{S}$ is the exponential reaching term, $-\boldsymbol{k}_1 \operatorname{sgn}(\boldsymbol{S})$ is the constant velocity reaching term, and the $\boldsymbol{k}_1$ and $\boldsymbol{k}_2$ are the control gain matrices,

$$\boldsymbol{k}_1 = \begin{bmatrix} k_{11} & 0 & 0 \\ 0 & k_{12} & 0 \\ 0 & 0 & k_{13} \end{bmatrix} \quad k_{11} / k_{12} / k_{13} > 0$$

$$\boldsymbol{k}_2 = \begin{bmatrix} k_{21} & 0 & 0 \\ 0 & k_{22} & 0 \\ 0 & 0 & k_{23} \end{bmatrix} \quad k_{21} / k_{22} / k_{23} > 0 \tag{7.13}$$

Combining Equations (7.11) and (7.12) yields the vector of the attitude control torque as

$$\boldsymbol{\tau} = \boldsymbol{B}^{-1} \left\lfloor \boldsymbol{C}\left(\boldsymbol{\varpi}, \dot{\boldsymbol{\varpi}}\right) - \boldsymbol{D}^{-1}\left(\boldsymbol{\varpi}\right)\left(\boldsymbol{k}_1 \operatorname{sgn}(\boldsymbol{S}) + \boldsymbol{k}_2 \boldsymbol{S} + \lambda \dot{\boldsymbol{\varpi}}_e\right) \right\rfloor \tag{7.14}$$

where the superscript $(\ )^{-1}$ denotes the inverse of a matrix.

To prove the stability of the proposed control law, consider the Lyapunov candidate function as

$$V = \frac{1}{2} \boldsymbol{S}^T \boldsymbol{S} \tag{7.15}$$

Taking the derivative of Equation (7.15) with respect to time t yields

$$\begin{aligned} \dot{V} &= \boldsymbol{S}^T \dot{\boldsymbol{S}} = \boldsymbol{S}^T \left(-\boldsymbol{k}_1 \operatorname{sgn}(\boldsymbol{S}) - \boldsymbol{k}_2 \boldsymbol{S}\right) \\ &= -\left(k_{11}\left|S_1\right| + k_{12}\left|S_2\right| + k_{13}\left|S_3\right|\right) - \left(k_{21} S_1^2 + k_{22} S_2^2 + k_{23} S_3^2\right) \le 0 \end{aligned} \tag{7.16}$$

Thus, the control law makes the E-sail system stable and asymptotically converges to the sliding surface.

It is important to point out that the attitude angles of the E-sail in this section are not state variables in the nodal position coordinates in the NPFEM-based high-fidelity model. Therefore, the control torque τ in Equation (7.14) derived from the reduced order analytical E-sail model is not applicable directly to the NPFEM-based high-fidelity model and must be mapped to either the control forces at remote units or the control voltages at the main tethers, depending on how the control is applied.

7.2.1.2 Mapping of Control Torque to Control Force

The relationship between the total control toques and the control forces at remote units can be written as,

$$\boldsymbol{\tau} = \sum_{i=1}^{N} \boldsymbol{\tau}_i = \sum_{i=1}^{N} \left(\boldsymbol{L}_i^{sp} \times \boldsymbol{F}_i^{sp} \right) \tag{7.17}$$

$$\boldsymbol{L}_i^{sp} = L \left[\cos\left(\omega_0 t + \frac{2\pi(i-1)}{N} \right), \quad \sin\left(\omega_0 t + \frac{2\pi(i-1)}{N} \right), \quad 0 \right]^T \tag{7.18}$$

where $\boldsymbol{L}_i^{sp}$ and $\boldsymbol{F}_i^{sp}$ are the position and control force vectors of the i^{th} remote unit in the $O_{sp}X_{sp}Y_{sp}Z_{sp}$ frame, and the $\boldsymbol{\tau}_i$ is the corresponding control torque, respectively.

Obviously, one cannot solve for the control force $\boldsymbol{F}_i^{sp}$ from Equation (7.17) directly if the number of the remote units N is greater than 3. Usually, the number of the remote units is between 10 and 100. Alternatively, it is assumed here that the distribution of the control forces along the remote units follows a sinusoidal function, that is,

$$\boldsymbol{\tau}_i = \boldsymbol{L}_i^{sp} \times \boldsymbol{F}_i^{sp} = \boldsymbol{\tau} \sin\theta_i \bigg/ \sum_{i=1}^{N} \sin\theta_i \tag{7.19}$$

where the angle θ_i is measured between the i^{th} main tether and the X_{sp} axis.

Therefore, the control force $\boldsymbol{F}_i^{sp}$ can be solved from Equation (7.19).

7.2.1.3 Mapping of Control Torque to Control Voltage

The control law is implemented by modulating the voltages on the main tethers in this section, which in turn controls the magnitude of propulsive force produced by the main tethers. The propulsive force is assumed to be uniformly distributed along the main tether, because the variation of solar wind electron and velocity along the tether length is negligible. Accordingly, the relationship between the total control toque and the voltages at main tethers can be obtained as,

$$\boldsymbol{\tau} = \sum_{i=1}^{N} \boldsymbol{\tau}_i = \sum_{i=1}^{N} \left(\frac{1}{2} \boldsymbol{L}_i^{sp} \times \boldsymbol{F}_{t,i} \right) = \sum_{i=1}^{N} \left[\frac{1}{2} \boldsymbol{L}_i^{sp} \times \int_0^{L_i} \boldsymbol{S}^T \left(\boldsymbol{A}_{s2t} \right)^T \boldsymbol{f}_{dl} dl \right] \tag{7.20}$$

where the propulsive force $\boldsymbol{F}_{t,i}$ is given in Equation (3.16), which depends on the voltage of the i^{th} main tether.

Assume the same torque distribution among the main tethers as Equation (7.19), such that,

$$\tau_i = \tau \sin\theta_i \Big/ \sum_{i=1}^{N} \sin\theta_i = \boldsymbol{L}_i^{sp} \times \boldsymbol{F}_{t,i} = \frac{1}{2} \boldsymbol{L}_i^{sp} \times \int_0^{L_i} \boldsymbol{S}^T \left(\boldsymbol{A}_{s2t} \right)^T \boldsymbol{f}_{dl} dl \tag{7.21}$$

Substituting Equation (3.16) into Equation (7.21) leads to

$$\boldsymbol{\tau}_i = \frac{1}{2} \int_0^{L_{e,i}} 0.18 \boldsymbol{S}^T \left(\boldsymbol{A}_{s2t} \right)^T \max\left(0, V_i - V_w\right) \sqrt{\varepsilon_0 m_p n \boldsymbol{v}}_{sw\perp} dl \tag{7.22}$$

Therefore, the voltage V_i of the i^{th} main tether can be solved accordingly. In the current work, the tether voltage is bounded because the power generated by the E-sail solar panels is limited. It is assumed the baseline voltage is 20kV and the minimum and maximum voltages are 0 and 40kV, which are the same as Refs. [16, 18], respectively.

7.2.2 Parameter Analysis

The proposed attitude control law for the E-sail is demonstrated through parametric analysis with different E-sail models in the simulation. It is assumed that the E-sail initially rotates in the heliocentric ecliptic plane at 1au from the Sun, and the spin plane is normal to the heliocentric ecliptic plane. It is also assumed that the initially spin rate of E-sail is $\omega_0 = 0.004 rad/s$ [71] and the magnitude of the solar wind velocity is constant. Further, the maximum sail angle is set as $\alpha_{\max} = 70^\circ$. The parameters of the E-sail are kept the same as Table 4-1, and the solar wind velocity is 400 km/s. The total number of main/auxiliary tethers is 12/12. The control parameters of the attitude control law and the initial sail and clock angles and the corresponding initial Euler angles are given in Table 7-1, where the sail and clock angles are mapped to the Euler angles by Equation (3.10). Two mission scenarios are considered to demonstrate the effectiveness of the proposed attitude control law. The first scenario is to verify the capability of the attitude maneuver of electric sail in a coplanar heliocentric transfer mission, where $\alpha_d = 55^\circ$ is the optimal angle for maximizing the transverse component of the propulsive force [38]. The second scenario is to verify the E-sail's capability to escape from the heliocentric ecliptic plane [21]. The simulation time step is 0.01s, and the total simulation time is three days.

The desired angles and angular velocities at the end of control are defined as:

Scenario 1: $\alpha_d = 55^\circ$, $\delta_d = 90^\circ$ ($\zeta_d = -55^\circ$, $\dot{\zeta}_d = 0^\circ/s$, $\eta_d = 0^\circ$, $\dot{\eta}_d = 0^\circ/s$, $\Theta_d = 90^\circ$, $\dot{\Theta}_d = 0^\circ/s$)

Scenario 2: $\alpha_d = 45^\circ$, $\delta_d = 45^\circ$ ($\zeta_d = -35.26^\circ$, $\dot{\zeta}_d = 0^\circ/s$, $\eta_d = 30^\circ$, $\dot{\eta}_d = 0^\circ/s$, $\Theta_d = 54.74^\circ$, $\dot{\Theta}_d = 0^\circ/s$)

Table 7-1 Parameters in attitude control.

Parameters	Values
Control gains $[\lambda_1 \quad \lambda_2 \quad \lambda_3]$	$\lfloor 3\times10^{-4} \quad 3\times10^{-4} \quad 3\times10^{-4} \rfloor$
Control gains $[k_{11} \quad k_{12} \quad k_{13}]$	$\lfloor 1\times10^{-11} \quad 1\times10^{-11} \quad 1\times10^{-11} \rfloor$
Control gains $[k_{21} \quad k_{22} \quad k_{23}]$	$\lfloor 3\times10^{-4} \quad 3\times10^{-4} \quad 3\times10^{-4} \rfloor$
Initial sail and clock angles $[\alpha \quad \delta]$	$\lfloor 30^\circ \quad 90^\circ \rfloor$
Initial Euler angles $[\zeta \quad \eta \quad \Theta]$	$\lfloor -30^\circ \quad 0^\circ \quad 90^\circ \rfloor$
Initial Euler angular rates $\lfloor \dot{\zeta} \quad \dot{\eta} \quad \dot{\Theta} \rfloor$	$\lfloor 0^\circ/s \quad 0^\circ/s \quad 0^\circ/s \rfloor$

7.2.2.1 Attitude Control of Reduced Order E-sail Model

The moment of inertia tensor of the reduced order analytical E-sail model is calculated by the physics parameters of system components in Table

4-1 as per Section 3.5.1. The corresponding control parameters and initial attitude conditions are presented in Table 7-1. The simulation results of control are presented in Figure 7-5 to Figure 7-8.

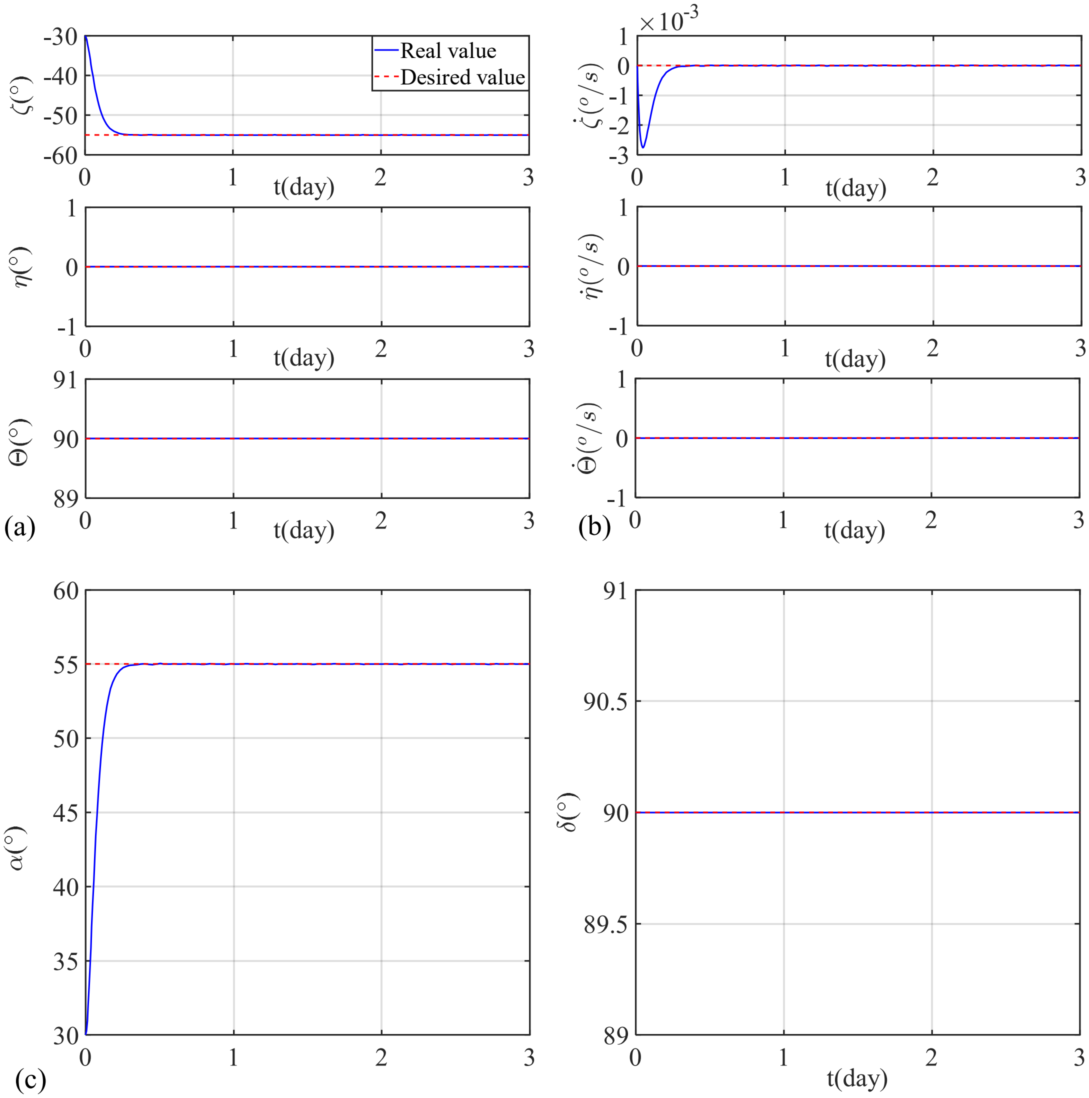

Figure 7-5 Time histories of (a) Euler angles (b) Euler angular rates and (c) sail and clock angles with the desired 55° sail angle.

In the first scenario, the Euler angle ζ quickly and smoothly approaches to the desired value (-55°) from the initial value (-30°) without any overshoot in about 0.3 days, while the other two Euler angles η and Θ are kept unchanged as required as shown in Figure 7-5(a). The same phenomena are observed in the Euler angular rates as shown in Figure 7-5(b), where they are zero if the Euler angles reach the desired values. Also, Figure 7-5(c) shows that the sail and clock angles reach the desired values as expected in the same manner. At the same time, Figure 7-6(a)-(b) show that the components of control torque and the sliding surface in the three axes decrease rapidly toward and maintain zero as the Euler angles reach the desired values. It demonstrates that the proposed control strategy is effective in controlling the large angle maneuvering of the E-sail in a coplanar heliocentric transfer mission in the ideal situation – reduced order analytical model.

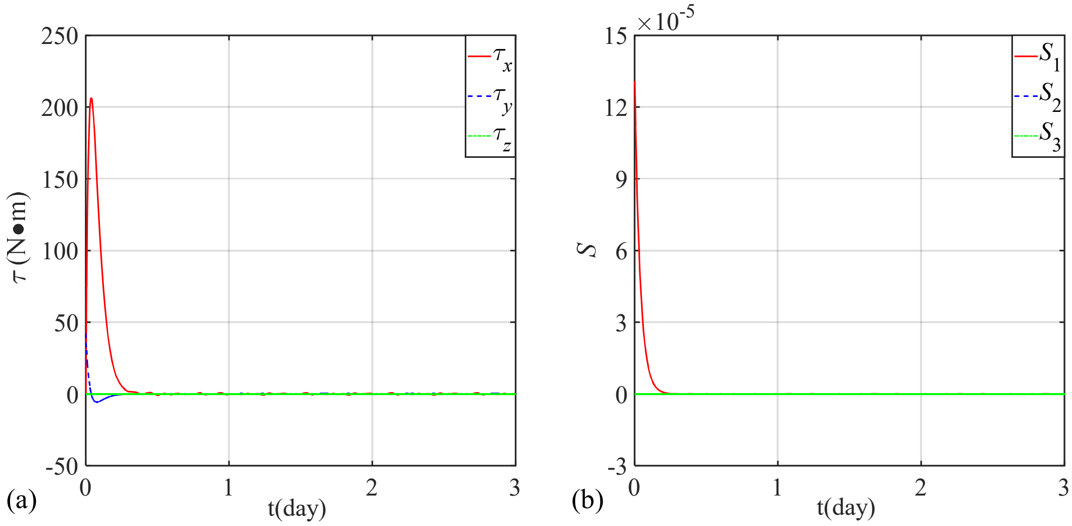

Figure 7-6 Time histories of (a) control torques in the $O_{sp}X_{sp}Y_{sp}Z_{sp}$ frame and (b) sliding surfaces with the desired 55° sail angle.

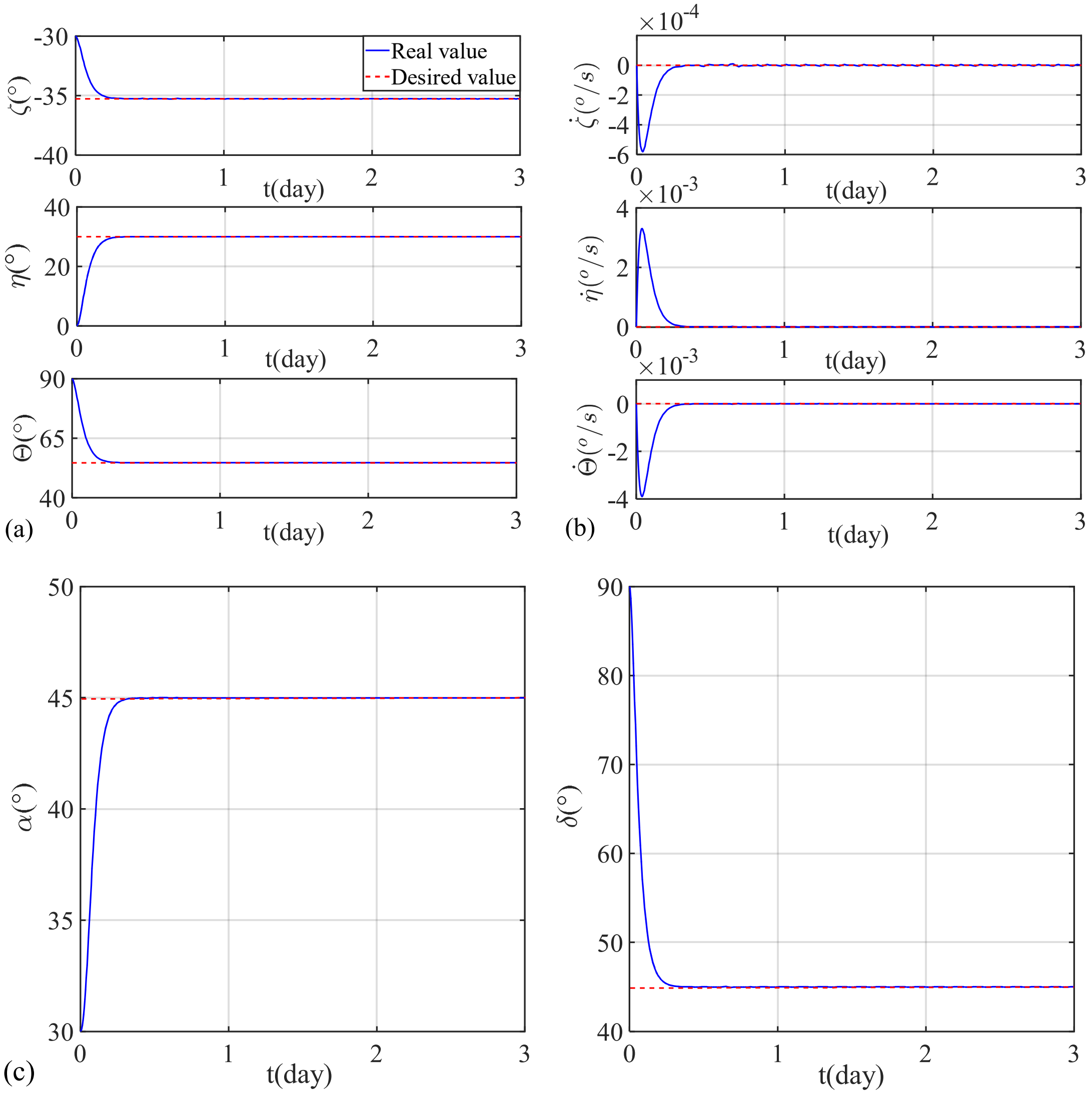

Figure 7-7 Time histories of (a) the Euler angles (b) the Euler angular rates and (c) the sail and clock angles with the desired 45° sail angle.

In the second scenario, similar performance is observed. The time histories of the Euler angles, Euler angular rates, corresponding sail and clock angles, control torques, and sliding surfaces all demonstrate that the proposed control law performs well for the mission of escaping from the heliocentric ecliptic plane in the ideal situation as illustrated in Figure 7-7 and Figure 7-8.

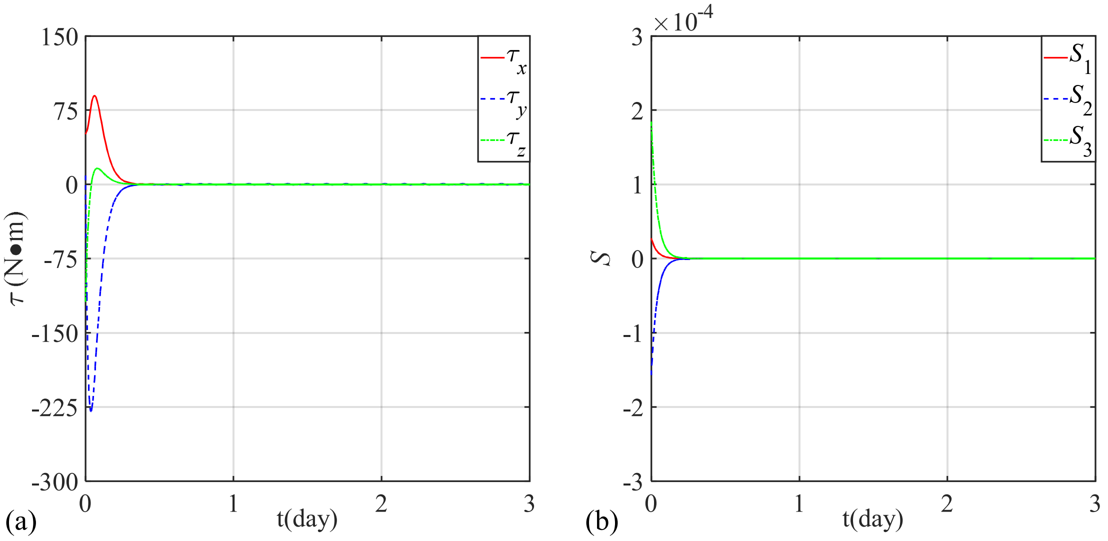

Figure 7-8 Time histories of (a) control torques in the $O_{sp}X_{sp}Y_{sp}Z_{sp}$ frame and (b) sliding surfaces with the desired 45° sail angle.

As mentioned above, the model uncertainty caused by the simplified reduced-order model may affect the control performance of the proposed controller. To verify the influence of the model uncertainty on the control performance, the moments of Inertia of the E-sail are assumed to be $I_{x\_new} = 1.1 I_x$, $I_{y\_new} = 0.9 I_y$, and $I_{z\_new} = 1.1 I_z$. Here, only the second scenario is considered, and the other parameters are kept the same. The simulation results are shown in Figure 7-9. It shows that the Euler angles, and the sail and clock angles are quickly controlled to the desired value in both cases. However, unlike the dynamic responses of the E-sail without the model uncertainty, it takes a longer time for the E-sail's attitude angles with the model uncertainty reach the desired values with overshoots due to the inaccurate model. It demonstrates that the control strategy law derived from the reduced order analytical model is applicable to the E-sail model with the model uncertainty.

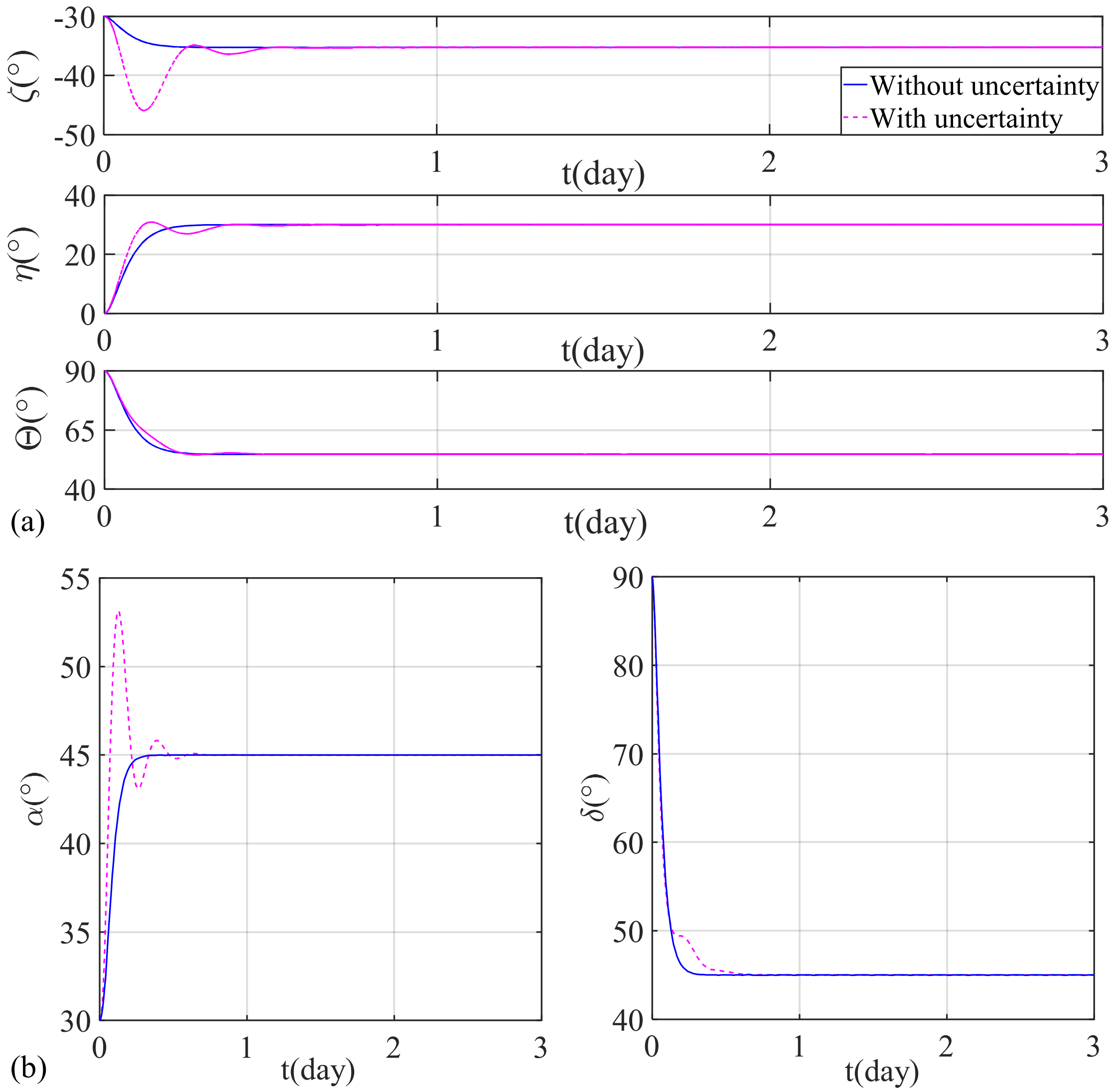

Figure 7-9 Time histories of (a) the Euler angles and (b) the sail and clock angles with and without model uncertainty.

Table 7-2 Parameters in feedback linearization controller.

Parameters	**Values**
Control gains $[\lambda_1 \quad \lambda_2 \quad \lambda_3]$	$\left\lfloor 5\times10^{-5} \quad 5\times10^{-5} \quad 5\times10^{-5} \right\rfloor$
Control gains $[k_{11} \quad k_{12} \quad k_{13}]$	$\left\lfloor 1\times10^{-10} \quad 1\times10^{-10} \quad 1\times10^{-10} \right\rfloor$
Control gains $[k_{21} \quad k_{22} \quad k_{23}]$	$\left\lfloor 5\times10^{-5} \quad 5\times10^{-5} \quad 5\times10^{-5} \right\rfloor$
Initial Euler angles $[\zeta \quad \eta \quad \Theta]$	$\left\lfloor 0^\circ \quad 0^\circ \quad 0^\circ \right\rfloor$
Initial Euler angular rates $\left\lfloor \dot{\zeta} \quad \dot{\eta} \quad \dot{\Theta} \right\rfloor$	$\left\lfloor 0^\circ/s \quad 0^\circ/s \quad 0^\circ/s \right\rfloor$
Moment of inertia I_x	$7.333\times10^{8} kg\cdot m^2$
Moment of inertia I_y	$7.333\times10^{8} kg\cdot m^2$
Moment of inertia I_z	$14.666\times10^{8} kg\cdot m^2$

Furthermore, the proposed control law is compared with the existing E-sail attitude feedback linearization controller [56] as a benchmark method. The parameters are kept the same with Ref. [56], where the desired angles at the end of control are defined as: $\zeta_d = 30^\circ$, and $\eta_d = -20^\circ$. The other parameters are presented in Table 7-2 and the model uncertainty is not considered. The simulation time step is 0.01s, and the total simulation time is five days. The dynamic responses of the E-sail are presented in Figure 7-10. The results show that the Euler angles are controlled to the desired value in both cases. For the E-sail model with the proposed controller, the Euler angles quickly and smoothly approaches to the desired value without any overshoot in about 1.5

days. However, it takes a longer time for the E-sail with the feedback controller reach the desired values with overshoots. For instance, the E-sail model with the feedback controller approaches to the desired values in about three days instead of 1.5 days in the case of E-sail model with the proposed controller. It indicates that the proposed control approach can be utilized as the benchmark method.

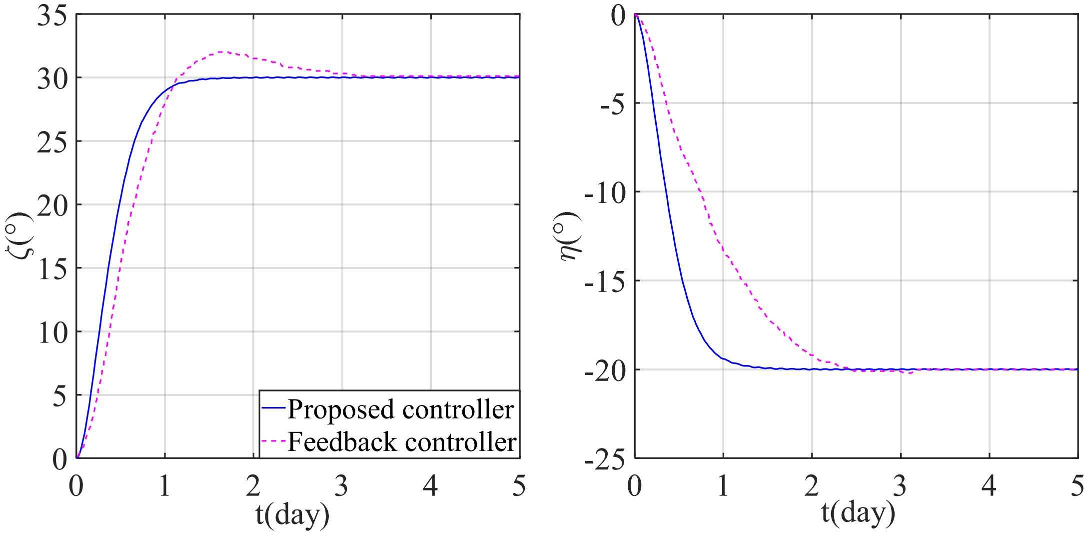

Figure 7-10 Time histories of (a) the Euler angles and (b) the sail and clock angles with both controllers.

Thus, in the rest of current paper, the results of the reduced order analytical E-sail model will be used as a benchmark, where the proposed control law is acting on the NPFEM-based high-fidelity E-sail model.

7.2.2.2 Attitude Control of NPFEM E-sail Model

The aim of this section is to validate the effectiveness of the attitude controller by applying it to the NPFEM-based high-fidelity electric sail model. The main tethers are not charged in this section and the control thrusts are applied at the remote units. Since the attitude dynamics of electric sail is defined by the nodal information of the NPFEM model instead of the angular parameters, the control torques derived from the proposed control law in Section 7.2.1 are replaced by the equivalent control forces acting on the remote units based on Equation (7.19). It should be noted that the Euler angles and angular rates are obtained numerically in the high-fidelity E-sail model at each time step by Equations (3.7)-(3.10) and Equation (3.101) using the nodal position and velocity information. The numerical simulation is performed for the same two mission scenarios as the ones in the previous section with the same parameters in Table 4-1 and Table 7-1. Each main tether is discretized into four tether elements while each auxiliary tether is discretized into one tether elements. The simulation results of the attitude dynamics under the proposed controller are illustrated in Figure 7-11 to Figure 7-16.

First, the Euler angles, Euler angular rates, and sail and clock angles are successfully controlled to the desired values in the first scenario as shown in Figure 7-11. It demonstrates that the control strategy law derived from the reduced order analytical model is applicable to the high-fidelity model, where the sail and clock angles are indirectly controlled by injecting appropriate control thrusts at the remote units. However, unlike the dynamic responses of the reduced order analytical model, it takes a longer time for the Euler angles or the sail and clock angles to reach the desired values and with overshoots. For instance, the high-fidelity model approaches to the desired values in about 1.5 days instead of 0.3 days in the case of reduced order model. The different response is attributed to the characteristics of rigid-body and flexible modes of the flexible tethers. The control torques applied to the reduced order analytical model results in an instantaneous response of attitude motion due to the rigid model assumption. The control forces acting on the remote units of the flexible electric sail model need to be transmitted to the entire system through the elastic deflection and elongation of tethers, which takes time. In addition, the control law includes the velocity feedback, which is analog to the viscous damping effect on a dynamic system. The response of the high-fidelity model resembles an underdamped dynamic system. The oscillation of an underdamped system can be reduced by increasing the damping effect, which is analog to increase the velocity feedback in a feedback control law. Thus, the difference between the two models can be reduced by increasing control gains in the high-fidelity model, which will be discussed in the following section. The high-fidelity model of E-sail provides a virtual experiment testbed to validate and tune the control law developed from the reduced order analytical model of E-sail before a real space mission.

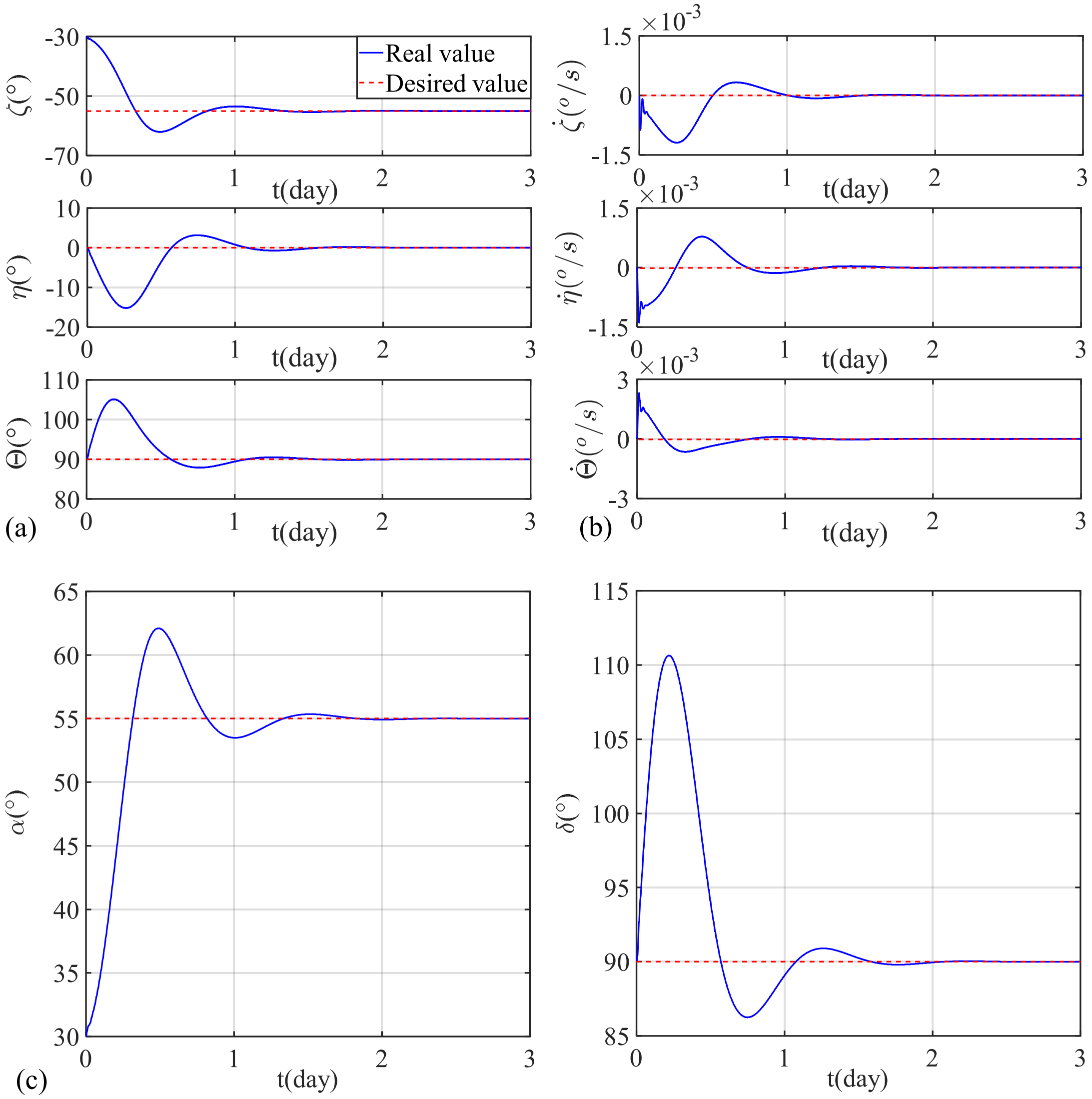

Figure 7-11 Time histories of (a) the Euler angles (b) the Euler angular rates and (c) the sail and clock angles with the desired 55° sail angle.

Furthermore, Figure 7-12 and Figure 7-13 show that the control torques, sliding surfaces, and control force acting on the 1st remote unit decreases as the attitude of the E-sail approached the desired state and eventually are maintained at zero as required. It demonstrates the effectiveness of the control law. The oscillation in control forces reflect the elastic deformation characteristics of tethers.

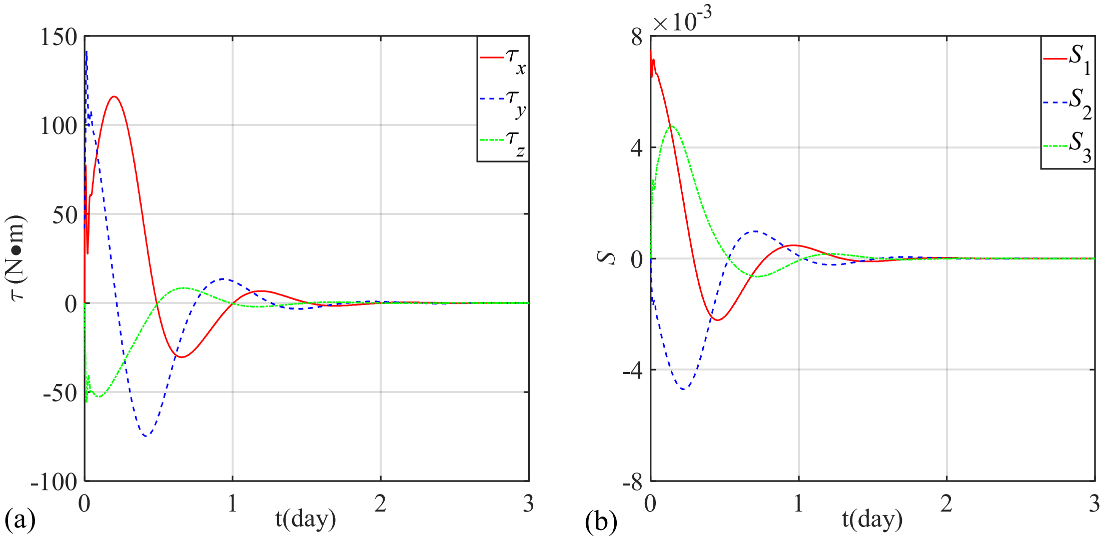

Figure 7-12 Time histories of (a) the control torques in the $O_{sp}X_{sp}Y_{sp}Z_{sp}$ frame and (b) sliding surfaces with the desired 55° sail angle.

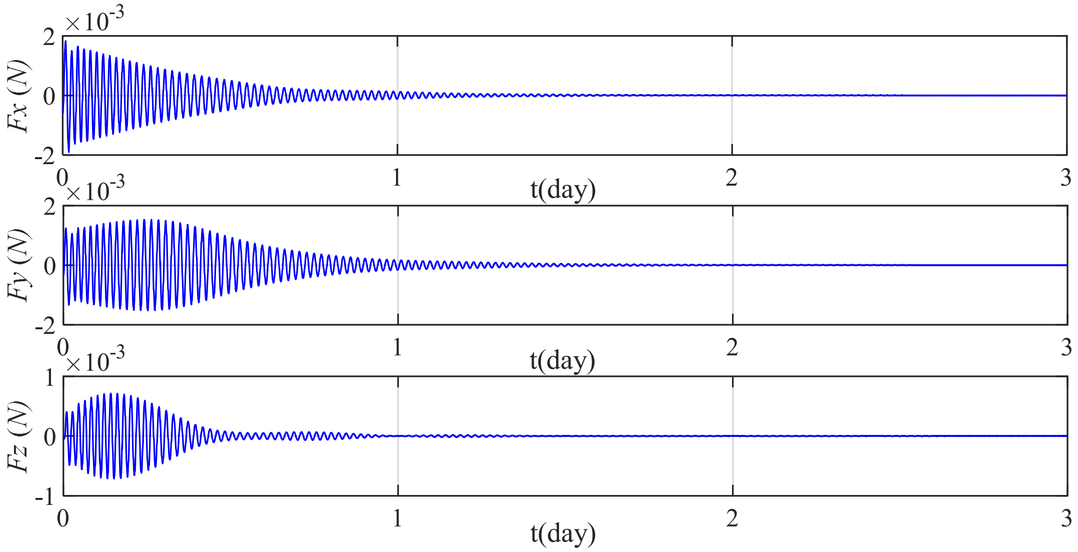

Figure 7-13 Time histories of control forces acting on the 1st remote unit in the $O_sX_sY_sZ_s$ frame with the desired 55° sail angle.

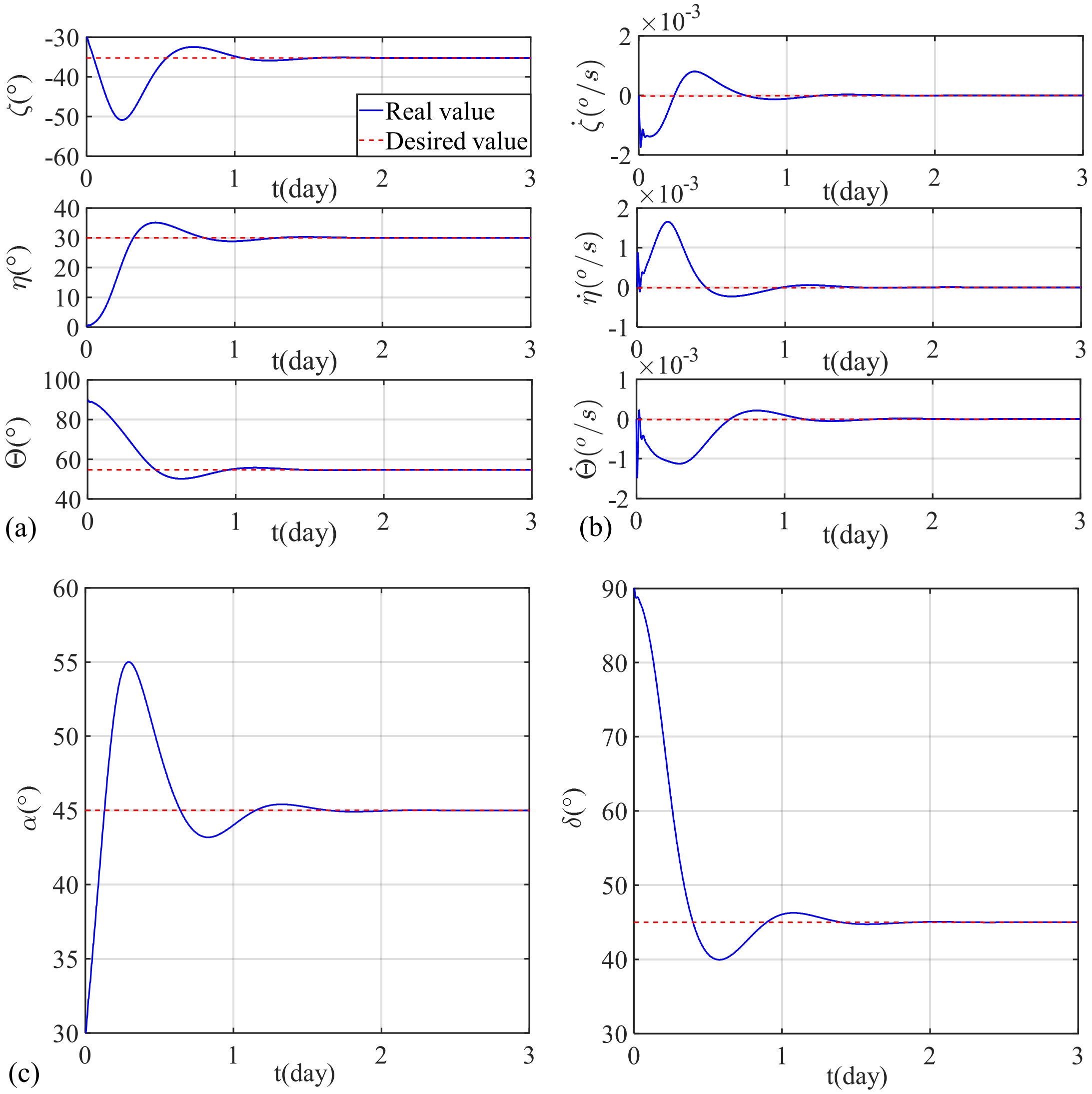

Figure 7-14 Time histories of (a) the Euler angles (b) the Euler angular rates and (c) the sail and clock angles with the desired 45° sail angle.

Finally, the simulation results of the high-fidelity NPFEM E-sail model in the second scenario is shown in Figure 7-14 to Figure 7-16. The results verify that the proposed control strategy is also effective in a heliocentric ecliptic plane escape mission. Similarly, the response of the high-fidelity model takes a longer time to reach the desired states with overshoots. Thus, it can be concluded that the developed control law is effective and accurate.

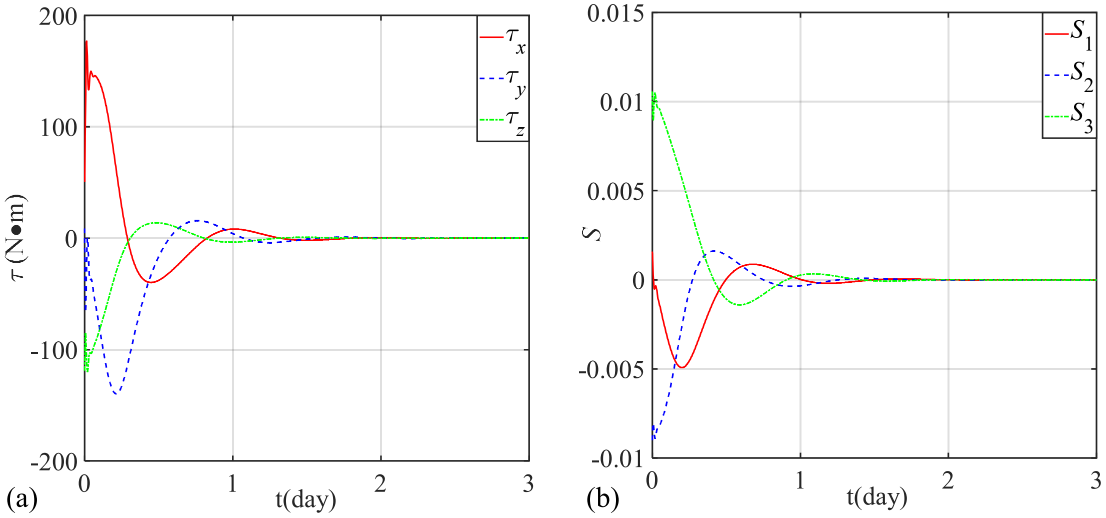

Figure 7-15 Time histories of (a) the control torques in the $O_{sp}X_{sp}Y_{sp}Z_{sp}$ frame and (b) sliding surfaces with the desired 45° sail angle.

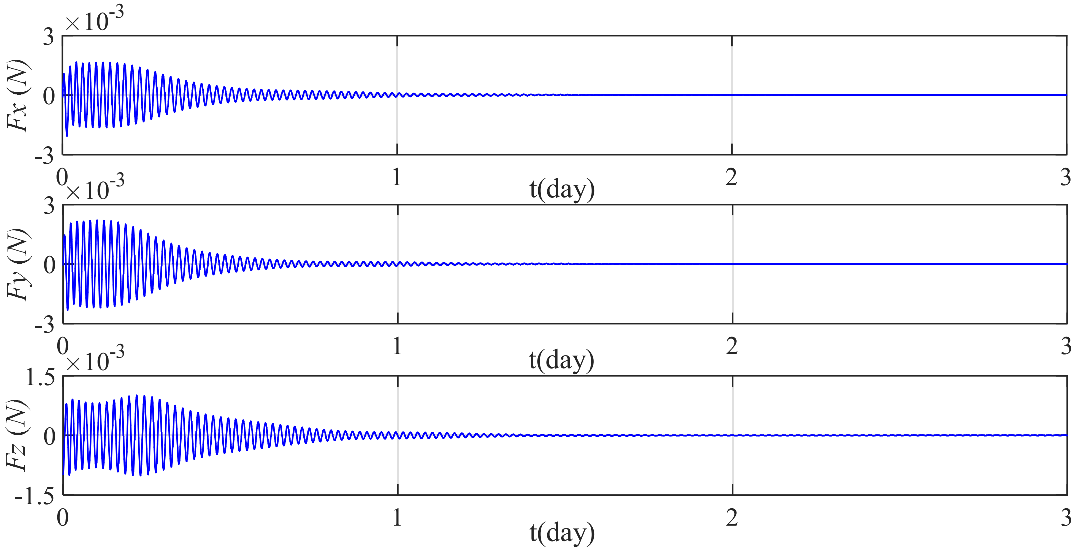

Figure 7-16 Time histories of control forces acting on the 1st remote unit in the $O_sX_sY_sZ_s$ frame with the desired 45° sail angle.

7.2.2.3 Influence of Control Gains on Attitude Control of NPFEM E-sail Model

This section further investigates the influence of the control gains on the electric sail attitude control in the dynamic responses of the high-fidelity E-sail model by varying the control gains. Three cases are tested here, that is, Case A, Case B and Case C. The gains of three cases are listed in Table 7-3. For the sake of simplicity, only the second scenario is considered here, such that, the desired sail and clock angles are $\alpha_d = 45^\circ$ and $\delta_d = 45^\circ$. The other parameters are kept the same as shown in Table 4-1 and Table 7-1. To eliminate the effect of the propulsive force, the main tethers are still uncharged. The finite element mesh of the tethers in the E-sail system is unchanged. The results of the numerical simulations are presented in Figure 7-17 and Figure 7-18. As comparisons, the control gains are also applied to the reduced order analytical E-sail model.

Table 7-3 Parameters of the control gains.

Label	Control gain $[\lambda_1 \quad \lambda_2 \quad \lambda_3]$	Control gains $[k_{11} \quad k_{12} \quad k_{13}]$	Control gains $[k_{21} \quad k_{22} \quad k_{23}]$
Case A	$3\times10^{-4}[1 \quad 1 \quad 1]$	$1\times10^{-11}[1 \quad 1 \quad 1]$	$3\times10^{-4}[1 \quad 1 \quad 1]$
Case B	$5\times10^{-4}[1 \quad 1 \quad 1]$	$1\times10^{-11}[1 \quad 1 \quad 1]$	$5\times10^{-4}[1 \quad 1 \quad 1]$
Case C	$1\times10^{-3}[1 \quad 1 \quad 1]$	$1\times10^{-11}[1 \quad 1 \quad 1]$	$1\times10^{-3}[1 \quad 1 \quad 1]$

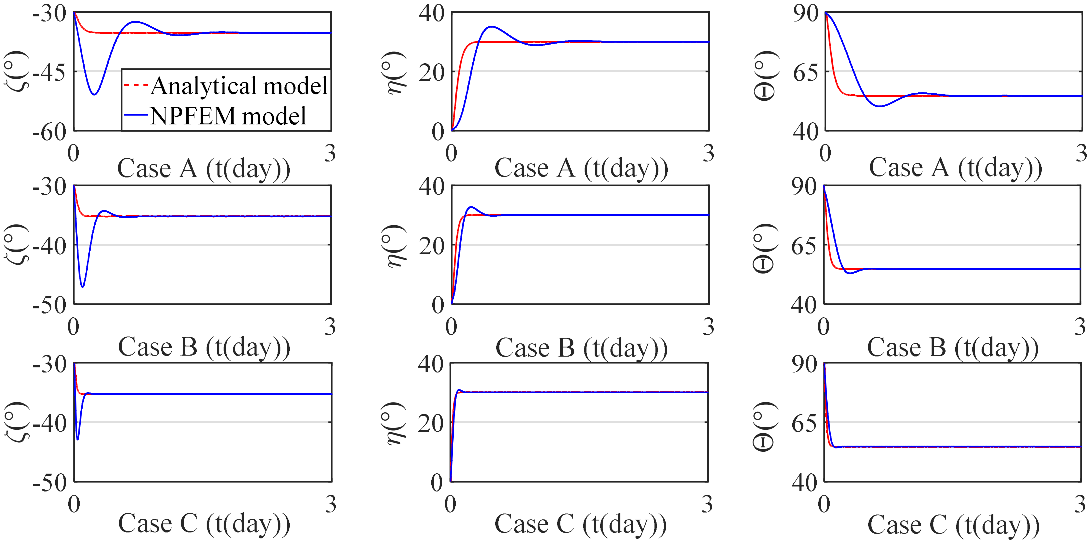

(a) Euler angles

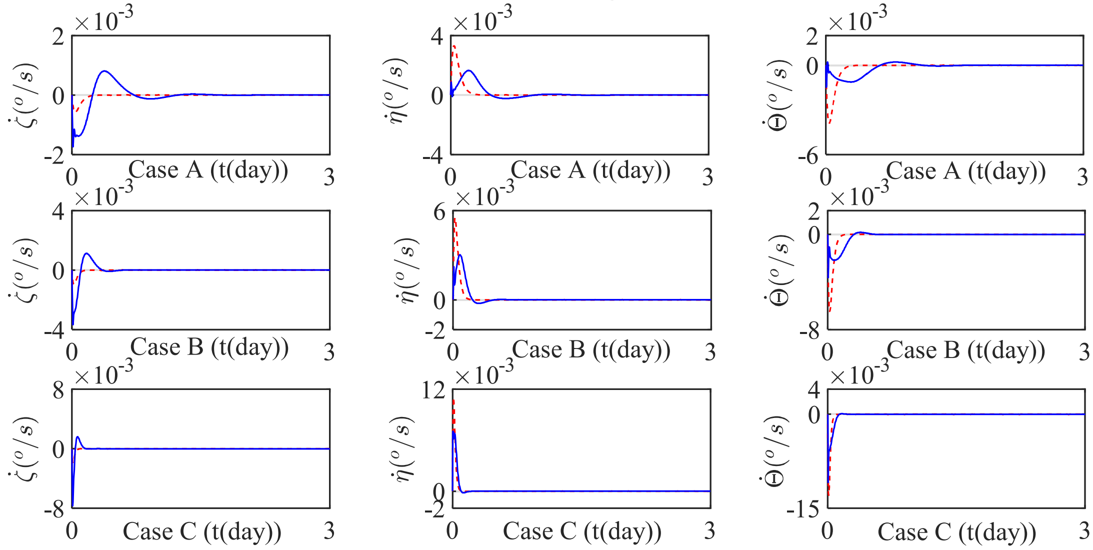

(b) Euler angular rates

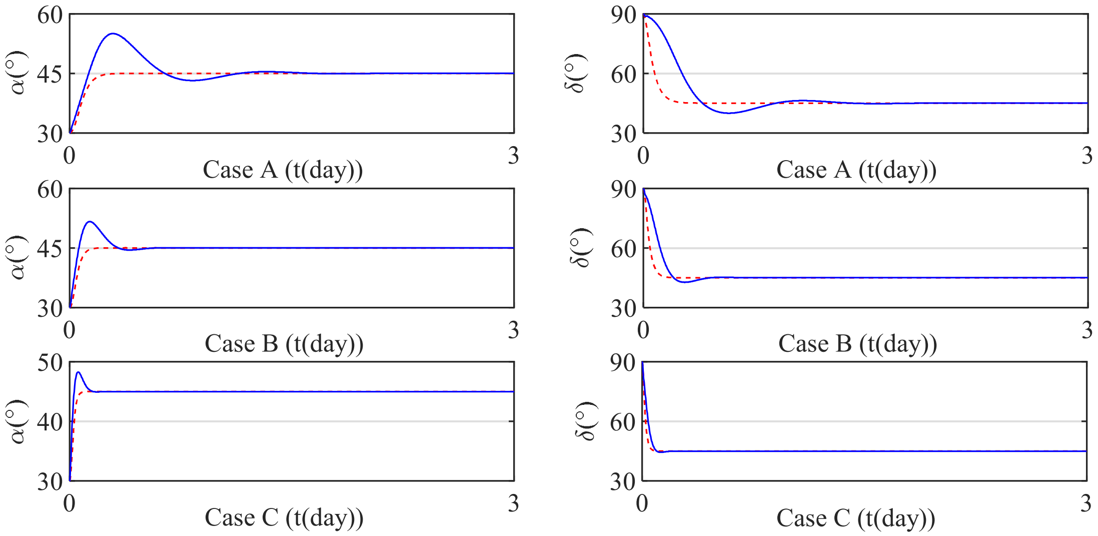

(c) Sail and clock angles

Figure 7-17 Comparison of time histories of attitude results of two models with different control gains.

Figure 7-17 shows that the difference between the Euler angles, Euler angular rates, and corresponding sail and clock angles of two models in three cases. The higher the control gains, the greater the control forces, and the faster the high-fidelity E-sail model approaches to the desired attitude. At the same time, the difference between the responses of the reduced order analytical model and the high-fidelity model is also diminished. For instance, when the control gains are large enough as shown in the Case C, the trajectories of the angles and angular rates under the two models are approximately the same and the overshoot diminishes. This verifies the explanation of the phenomena in the previous section, that is, the shorter force transmission caused by the larger control forces will lead to the same attitude trajectories of the two models approximately.

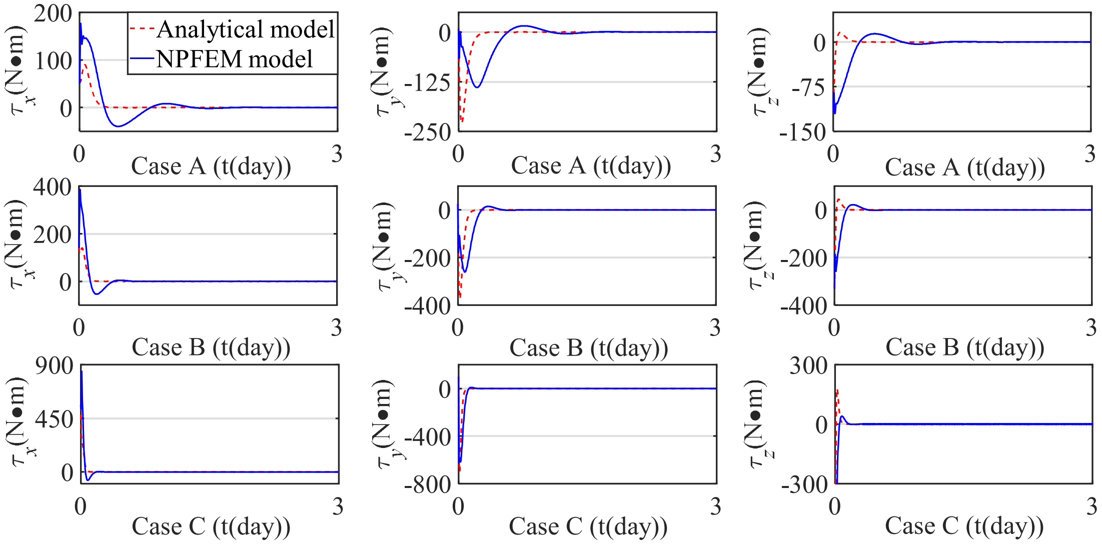

(a) Control torques

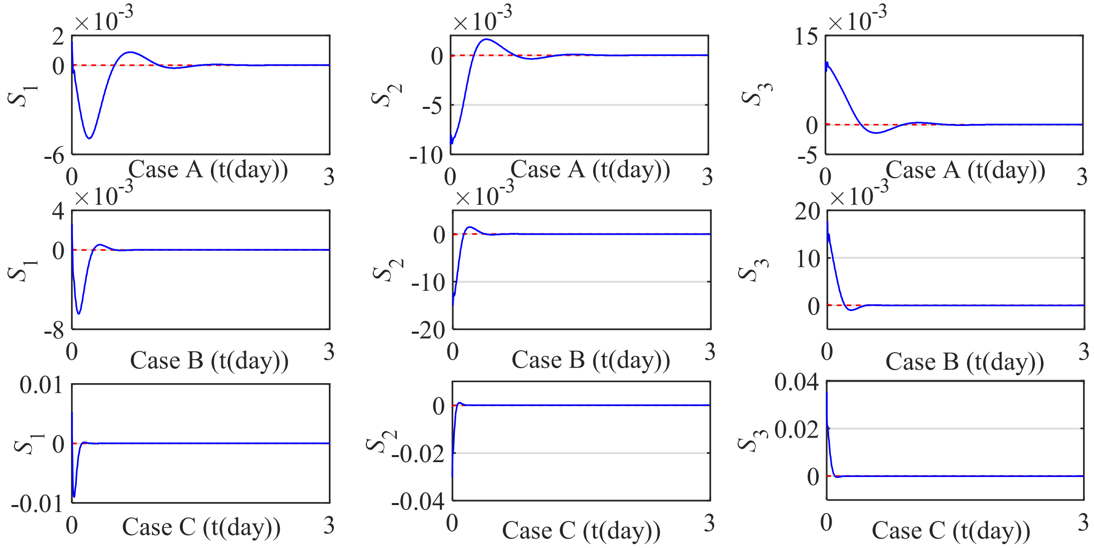

(b) Sliding surfaces

Figure 7-18 Comparison of time histories of control outputs of two models with different control gains.

The time histories of the control torque and sliding surfaces demonstrate the similar findings, as illustrated in Figure 7-18. Therefore, it can be concluded that the actual influence of the control strategy can be verified through the flexible E-sail model.

7.2.2.4 Attitude Control of NPFEM Model by Modulating the Voltage of Main Tethers

In this section, the attitude control derived from the reduced order analytical model is used to individually adjust the main tethers' voltage to generate the required control torque. The voltage is assumed to be bounded by the minimum and maximum voltages between 0 and 40kV as mentioned before. The baseline voltage is assumed as 20kV. It is calculated by the solution of Equation (7.22). The first mission scenario is selected to conduct the numerical simulation, and the control gains are the same as Case A, which are given in Table 7-3. The other parameters are consistent with Table 4-1 and Table 7-1.

Figure 7-19 shows that the Euler angles, Euler angular rates, and sail and clock angles are successfully controlled to the desired states with small oscillations. This demonstrates that the attitude of the high-fidelity electric sail model can be controlled through individually adjusting the main tethers' voltage based on the proposed control strategy. Compared with the results in Figure 7-11, it takes 2 days to reach the desired states in Figure 7-19 instead of 1.5 days in Figure 7-11. This is due to the insufficient control torque in the case of voltage modulation due to the voltage limitation. For instance, the voltage time history of the 1st main tether shows that the tether voltage reaches the maximum threshold, see Figure 7-20. Meanwhile, it is known that the coning motion of the main tethers [27, 72] will slightly reduce the control torque, leading to a longer time to reach the desired states.

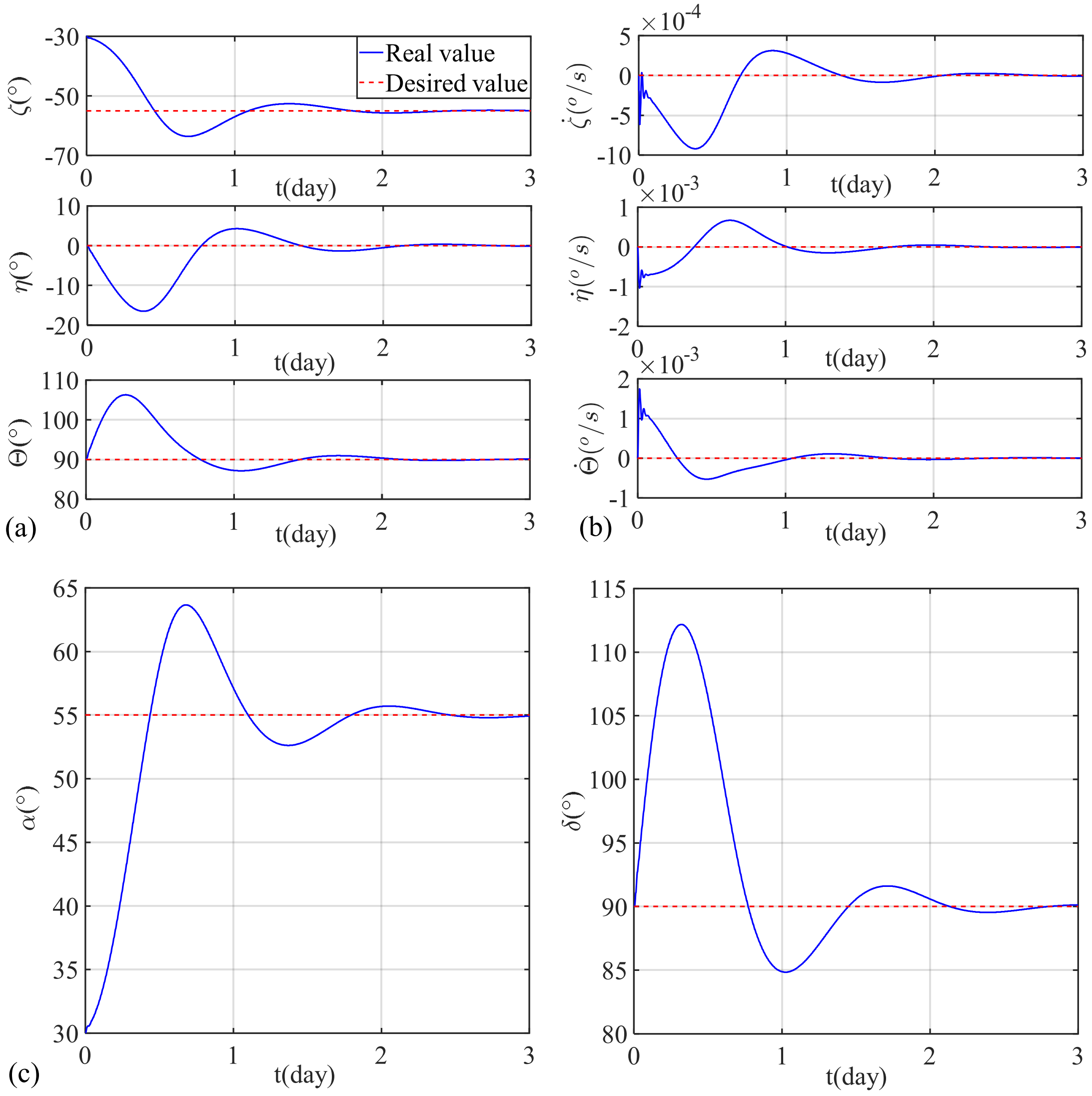

Figure 7-19 Time histories of (a) Euler angles (b) Euler angular rates and (c) sail and clock angles with the voltage control.

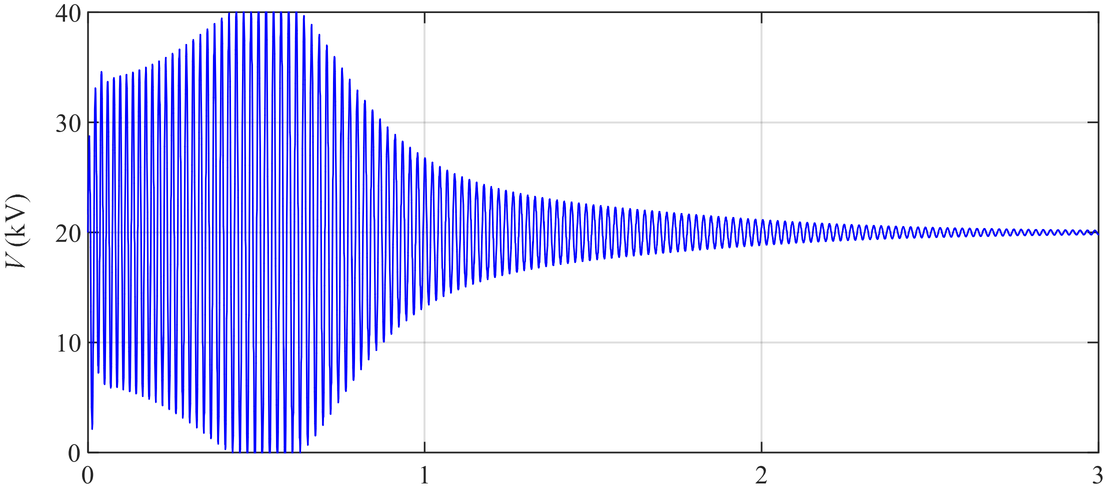

Figure 7-20 Time histories of the 1st main tether's voltage.

In summary, the proposed control strategy is applicable to both control schemes, in which the control forces are generated by thrust at remote units and voltage modulation of main tethers, respectively.

7.3 Trajectory Design and Tracking for Mars Exploration Using E-sail

The performance of E-sail in the Mars exploration is investigated in this section. First, the minimum-time trajectory of E-sail is designed by using the propulsive force model that is composed of each tether's voltage and attitude angles. Then, the designed trajectory is tracked by using the torques generated by each tether's voltage. Moreover, the attitude dynamics of the central spacecraft and remote units are ignored, and all tethers are straight, rigid and in the spin plane without consideration of coning motion.

7.3.1 Minimum-time Earth-Mars Trajectory of E-sail

7.3.1.1 Mathematical Model of E-sail Propulsive Force

Letting $V_{new} = V - V_w \geq 0$, Equations (3.16) and (3.17) can be rewritten as

$$\boldsymbol{f}_{dl} = 0.18 V_{new} \sqrt{\varepsilon_0 m_p n}\ \boldsymbol{v}_{sw\perp} \tag{7.23}$$

Recall Equation (4.30), the component of the solar wind velocity ($\boldsymbol{v}_{sw\perp}^b$) perpendicular to the i^{th} main tether in the $O_o X_o Y_o Z_o$ frame can be written as

$$\boldsymbol{v}_{sw\perp}^o = \mathrm{v}\left(\boldsymbol{l}_i^o \times \boldsymbol{r}^o\right) \times \boldsymbol{l}_i^o \tag{7.24}$$

where $i = 1, \cdots N$, N is the total number of the main tethers/remote units, $\boldsymbol{r}^o = \begin{bmatrix} 0 & 0 & 1 \end{bmatrix}^T$ is the Sun-spacecraft unit vector, and $\boldsymbol{l}_i^o$ is the unit vector aligned with the i^{th} main tether, that is,

$$\begin{aligned} \boldsymbol{l}_i^o &= \left(\boldsymbol{T}_{o2sp}\right)^T \left(\boldsymbol{T}_{sp2b}\right)^T \boldsymbol{l}_i^b \\ &\begin{bmatrix} \left\{\cos\eta\cos\Theta\cos\left(2\pi(i-1)/N + \omega_0 t\right) - \cos\eta\sin\Theta\sin\left(2\pi(i-1)/N + \omega_0 t\right)\right\} \\ \left\{\begin{matrix} \left(\sin\zeta\sin\eta\cos\Theta + \cos\zeta\sin\Theta\right)\cos\left(2\pi(i-1)/N + \omega_0 t\right) + \\ \left(\cos\zeta\cos\Theta - \sin\zeta\sin\eta\sin\Theta\right)\sin\left(2\pi(i-1)/N + \omega_0 t\right) \end{matrix}\right\} \\ \left\{\begin{matrix} \left(\sin\zeta\sin\Theta - \cos\zeta\sin\eta\cos\Theta\right)\cos\left(2\pi(i-1)/N + \omega_0 t\right) + \\ \left(\cos\zeta\sin\eta\sin\Theta + \sin\zeta\cos\Theta\right)\sin\left(2\pi(i-1)/N + \omega_0 t\right) \end{matrix}\right\} \end{bmatrix} \end{aligned} \tag{7.25}$$

where $\boldsymbol{l}_i^b$ is given in Equation (3.89).

Substituting Equation (7.25) into Equation (7.24) yields

$$
\boldsymbol{v}^{o}_{sw\perp} = \nu \left[\begin{array}{l}
\cos\eta\left(\sin\Theta\sin\left(2\pi(i-1)/N+\omega_0 t\right)-\cos\Theta\cos\left(2\pi(i-1)/N+\omega_0 t\right)\right) \\
\left\{\sin\zeta\cos\Theta\sin\left(2\pi(i-1)/N+\omega_0 t\right)+\sin\zeta\sin\Theta\cos\left(2\pi(i-1)/N+\omega_0 t\right)-\right. \\
\left.\cos\zeta\sin\eta\cos\Theta\cos\left(2\pi(i-1)/N+\omega_0 t\right)+\cos\zeta\sin\eta\cos\Theta\cos\left(2\pi(i-1)/N+\omega_0 t\right)\right\} \\
\left(\cos^2\zeta\sin\eta\sin\Theta\cos\Theta-\sin\zeta\cos\zeta\sin^2\Theta\right)\cos^2\left(2\pi(i-1)/N+\omega_0 t\right)- \\
\sin\zeta\cos\zeta\cos^2\Theta\sin^2\left(2\pi(i-1)/N+\omega_0 t\right)+ \\
\cos^2\zeta\sin\eta\cos^2\Theta\sin\left(2\pi(i-1)/N+\omega_0 t\right)\cos\left(2\pi(i-1)/N+\omega_0 t\right)- \\
\sin^2\zeta\sin\eta\sin\Theta\cos\Theta\cos^2\left(2\pi(i-1)/N+\omega_0 t\right)- \\
\cos^2\zeta\sin\eta\sin\Theta\cos\Theta\sin^2\left(2\pi(i-1)/N+\omega_0 t\right)- \\
\left(\cos^2\zeta\sin^2\Theta+\sin^2\zeta\cos^2\Theta\right)\sin\eta\sin\left(2\pi(i-1)/N+\omega_0 t\right)\cos\left(2\pi(i-1)/N+\omega_0 t\right)+ \\
\left(\begin{array}{l}\sin\Theta\cos\left(2\pi(i-1)/N+\omega_0 t\right) \\ +\cos\Theta\sin\left(2\pi(i-1)/N+\omega_0 t\right)\end{array}\right)\sin^2\zeta\sin\eta\sin\Theta\sin\left(2\pi(i-1)/N+\omega_0 t\right)+ \\
\sin\zeta\cos\zeta\sin^2\eta\left(\cos^2\Theta\cos^2\left(2\pi(i-1)/N+\omega_0 t\right)+\sin^2\Theta\sin^2\left(2\pi(i-1)/N+\omega_0 t\right)\right)- \\
2\sin\zeta\cos\zeta\sin\Theta\cos\Theta\sin\left(2\pi(i-1)/N+\omega_0 t\right)\cos\left(2\pi(i-1)/N+\omega_0 t\right)\left(1+\sin^2\eta\right) \\
\left(\sin^2\zeta\sin^2\eta+\cos^2\eta\right)\left(\begin{array}{l}\sin^2\Theta\sin^2\left(2\pi(i-1)/N+\omega_0 t\right) \\ +\cos^2\Theta\cos^2\left(2\pi(i-1)/N+\omega_0 t\right)\end{array}\right)+ \\
\cos^2\zeta\left(\sin^2\Theta\cos^2\left(2\pi(i-1)/N+\omega_0 t\right)+\cos^2\Theta\sin^2\left(2\pi(i-1)/N+\omega_0 t\right)\right)+ \\
2\left(\cos^2\zeta-\cos^2\eta\right)\sin\Theta\cos\Theta\sin\left(2\pi(i-1)/N+\omega_0 t\right)\cos\left(2\pi(i-1)/N+\omega_0 t\right)+ \\
2\left(\cos^2\Theta-\sin^2\Theta\right)\sin\zeta\cos\zeta\sin\eta\sin\left(2\pi(i-1)/N+\omega_0 t\right)\cos\left(2\pi(i-1)/N+\omega_0 t\right)+ \\
2\sin\zeta\cos\zeta\sin\eta\sin\Theta\cos\Theta\left(\cos^2\left(2\pi(i-1)/N+\omega_0 t\right)-\sin^2\left(2\pi(i-1)/N+\omega_0 t\right)\right)- \\
2\sin^2\zeta\sin^2\eta\sin\Theta\cos\Theta\sin\left(2\pi(i-1)/N+\omega_0 t\right)\cos\left(2\pi(i-1)/N+\omega_0 t\right)
\end{array} \right]
$$

(7.26)

Thus, the propulsive force of the i^{th} main tether in the $O_sX_sY_sZ_s$ frame is

$$\boldsymbol{F}_i^s = \left(\boldsymbol{A}_{s2o}\right)^T \boldsymbol{F}_i^o = \sigma_{new}\ V_{new\_i}\left(\boldsymbol{A}_{s2o}\right)^T \boldsymbol{v}_{sw\perp}^o \tag{7.27}$$

where V_{new_i} is the voltage of the i^{th} main tether, $\sigma_{new} = 0.18\sqrt{\varepsilon_0 m_p n}$.

Then, the total propulsive force of E-sail in the $O_sX_sY_sZ_s$ frame can be obtained as

$$\boldsymbol{F}\left(V_{new\_1}, V_{new\_2}, \cdots, V_{new\_N}\right) = \sum_{i=1}^{N} \boldsymbol{F}_i^s \tag{7.28}$$

When the voltage of each main tether are the same, that is $V_{new\_1} = V_{new\_2} = \cdots V_{new\_N} = V_{new}$, the total propulsive force in Equation (7.28) can be simplified as

$$\boldsymbol{F}\left(V_{new\_1}, V_{new\_2}, \cdots, V_{new\_N}\right) = \frac{1}{2} NL\sigma_{new}V_{new}\nu \begin{bmatrix} \left\{ \begin{array}{l} \cos\psi\cos\phi\cos\zeta\sin\eta\cos\eta + \\ \sin\psi\sin\zeta\cos\zeta\cos^2\eta + \\ \sin\phi\cos\psi\left(\cos^2\zeta + 1\right) \end{array} \right\} \\ \left\{ \begin{array}{l} \cos\phi\sin\psi\cos\zeta\sin\eta\cos\eta - \\ \cos\psi\sin\zeta\cos\zeta\cos^2\eta + \\ \sin\phi\sin\psi\left(\cos^2\zeta + 1\right) \end{array} \right\} \\ \left\{ \begin{array}{l} -\sin\phi\cos\zeta\sin\eta\cos\eta + \\ \cos\phi\left(\cos^2\zeta + 1\right) \end{array} \right\} \end{bmatrix} \tag{7.29}$$

It should be noted that the propulsive force is independent with the

Euler angle Θ in this situation.

7.3.1.2 Orbital Dynamic Equations and Trajectory Optimization of E-sail

The orbital dynamic equations of the E-sail in the $O_sX_sY_sZ_s$ frame can be written as

$$\begin{aligned}
\dot{r}_x &= v_x \\
\dot{v}_x &= -\frac{\mu_\odot}{r^3} r_x + \kappa \frac{F_x\left(V_{new\_1}, V_{new\_2}, \cdots, V_{new\_N}\right)}{m_E} \\
\dot{r}_y &= v_y \\
\dot{v}_y &= -\frac{\mu_\odot}{r^3} r_y + \kappa \frac{F_y\left(V_{new\_1}, V_{new\_2}, \cdots, V_{new\_N}\right)}{m_E} \\
\dot{r}_z &= v_z \\
\dot{v}_z &= -\frac{\mu_\odot}{r^3} r_z + \kappa \frac{F_z\left(V_{new\_1}, V_{new\_2}, \cdots, V_{new\_N}\right)}{m_E}
\end{aligned} \tag{7.30}$$

where $\kappa \in \left[0 \quad 1\right]$ is the coefficient to control the propulsive force on-off, $\mu_\odot$ is the Standard gravitational parameter of the Sun, m_E is the total mass of E-sail, $\boldsymbol{r} = \left[r_x \quad r_y \quad r_z \right]^T$ and $\boldsymbol{F} = \left[F_x \quad F_y \quad F_z \right]^T$ are the position and propulsive force vectors of E-sail in the $O_sX_sY_sZ_s$ frame, respectively.

Because the E-sail is a propellantless propulsion system, the performance index of the Earth-Mars trajectory optimization of E-sail is time-optimal, which can be written as

$$J = \Delta t = t_f - t_0 \tag{7.31}$$

where t_0 and t_f are the initial and final times of the Earth-Mars orbital transfer, respectively.

Then, the boundary conditions of the E-sail can be given by

$$\begin{cases} \boldsymbol{r}_0 = \begin{bmatrix} r_{x0} & r_{y0} & r_{z0} \end{bmatrix}^T \\ \boldsymbol{v}_0 = \begin{bmatrix} \sqrt{\mu_{\odot}/r_{x0}} & \sqrt{\mu_{\odot}/r_{y0}} & \sqrt{\mu_{\odot}/r_{z0}} \end{bmatrix}^T \end{cases}$$

$$\begin{cases} \boldsymbol{r}_f = \begin{bmatrix} r_{xf} & r_{yf} & r_{zf} \end{bmatrix}^T \\ \boldsymbol{v}_f = \begin{bmatrix} \sqrt{\mu_{\odot}/r_{xf}} & \sqrt{\mu_{\odot}/r_{yf}} & \sqrt{\mu_{\odot}/r_{zf}} \end{bmatrix}^T \end{cases} \tag{7.32}$$

where $\boldsymbol{r}_0$ and $\boldsymbol{v}_0$ are the initial position and velocity vectors, $\boldsymbol{r}_f$ and $\boldsymbol{v}_f$ are the final position and velocity vectors, respectively.

As mentioned before, the maximum sail angle is set as 70° [3]. Thus, the inequality path constraints can be obtained as

$$\cos\zeta \cos\eta \le \cos\alpha_{\max} \tag{7.33}$$

7.3.1.3 Numerical Results

The minimum-time Earth-Mars trajectory is obtained by using the optimization software GPOPS-II [108] with the 1×10^{-8} tolerance of the residual error. As the voltages of all the tethers are kept the same, the propulsive force equation (7.29) is used in the orbital dynamic equations of

Equation (7.30). The simulation parameters of the Earth-Mars trajectory optimization problem are presented in Table 7-4. The physics parameters of tethers are the same with Table 4-1, which is consistent with Ref. [12]. The simulation results are illustrated in Figure 7-21 to Figure 7-24.

Table 7-4 Parameters of the Earth-Mars trajectory optimization.

Parameters	Values
Initial position vector $\boldsymbol{r}_0$ (au)	$\begin{bmatrix}1 & 0 & 0\end{bmatrix}^T$
Final position r_f (au)	1.524
Initial spin rate ω_0 (rad/s)	0.004
Mass of central spacecraft (kg)	100
Mass of remote unit (kg)	1.5
Solar wind velocity (km/s)	400
Tether voltage V_{new} (kV)	21
Number of tethers (N)	40
Length of Main tether (km)	10

Figure 7-21 shows that the transfer trajectory of E-sail can arrive on Mars from Earth at about 518 days. It demonstrates the effectiveness of the designed trajectory. Meanwhile, the maximum attitude angles are less than 60 degrees, which satisfies the path constraint as shown in Figure 7-22. It can be seen that the change curves of the angles are continuous and smooth, which makes it very convenient for attitude tracking control of the E-sail during the orbital transfer. Further, Figure 7-23 illustrates that the propulsive force is shut down during the orbital transfer for about 150 days, which can be achieved by turning off the voltage of the main tethers. It indicates the minimum-time trajectory includes a coasting arc. Finally, the time histories of the mesh refinement is presented in Figure 7-24.

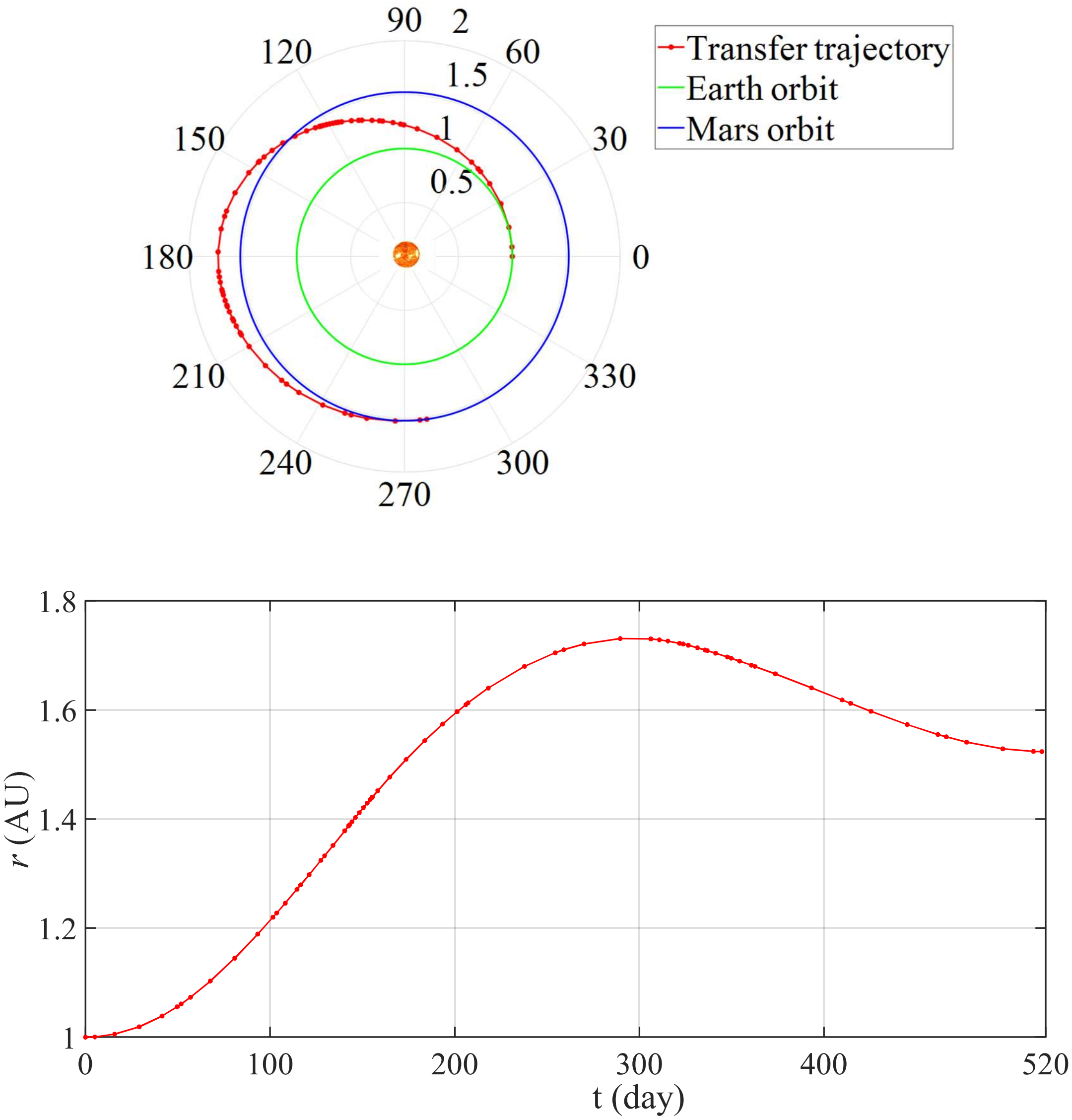

Figure 7-21 Transfer trajectory of E-sail from Earth to Mars.

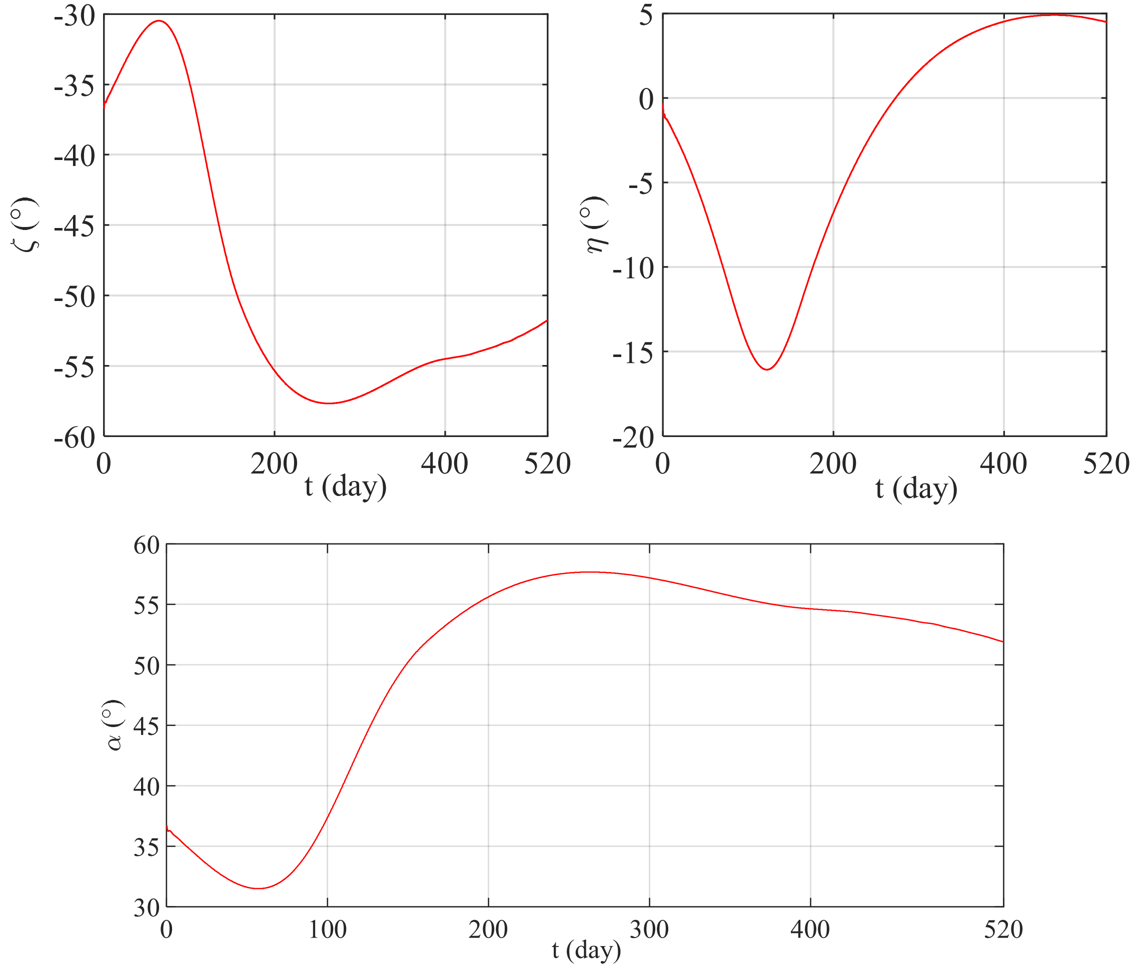

Figure 7-22 Time histories of attitude angles.

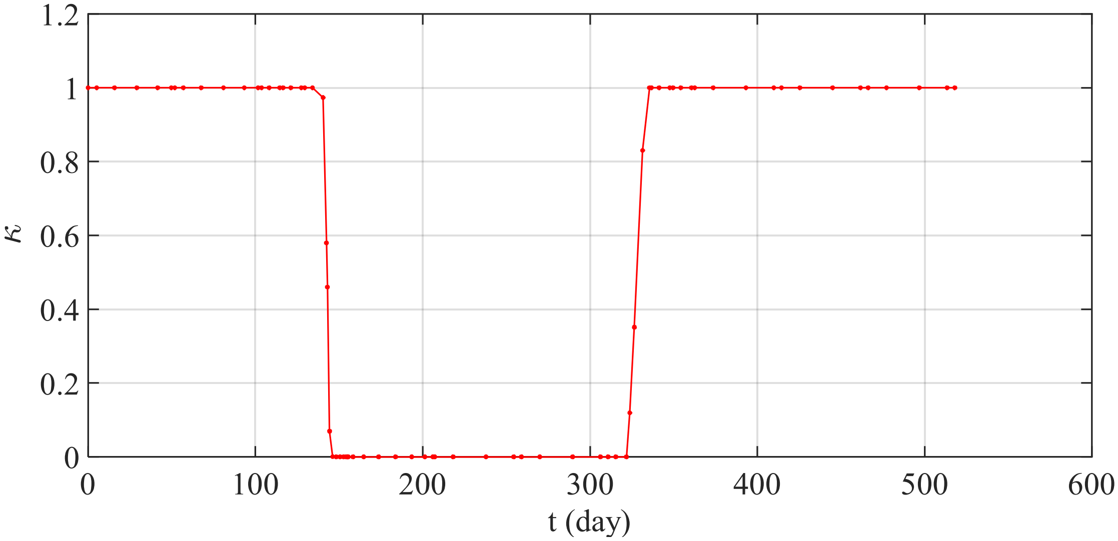

Figure 7-23 Time histories of propulsive force coefficient.

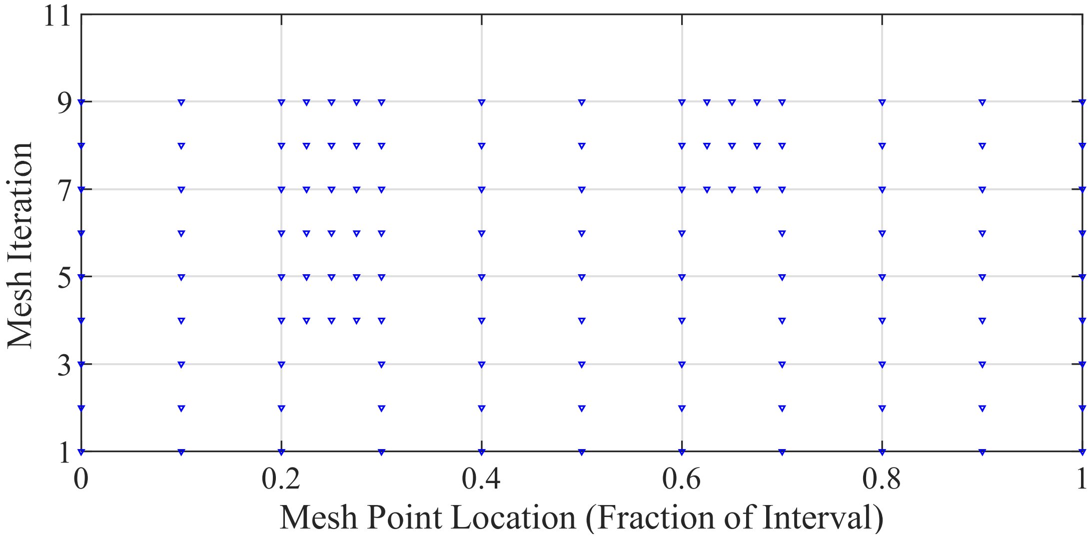

Figure 7-24 Time histories of mesh refinement iteration.

7.3.2 Earth-Mars Trajectory Tracking of E-sail with Voltage Modulation

7.3.2.1 Mathematical Model of E-sail Propulsive Force Torque

The infinitesimal propulsion torque $d\tau_{t\_i}$ of the i^{th} main tether in the

$O_{sp}X_{sp}Y_{sp}Z_{sp}$ frame is given by

$$d\tau_{t\_i} = \boldsymbol{l}_i^{sp} l \times \boldsymbol{f}_{dl}^{sp} dl \tag{7.34}$$

$$\boldsymbol{f}_{dl}^{sp} = \boldsymbol{T}_{o2sp}\boldsymbol{T}_{s2o}\boldsymbol{T}_{t2s}^{k}\boldsymbol{f}_{dl}\boldsymbol{f}_{dl} \tag{7.35}$$

where dl is the infinitesimal tether length at the distance of l from the central spacecraft, $\boldsymbol{l}_i^{sp}$ is given in Equation (3.90), $\boldsymbol{f}_{dl}^{sp}$ is the propulsive force of the i^{th} main tether in the $O_{sp}X_{sp}Y_{sp}Z_{sp}$ frame, respectively.

The component of the solar wind velocity ($\boldsymbol{v}_{sw\perp}^{sp}$) can be obtained as

$$\boldsymbol{v}_{sw\perp}^{sp} = \left(\boldsymbol{T}_{o2sp}\right)^{T}\boldsymbol{v}_{sw\perp}^{o} \tag{7.36}$$

Substituting Equations (7.35) and (7.36) into Equation (7.34) yields

$$d\tau_{t\_i} = \sigma_{new} v l V_{new\_i} \begin{bmatrix} \cos\zeta\cos\eta\sin\left(2\pi(i-1)/N+\omega_0 t\right) \\ -\cos\zeta\cos\eta\cos\left(2\pi(i-1)/N+\omega_0 t\right) \\ \sin\zeta\cos\Theta\cos\left(2\pi(i-1)/N+\omega_0 t\right)-\sin\zeta\sin\Theta\sin\left(2\pi(i-1)/N+\omega_0 t\right)+ \\ \cos\zeta\sin\eta\cos\Theta\sin\left(2\pi(i-1)/N+\omega_0 t\right)+\cos\zeta\sin\eta\sin\Theta\cos\left(2\pi(i-1)/N+\omega_0 t\right) \end{bmatrix} dl$$

(7.37)

Integrating Equation (7.37) over the length of the i^{th} main tether results the torque of propulsion force

$$\begin{aligned}\tau_{t\_i} &= \frac{1}{2}\sigma_{new}\nu L^2 V_{new\_i}\begin{bmatrix} \cos\zeta\cos\eta\sin\left(2\pi(i-1)/N+\omega_0 t\right) \\ -\cos\zeta\cos\eta\cos\left(2\pi(i-1)/N+\omega_0 t\right) \\ \sin\zeta\cos\Theta\cos\left(2\pi(i-1)/N+\omega_0 t\right)-\sin\zeta\sin\Theta\sin\left(2\pi(i-1)/N+\omega_0 t\right)+ \\ \cos\zeta\sin\eta\cos\Theta\sin\left(2\pi(i-1)/N+\omega_0 t\right)+\cos\zeta\sin\eta\sin\Theta\cos\left(2\pi(i-1)/N+\omega_0 t\right) \end{bmatrix} \\ &= \frac{1}{2}\sigma_{new}\nu L^2 \boldsymbol{Q}\boldsymbol{R}_i V_{new\_i}\end{aligned} \tag{7.38}$$

where

$$\boldsymbol{Q} = \begin{bmatrix} \cos\zeta\cos\eta & 0 & 0 \\ 0 & -\cos\zeta\cos\eta & 0 \\ \cos\zeta\sin\eta\cos\Theta-\sin\zeta\sin\Theta & \cos\zeta\sin\eta\sin\Theta\sin\zeta\cos\Theta & 0 \end{bmatrix}$$

$$\boldsymbol{R}_i = \begin{bmatrix} \sin\left(2\pi(i-1)/N+\omega_0 t\right) & \cos\left(2\pi(i-1)/N+\omega_0 t\right) & 0 \end{bmatrix}^T \tag{7.39}$$

Thus, the total propulsive force torques of E-sail can be obtained as

$$\tau_t = \frac{1}{2}\sigma_{new}\nu L^2 \boldsymbol{Q}\boldsymbol{R} V_{new\_total} \tag{7.40}$$

where $\boldsymbol{R} = \boldsymbol{R}_1 + \boldsymbol{R}_2 + \cdots \boldsymbol{R}_N$, $V_{new\_total} = V_{new\_1} + V_{new\_2} + \cdots + V_{new\_N}$ is the total voltage of main tethers.

7.3.2.2 Attitude Tracking Control of the E-sail using Charged Main Tethers

Recalling Equation (7.7), the second-order attitude dynamical equations of motion of the E-sail with the new torque can be written as

$$\ddot{\boldsymbol{\varpi}} = \boldsymbol{D}(\boldsymbol{\varpi})\left(\boldsymbol{U}_{new} - \boldsymbol{C}(\boldsymbol{\varpi},\dot{\boldsymbol{\varpi}})\right) \tag{7.41}$$

where $\boldsymbol{\varpi}$, $\dot{\boldsymbol{\varpi}}$, $\ddot{\boldsymbol{\varpi}}$ are the vector of Euler angles, $\boldsymbol{C}(\boldsymbol{\varpi},\dot{\boldsymbol{\varpi}})$ is given in Equation (7.8), $\boldsymbol{U}_{new}=\boldsymbol{B}_{new}\boldsymbol{QR}V_{new\_total}$, $\boldsymbol{B}_{new}$ is given by

$$\boldsymbol{B}_{new}=\frac{1}{4J}\sigma_{new}\nu L^2\begin{bmatrix}2&0&0\\0&2&0\\0&0&1\end{bmatrix} \tag{7.42}$$

The SMC is also used to tracking the attitude angles of the E-sail during the orbital transfer from Earth to Mars, which is kept the same with Section 7.2.1.1. Also, the exponential control law is also adopted in this section. Thus combining Equations (7.11) and (7.12) yields

$$\dot{\boldsymbol{S}}=-\boldsymbol{k}_1\operatorname{sgn}(\boldsymbol{S})-\boldsymbol{k}_2\boldsymbol{S}=\boldsymbol{D}(\boldsymbol{\varpi})\left(\boldsymbol{U}_{new}-\boldsymbol{C}(\boldsymbol{\varpi},\dot{\boldsymbol{\varpi}})\right)+\boldsymbol{\lambda}\dot{\boldsymbol{\varpi}}_e \tag{7.43}$$

Thus, the voltage modulation of the main tethers for generating the attitude control torque vector is

$$\boldsymbol{R}V_{new\_total}=\left(\boldsymbol{B}_{new}\boldsymbol{Q}\right)^{-1}\left[\boldsymbol{C}(\boldsymbol{\varpi},\dot{\boldsymbol{\varpi}})-\boldsymbol{D}^{-1}(\boldsymbol{\varpi})\left(\boldsymbol{k}_1\operatorname{sgn}(\boldsymbol{S})+\boldsymbol{k}_2\boldsymbol{S}+\boldsymbol{\lambda}\dot{\boldsymbol{\varpi}}_e\right)\right] \tag{7.44}$$

Similar, the distribution of the main tethers' voltages also follows the sinusoidal function, that is,

$$V_{new\_i}=V_{baseline}\left(1+\sin\theta_i\Big/\sum_{i=1}^{N}\sin\theta_i\right) \tag{7.45}$$

where $V_{baseline}$ is the baseline voltage of the main tether.

Therefore, the voltage V_{new_i} of the i^{th} main tether can be solved accordingly. Moreover, it should be mentioned that the attitude angle Θ is 90° during the orbital transfer. As presented in Equations (7.30) and (7.41), the equations of motion of the coupled orbital-attitude dynamics of the E-sail are given. The attitude angles of the E-sail can be tracked by using the designed voltage modulation controller.

7.3.2.3 Numerical Results

In this section, the attitude tracking control of the E-sail is investigated by parametric analysis. The parameters of the E-sail are consistent with Table 7-4. Further, the control parameter of the attitude controller is the same with Table 7-3, and the initial Euler angles are given by Figure 7-22. The baseline voltage of the main tether is 20 kV, and the minimum/maximum voltage of the main tether is 0/40 kV. The simulation results are shown in Figure 7-25 to Figure 7-27.

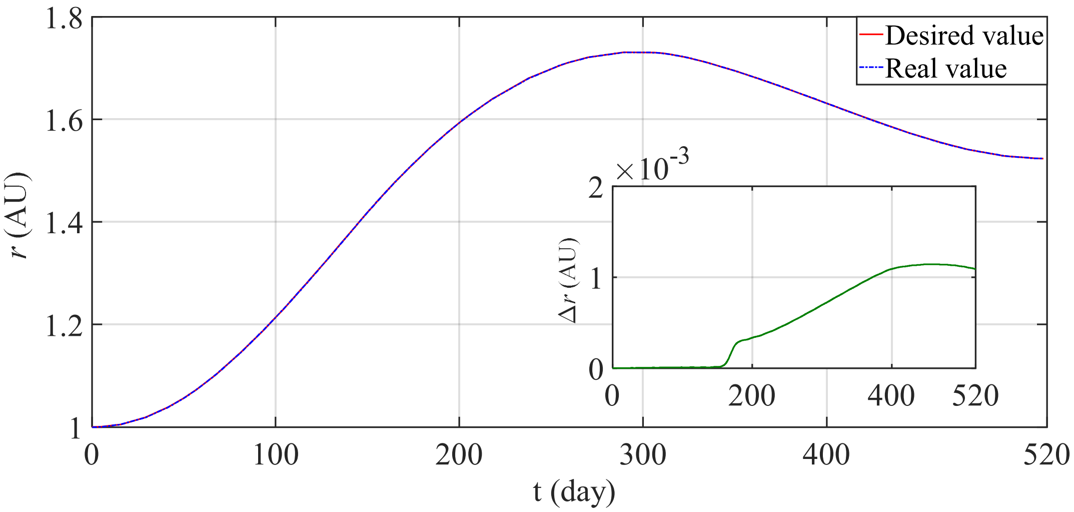

Figure 7-25 Time histories of the desired, real and error distances from the Sun to E-sail.

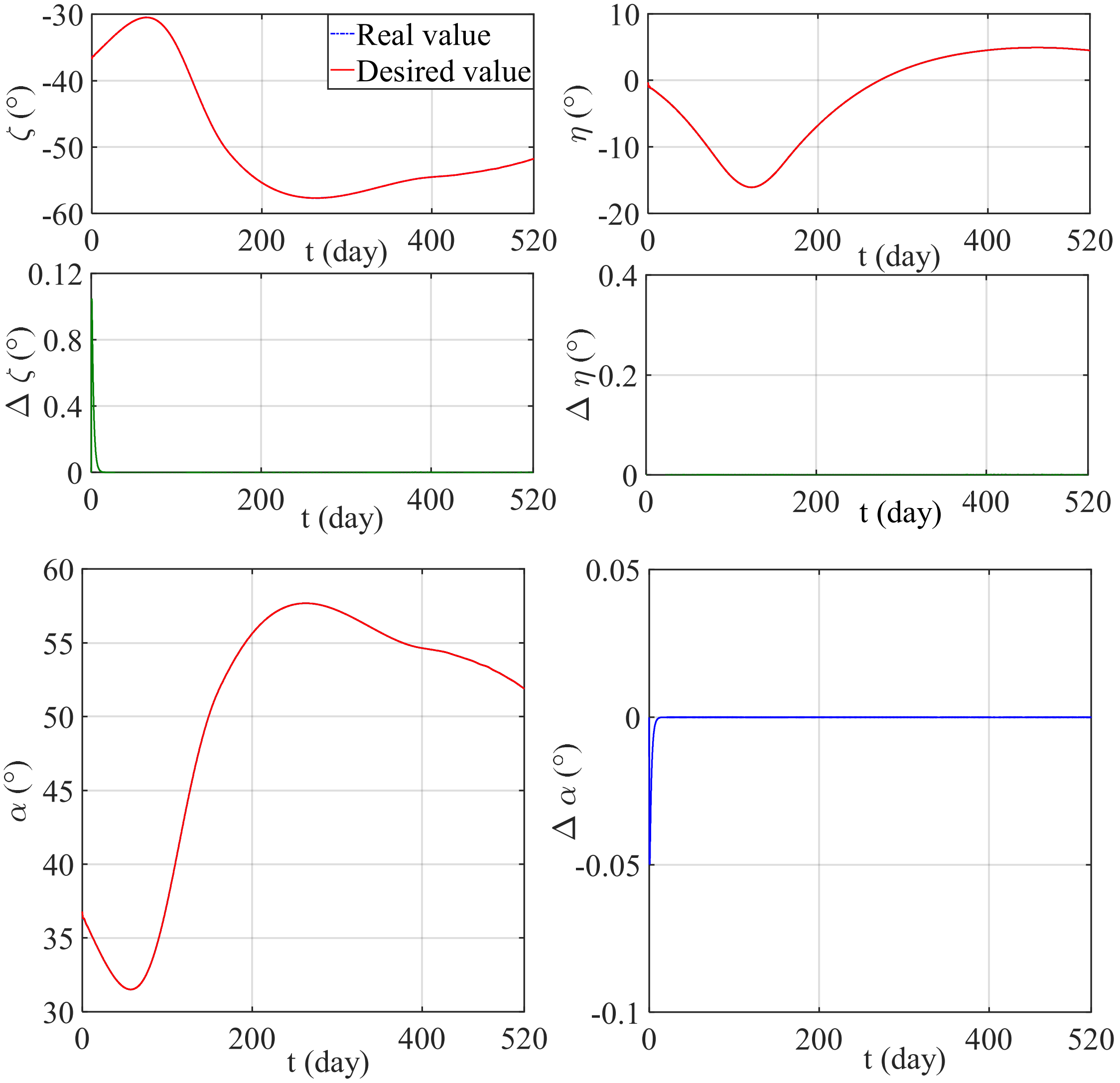

Figure 7-26 Time histories of the desired, real and error attitude angles.

Figure 7-25 shows the desired Sun/E-sail distance is tracked in the duration of simulation with the small distance error. This can be explained by the time histories of the attitude angles, where the real attitude angles track the desired attitude angles obtained by the last section with very small error, as shown in Figure 7-26. This attitude control is achieved by modulating the voltage of main tethers, which will generate the control torque to tilt the E-sail orientation, as presented in Figure 7-27. In summary, it can be concluded that the developed controller is effective and high-accuracy to track the desired Earth-Mars trajectory.

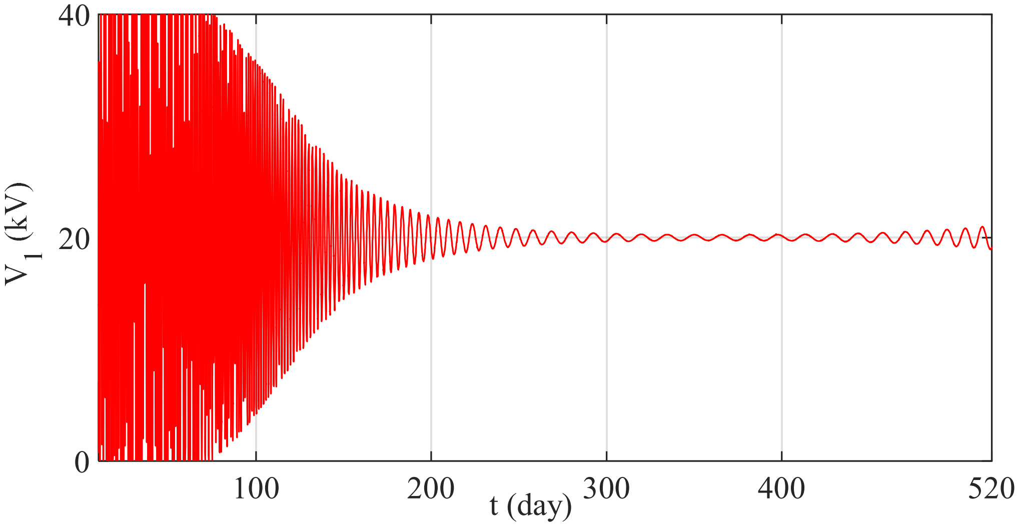

Figure 7-27 Time histories of the 1st main tether's voltage.

Chapter 8 CONCLUSION AND FUTURE WORK

Summary: In this chapter, the conclusions and contributions of the thesis are outlined. Furthermore, a brief description of further work is provided.

8.1 General Conclusion

This dissertation conducts in-depth research on the dynamics, attitude control, and trajectory tracking control of E-sail, which is adopted as a promising propellant propulsion for deep space exploration. To thoroughly investigate the E-sail, three different mathematical models are developed. First, the NPFEM E-sail model is applied to reveal the unknown mechanism behind the periodic coning motion and the physics that dictates the upper and lower spin bounds. The influences of propulsive force models, initial sail angle, and configuration stability on the dynamic characteristics of E-sail are investigated by the parameter analysis. Also, a simple PD controller acting on the remote units is proposed and demonstrated to control the orientation of E-sail. Meanwhile, a sliding mode control law is proposed to investigate the attitude control and stability analysis of E-sail. Then, the generalized E-sail model is adopted to study the modeling of rigid-flexible coupling influence on the attitude dynamics and spin control of the E-sail. In addition, the effect of

E-sail system parameters on the attitude dynamics of E-sail is studied. Finally, the reduced order analytical E-sail model is used to approximate the full-dimensional E-sail's attitude dynamics, develop a nonlinear control law that can be applied to the NPFEM E-sail model to stable the E-sail system, and deal with a trajectory tracking problem.

8.2 Thesis Contributions

This dissertation focuses on the dynamics and control of extraplanetary exploration through an E-sail. The main contributions of the current work are summarized as follows.

8.2.1 Mathematic Formulations of the E-sail

The mathematical formulations of the E-sail are developed to meet the requirements of E-sail in different scenarios. To capture the coupling effects of orbital and self-spinning motions of the E-sail, and the elastic deformation of tethers, the high-fidelity E-sail model is obtained by using the nodal position finite element method. To study the influence of rigid-flexible coupling on the attitude dynamics and spin control of E-sail, a generalized E-sail model with the attitude of central spacecraft is developed. Finally, a reduced order analytical E-sail model is derived to thoroughly study the stability control of the flexible E-sail in attitude maneuver.

8.2.2 Dynamic Characteristics of the E-sail

Some significant findings are presented in this section based on these three models. First, the periodic coning motion is theoretically explained, and the analytic solution of its frequency is derived and verified by numerical simulation. The equilibrium shape of the main tether of the E-sail without auxiliary tethers is obtained. Through the parametric analysis, it is discovered that the coning motion has little influence on the macro dynamic behaviors of E-sail. Next, the new theoretical lower bounds of spin rate for E-sail with auxiliary tether is derived for any sail angle. The result shows the lower bound of the E-sail with auxiliary tethers depends on the strain of the main tethers and the stable configuration of the E- sail. It also indicates that auxiliary tethers are essential for a stable configuration of E-sail at non-zero sail angle even if the parameters change.

Furthermore, the analysis shows the offset of CM and thrust of E-sail varies dynamically due to the tether deformation. Also, it is revealed that the disturbance torques has significant influences on the dynamic characteristics of the E-sail. Moreover, the influence of the solar wind fluctuations and E-sail geometrical configuration on the dynamic responses of E-sail is noticeable. Finally, it is suggested that the spin plane of the E-sail should pass through the CM of central spacecraft for better stability to avoid the potential tether wrapping around the central spacecraft.

8.2.3 Control Strategy of the E-sail

Through parameter analysis, the control performance of E-sail spin rate is demonstrated. It indicates the spin rate can be controlled to the desired value within finite time by a simple control law, even in the tether deployment process, with finite control input mainly at the remote units. Then, it is verified that the alternative sail angle control strategy is effective in maneuvering and controlling the desired sail angle. Further, the investigation finds that the control law has the similar performances in both the high-fidelity and reduced order analytical E-sail models if the proper control gains are selected. It shows the attitude of the E-sail can be stably controlled by a control law developed from a reduced order analytical E-sail model. The current work also shows the high-fidelity E-sail model provides virtual testbed to evaluate the control performance of the control strategy for E-sail attitude control. Finally, numerical results indicates that the proposed trajectory tracking law works properly by considering the deformation of tethers.

8.3 Further Work

The following research is summarized as follows to continue and expand the current work.

(i) Investigate the long-term influences of the space environment perturbations on the E-sail dynamics by using the measured data of solar wind velocity by Voyage 1 and 2.

(ii) Actively control the nutation angle to stability the attitude of E-sail, which is caused by the violent oscillation of the central spacecraft angular velocity. To suppress the angular velocity of nutation, the control torques perpendicular to the main spin axis should be applied.

(iii) Investigate the dynamics and stability of an E-sail in the displaced non-Keplerian orbit by using the high-fidelity E-sail model, where the elastic deformations of the tethers, the coupling effects of orbital and self-spinning motions are considered.

(iv) Consider the effect of the thermal contraction and expansion of tethers on the long-term dynamics of E-sail with NPFEM model.

(v) Track the designed trajectory of E-sail mission scenario with the NPFEM E-sail model in order to perform an approximate analysis before the real space E-sail mission.

Bibliography

[1] P. Janhunen, Electric sail for spacecraft propulsion, Journal of Propulsion and Power, 20(4) (2004) 763-767.

[2] P. Janhunen, U.S. Patent No. 7,641,151 (2010).

[3] P. Janhunen, P.K. Toivanen, J. Polkko, S. Merikallio, P. Salminen, E. Haeggström, H. Seppänen, R. Kurppa, J. Ukkonen, S. Kiprich, G. Thornell, H. Kratz, L. Richter, O. Krömer, R. Rosta, M. Noorma, J. Envall, S. Lätt, G. Mengali, A.A. Quarta, H. Koivisto, O. Tarvainen, T. Kalvas, J. Kauppinen, A. Nuottajärvi, A. Obraztsov, Invited article: Electric solar wind sail: Toward test missions, Review of Scientific Instruments, 81 (2010) 1–11.

[4] H. Seppänen, T. Rauhala, S. Kiprich, J. Ukkonen, M. Simonsson, R. Kurppa, P. Janhunen, E. Hæggström, One kilometer (1 km) electric solar wind sail tether produced automatically, Review of Scientific Instruments, 84(9) (2013) 095102.

[5] J.A. Fulton, H. Schaub, Fixed-axis electric sail deployment dynamics analysis using hub-mounted momentum control, Acta Astronautica, 144 (2018) 160–170.

[6] G. Li, Z.H. Zhu, C. Du, Stability and control of radial deployment of electric solar wind sail, Nonlinear Dynamics, 7 (2021) 8–10.

[7] M. Bassetto, L. Niccolai, A.A. Quarta, G. Mengali, A comprehensive

review of Electric Solar Wind Sail concept and its applications, Progress in Aerospace Sciences, 128 (2022) 100768.

[8] B. Wie, Solar sail attitude control and dynamics, part 1, Journal of Guidance, Control, and Dynamics, 27 (4) (2004) 526–535.

[9] B. Wie, Solar sail attitude control and dynamics, part 2, Journal of Guidance, Control, and Dynamics, 27 (4) (2004) 536–544.

[10] A. Pizarro-Chong, A.K. Misra, Dynamics of multi-tethered satellite formations containing a parent body, Acta Astronautica, 63 (2008) 1188–1202.

[11] G. Avanzini, M. Fedi, Refined dynamical analysis of multi-tethered satellite formations, Acta Astronautica, 84 (2013) 36–48.

[12] P. Janhunen, A.A. Quarta, G. Mengali, Electric solar wind sail mass budget model, Geoscientific Instrumentation Methods and Data Systems, 2 (2013) 85-95.

[13] P. Janhunen, A. Sandroos, Simulation study of solar wind push on a charged wire: Basis of solar wind electric sail propulsion, Annales Geophysicae, 25 (2007) 755–767.

[14] P.K. Toivanen, P. Janhunen, Spin Plane Control and Thrust Vectoring of Electric Solar Wind Sail, Journal of Propulsion and Power, 29 (2013) 178–185.

[15] M. Huo, G. Mengali, A.A. Quarta, Electric sail thrust model from a

geometrical perspective, Journal of Guidance, Control, and Dynamics, 41 (2018) 735–741.

[16] P. Janhunen, P. Toivanen, TI tether rig for solving secular spinrate change problem of electric sail, (2016).

[17] P. Janhunen, P. Toivanen, A scheme for controlling the E-sail's spin rate by the E-sail effect itself, Space Propulsion 2018, Seville, Spain, 2018.

[18] G. Li, Z.H. Zhu, C. Du, Flight dynamics and control strategy of electric solar wind sails, Journal of Guidance, Control, and Dynamics, 43 (2020) 462–474.

[19] M. Bassetto, G. Mengali, A.A. Quarta, E-sail attitude control with tether voltage modulation, Acta Astronautica, 166 (2020) 350-357.

[20] L. Huang, H. Wen, L. Cheng, S. Xu, Nonlinear model predictive control for attitude maneuver of a barbell electric sail through voltage regulation, Acta Astronautica, 179 (2021) 146-152.

[21] A.A. Quarta, G. Mengali, Electric sail mission analysis for outer solar system exploration, Journal of Guidance, Control, and Dynamics, 33 (2010) 740–755.

[22] A. A. Quarta, G. Mengali, P. Janhunen, Optimal interplanetary rendezvous combining electric sail and high thrust propulsion system, Acta Astronautica, 68 (2011) 603–621.

[23] A.A. Quarta, G. Mengali, Optimal nodal flyby with near-Earth asteroids

using electric sail, Acta Astronautica, 82 (2013) 189-196.

[24] M. Huo, H. Liao, Y. Liu, N. Qi, The Coupled Orbit-Attitude Dynamics and Control of Electric Sail in Displaced Solar Orbits, International Journal of Aerospace Engineering, 2017 (2017) 12.

[25] G. Aliasi, G. Mengali, A. A. Quarta, Artificial equilibrium points for an electric sail with constant attitude, Journal of Spacecraft and Rockets, 50(6) (2013) 1295-1298.

[26] S. Merikallio, P. Janhunen, Moving an asteroid with electric solar wind sail, Astrophysics and Space Sciences Transactions (ASTRA), 6 (2010) 41.

[27] C. Du, Z.H. Zhu, G. Li, Analysis of thrust-induced sail plane coning and attitude motion of electric sail, Acta Astronautica, 178 (2021) 129-142.

[28] F. Liu, Q. Hu, Y. Liu, Attitude Dynamics of Electric Sail from Multibody Perspective, Journal of Guidance, Control, and Dynamics, 41 (2018) 2633-2646.

[29] M. Bassetto, G. Mengali, A.A. Quarta, Stability and control of spinning electric solar wind sail in heliostationary orbit, Journal of Guidance, Control, and Dynamics, 42 (2019) 425–431.

[30] G. Li, Z.H. Zhu, C. Du, S.A. Meguid, Characteristics of coupled orbital-attitude dynamics of flexible electric solar wind sail, Acta Astronautica, 159 (2019) 593-608.

[31] P. Toivanen, P. Janhunen, Thrust vectoring of an electric solar wind sail with a realistic sail shape, Acta Astronautica, 131 (2017) 145–151.

[32] M. Bassetto, G. Mengali, A.A. Quarta, Thrust and torque vector characteristics of axially-symmetric E-sail, Acta Astronautica, 146 (2018) 134–143.

[33] M. Bassetto, G. Mengali, A.A. Quarta, Attitude dynamics of an electric sail model with a realistic shape, Acta Astronautica, 159 (2019) 250–257.

[34] P.K. Toivanen, P. Janhunen, Electric sailing under observed solar wind conditions, Astrophysics and Space Sciences Transactions, 5 (2009) 61–69.

[35] L. Niccolai, A. Anderlini, G. Mengali, A.A. Quarta, Electric sail displaced orbit control with solar wind uncertainties, Acta Astronautica, 162 (2019) 563–573.

[36] A. Caruso, L. Niccolai, G. Mengali, A.A. Quarta, Electric sail trajectory correction in presence of environmental uncertainties, Aerospace Science and Technology, 94 (2019) 105395.

[37] G. Mengali, A.A. Quarta, P. Janhunen, Electric sail performance analysis, Journal of Spacecraft and Rockets, 45 (2008) 122–129.

[38] M. Huo, G. Mengali, A. A. Quarta, Mission analysis for vesta and ceres exploration using electric sail with classical and advanced thrust models, IEEE Transactions on Aerospace and Electronic Systems, 55(6) (2019)

2796-2804.

[39] L. Niccolai, A. A. Quarta, G. Mengali, Trajectory Approximation of a Solar Sail with Constant Pitch Angle and Optical Degradation, IEEE Transactions on Aerospace and Electronic Systems, (2021).

[40] P. Janhunen, Increased electric sail thrust through removal of trapped shielding electrons by orbit chaotisation due to spacecraft body, Annales Geophysicae, 27 (2009) 3089–3100.

[41] A. Sanchez-Torres, Propulsive force in electric solar sails for missions in the heliosphere, IEEE Transactions on Plasma Science, 47 (2019) 1657–1662.

[42] Y. Leblanc, G.A. Dulk, J.L. Bougeret, Tracing the electron density from the corona to 1 au, Solar Physics, 183 (1998) 165–180.

[43] E.C. Sittler, J.D. Scudder, An empirical polytrope law for solar wind thermal electrons between 0.45 and 4.76 AU: Voyager 2 and Mariner 10, Journal of Geophysical Research, 85 (1980) 5131–5137.

[44] P. Janhunen, PIC Simulation of Electric Sail with Explicit Trapped Electron Modeling, in: ASP Conference Series, vol. 459, Astronomical Society of the Pacific, San Francisco, 2012, 271–277.

[45] A. Sanchez-Torres, Propulsive force in an electric solar sail, Contributions to Plasma Physics, 54 (2014) 314–319.

[46] P. Janhunen, Boltzmann electron PIC simulation of the E-sail effect,

Annales Geophysicae, 33 (2015) 1507–1512.

[47] B.M. Wiegmann, Summary of NASA's electric sail propulsion system investigations from 2014-2017, AIAA Aerospace Sciences Meeting, 2018.

[48] M. Bassetto, A. A. Quarta, G. Mengali, Locally-optimal electric sail transfer. Proceedings of the Institution of Mechanical Engineers, Part G: Journal of Aerospace Engineering, 233(1) (2019) 166-179.

[49] K. Yamaguchi, H. Yamakawa, Study on orbital maneuvers for electric sail with on-off thrust control, Aerospace Technology Japan, the Japan Society for Aeronautical and Space Sciences, 12 (2013) 79-88.

[50] K. Yamaguchi, H. Yamakawa, Electric solar wind sail kinetic energy impactor for asteroid deflection missions, The Journal of the Astronautical Sciences, 63(1) (2016) 1-22.

[51] K. Yamaguchi, K. Miyata, Orbital maneuvering of electric solar wind sail based on an advanced solar wind force model, Acta Astronautica, 166, (2020) 417-430.

[52] P. Toivanen, P. Janhunen, J. Envall, Electric sail control mode for amplified transverse thrust, Acta Astronautica, 106 (2015) 111-119.

[53] K. D. Kumar, Review on dynamics and control of nonelectrodynamic tethered satellite systems, Journal of spacecraft and rockets, 43(4) (2006) 705-720.

[54] P. Huang, F. Zhang, L. Chen, Z. Meng, Y. Zhang, Z. Liu, Y. Hu, A review

of space tether in new applications, Nonlinear Dynamics 94(1) (2018) 1-19.

[55] M. Simmons, C. J. Montalvo, Reduced order model of a barbell electric sail, In AIAA Scitech 2019 Forum, 2019.

[56] M. Huo, J. Zhao, S. Xie, N. Qi, Coupled attitude-orbit dynamics and control for an electric sail in a heliocentric transfer mission, PloS one, (2015) 10(5) p.e0125901.

[57] T. D. Lillian, Modal Analysis of Electric sail, Acta Astronautica, 185 (2021) 140-147.

[58] J. Fulton, H. Schaub, Fixed-axis electric sail deployment dynamics analysis using hub-mounted momentum control, Acta Astronautica, 144, (2018) 160-170.

[59] F. Liu, Q. Hu, J. Zhang, K. Yang, Y. Li, Dynamics of Single Charged Wire for Solar Wind Electric Sail, In 31st International Symposium on Space Technology and Science, 2017.

[60] C. Montalvo, H. White, Braking control law for a barbell Electric Sail, Acta Astronautica, 160 (2019) 1-6.

[61] C. Montalvo, B. Wiegmann, Electric sail space flight dynamics and controls, Acta Astronautica, 148 (2018) 268-275.

[62] M. Simmons, C. Montalvo, Vibration modes of an electric sail, Journal of Guidance, Control, and Dynamics, 43(7) (2020) 1393-1398.

[63] L. Boni, M. Bassetto, G. Mengali, A. A. Quarta, Electric sail static structural analysis with finite element approach, Acta Astronautica, 175 (2020) 510-516.

[64] Z. H. Zhu, S. A. Meguid, Elastodynamic analysis of aerial refueling hose using curved beam element, AIAA journal, 44(6) (2006) 1317-1324.

[65] K. U. Kristiansen, P. L. Palmer, R. M. Roberts, Numerical modelling of elastic space tethers, Celestial Mechanics and Dynamical Astronomy, 113(2) (2012) 235-254.

[66] A. Shabana, Dynamics of multibody systems, Cambridge university press, 2020.

[67] F. J. Sun, Z. H. Zhu, M. LaRosa, Dynamic modeling of cable towed body using nodal position finite element method, Ocean Engineering, 38(4) (2011) 529-540.

[68] R. Wang, C. Wei, Y. Wu, Y. Zhao, The study of spin control of flexible electric sail using the absolute nodal coordinate formulation, In 2017 IEEE International Conference on Cybernetics and Intelligent Systems (CIS) and IEEE Conference on Robotics, Automation and Mechatronics (RAM), 2017.

[69] H. Ren, K. Yang, A referenced nodal coordinate formulation, Multibody System Dynamics, 51(3) (2021) 305-342.

[70] H. Ren, T. Yuan, M. Huo, C. Zhao, S. Zeng, Dynamics and control of a

full-scale flexible electric solar wind sail spacecraft, Aerospace Science and Technology, 119 (2021) 107087.

[71] C. Du, Z.H. Zhu, Dynamic characterization and sail angle control of electric solar wind sail by high-fidelity tether dynamics, Acta Astronautica, 189 (2021) 504-513.

[72] C. Du, Z.H. Zhu, G. Li, Rigid-flexible coupling effect on attitude dynamics of electric solar wind sail, Communications in Nonlinear Science and Numerical Simulation, 95 (2021) 105663.

[73] A. A. Quarta, G. Mengali, Analysis of Electric Sail Heliocentric Motion Under Radial Thrust, Journal of Guidance, Control, and Dynamics, 39(6) (2016) 1433–1437.

[74] P. Janhunen, Photonic spin control for solar wind electric sail, Acta Astronautica, 83 (2013) 85-90.

[75] P. Janhunen, P. Toivanen, An intrinsic way to control E-sail spin, (2014) arXiv preprint arXiv:1406.6847.

[76] C. Bombardelli, E. C. Lorenzini, M. B. Quadrelli, Retargeting Dynamics of a Linear Tethered Interferometer, Journal of Guidance, Control, and Dynamics, 27(6) (2004) 1061– 1067.

[77] S. Gong, J. Li, A new inclination cranking method for a flexible spinning solar sail, Transactions on Aerospace and Electronic Systems, 51(4) (2015) 2680-2696.

[78] C. R. McInnes, J. F. Simmons, Solar sail halo orbits part II-geocentric case, Journal of Spacecraft and Rockets, 29(4) (1992) 472-479.

[79] P. Janhunen, P. Toivanen, J. Envall, S. Merikallio, G. Montesanti, J. G. del Amo, U. Kvell, M. Noorma, S. Lätt, Electric solar wind sail applications overview, (2014) arXiv preprint arXiv:1404.5815.

[80] G. Mengali, A. A. Quarta, Non-Keplerian orbits for electric sails, Celestial Mechanics and Dynamical Astronomy, 105(1) (2009) 179-195.

[81] L. Niccolai, A. A. Quarta, G. Mengali, Electric sail elliptic displaced orbits with advanced thrust model. Acta Astronautica, 138 (2017) 503-511.

[82] L. Niccolai, A. Anderlini, G. Mengali, A. A. Quarta, Electric sail displaced orbit control with solar wind uncertainties, Acta Astronautica, 162 (2019) 563-573.

[83] X. Pan, A. A. Quarta, G. Mengali, M. Xu, Linearized relative motion and proximity control of E-sail-based displaced orbits, Aerospace Science and Technology, 99 (2020) 105574.

[84] W. Wang, G. Mengali, A. A. Quarta, J. Yuan, Formation flying for electric sails in displaced orbits. Part I: geometrical analysis, Advances in Space Research, 60(6) (2017) 1115-1129.

[85] W. Wang, G. Mengali, A. A. Quarta, J. Yuan, Formation flying for electric sails in displaced orbits. Part II: distributed coordinated control,

Advances in Space Research, 60(6) (2017) 1130-1147.

[86] P. Janhunen, J. P. Lebreton, S. Merikallio, M. Paton, G. Mengali, A. A. Quarta, E-sail Uranus entry probe mission, Planetary and Space Science, 104 (2014) 141-146.

[87] A. A. Quarta, G. Mengali, Electric sail missions to potentially hazardous asteroids, Acta Astronautica, 66(9-10) (2010) 1506-1519.

[88] A. A. Quarta, G. Mengali, P. Janhunen, Electric sail for a near-Earth asteroid sample return mission: Case 1998 KY26, Journal of Aerospace Engineering, 27(6) (2014) 04014031.

[89] M. Huo, G. Zhang, N. Qi, Y. Liu, X. Shi, Initial trajectory design of electric solar wind sail based on finite Fourier series shape-based method, IEEE Transactions on Aerospace and Electronic Systems, 55(6) (2019) 3674-3683.

[90] A. A. Quarta, G. Mengali, Minimum-time trajectories of electric sail with advanced thrust model, Aerospace Science and Technology, 55 (2016) 419-430.

[91] M. Huo, G. Mengali, A. A. Quarta, N. Qi, Electric sail trajectory design with Bezier curve-based shaping approach, Aerospace Science and Technology, 88 (2019) 126-135.

[92] Y. Wang, B. Bian, Trajectory tracking control of electric sail with input uncertainty and saturation constraint, Transactions of the Institute of

Measurement and Control, 39(7) (2017) 1007-1016.

[93] A. Caruso, L. Niccolai, G. Mengali, A. A. Quarta, Electric sail trajectory correction in presence of environmental uncertainties, Aerospace Science and Technology, 94 (2019) 105395.

[94] G. Aliasi, G. Mengali, A. A. Quarta, Artificial equilibrium points for electric sail with constant attitude, Journal of Spacecraft and Rockets, 50(6) (2013) 1295-1298.

[95] L. Niccolai, A. Caruso, A. A. Quarta, G. Mengali, Artificial collinear Lagrangian point maintenance with electric solar wind sail, IEEE Transactions on Aerospace and Electronic Systems, 56(6) (2020) 4467-4477.

[96] NASA Report to Congress: Near-earth object survey and definition: analysis of alternatives, 2007.

[97] S. Merikallio, P. Janhunen, Moving an asteroid with electric solar wind sail, Astrophysics and Space Sciences Transactions (ASTRA), 6(1) (2010) 41.

[98] K. Yamaguchi, H. Yamakawa, Electric solar wind sail kinetic energy impactor for asteroid deflection missions, The Journal of the Astronautical Sciences, 63(1) (2016) 1-22.

[99] G. Li, Z.H. Zhu, Long-term dynamic modeling of tethered spacecraft using nodal position finite element method and symplectic integration,

Celestial Mechanics and Dynamical Astronomy, 123(4) (2015) 363-386.

[100] H. Ding, X. Yin, Z.H. Zhu, L. Zhang, A high accurate hamiltonian nodal position finite element method for spatial cable structures undergoing long-term large overall motion, Communications in Nonlinear Science and Numerical Simulation, 70 (2019) 203–222.

[101] C. Liu, Q. Tian, H. Hu, Dynamics and control of a spatial rigid-flexible multibody system with multiple cylindrical clearance joints, Mechanism Machine Theory. 52 (2012) 106–129.

[102] C. Liu, Q. Tian, H. Hu, García-Vallejo D, Simple formulations of imposing moments and evaluating joint reaction forces for rigid-flexible multibody systems, Nonlinear Dynamics, 69 (2012) 127–147.

[103] H. Seppänen, S. Kiprich, R. Kurppa, P. Janhunen, E. Hæggström, Wire-to-wire bonding of μm- diameter aluminum wires for the Electric Solar Wind Sail, Microelectronic Engineering, 88 (2011) 3267–3269.

[104] J. Tang, G. Ren, W. Zhu, H. Ren, Dynamics of variable-length tethers with application to tethered satellite deployment. Communications in Nonlinear Science and Numerical Simulation, 16(8) (2011) 3411–3424.

[105] M. Gärdsback, and G. Tibert, Deployment control of spinning space webs, Journal of guidance, control, and dynamics, 32(1) (2009) 40-50.

[106] G. Shi, G. Li, Z. Zhu, and Z.H. Zhu, A virtual experiment for partial space elevator using a novel high-fidelity FE model, Nonlinear

Dynamics, 95(4) (2019) 2717-2727.

[107] V. I. Utkin, Sliding Modes in Control and Optimization, Springer-Verlag, Berlin, 1992.

[108] M. a Patterson, GPOPS – II Version 1 . 0 : A General-Purpose MATLAB Toolbox for Solving Optimal Control Problems Using the Radau Pseudospectral Method, (2014) 1–61.